SAND81-8008
Unlimited Release
UC-62c

Testing of the Prototype Heliostats for the Solar Thermal Central Receiver Pilot Plant

Prepared by Sandia National Laboratories, Albuquerque, New Mexico 87185 and Livermore, California 94550 for the United States Department of Energy under Contract DE-AC04-76DP00789.

Printed April 1981

Sandia National Laboratories
energy report

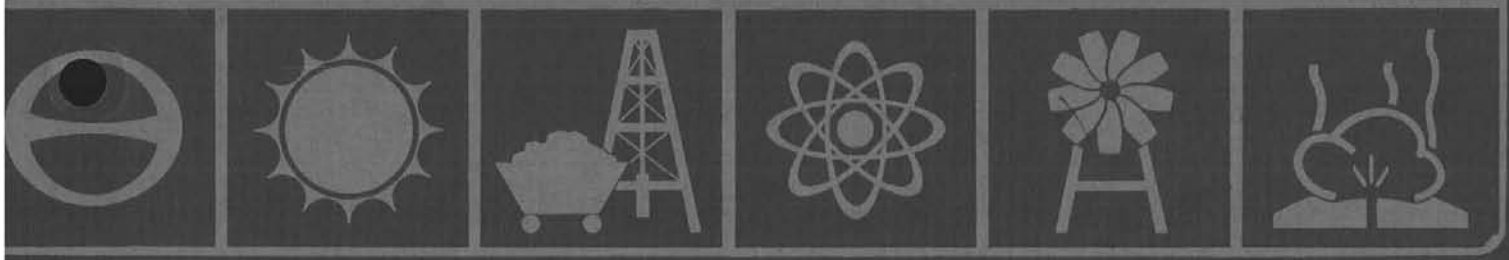

SF 2900-Q0B(3-80)

Issued by Sandia National Laboratories, operated for the United States Department of Energy by Sandia Corporation.

NOTICE

Printed in the United States of America
Available from
National Technical Information Service
U. S. Department of Commerce
5285 Port Royal Road
Springfield, VA 22161
Price: Printed Copy $9.50 ; Microfiche $3.00

SAND81-8008
Unlimited Release
Printed April 1981

UC-62c

TESTING OF THE PROTOTYPE HELIOSTATS FOR THE SOLAR THERMAL CENTRAL RECEIVER PILOT PLANT

Solar Programs Department
Sandia National Laboratories, Livermore

Central Receiver Test Facility Division
Sandia National Laboratories, Albuquerque

ABSTRACT

As part of the competition for production of heliostats for the pilot plant, the Martin Marietta Corporation and the McDonnell Douglas Astronautics Company each built prototype heliostats and components (drive mechanisms and mirror modules) which were subjected to an extensive test program by Sandia National Laboratories in 1979. The purpose of this report is to present an overview of the tests and their results.

TABLE OF CONTENTS

INTRODUCTION

In September 1978, the Department of Energy (DOE) and the San Francisco Operations Office of the DOE initiated a one-year competitive heliostat design phase program on a generic glass/metal single-pedestal design concept recommended by Sandia National Laboratories (SNL) for the Barstow 10-MW_e pilot plant. Martin Marietta Corporation (MMC) of Denver, Colorado, and McDonnell Douglas Astronautics Company (MDAC) of Huntington Beach, California, were the selected contractors. These competitive contracts, designated as Phase I Preproduction Activity, covered the detail design, development, and fabrication of prototype test hardware. The outcome became part of the basis for the DOE's evaluation and ultimate contractor selection for Phase II Heliostat Production.

SNL in Livermore (SNLL), in support of the DOE/Solar Ten Megawatt Project Office (STMPO) in El Monte, California, was responsible for defining and executing the heliostat test evaluation program. The program began in June 1979 and, with some exception, concluded in early October 1979. Partial (90 percent) results of this test program were initially reported to the 2nd-Generation Heliostat development contractors at an all-day workshop presentation at Howard Johnson's Motor Lodge, Dublin, California, on January 24, 1980. Another short review of the test results was presented at the DOE/Semiannual Review at Albuquerque, New Mexico, on March 20, 1980. This report represents the complete and final test report.

Although the comparative results of the heliostat test evaluation program were a major factor in selecting the Phase II production contractor, they were not the sole basis for judging the competitive designs. Other considerations, such as contractor performance, O&M evaluations, and quoted costs, all determined the ultimate selection of MMC as the heliostat production contractor for Barstow.

Design Descriptions

Before describing the test activities, it seems appropriate to first give a brief description of the two competitive heliostat designs, at least to understand their significant differences. Figure 1 is a photograph taken of the preproduction heliostats installed at the Central Receiver Test Facility (CRTF), SNL in Albuquerque, New Mexico (SNLA). The two on the right are MMC's heliostats, and the two on the left are MDAC's. At first glance, particularly from a front view, they have an obvious similar appearance since the generic design (glass/pedestal/inverted stow) was dictated by the DOE's request for quotation and SNL's generated specification. Upon closer inspection, however, the uniqueness of each design becomes apparent.

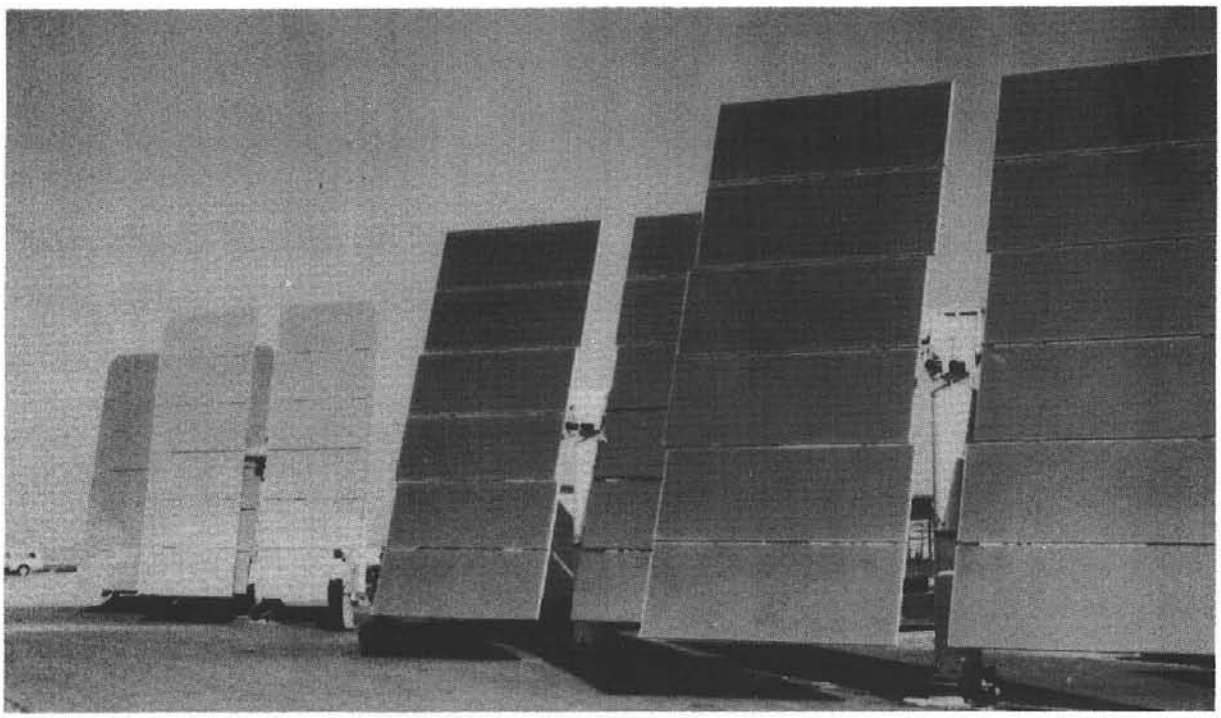

Figure 1. Preproduction Heliostats Installed at CRTF

Figure 2 is an artist's conception of the backside view of the MMC heliostat design. Here the use of open welded/steel trusses with three-point attachment of the mirror modules is evident. Note the dimensional offset of the through torque-tube with regard to the vertical center of the module array, thus minimizing the mass/center of gravity offset of the total reflective assembly with regard to the elevation axis of the drive mechanism. Figure 3 conveys the overall size/dimensions of the heliostat envelope. Figure 4 shows an external view of the drive assembly, complete with the connecting arms, limit switch, plus encoder mounting bracketry, and pedestal adaptor. Figure 5 shows the internal design/arrangement of the gear box. Note that both AZ and EL drive trains employ the identical first stage worm/gear reduction system and intermediate helical pinion shafts. It is only in the helical output gearing and drive shafts that the two systems differ. The three shaft exits of the gear box are all double sealed, and "thermal pumping" past the seals is prevented by the equalizing pressure diaphragm shown in the upper left view. Figure 6 shows the honeycomb core structure of the mirror module assembly.

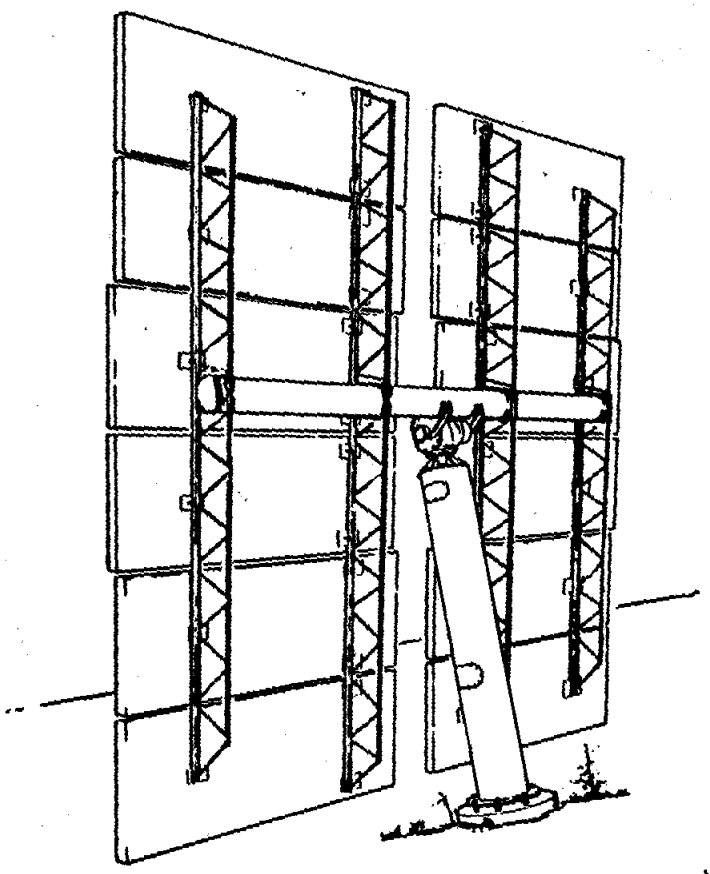

Figure 2. MMC 10 MW_e Solar Pilot Plant Heliostat

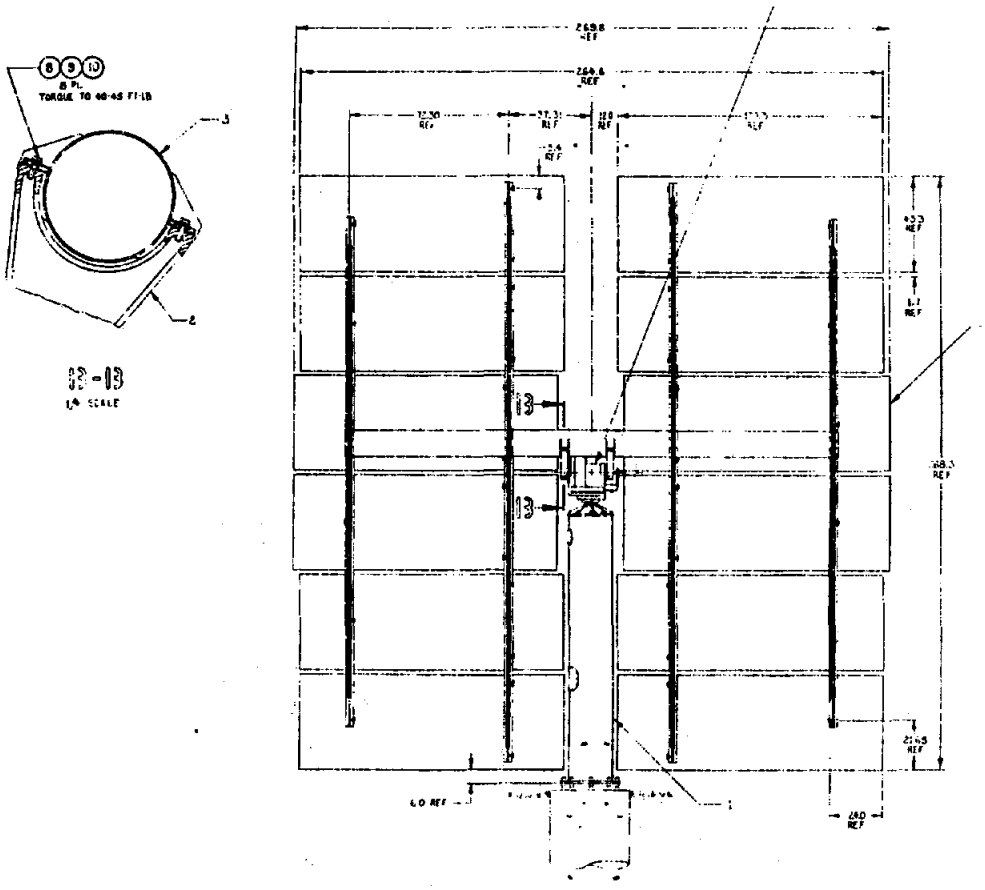

Figure 3. MMC Heliostat Envelope (rear view)

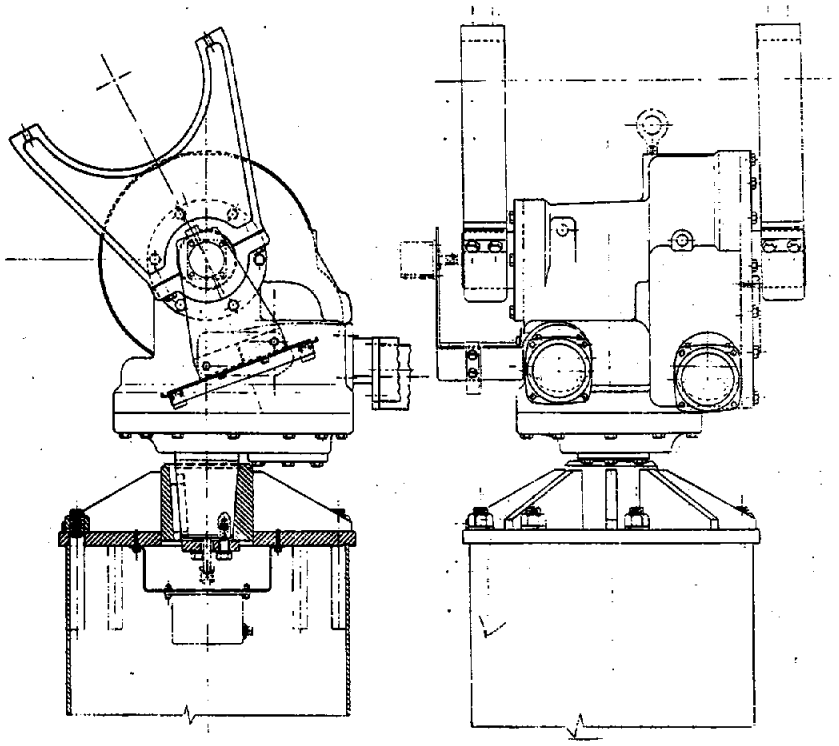

Figure 4. MMC 10 MWe Solar Power Plant Drive Mechanism Assembly

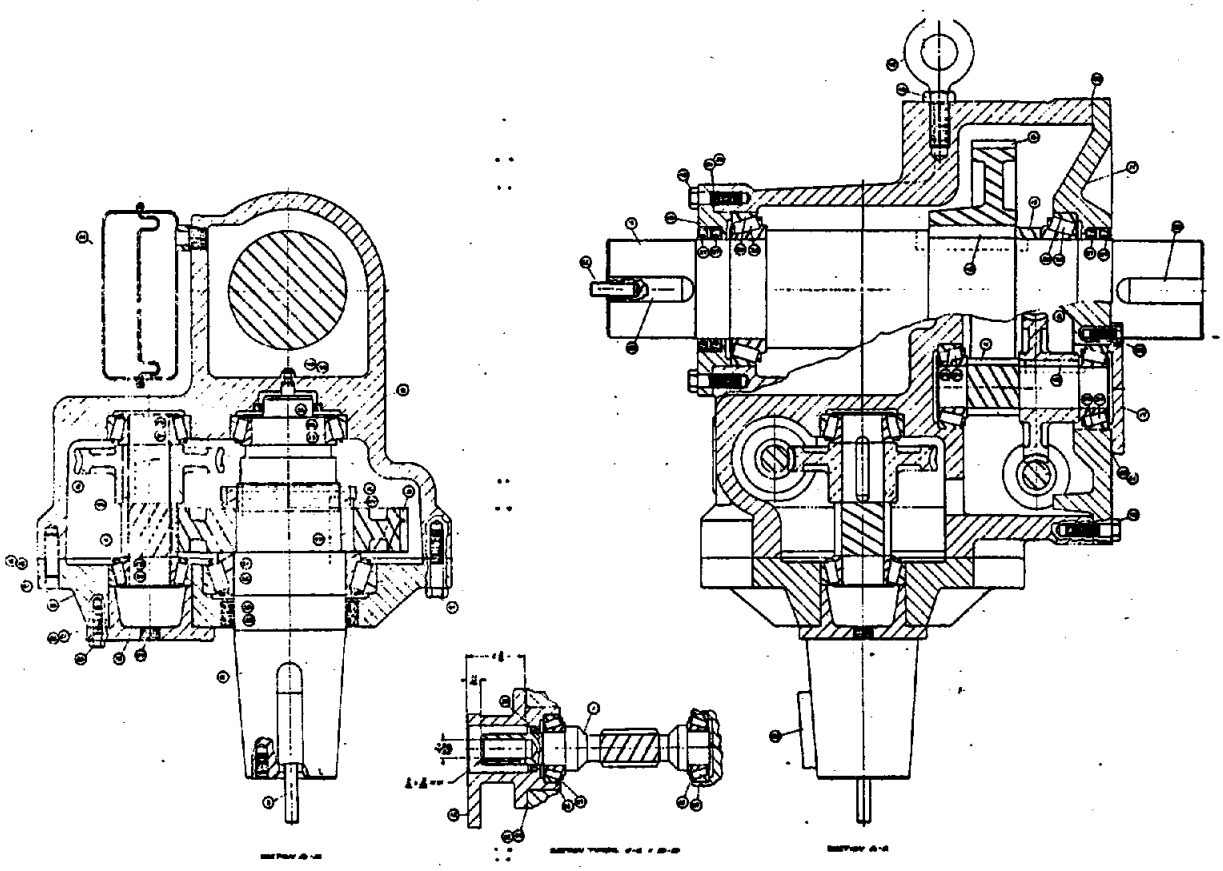

Figure 5. MMC Gear Box Internal Design

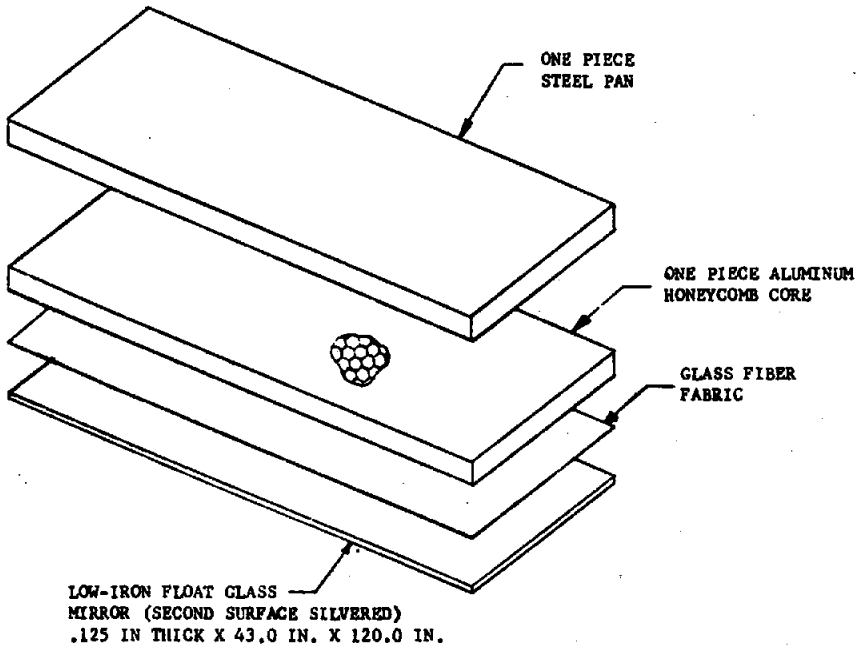

Figure 6. MMC Mirror Module Assembly Honeycomb Core Structure

Figure 7 is an artist's conception of the backside of MDAC's heliostat design. Here 18-inch deep roll-formed steel C-sections, flange bolted to a 16-inch diameter one-piece torque tube, supports the mirror modules via a four-point attachment design. The diagonal bracing was added to provide lateral stiffness to the deep, thin-wall cross beams. Unlike the MMC design, MDAC employs two distinctly different design concepts for the AZ and EL drive systems. Two linear screw jacks, interconnected in series through a drag link member, are used to accomplish 180 degrees total elevation travel. Figure 8 shows further details of the elevation linear drive action, with one jack used for 90 degrees of tracking motion and another jack to achieve the inverted stow position. The approximate 270 degrees of azimuth rotation needed is accomplished through a harmonic drive system, a cross section of which is shown in Figure 9. A first-stage worm/gear reduction is used to drive the three-lobe wave generator. Figure 10 conveys the overall envelope size of the heliostat, but note that the inverted stow position results in a different envelope outline due to the off-center arc swing of the torque tube. Figure 11 shows the glass/styrofoam core/steel-backface structure of MDAC's mirror module assembly.

In summary, Table I itemizes the significant features of each contractor's design.

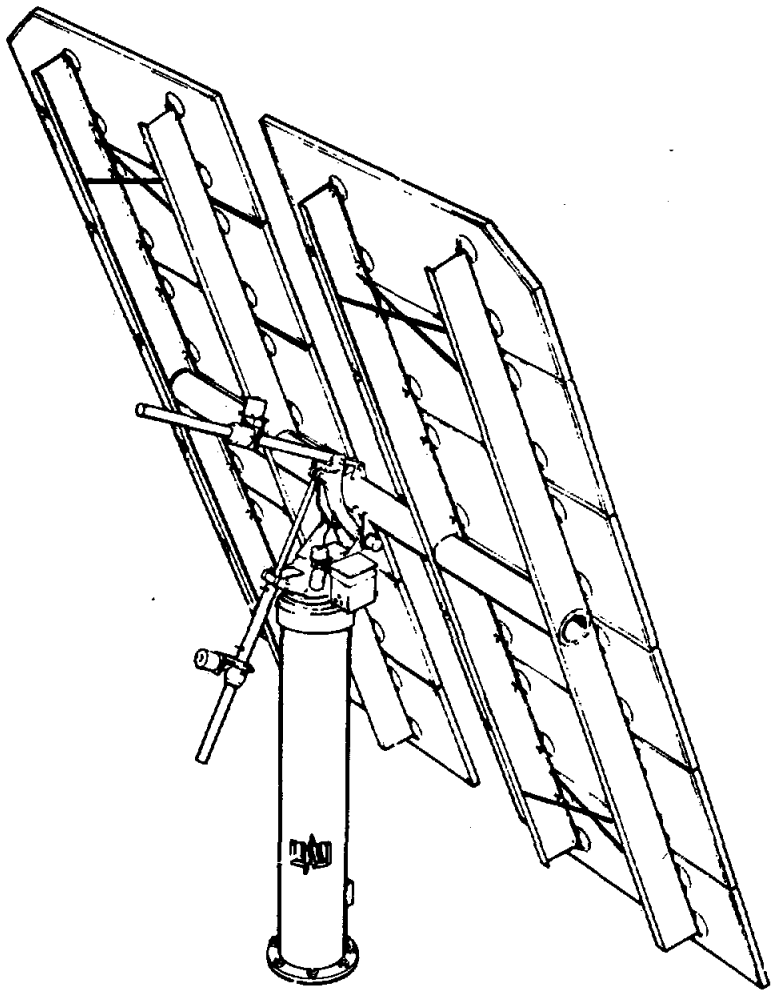

Figure 7. MDAC Heliostat Design, 10 MW_e Pilot Plant

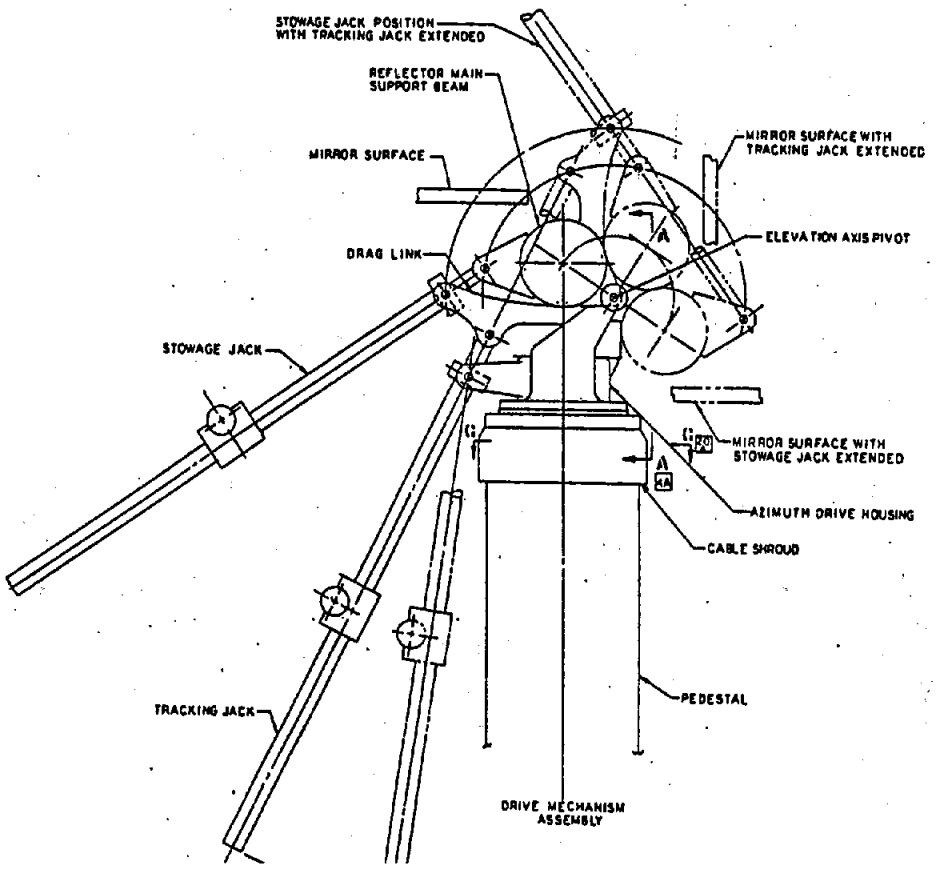

Figure 8. MDAC Elevation Drive System

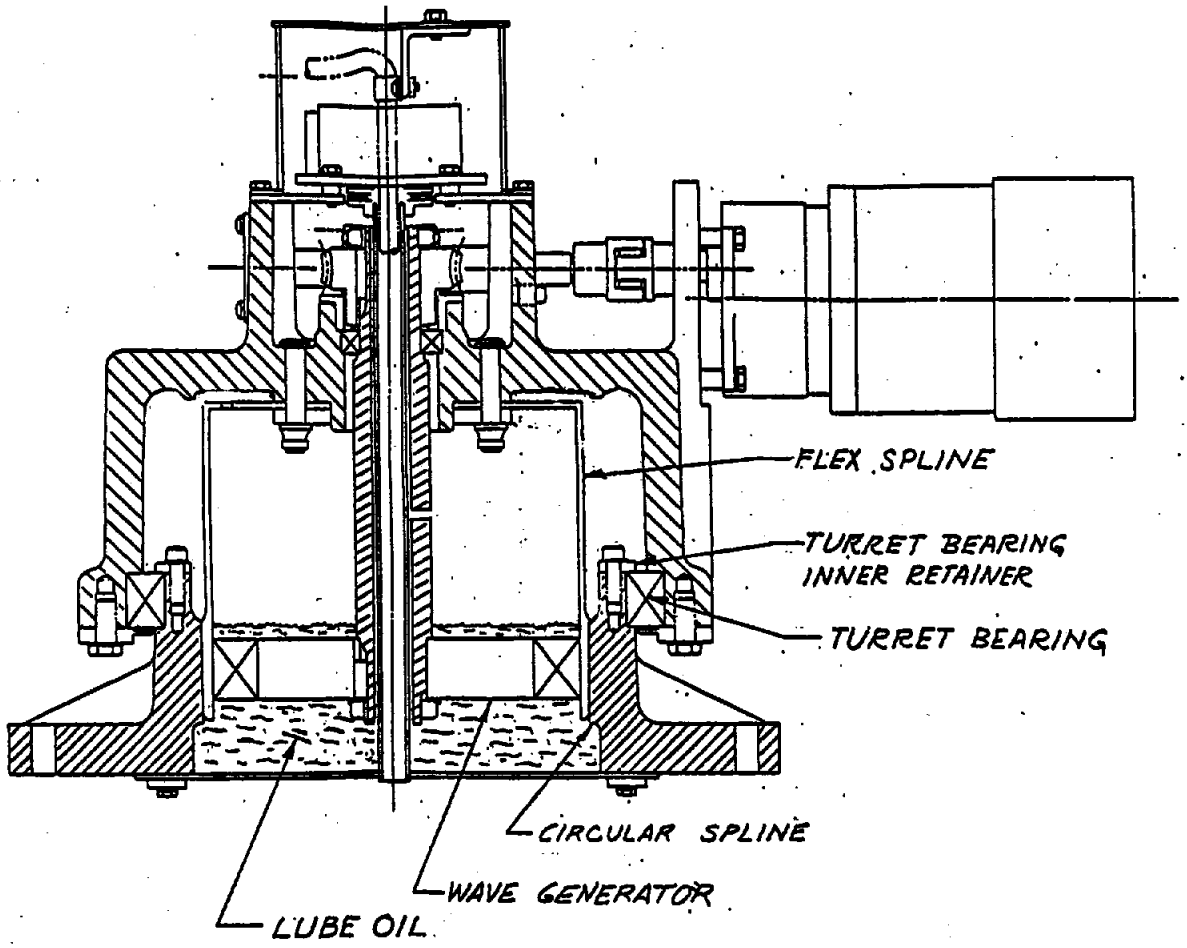

Figure 9. MDAC Azimuth Drive System

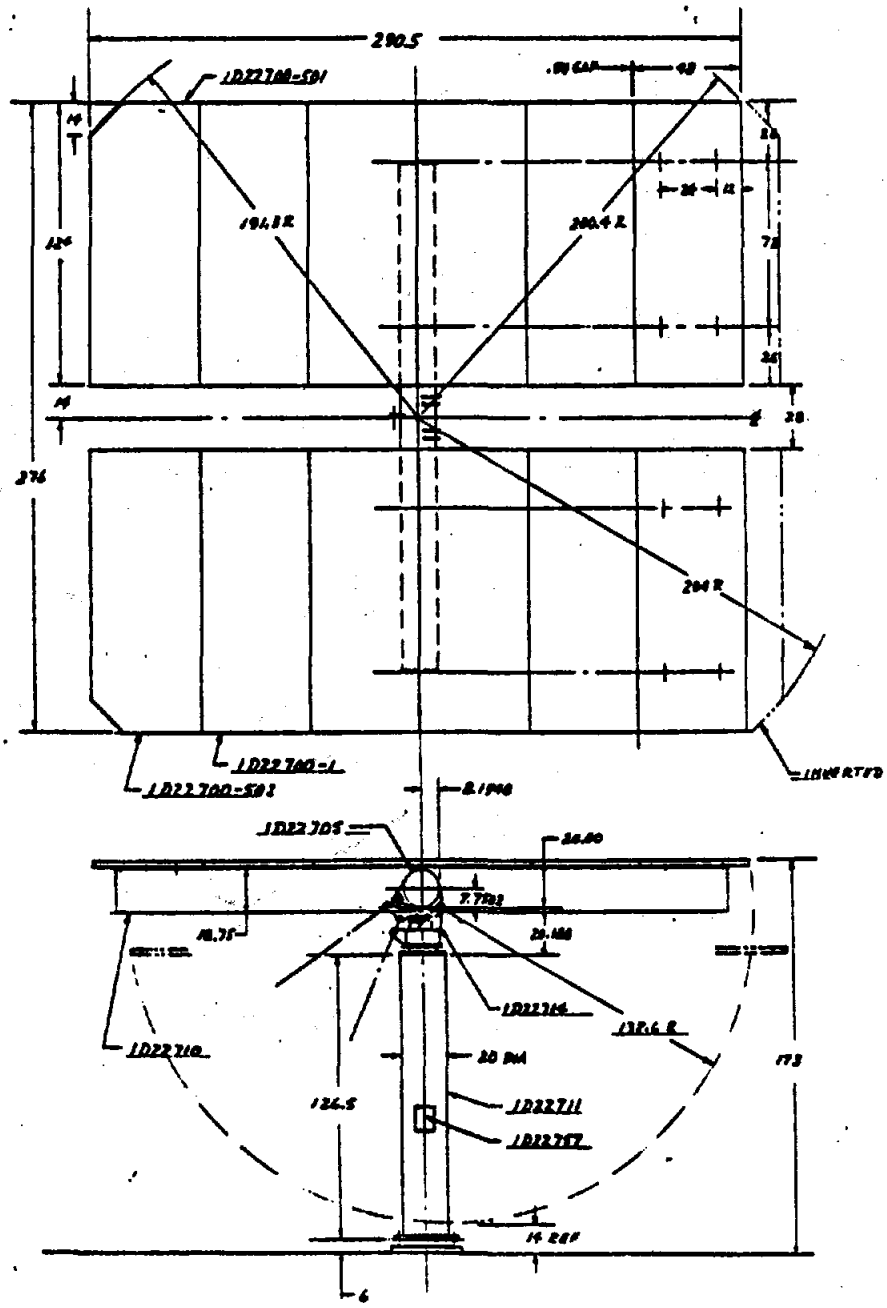

Figure 10. MDAC Heliostat Assembly

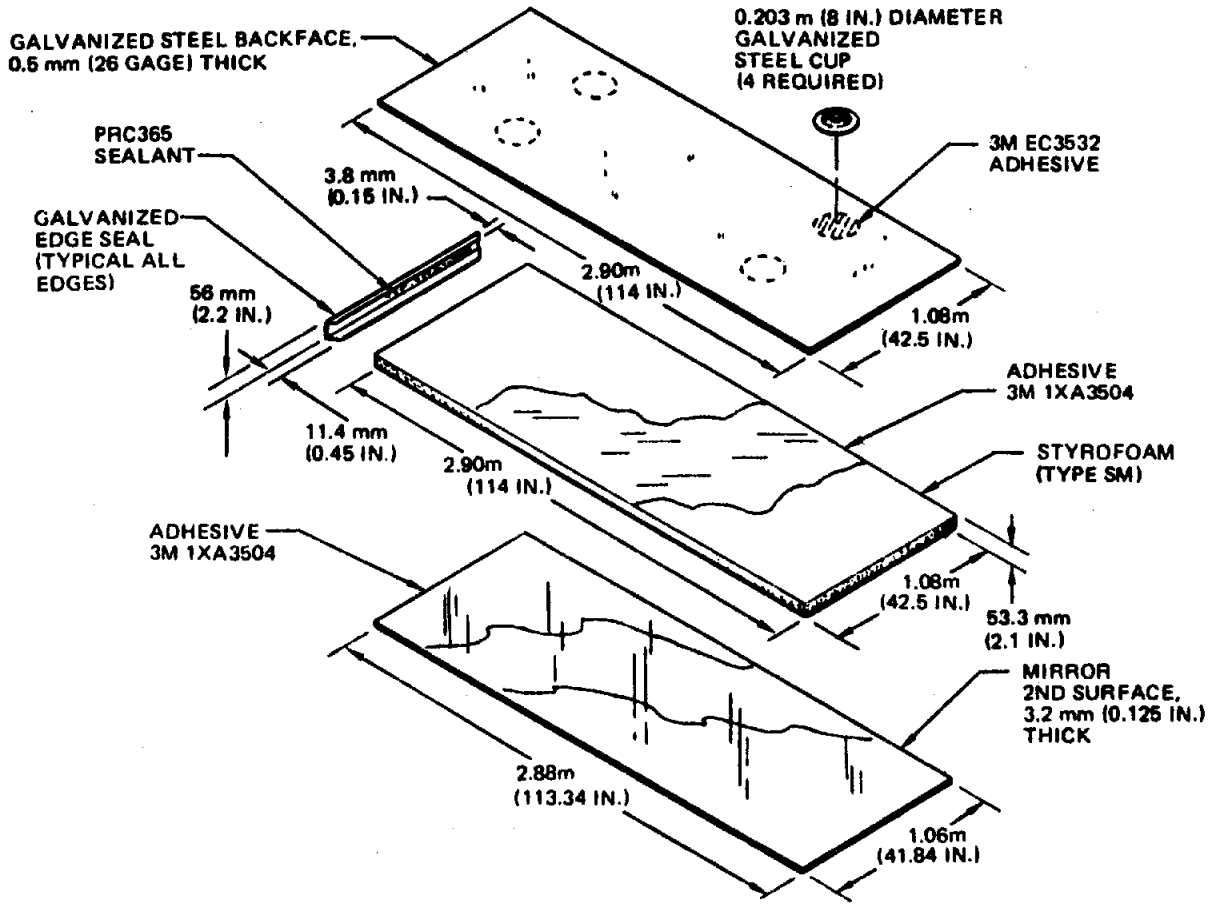

Figure 11. MDAC Mirror Module Components (exploded view showing steel, foam, glass, edge seal, and adhesives)

TABLE I

DESIGN DESCRIPTIONS AND COMPARISONS

MMC	MDAC
Mirror Module Assemblies:	
•430 ft^2 total reflective area	•479 ft^2 total reflective area
•Glass-1/8" thick, 43" x 120"	•Glass-1/8" thick, 48" x 124"
•Aluminum honeycomb core 2.5" thick	•Styrofoam core, 2" thick
•3-point mount, flush plate mounts	•4-point mount, formed cup mounts
•1-piece formed pan backing	•Flat sheet back with edge caps
•High temperature epoxy adhesive	•Room temperature urethane adhesive
•"Spherical" (2-axis) curvature	•Cylindrical (single-axis) curvature
•1 component edge seal	•2 component edge seal
•Painted finish	•Galvanized finish
Mirror Support Structure:	
•Cross beams: 14" deep welded steel truss members (EI = 3.1 x 10^9 lb-in^2)	•Cross beams: 18" deep roll-formed steel sections (EI = 2.7 x 10^9 lb-in^2)
•Torque tube: 12" dia., .188" wall steel cylinder (EI = 3.5 x 10^9 lb-in^2)	•Torque tube: 16" dia., .105" wall steel cylinder (EI = 4.8 x 10^9 lb-in^2)
•Weight: 1294 lb. (torque tube and cross beams)	•Weight: 936 lb (torque tube and cross beams)
•Joints: (cross beam/torque tube): bolted mech./friction joint, weld beads added for tested units	•Joints: (cross beam/torque tube); flange/friction bolted
•Finish: painted	•Diagonally braced cross beams for added lateral stiffness
	•Finish: galvanized
AZ-EL Drive Mechanisms:	
•Combined AZ-EL drives contained in single housing; totally sealed unit	•Azimuth drive: 1st stage reduction (input) -- worm/gear; 2nd stage reduction (output) -- harmonic drive (3-lobe generator)
•Azimuth drive: 1st stage reduction (input) -- worm/gear; 2nd stage reduction (output) -- helical pinion/gear	•Elevation drive: two linear screw/jacks in series, one for tracking and one for stowage, interconnected thru drag link
•Elevation drive: same internal drive as azimuth, with external connecting arms to torque tube	•Motors: three, each requiring 208 volts, 3ϕ
•Motors: two, each requiring 18 VDC for tracking and 120 VDC for slewing	•Pedestal mount integral to azimuth housing
•Separate azimuth drive-to-pedestal adapter	
Pedestal Structures:	
•121.5" long, 20" dia., .250" wall	•126.5" long, 20" dia., .125 wall as tested (.188" wall as proposed)
•Base flange: 1" thick	•Base flange: 3" thick as tested, (1.5" thick as proposed)
Finish: painted	•Finish: galvanized
•Cutouts: 8.8" (horizontal) x 16.2" (vertical), with stiffeners, near center; 10.0" (horizontal) x 5.0" (vertical) near top	•Cutouts: 8.9" (horizontal) x 10.9" (vertical) with doublers as tested, (without doublers as proposed)
Total Weight: •4132 lbs	•4211 lbs

Specification Requirements

To provide a better background of understanding of the testing performed and reported, a review of the major specification requirements is included here. These typically separate into operational/performance vs survival type requirements due to the wide range of environmental conditions the heliostat experiences on an annual basis. A summary of the important requirements are shown in Tables II-IV.

TABLE II

PERFORMANCE SPECIFICATION

Pointing Error
1.5-mrad reflected beam pointing error, standard deviation, is allowed for each gimbal axis (no wind).
Beam Quality
Minimum of 90 percent of reflected energy must fall within theoretical beam shape plus 1.4-mrad fringe (no wind).
Maximum Deflection under Wind Load
1.7-mrad standard deviation reflective surface slope error in 27-mph wind is allowed for a field of heliostats, including foundations. 3.6 mrad (3 sigma) is allowed for a single heliostat at worst-case conditions, excluding foundations.
Foundation Deflection
In a 27-mph wind, 1.5-mrad (3-sigma) total deflection is allowed for a single foundation at worst-case conditions, including elastic and permanent deformations. A maximum 0.45-mrad (3-sigma) permanent deformation is allowed for a 50-mph wind load.

TABLE III

OPERATIONAL ENVIRONMENT SPECIFICATION

Environment	Operational Limit
Temperature	+32°F to +122°F; reduced performance from +16°F to 32°F
Wind (including gusts)	
Operational	up to 27 mph
Continue to track	up to 35 mph (@ reduced performance)
Initiate stowage	> 35 mph
Wind rise rate	1.3 mph/min
Hail - SG = 0.9 (20°F)	0.75 in diameter @ 65 ft/s

TABLE IV

SURVIVAL ENVIRONMENT SPECIFICATION

Environment	Survival Limit
Temperature (ambient air)	-9°F to +122°F
Wind (including gusts)	
Heliostat integrity	50 mph any orientation
Survival wind (stow)	90 mph at tow $\pm$ 10 degrees angle of attack
Ice	2" thick max on one surface
Hail - SG = 0.9 (stow position)	1" diameter @ 75 ft/s
Rain	3" max per 24 hr
Snow	5 lb/ft^2 max
Earthquake	Seismic Zone 3 (Uniform Bldg Code)

Pilot Plant Heliostat Test Plan

The purpose of the heliostat evaluation program was to interpret the design specifications into various tests and analysis requirements that would determine whether compliance to specification requirements had been met. This effort involved qualification and design verification of the complete collector

subsystem, including all of the heliostat's electronic control system and the mechanical reflective assemblies. For sake of brevity, however, the word "heliostat" as used herein is intended to mean the complete collector subsystem.

Some of the considerations that influenced the test planning and its implementation were:

The wide range of annual environmental conditions resulted in design specification and test requirements being separated into operational/performance vs survival-type requirements.

The impossibility of testing for specification compliance under all operating conditions required use of NASTRAN and HELIOS computer codes for complete performance and survival analysis.

The test program needed to provide data points that would verify results predicted by computer analysis.

The use of codes could reduce the amount of testing and associated costs for proving specification compliance.

DOE/STMPO schedule constraints, plus other logistic considerations, dictated various hardware configurations being tested in parallel at multiple test site locations.

As a result of these considerations, the SNL evaluation program became an integration of both testing and computer analysis that could assess different heliostat designs in a timely and cost-effective manner. In consideration of the various test hardware configurations, number of test site locations, and different test personnel involved, the test portion of the evaluation program was structured into four separate sections, as summarized below.

Section A--Heliostats and Controls Tests (at CRTF)

Two complete heliostats from each contractor, including a trailer-housed control system, were operationally tested at CRTF. Heliostat optical performance, required operational modes, limited life cycling, and some structural testing were assessed.

Test	Purpose
1. Point Loading	Apply loads to heliostat structure and measure deflections for NASTRAN verification
2. Facet Canting	Verify initial facet cant for on-axis alignment
3. Facet Recant	Demonstrate individual facet replacement and recant capability
4. Operational Modes	Verify required field operations

Test	Purpose
5. Control/Drive Pointing	Assess heliostat pointing accuracy with laser system
6. Beam Centroid Pointing	Assess beam pointing accuracy with BCS
7. Beam Quality	Assess beam quality (flux density distribution) with BCS
8. Life Cycle Test	Obtain limited life-cycle data using a simulated daily tracking scheme
9. Wind Loading (90 mph)	Verify survival of simulated 90-mph wind load in stowed position

Section B--Structural Drive Assembly Tests (at SNLL)

One drive unit from each contractor was statically load tested at SNLL. Backlash, torsional stiffness, "backdrive" resistance, and stall torques were measured.

Test	Purpose
1. Backlash and Stiffness	Measure backlash and torsional stiffness of drives for NASTRAN input. Also, test azimuth drive to survival wind load
2. Mechanical Drift	Determine whether the drives "back-drive" under applied load
3. Motor Stall Torques	Determine whether motors produce sufficient torque for all operational conditions

Section C--Environmental Drive Assembly Tests (at Pt. Mugu, CA)

One drive unit from each contractor was tested in an environmental chamber at Pt. Mugu, CA. Ability to operate at temperature extremes and to resist moisture penetration was assessed, along with limited life-cycle testing.

Test	Purpose
1. Temperature Extremes	Determine whether drives and controls can operate and/or survive at temperature extremes (5-1/2 weeks of various temperature cycling)

Test	Purpose
2. Moisture Exposure	Determine resistance to moisture penetration (2-1/2 weeks of temperature/humidity cycling plus rain/wash spray test)

Secondary purpose of both tests was to obtain limited life-cycle data. Posttest disassembly and inspections were done to assess moisture penetration, malfunction, or excessive wear.

Section D--Mirror Module Tests (at SNLA)

Six mirrors from each contractor were tested at various test sites at SNLA. Tests determined mirror facet characteristics as they applied to HELIOS analysis, and mirror module survivability was also assessed.

Test	Purpose
1. Residual Glass Stress	Measure combined residual and fabrication-induced stresses along mirror edges
2. Specular Reflectivity	Measure specular reflectivity of mirrors (input for HELIOS)
3. Contour and Gravity Sag	Measure large-scale mirror contour and gravity sag (input for HELIOS)
4. Mirror Waviness	Measure effective mirror waviness with laser ray-trace (input for HELIOS)
5. Hail Test	Determine whether mirrors meet hail impact requirements
6. Wind Load Stress	Measure glass stress due to maximum wind loads
7. Thermal Stress/Contour	Measure stress in glass and mirror contour change due to temperature (input for HELIOS)
8. Thermal Cycling	Assess structural and functional integrity of mirror modules after 40 days of temperature cycling
9. Temperature/Humidity Cycling	Assess integrity of moisture seals after 30 days of alternating high and low humidity, UV radiation, and temperature cycling
10. Cold Water Shock	Assess ability to survive cold rain or wash on hot day

The two computer analyses, which were performed concurrently with the testing, are summarized in Table V. Figure 12 illustrates the data flow and interaction of the two analysis processes.

TABLE V

COMPUTER ANALYSES

NASTRAN Structural Analysis

1. Both heliostat designs were modeled by NASTRAN to determine mirror facet pointing errors due to gravity and wind loads.

2. Measured values of drive mechanism backlash and stiffness were modeled into NASTRAN for calculating wind deflections, and for determining the dynamic natural frequencies and mode shapes of the structure.

3. Several "point load" test/deflection measurements were taken to verify NASTRAN predictions.

HELIOS Optical Performance Analysis

1. Heliostat beam quality was calculated by HELIOS for a variety of field positions and environmental conditions to determine whether the beam quality performance specification was met.

2. Along with the facet pointing errors from NASTRAN, measured values of mirror reflectivity, specularity, waviness, and contour as a function of temperature were incorporated into HELIOS.

3. HELIOS beam quality calculations were verified by comparison of calculated beam shapes with actual beam flux distributions measured with a video BCS.

Figure 13 is a copy of a schedule/status report that STMPO used for progress reporting during the course of the evaluation program. The purpose of presenting it here is not to interpret every detailed activity shown, but to help in comprehending the full scope and simultaneity of the evaluation activities. Note that the scheduled activities included the computer analyses, committee evaluation efforts, and the testing activities at the four different site locations.

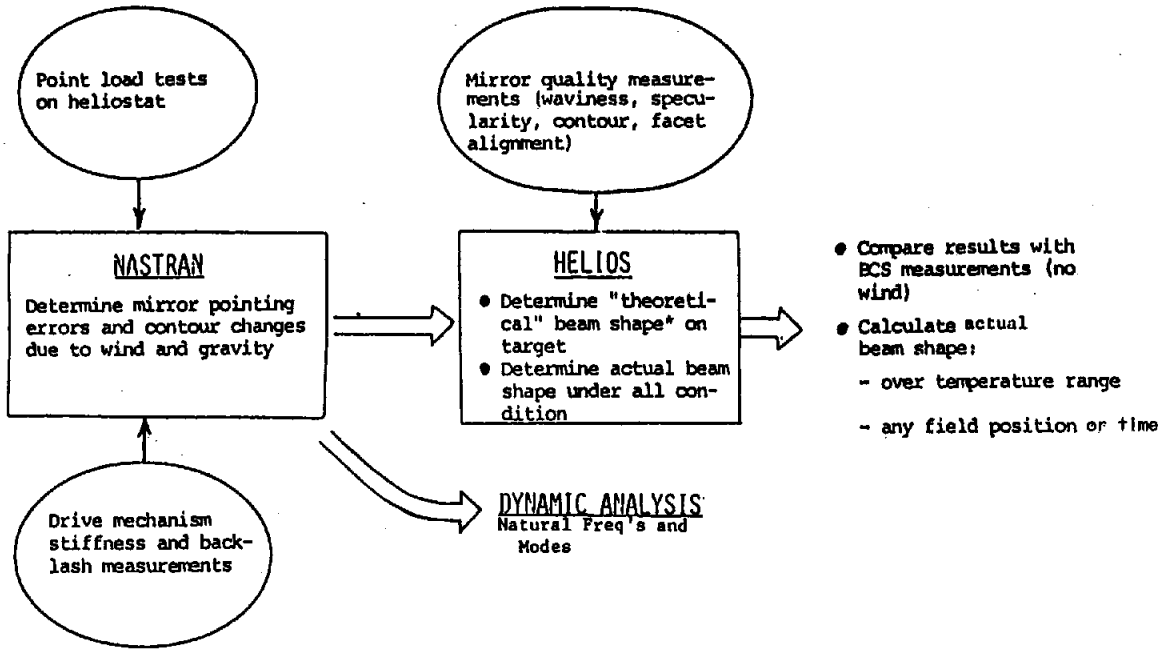

Figure 12. Pilot Plant Heliostat Performance Evaluation Analysis

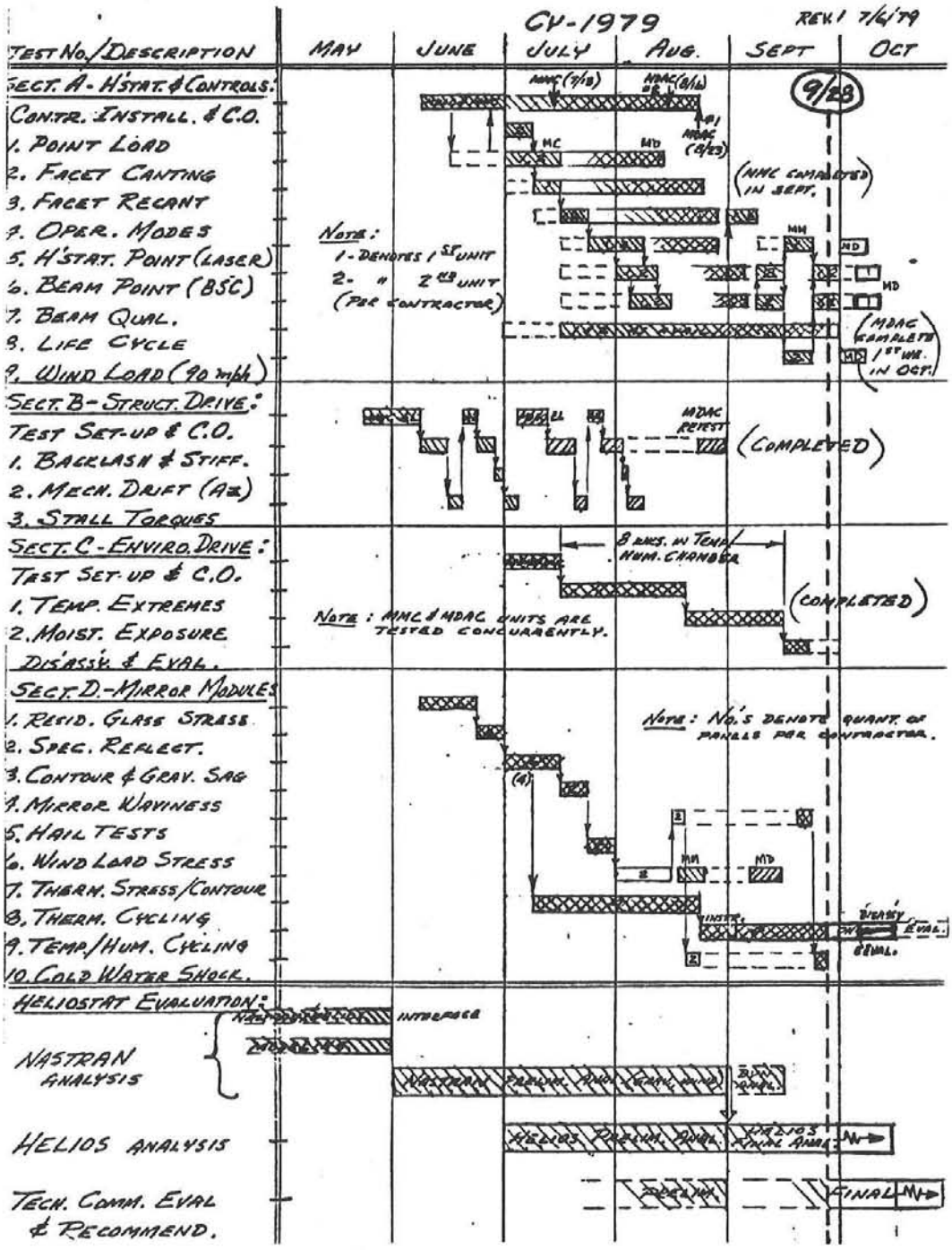

Figure 13. STMPO Schedule Status Report

Summary of Testing and Results

The test program was successful by any standard. It was the most extensive test program to characterize and evaluate heliostat performance ever attempted. The testing required close coordination of numerous personnel who were spread out over a large geographic area. The test program successfully used for the first time, in an operational (as opposed to demonstration) program, new heliostat testing procedures; in particular, the ability to verify or test compliance with the performance specification of a field of heliostats over a range of environmental conditions by using a combination of limited testing and computer modeling (NASTRAN and HELIOS).

The heliostats generally performed well in the testing. The MMC design, at the end of the testing, had two major unresolved problems. First, severe mirror corrosion was observed on the mirror modules. This corrosion was observed late in the test program and was believed due to an inadequate edge seal that allowed water to get to the back of the mirrors. Second, during the 90-mph wind survival test the azimuth drive took a set; that is, there was a residual beam pointing error that showed up in performance testing after the wind survival test had been done. It was believed that a design change in the roller bearings in the azimuth drive would solve the problem.

MDAC was plagued by problems in heliostat controls from the installation of the heliostats through the entire test program. The system was not fully developed prior to installation of the heliostats. This prevented the design from successfully demonstrating all the required operational modes.

The MDAC heliostat design also failed the beam pointing test. There seem to be several possible reasons. The transfer movement involving the elevation and stow jacks was unrepeatable. The corrections for pedestal tilt and nonorthogonality of azimuth and elevation drive axes in the control algorithms may have been incorrect. In addition, there may have been wear in the drive systems during testing that led to the failure of the beam pointing test. In the environmental testing of the drives, heavy wear was observed in the drag link pivot bushings and the elevation screw jack. Finally, the heliostat failed the beam quality specification test at lower temperatures. Because of inadequate curvature being manufactured in the mirror module, the mirrors became concave at temperatures below 40°F.

None of the problems was resolved or repaired by the end of testing. The problems were left for solution by the contractor chosen to produce the heliostats for the pilot plant.

SECTION A--HELIOSTAT AND CONTROLS TESTS

General

Introduction

This section describes the tests performed on the prototype heliostats installed at the CRTF by MMC and MDAC. MMC and MDAC installed two heliostats each, along with their associated control systems, at the CRTF during the preproduction phase of heliostat development for the 10-MW_e central receiver pilot plant. A series of nine different tests, as briefly outlined in Table A-I, were conducted at the CRTF. The general purpose of these tests was to verify that the heliostats and their associated control systems were capable of meeting the performance and survival criteria that were required for successful operation at the pilot plant. All testing at the CRTF was completed during the months of July-September 1979.

TABLE A-I

HELIOSTATS AND CONTROLS TESTS AT THE CRTF

Test No./Description	Purpose	Technique
1. Point load	Verification of NASTRAN Structural code model. HELIOS input	Apply point loads and measure deflections
2. Mirror alignment (canting)	Provide measurement of mirror canting for input to code HELIOS	Mirror covers and BCS or other method
3. Mirror realignment (re-cant)	Evaluate mirror replacement and re-cant technique	BCS
4. Operational modes	Verify required field operation modes	Encoder position data and BCS
5. Control/drive pointing	Determine pointing capability and repeatability of control and drive	Laser mounted on heliostat
6. Beam centroid pointing (tracking accuracy)	Determine beam centroid pointing capability versus time	BCS
7. Beam quality	Determine heliostat beam quality relative to performance specification	BCS measurement with HELIOS comparison
8. Life cycle	Observe failure and maintenance requirements	Three months continuous cycling
9. 90-mph wind load	Verify survival of simulated 90-mph wind	Static load and BCS evaluation

CRTF Test Layout

An aerial view of the CRTF and the prototype heliostat test area is shown in Figure A-1. The relative positions of the prototype heliostat test area and the Beam Characterization System (BCS) can be seen in relation to the general CRTF layout. Figure A-2 shows a more detailed layout of the MMC and MDAC prototype heliostats and their associated control systems. The dimensions given are in the tower coordinate system with the origin at the base of the CRTF tower. MDAC heliostats were located on Foundations 1 and 2 and MMC heliostats were located on Foundations 4 and 5.

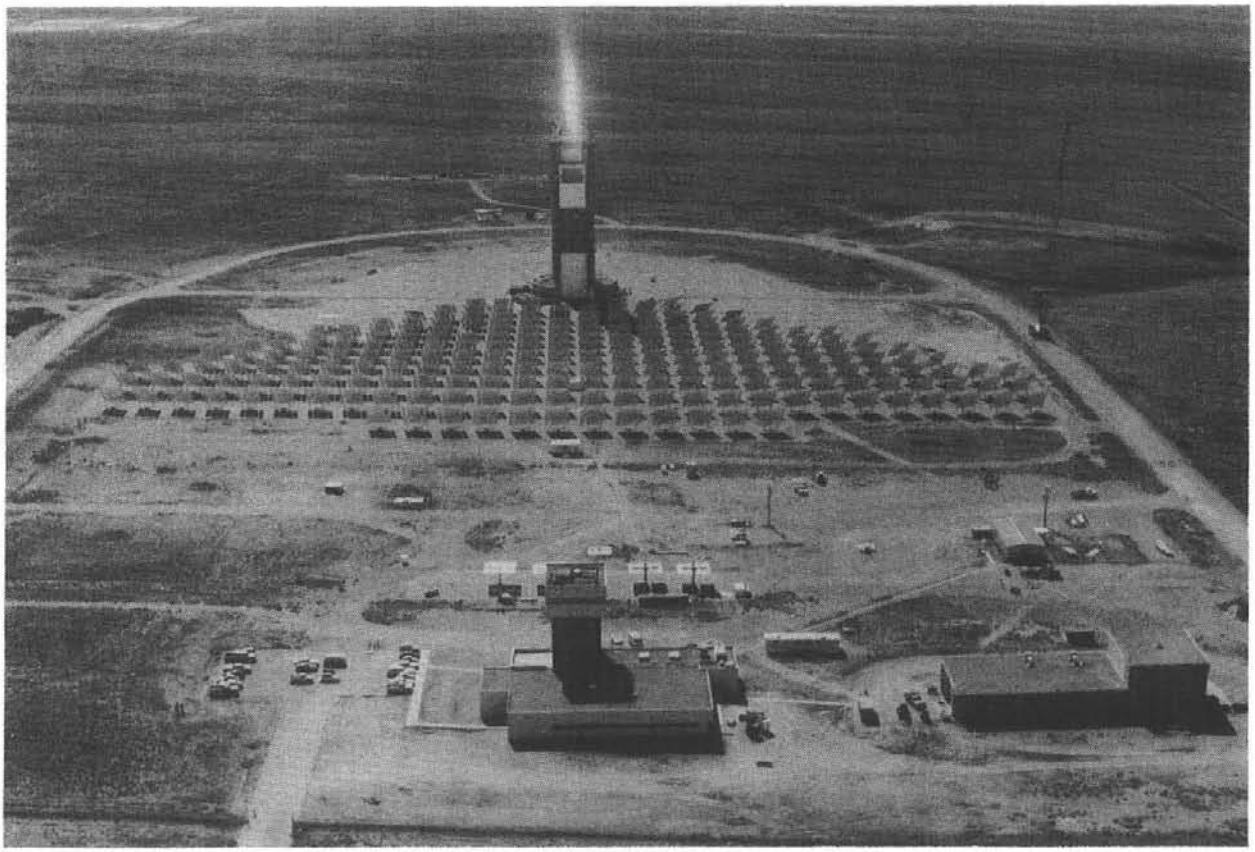

Figure A-1. Aerial View of the CRTF and the Prototype Heliostat Test Area

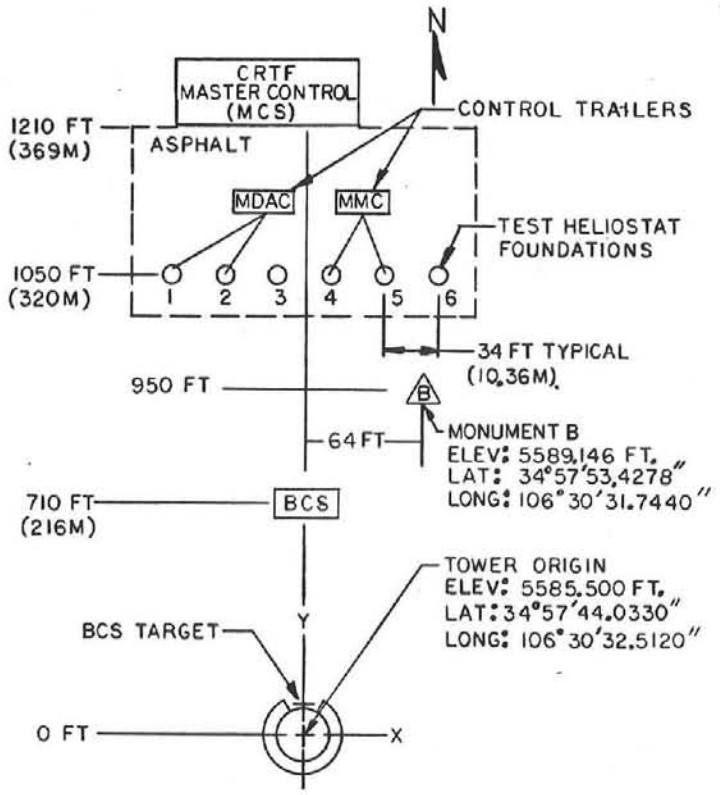

Figure A-2. Prototype Heliostat Test Layout

The foundations used during the testing were the same as those used by the CRTF heliostats. It was decided to use these foundations, shown in Figure A-3, since the foundation design to be used at the pilot plant had not been completed. Additionally, using the CRTF design expedited the preparation necessary prior to heliostat installation and testing. An interface adapter was used to mount the prototype heliostats to these foundations since the bolt pattern required by the heliostat pedestals was different from the foundation bolt pattern. After installation of the test foundations a final survey was made to accurately locate the center of the bolt circle at the level of the steel base plate (Figure A-3) for each of the six foundations installed. Table A-II gives the results of this survey in terms of the X, Y, and Z coordinates of each foundation (tower coordinate system). The additional vertical distance from the foundation to the height of the heliostat elevation axis is also given.

The BCS target is 9.14 m by 9.14 m in dimension and is located on the north face of the CRTF tower. The target is canted north of vertical by approximately 6 degrees. Figure A-4 shows the location of the target and gives the tower coordinates of the aimpoint (A1), standby (SB), and line bottom (LB) points. Point A1 was used for all beam quality and tracking accuracy testing. CRTF safety considerations also dictated that heliostat beams be moved in a controlled fashion. Beams were typically moved along the ground to the line bottom point, moved along Wire #1 (a line defined by a moving aimpoint) to the standby point, and remained at standby prior to movement onto the BCS target during testing.

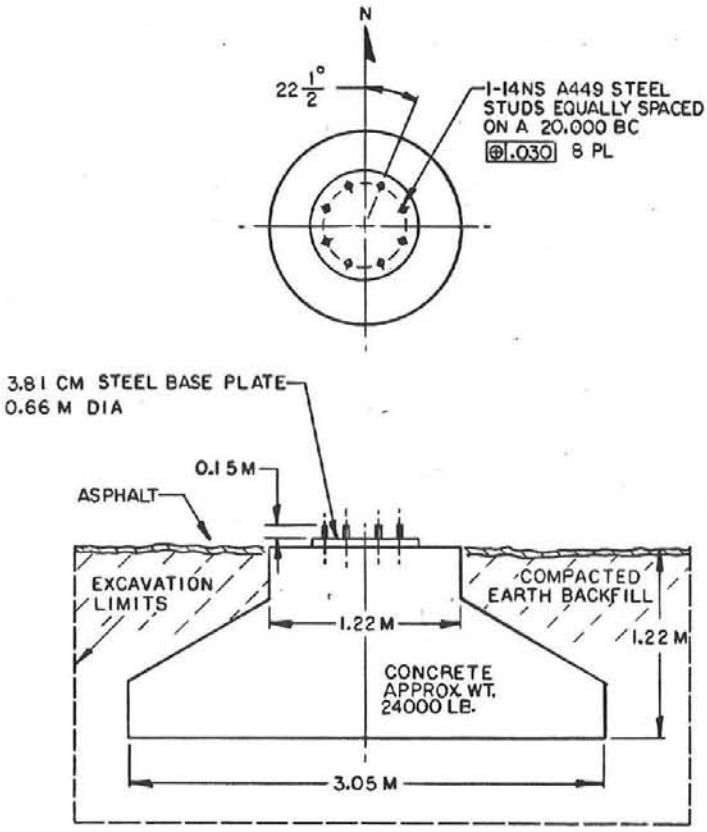

Figure A-3. Typical CRTF Foundation Used during 10-MW_e Prototype Testing

TABLE A-II

PROTOTYPE HELIOSTAT FOUNDATION LOCATIONS IN TOWER COORDINATE SYSTEM

Foundation	Heliostat	X (m)	Y (m)	Z (m)*
1	MDAC #1	-24.995	320.023	-0.189
2	MDAC #2	-14.615	320.031	0.106
3		-4.288	320.037	0.298
4	MMC #1	6.081	320.034	0.570
5	MMC #2	16.469	320.039	0.817
6		26.808	320.032	1.024

*Distance from base plate to height of elevation axis during CRTF testing was 3.78 m for MMC heliostats and 4.04 m for MDAC heliostats.

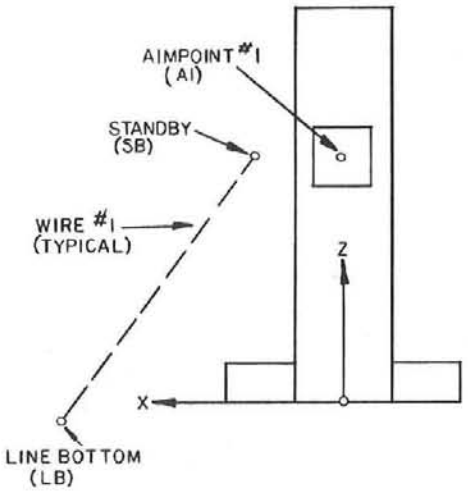

COORDINATES (METERS)

POINT	X	Y	Z
AI	0.051	9.778	37.578
LB	60.00	0.00	-2.00
SB	25.00	0.00	37.59

Figure A-4. BCS Aimpoint and Standby Coordinates

Figure A-5 shows the completed installation of the MDAC and the MMC prototype heliostats prior to testing at the CRTF.

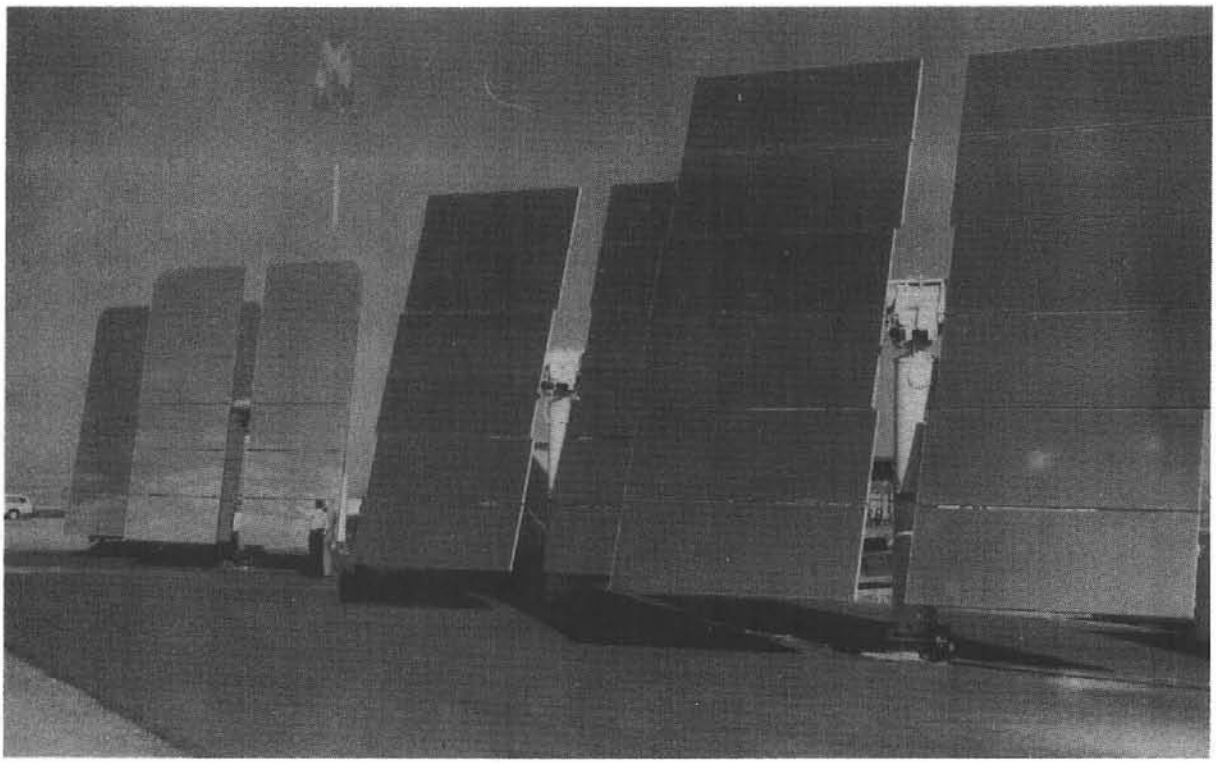

Figure A-5. Completed Installation of the MMC (foreground) and the MDAC Prototype Heliostats

Beam Characterization System

The primary tools used at the CRTF during this heliostat evaluation were BCS and a simple laser-based system. A brief description of these systems is given below.

Beginning in April 1978 an extensive effort was made to develop a versatile means of optically characterizing heliostats. This system was to provide a means of assessing the beam quality and tracking accuracy of new prototype heliostats. Approximately a year's effort resulted in the development of the BCS[1] (Figure A-6). The BCS consists of a silicon diode array video camera, a 256x256-point 8-bit video digitizer, a minicomputer, a remote data acquisition link, and a 9.14 m x 9.14 m target that is painted with a white lambertian paint. A systematic video camera calibration technique[2] was developed to correct for nonuniform sensitivity of the silicon tube in the camera. The use of a high linearity deflection yoke in the camera reduces geometric distortions by the camera to a negligible level. With a heliostat beam incident on the BCS target, a pyrheliometer located in the center of the target provides a measurement of the incident flux density. This value is used with the BCS to provide a correlation between digitized video levels and their associated flux density levels. The resulting system is capable of digitizing the heliostat beam image in a snapshot fashion in 0.017 second. Typical outputs from the BCS include total incident power, flux density distribution, flux density weighted centroid location, and percent power vs radius from the centroid. Rapid sampling and calculation of only centroid location at approximately four-second intervals provides a means for assessing heliostat beam tracking accuracy. Error analysis indicates a system inaccuracy of approximately ±5 percent and a system repeatability of approximately ±3 percent.

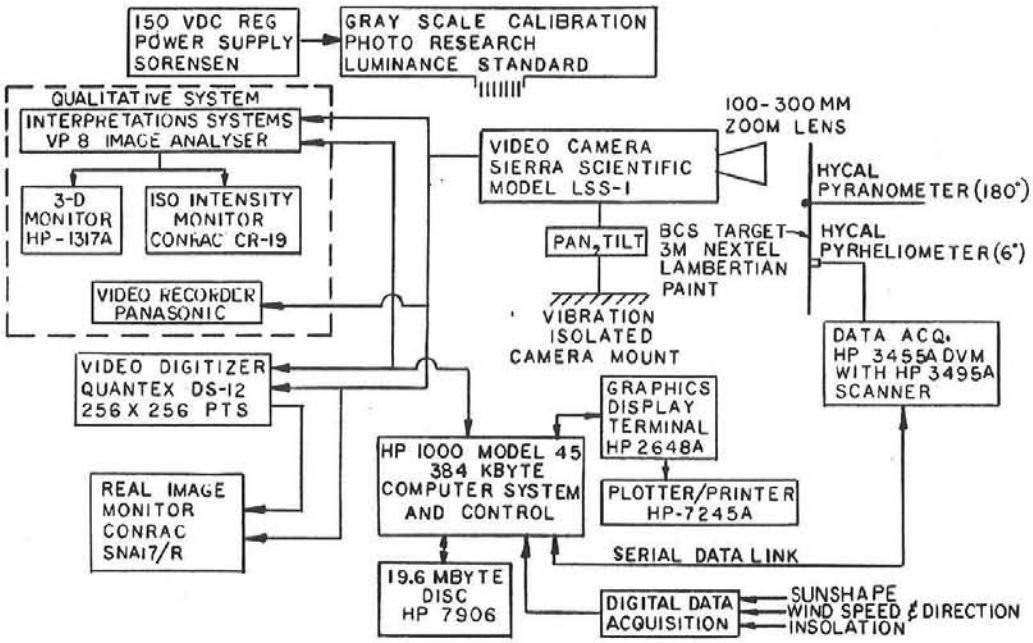

Figure A-6. Schematic Representation of the CRTF Beam Characterization System

The BCS in conjunction with an optical model can be used to assess the performance of prototype heliostats.[3] The optical model used during all heliostat beam analysis at the CRTF was the code HELIOS.[4,5]

A second evaluation tool used at the CRTF was a laser-based system, depicted in Figure A-7. By mounting a laser near the center of a test heliostat and recording the laser's movement on a target located at a distance from the heliostat, it is possible to assess the repeatability of heliostat angular movements. The target used is a 1.22x1.22-m translucent plexiglass sheet with a 2.54-cm grid painted on one side. Laser movements on the target are recorded by a video camera with an associated time input generator and a video recorder. Figure A-8 shows the system in use during evaluation of the MDAC #2 heliostat. This system was also used to measure deflections of the heliostat drive units during simulated wind load testing.

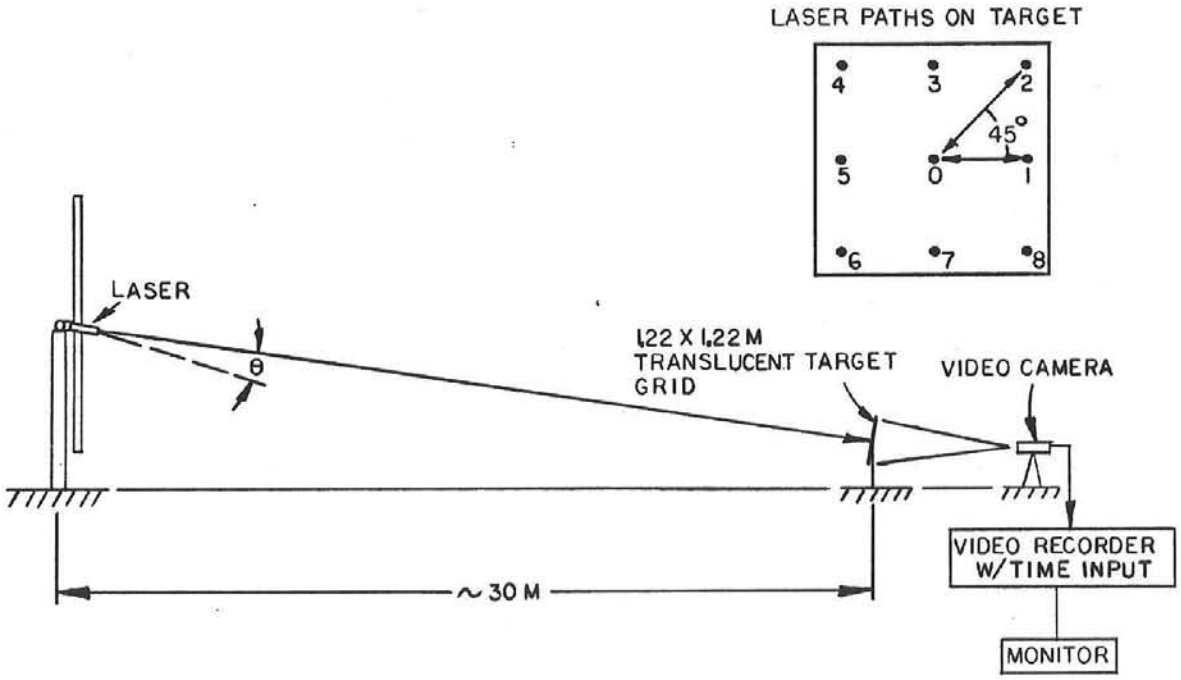

Figure A-7. Laser-Pointing Evaluation System

The laser spot size on the target located at a distance of ~ 30 m is approximately 3.2 mm (1/8 in.) in diameter. By standing behind the laser target and measuring laser movements directly, heliostat angular movements of approximately 0.1 milliradians can be resolved. If the video camera system is used to record the laser movements for subsequent analysis, the angular resolution is decreased to approximately 0.3 milliradian due to slight blooming of the laser spot on the vidicon tube, slight video geometric distortion, and difficulty in scaling distances off the screen of a monitor. System and procedural improvements will improve the measurement resolution of this system during future testing.

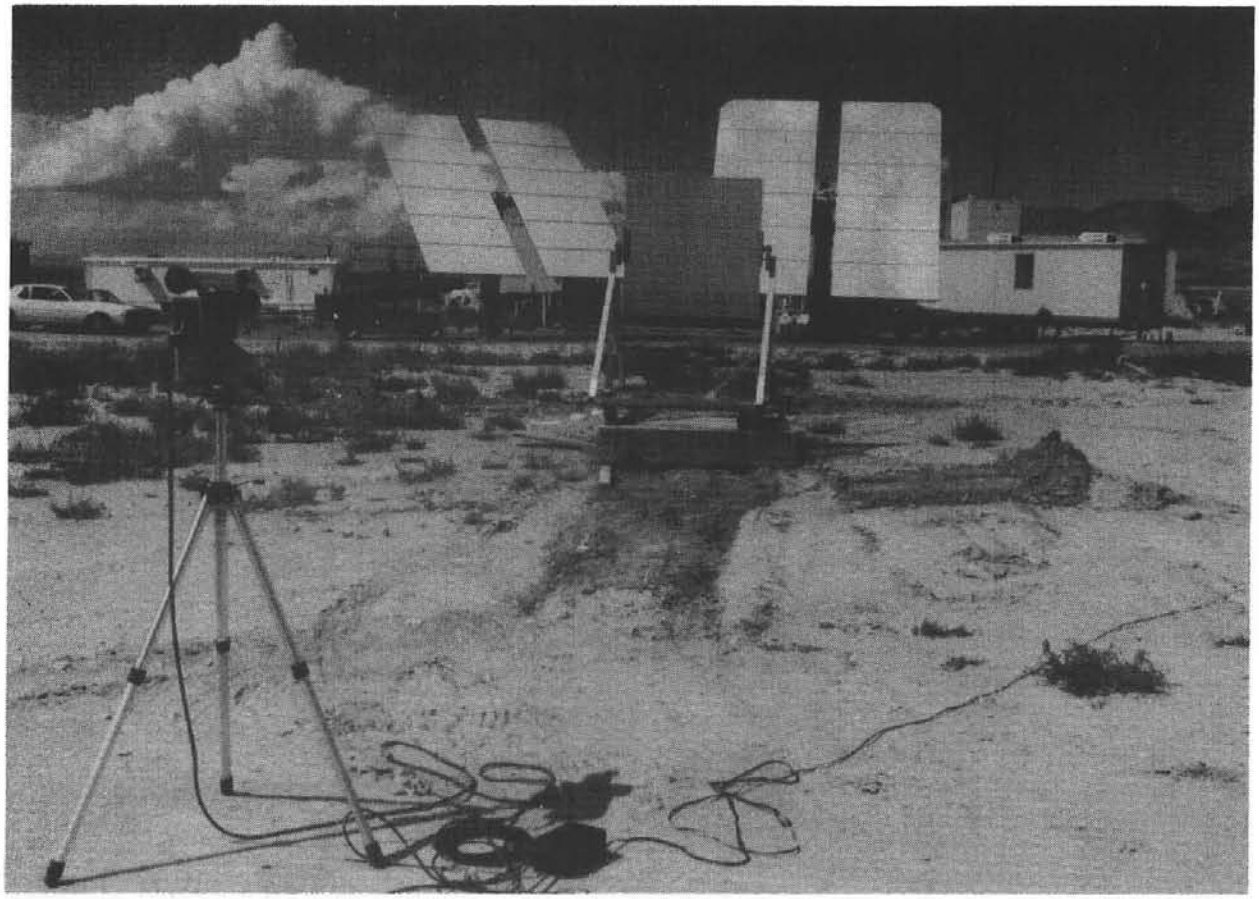

Figure A-8. Laser Pointing Evaluation System during Testing of the MDAC #2 Heliostat

Prototype Heliostat Assembly and Installation

The following is a brief description of the procedures used for the assembly and installation of the MDAC and MMC prototype heliostats at the CRTF prior to testing. These procedures were the most expedient method of installing the two prototype heliostats at the CRTF. Consequently, they are not totally representative of procedures that would be followed during assembly and installation at the 10-MW_e pilot plant. The general procedures, however, illustrate the basic steps involved.

On 6/5/79 MDAC personnel began assembling heliostat hardware at the CRTF. Initially, the pedestals were installed on the CRTF foundations as shown in Figure A-9. During installation the pedestals were roughly leveled by using a level across the top end of the pedestal. The MDAC approach to field installation involved only a rough leveling of the drive unit in the field with subsequent compensation for azimuth axis tilt done in the control software (a further discussion of this approach will be given during description of tracking accuracy testing). The drive units were then installed to the top of the pedestals, as shown in Figure A-10, with the elevation tube of the helio-

stat pinned at two points. The elevation tube, crossbeams, and mirror modules were all assembled as a unit in the CRTF assembly building, as shown in Figure A-11 (a more detailed discussion of the procedure used during alignment (canting) of the mirror modules is given later in this report).

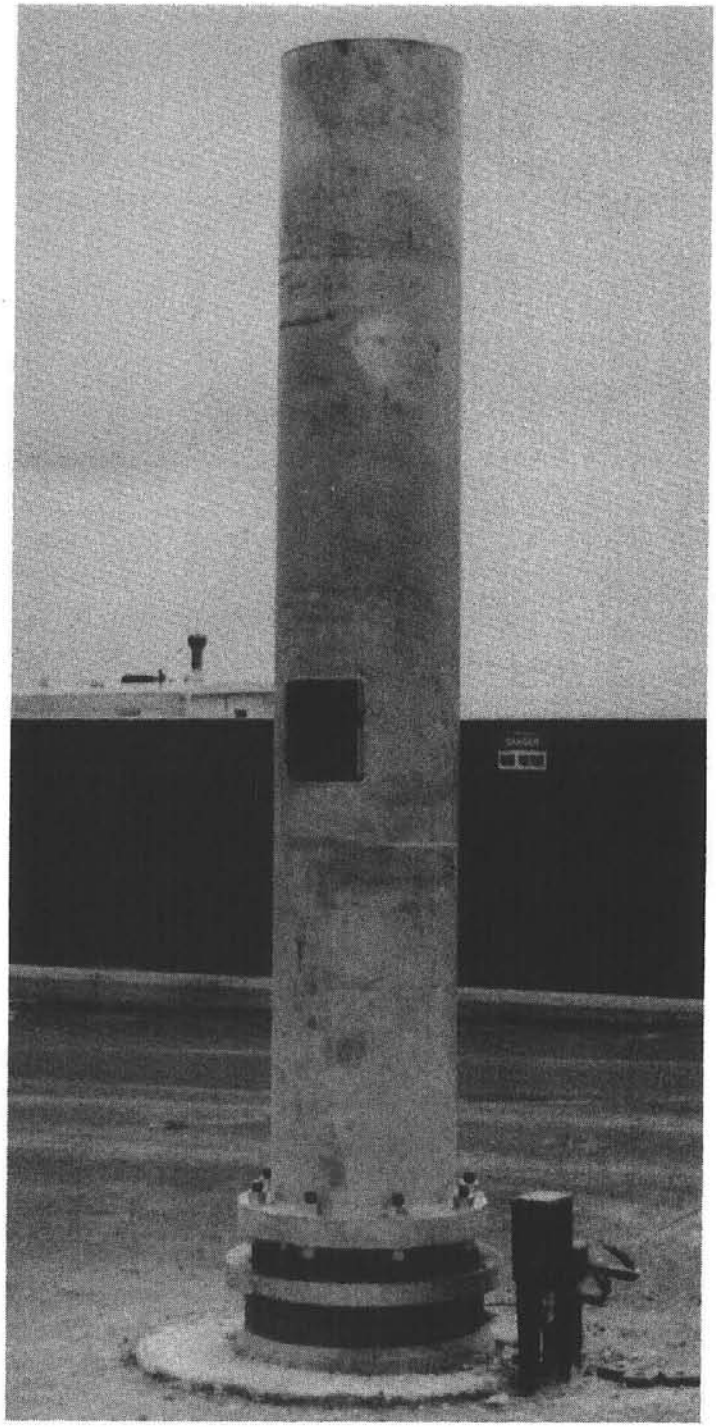

Figure A-9. MDAC Pedestal Installation on CRTF Test Foundations

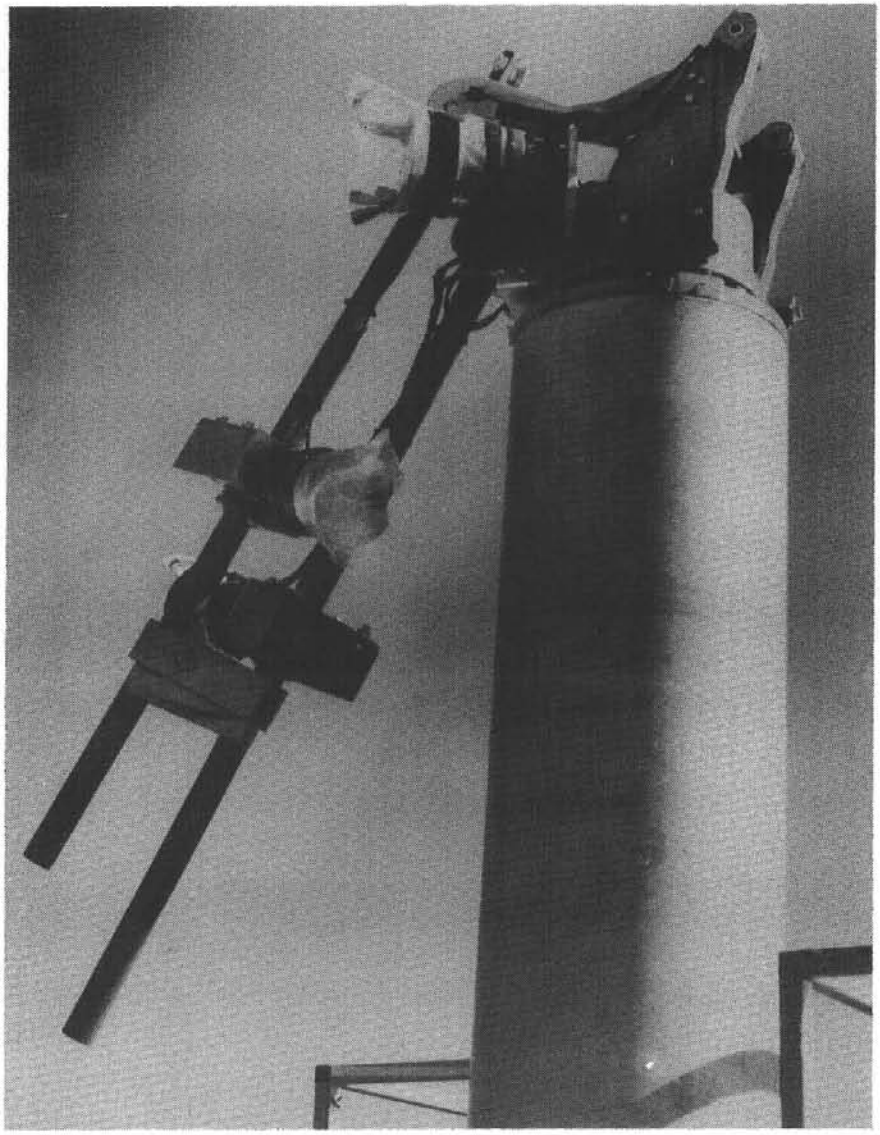

Figure A-10. MDAC Drive Unit Installed on Pedestal

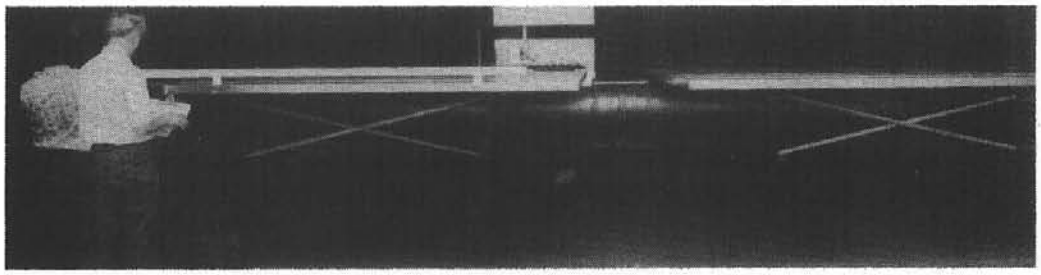

Figure A-11. Assembly of MDAC Elevation Tube, Crossbeams, and Mirror Modules in CRTF Assembly Building

After assembly of the mirror modules and their support structure, a mobile crane was used to transport the mirror assembly to the pedestal location. With the mirror assembly horizontal (mirrors face up) the unit was lowered onto the drive unit and pinned in place, as shown in Figure A-12 (the CRTF assembly building is shown in the background). Assembly of the hardware components of both MDAC heliostats was completed on 6/16/79. A front and a rear view of a fully assembled MDAC heliostat are shown in Figures A-13 and A-14.

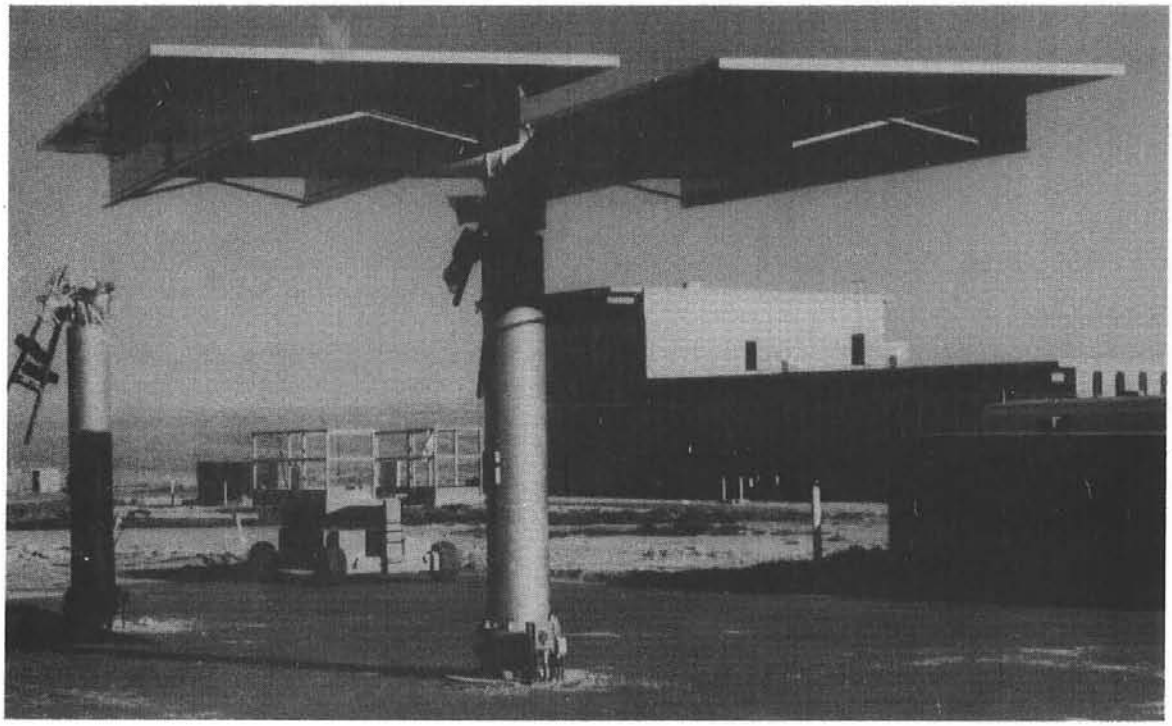

Figure A-12. MDAC Heliostat Following Field Assembly of Mirror Structure to the Drive Unit

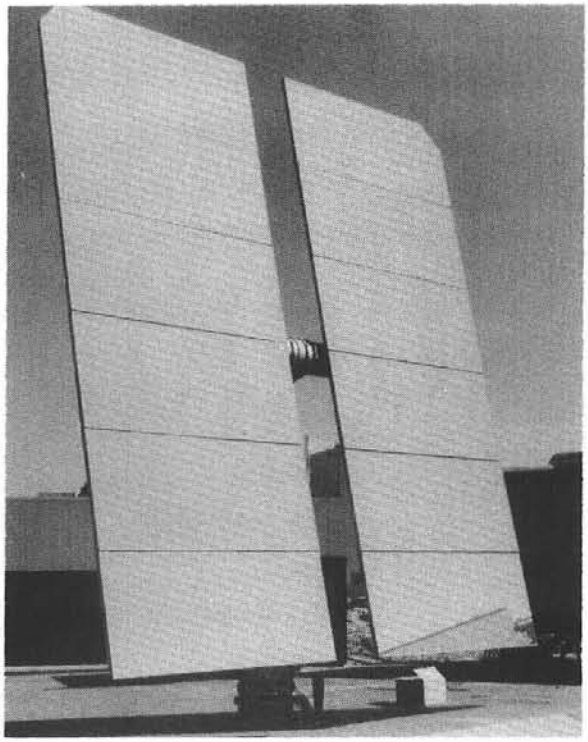

Figure A-13. Front View of Fully Assembled MDAC Heliostat

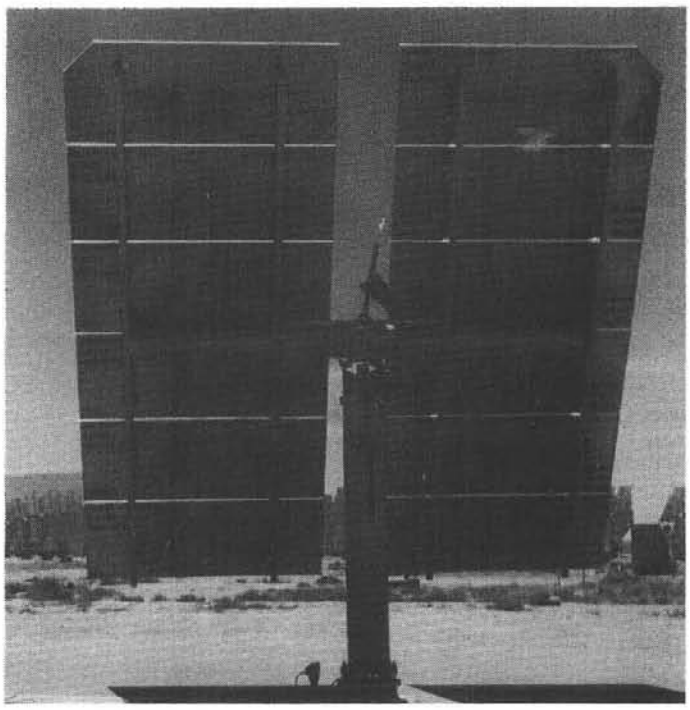

Figure A-14. Rear View of Fully Assembled MDAC Heliostat

On 6/27/79 the MDAC control trailer and computer control system arrived at the CRTF. The control system was interfaced to the heliostat electronics. However, due to repeated heliostat control electronic failures and other checkout difficulties, the MDAC heliostats were not fully operational until the second week in August.

MMC personnel began assembling their heliostats at the CRTF on 6/12/79. All hardware was off-loaded at the foundation site and the pedestals and drive units were installed on the foundations (Figure A-15). After the drive units were secured to the pedestals they wre leveled to within 0.14 milliradians (30 seconds) using an electronic inclinometer. Leveling was achieved by adjusting the mounting bolts at the base of the heliostat pedestal as the drive unit was rotated to different azimuth positions. This procedure is indicated in Figure A-16 where the inclinometer can be seen sitting on the top of the drive unit.

Figure A-15. Field Assembly of MMC Prototype Heliostats

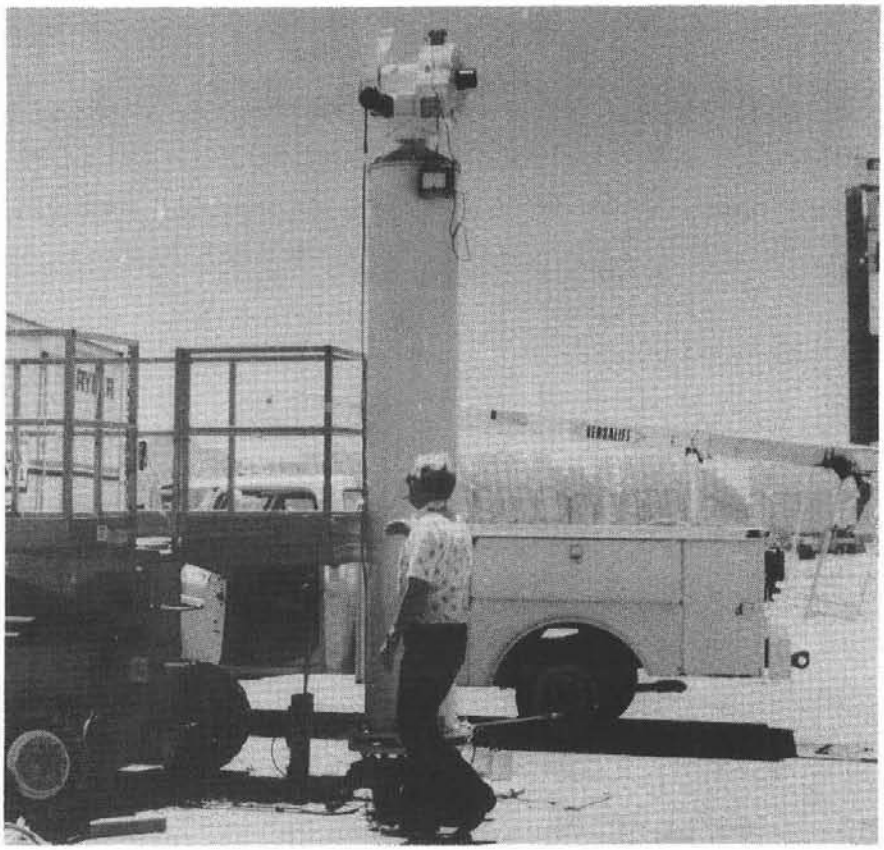

Figure A-16. MMC Heliostat During Field Leveling of the Drive Unit

The welded truss cross beams were assembled on the elevation (torque) tubes (Figure A-17) and the completed assembly was then installed on the drive unit (Figure A-18). Installation of the mirror modules (Figure A-19) was completed on 6/18/79. A field procedure utilizing the sun and mirror covers was used to align (cant) the individual mirrors with respect to each other. This procedure will be discussed in more detail later in this report.

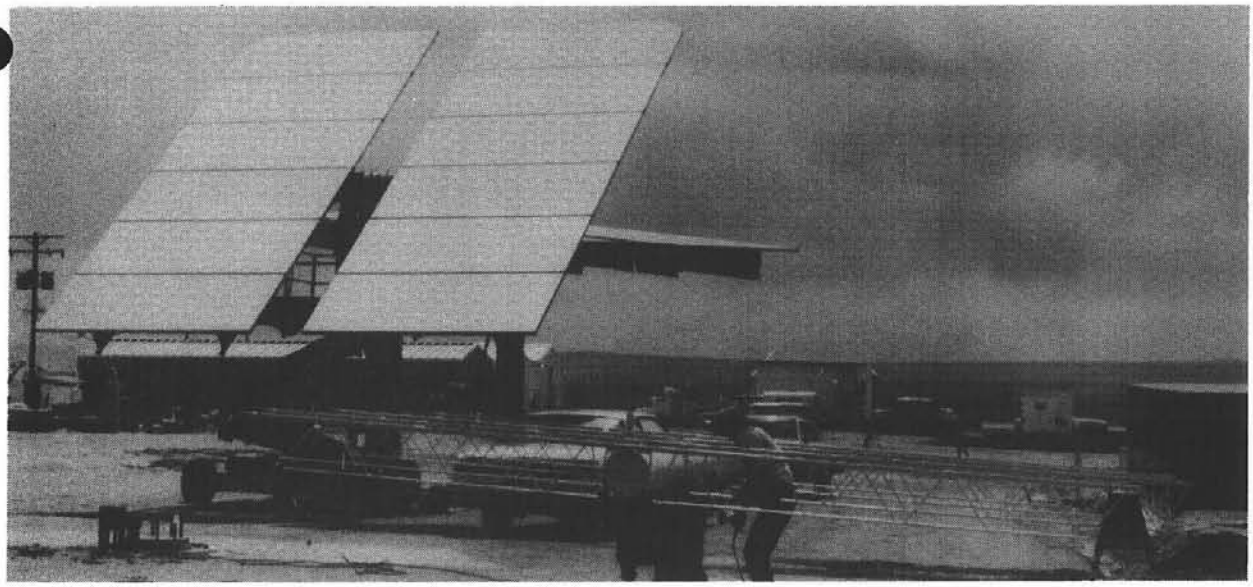

Figure A-17. Field Assembly of Cross Beams to Elevation Tube on MMC Heliostat

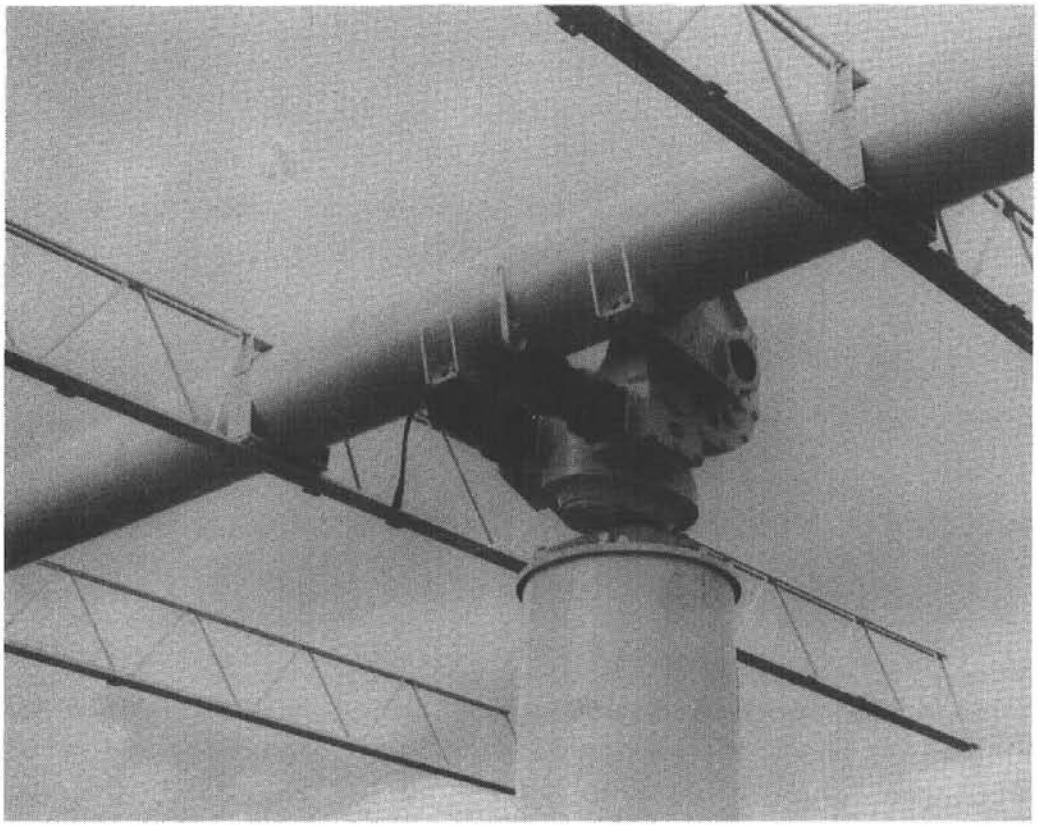

Figure A-18. Installation of Cross Beams and Elevation Tube to MMC Drive Unit

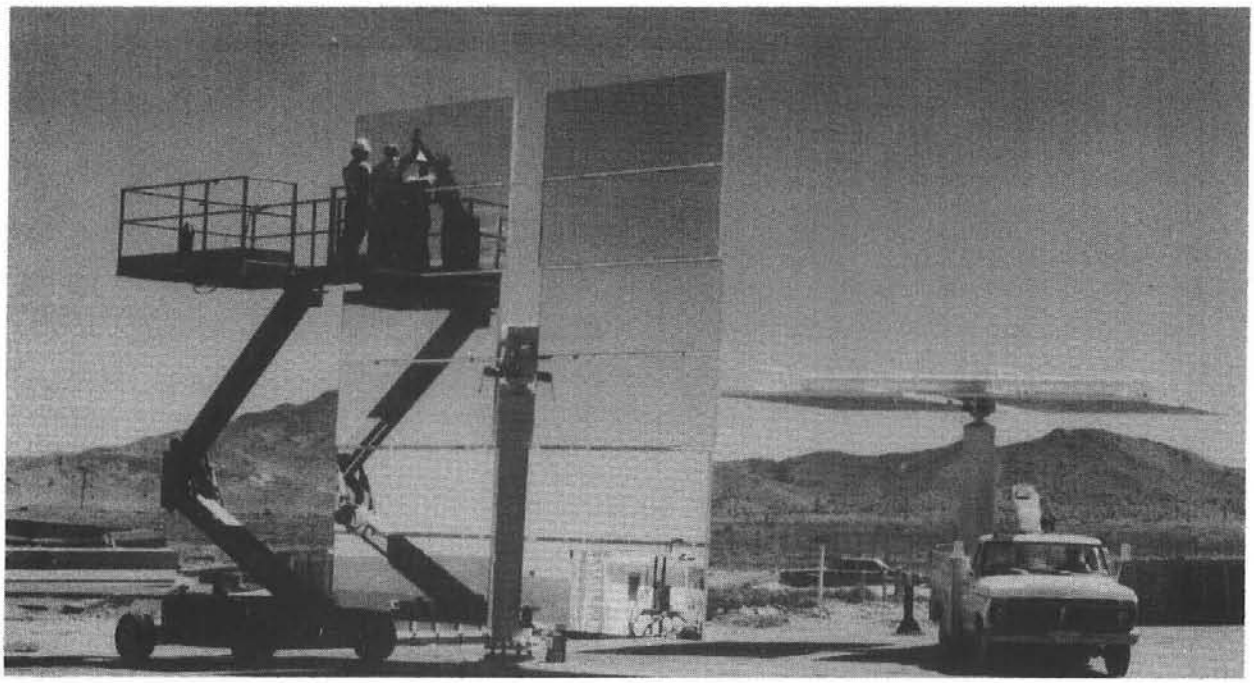

Figure A-19. Field Installation of Mirror Modules on MMC Heliostat

The MMC control trailer and computer control system arrived at the CRTF on 6/21/79. System interface and checkout proceeded smoothly and the MMC heliostats were fully operational by the first week in July. A front and a rear view of a fully assembled MMC heliostat are shown in Figures A-20 and A-21.

Additional details concerning heliostat design and operation will be provided in the discussions of each test that was performed at the CRTF. The following sections of this report detail the objective, procedure, and results of each of the nine tests previously outlined in Table A-I.

Test A-1: Point Loading

Objective

As part of the prototype heliostat evaluation, a detailed finite element structural model was generated for each type of heliostat using MSC/NASTRAN.[6] A representation of these models is shown in Figure A-1.1. The purpose of the NASTRAN model was to provide heliostat structural response information for a large variety of conditions that were representative of actual operating environments. NASTRAN analysis was to provide predicted heliostat structural deflections as a result of gravity and wind loading of the structure, to identify highly stressed areas under survival wind load (40 m/sec) conditions, and to determine natural vibrational frequencies of the heliostat.

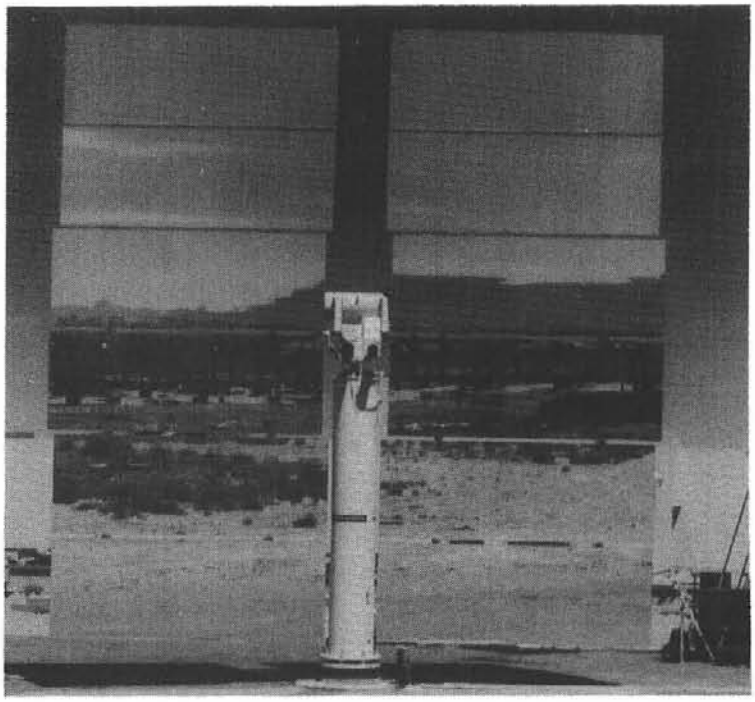

Figure A-20. Front View of Fully Assembled MMC Heliostat

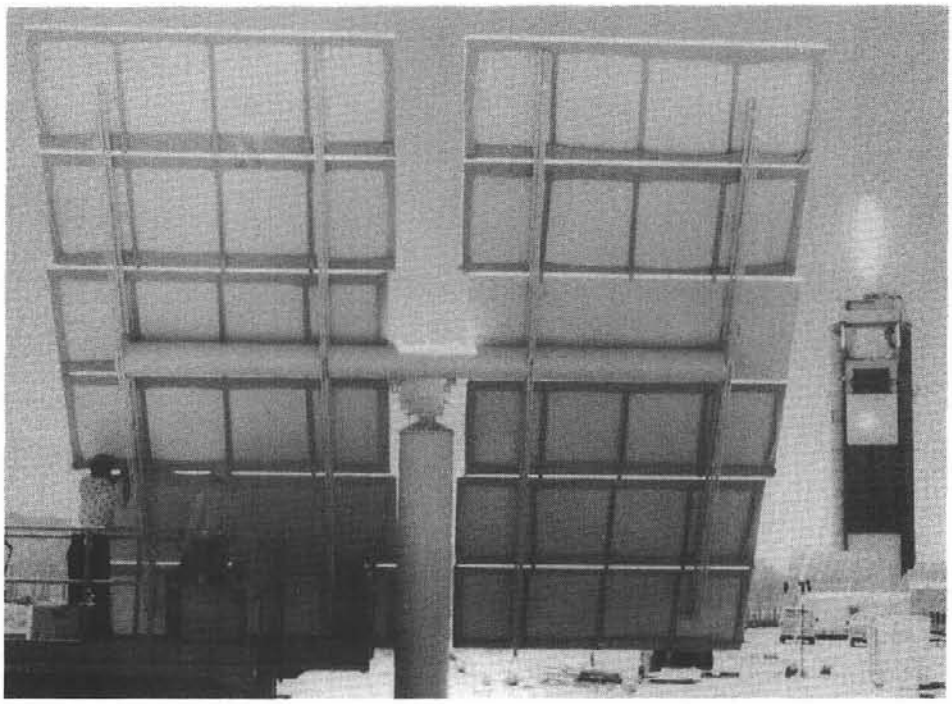

Figure A-21. Rear View of Fully Assembled MMC Heliostat

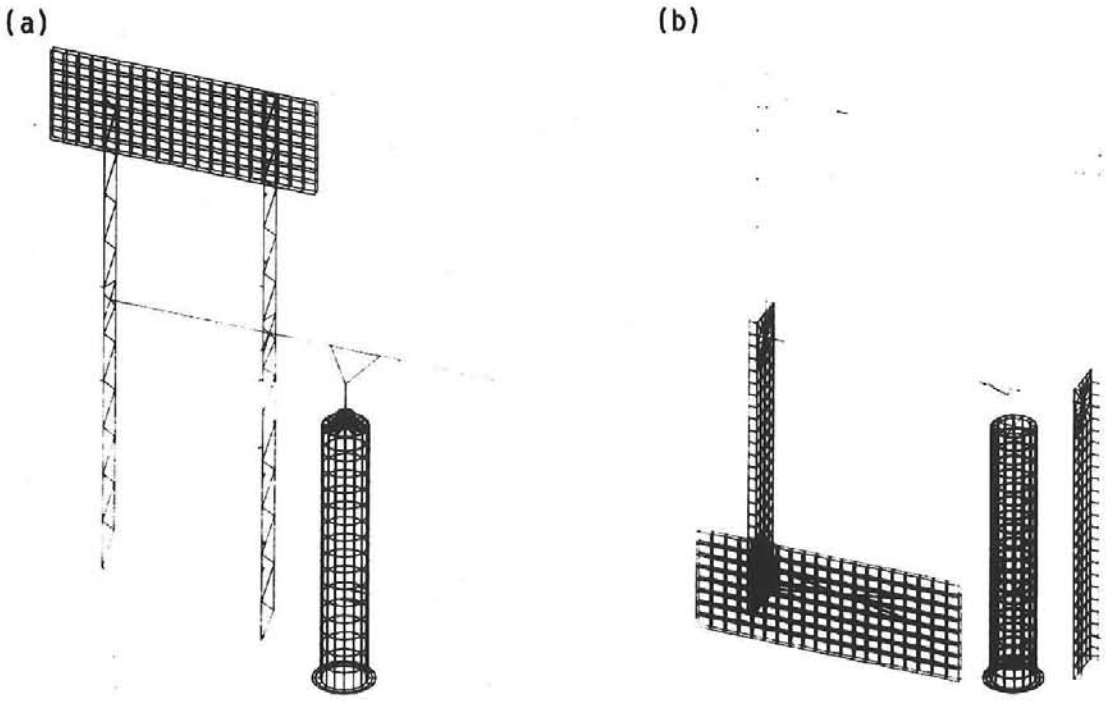

Figure A-1.1 Finite Element Model for Prototype Heliostats (a) MMC and (b) MDAC

A large degree of emphasis was placed on the outputs from the NASTRAN code, therefore, a relatively simple point loading scheme was employed to verify the NASTRAN code for a particular set of load configurations. It was felt that if reasonable agreement between measured and NASTRAN-predicted deflections was obtained for these specific load conditions then a reasonable degree of confidence could be placed in the NASTRAN predicted deflections under a variety of gravity and wind loading conditions.

The objective of this point loading test was to verify the NASTRAN structural model of the heliostats. This was done by statically loading the heliostats with point loads and comparing the measured deflections with those predicted by NASTRAN.

Description

Figure A-1.2 illustrates the four different loading configurations that were employed. Two levels of loading were done for each configuration. Eight dial indicator measurement locations were used for each loading (Figure A-1.3). Typically, measurements were repeated two or three times at each load level in order to compensate for any residual deflection in the structure following the removal of the load. Since the loads and resulting deflections were relatively small, care had to be taken since even a slight wind condition would influence the dial indicator readings. Figures A-1.4 and A-1.5 show the point load test setup for the MMC and the MDAC heliostats, respectively.

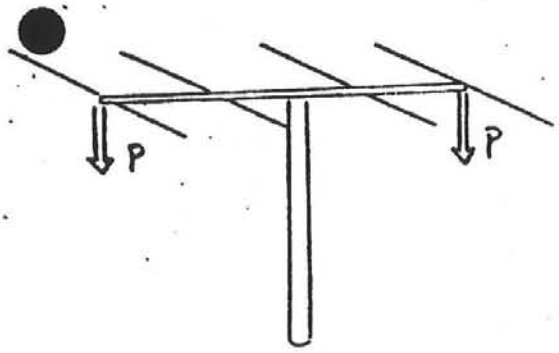

Load Configuration 1
Heliostat face up
Torque tube ends loaded
Load Set 1: P = 100 lb
Load Set 2: P = 500 lb

Load Configuration 2
Heliostat face up
Corners loaded
Load Set 1: P = 50 lb
Load Set 2: P = 250 lb

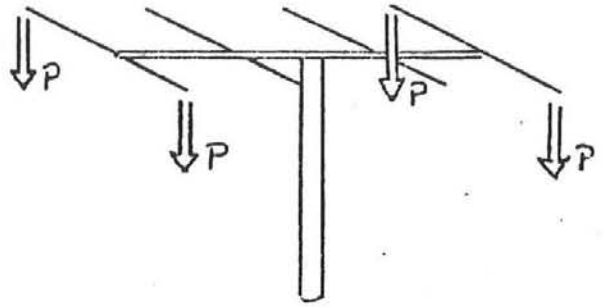

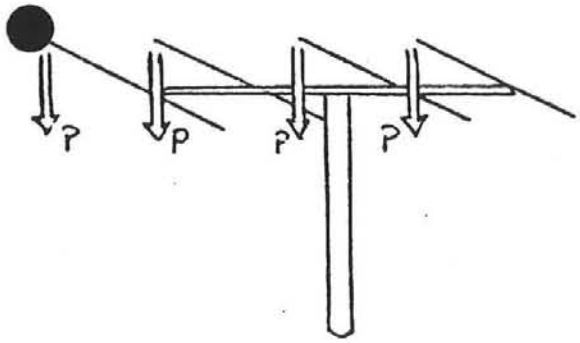

Load Configuration 3
Heliostat face up
Cross beams loaded on one side
Load Set 1: P = 50 lb
Load Set 2: P = 250 lb

Load Configuration 4
Heliostat vertical
Torque tube ends loaded
Load Set 1: P = 100 lb
Load Set 2: P = 500 lb

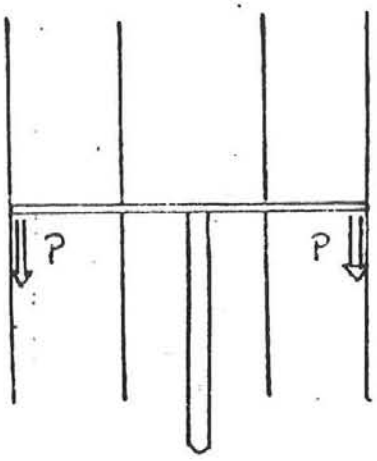

Figure A-1.2. Load Configurations and Loading Levels for Point Load Test

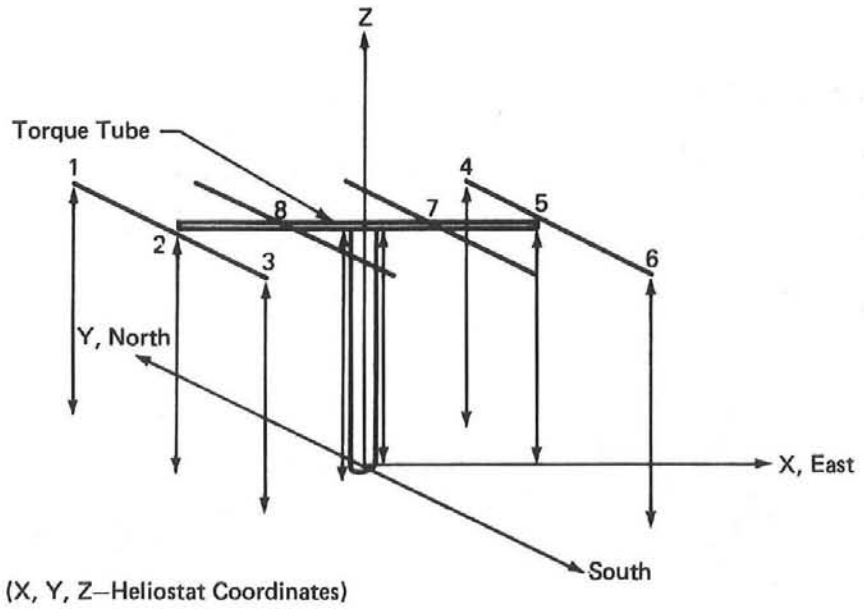

Figure A-1.3. Deflection Measurement Locations

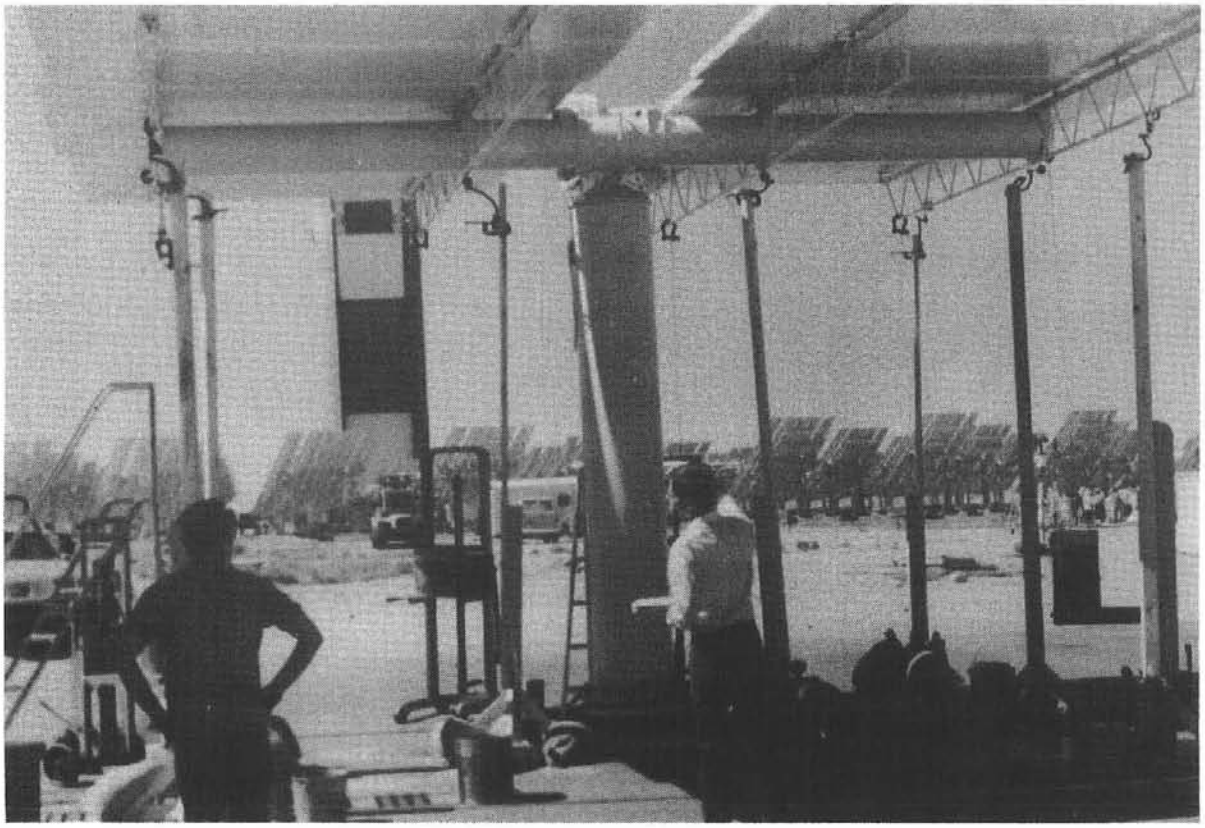

Figure A-1.4. Point Load Test Setup on the MMC Heliostat

Figure A-1.5. Point Load Test Setup on the MDAC Heliostat

Results

For the MDAC heliostat, comparison of predicted vs measured deflections shows that the computer model differs from the measured results for both the elevation tube and cross beams by less than 10 percent. The finite element model is stiffer than the actual structure, which is to be expected since the finite element model has much stiffer connections between components than the actual heliostat. Most of the differences between measured and computed results can probably be attributed to flexibilities in the actual component connections that the finite element model does not capture. The differences between measured and computed results are not significant, and the MDAC finite element model was concluded to be an accurate representation of the real heliostat.

For the MMC heliostat, comparison of differences in deflections between various stations in the measured and computed results was not always within a 10-percent range. The calculated displacements for the elevation tube, for example, differed from the measured results by approximately 15 percent in one case. The MMC heliostat proved to be a more difficult structure on which to take repeatable displacement measurements. During deflection measurements the dial gauges were zeroed, the heliostat was loaded, and measurements were taken. The dial gauges were then rezeroed after the load was removed. The MMC heliostat measurements often showed a fairly substantial difference in the preload and postload zero readings. Because of various flexibilities in the

couplings between the cross trusses and elevation tubes, the heliostat cross beam assembly took a "set" as a result of the loads applied. Subsequent loading and unloading of the structure resulted in a different set. This behavior was later isolated during simulated 40-m/sec (90-mph) wind load testing (Test 9) and will be discussed later in this report. In spite of these difficulties, it was possible to obtain fairly good agreement between the raw data and computed results. This is indicated by the results shown in Table A-1.I. These results are the measured and computed displacements for Load Configuration 3 with 113.6-kg (250-lb) loads applied. The ability of the computer model to match most of the raw data indicated that there were no serious flaws in the model. It is believed that this also indicated that the model was an accurate representative of the real structure.

TABLE A-1.I

MEASURED AND PREDICTED DEFLECTIONS FOR LOAD CONFIGURATION 3
(MMC Heliostat)

Location	Computed Deflection Z (cm)	Measured Deflections (cm)		
		Z_1	Z_2	$\bar{Z}$
1	2.34	2.44	2.22	2.33
2	0.29	0.44	0.42	0.43
3	-2.65	-3.04	-2.76	-2.90
4	2.34	2.60	2.58	2.59
5	0.28	0.64	0.55	0.59
6	-2.67	-2.84	-2.60	-2.72
7	0.35	0.53	0.48	0.50
8	0.35	0.58	0.50	0.54

Conclusions

It is believed that the NASTRAN models were good representations of both prototype heliostat structures; and consequently, a corresponding level of confidence was placed on NASTRAN predicted deflections. The influence on optical performance (beam quality) of NASTRAN predicted gravity deflections will be discussed later in this report (Test A-7).

Test A-2: Mirror Alignment (Canting)

Objective

In order to assess the optical performance of a heliostat by comparing a measured beam to that predicted by a model, it is necessary to determine the relative angular orientation of the individual mirrors on the heliostat with

respect to each other. This is referred to by different terms: mirror pre-alignment, mirror alignment, or mirror canting. There are essentially two different schemes for mirror canting, on-axis canting and off-axis canting. If individual heliostat mirrors are canted on-axis they approximate a spherical surface. In this case, the normals to the center of each mirror are orthogonal to the surface of an imaginary sphere with a desired radius of curvature. The desired radius of curvature chosen depends on the slant range from the heliostat to receiver (target) because the focal point (location of minimum beam size) occurs at a slant range of 1/2 the radius of curvature for a spherical reflective surface. If individual heliostat mirrors are canted off-axis, the central reflected rays from the individual mirrors are coincident at a point on the target for a particular heliostat/target geometry and for a particular sun position. If the sun were artificially placed in line with the target center and the heliostat center an off-axis canting of the heliostat would actually produce on-axis canting.

The objective of this test was to identify the canting scheme that was used for the prototype heliostats and to assess the degree of canting error associated with the particular procedure used during canting. The results of this test provided necessary canting input parameters to the optical model HELIOS.

Description

Before the installation of the MMC and the MDAC prototype heliostats at the CRTF it was understood that the procedure used for mirror canting prior to testing would probably not be completely representative of the canting procedure planned for mass production of the heliostats. This was primarily due to the cost associated with developing a large mirror canting tool which would be used during mass production. It was decided that because of the competitive nature of the testing, the same procedure would be used to cant the mirrors on both contractors' heliostats. This procedure was relatively straightforward involving only the use of mirror covers and resulted in an off-axis alignment. In addition to the evaluation of both contractors' heliostats using this off-axis alignment scheme, an additional evaluation of the MDAC heliostats was done for an on-axis mirror canting.

Figure A-2.1 shows MMC Heliostat #1 during off-axis canting. Cloth covers are masking all but the mirror to be used as a reference during canting. The spot on the BCS target is the reflected beam image from this single mirror.

The basic procedure followed was to uncover each mirror in sequence and visually superimpose the image from each facet on the image from the reference mirror. This procedure is indicated in Figure A-2.2 where mirror module Number 10 is being canted to superimpose its image on the image from the reference mirror module Number 5. The degree of superposition was determined both visually and by observing isoflux density contours generated by the image analyzer in the BCS. After a mirror module was canted with respect to the reference, then it was recovered and the next mirror to be canted was uncovered. This canting procedure required a finite period of time (approximately one hour) to complete. Consequently, the resulting mirror alignment was not an ideal off-axis cant in that the sun/heliostat/target geometry was changing

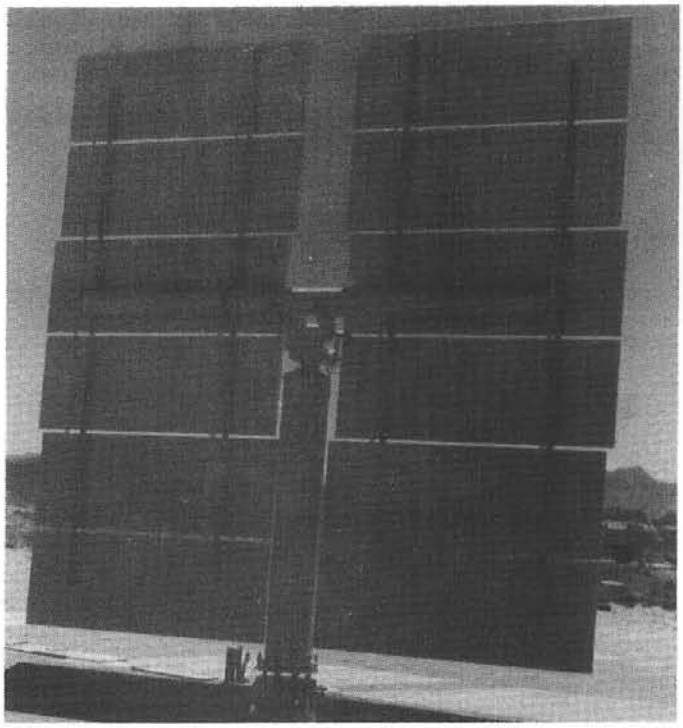

Figure A-2.1. MMC Heliostat #1 During Off-Axis Canting of the Mirror Modules

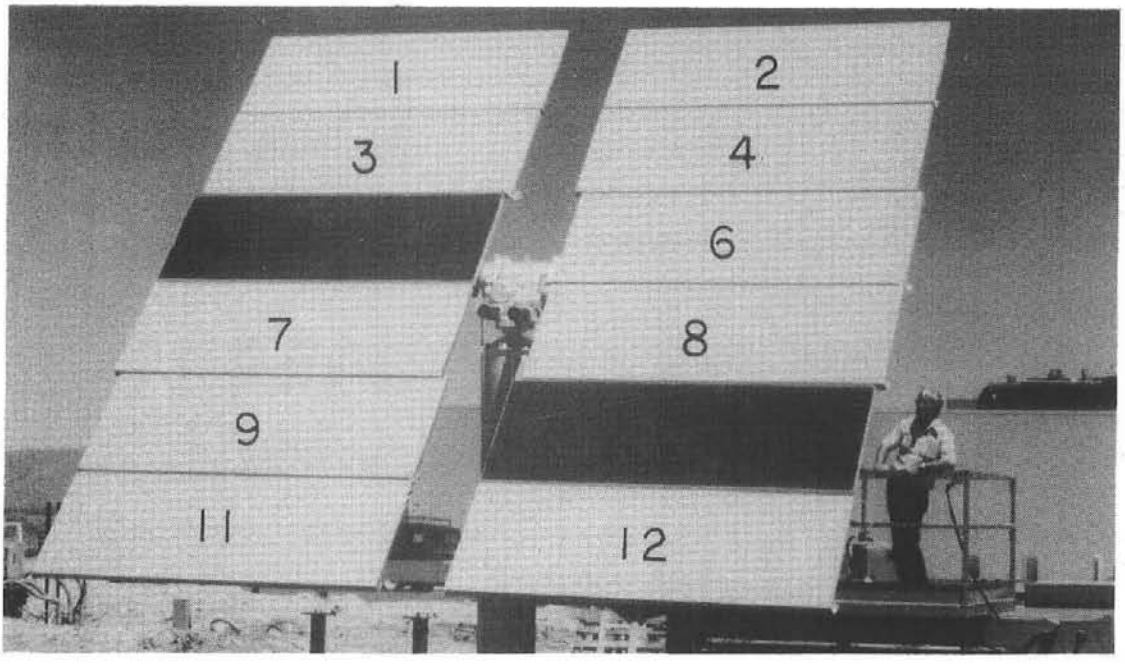

Figure A-2.2. Mirror Module #10 Being Canted with Respect to Reference Mirror Module #5 on MMC Heliostat

during the time interval. However, during the optical analysis of these heliostats with the HELIOS code they were assumed to have an ideal off-axis cant at a time corresponding to the midpoint of the canting time interval.

The mirror canting scheme used by MDAC to obtain an on-axis cant of their heliostats at the CRTF was conducted in the CRTF assembly building. The heliostat torque (elevation) tube was first pinned to a support fixture in the assembly building (Figure A-2.3). The heliostat cross beams were then installed on the torque tube and leveled with respect to a small reference plane located in the center of the torque tube (Figure A-2.4). Spacers of predetermined thickness were placed between the mirror modules and cross beams to provide an initial cut at the canting of the individual mirrors relative to the plane defined by the cross beams (Figure A-2.5). The mirror canting was then fine-tuned using two different leveling tools in conjunction with an electronic inclinometer. A long tool was used along the long dimension of each mirror (Figure A-2.6) and a short leveling tool was used across the short dimension. On completion of the canting procedure, the heliostat mirrors were canted to approximate an on-axis alignment with an effective focal length of 312 m, which corresponded to the test slant range at the CRTF. The final cant angles set with the inclinometer leveling tools also contained a bias to compensate for analytically determined gravity-induced deflections of the mirror support structure at a heliostat elevation angle of 45 degrees.

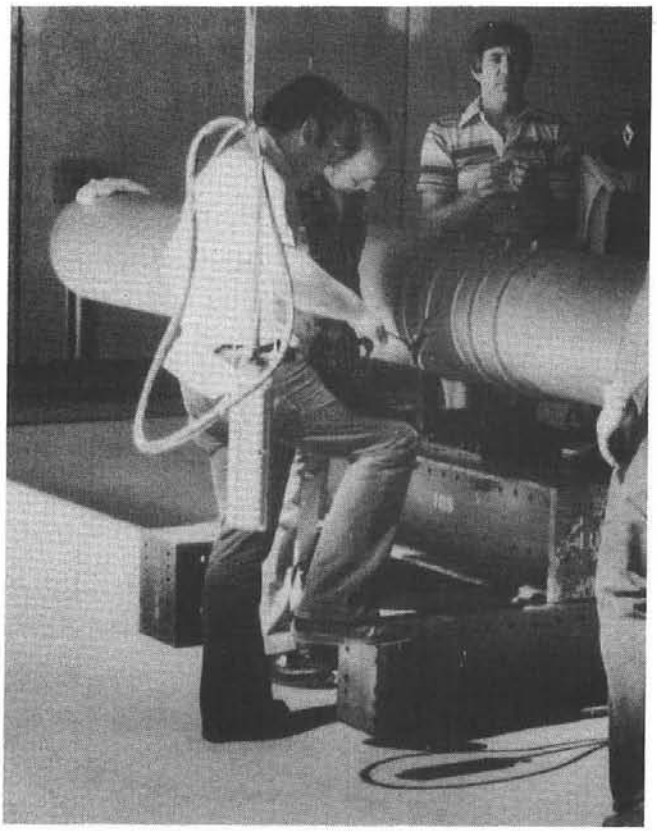

Figure A-2.3. MDAC Elevation Tube Pinned to Assembly Fixture

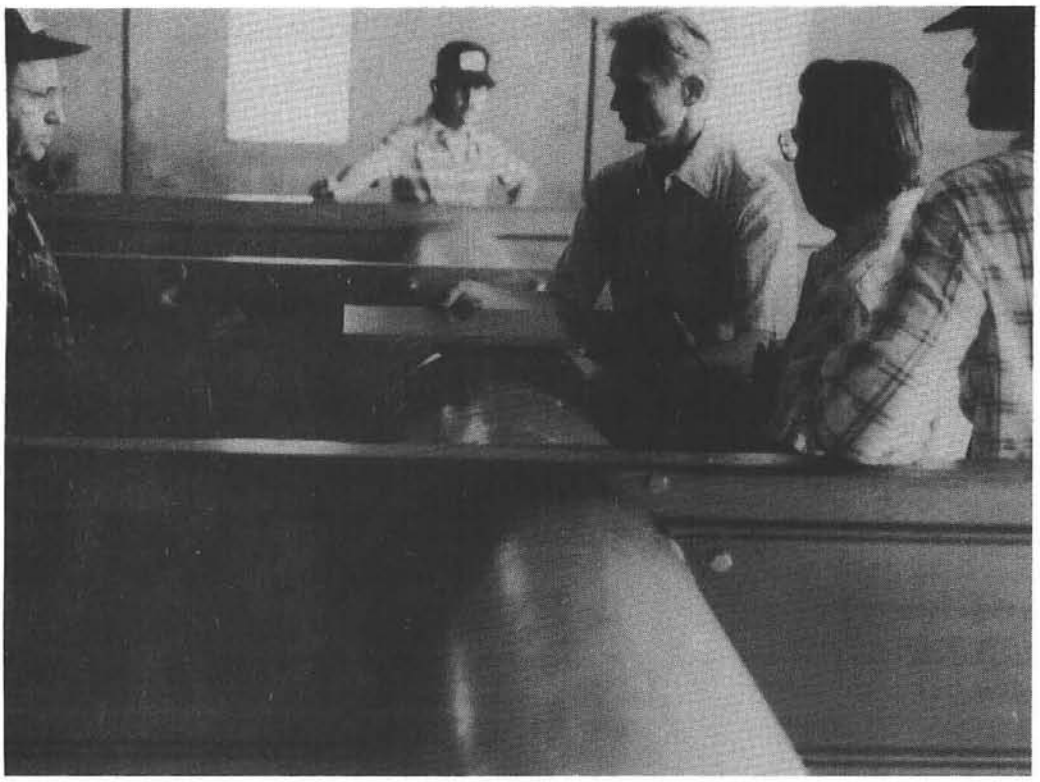

Figure A-2.4. MDAC Cross Beams Assembled with Respect to Reference Plane in the Center of the Elevation Tube

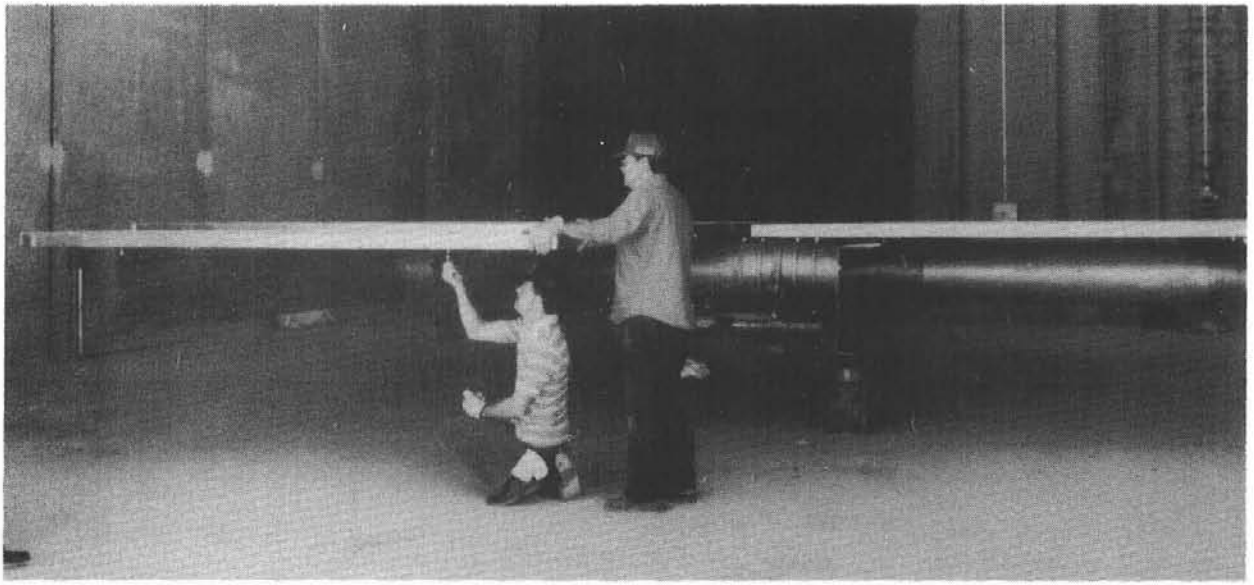

Figure A-2.5. Assembly of MDAC Mirror Modules to the Cross Beams

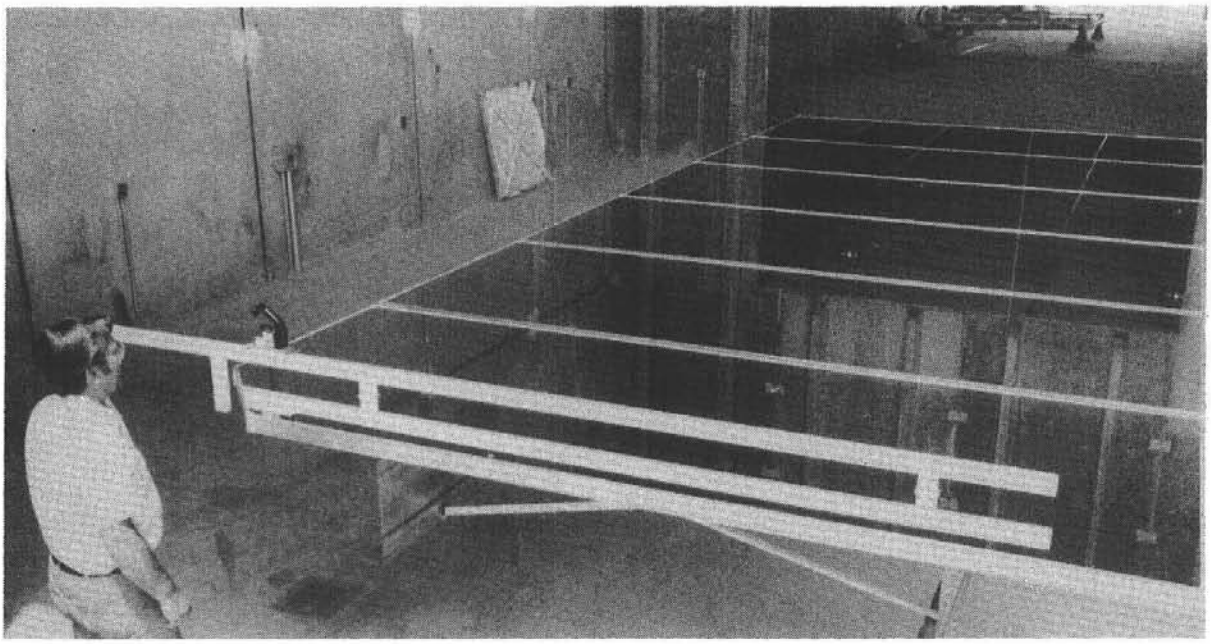

Figure A-2.6. On-Axis Canting of MDAC Mirror Modules Using an Electronic Inclinometer Canting Tool

Results

The final mirror canting conditions that were evaluated at the CRTF are shown in Table A-2.I. This table shows the day the off-axis canting was done, the actual time interval required to do the canting, and the midpoint time that was assumed to represent the alignment condition. The heliostat/target geometry for each case is that defined previously in Figures A-2 and A-4. It took approximately twice as long to cant the mirrors on the MDAC heliostats because of the greater difficulty in installing and removing covers, and because it was more difficult to cant mirrors with a four-point mounting system.

The effect of the time interval required in actually doing the off-axis mirror canting is shown in Figure A-2.7. This figure shows the relative motions of the central reflected rays from each mirror module on MMC Heliostat #1, assuming an ideal off-axis alignment for Day 171 at Solar Time -0.337 hour and for the CRTF test geometry. The units on the axis represent distances on the BCS target. The arcs traced out by the intersection of the central reflected ray from each mirror module and the BCS target plane represent the path followed by the central reflected rays during a 23-minute time interval either side of the -0.337 alignment time. All the separate central rays intersect at the off-axis alignment time of -0.337 hour.

TABLE A-2.I

MIRROR CANTING CONDITIONS AS TESTED AT THE CRTF

Heliostat	On-Axis Focal Length (m)	Day	Solar Time (hr)	Geometry	Actual Canting Time Interval (MDT)
MDAC #1	312*	219	0.172	CRTF	12:15-2:30
MDAC #2	312*	223	-0.152	CRTF	12:05-2:00
MMC #1	-	171	-0.337	CRTF	12:25-1:10
MMC #2	-	170	0.066	CRTF	12:45-1:38 Off-Axis

*With compensation for gravity at heliostat elevation angle of 45°.

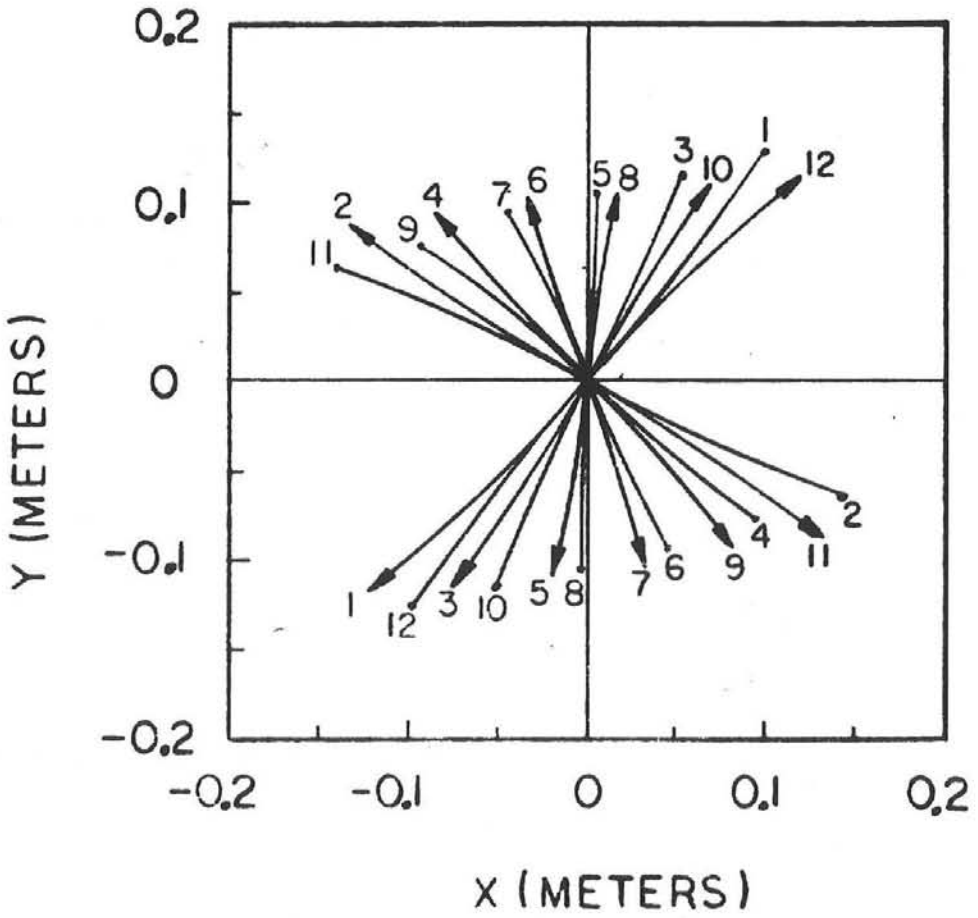

Figure A-2.7. Relative Motion on BCS Target of the Central Reflected Rays from Each Mirror Module on the MMC Heliostat #1 Assuming Off-Axis Mirror Canting for Day 171 at Solar Time -0.337 hr. Time interval indicated is from -0.720 to 0.046 hr.

The numbering scheme for the arcs in Figure A-2.7 corresponds to the mirror module numbering scheme shown in Figure A-2.2. For instance, 23 minutes prior to the -0.337-hour alignment time the central reflected ray from mirror Number 1 is in the upper right quadrant of Figure A-2.7, at exactly -0.337 hour it is at the origin, and 23 minutes following -0.337 hour it is in the lower left quadrant. Using these relative motions of the reflected rays, and knowing the order in which mirror images were superimposed on the reference mirror image, it is possible to estimate the degree of canting error relative to an ideal canting at time -0.337 hour.

Figure A-2.8 illustrates the estimated canting error for heliostat MMC #1 for which the mirror modules were canted in the following order: 5, 4, 3, 1, 2, 12, 11, 8, 10, 7, 9. Module 6 was used as the reference for this heliostat.

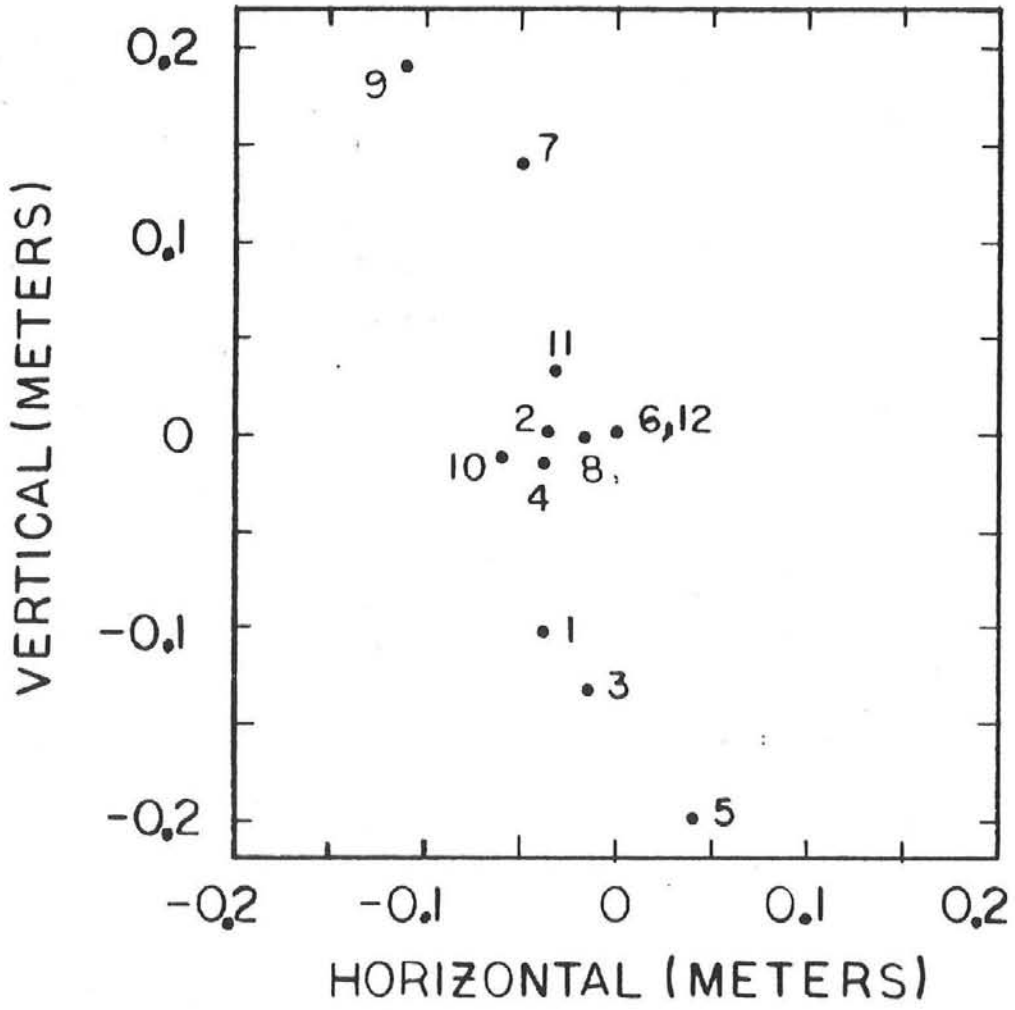

Figure A-2.8. Estimate of MMC #1 Mirror Module Canting Error Relative to Assumed Off-Axis Alignment Condition (Day 171 at Solar Time -0.337 hour)

Figure A-2.8 indicates a larger canting error spread vertically than horizontally. However, the maximum error is approximately 0.2 m (Module 5) which translates to a mirror normal angular error of approximately 0.35 milliradians. The longer time interval required for doing the off-axis canting of the MDAC heliostats resulted in a larger degree of canting error; however, the maximum mirror normal angular error is estimated to be less than 1 milliradian. These canting errors represent one of the sources of error that result in a nonideal optical performance of a heliostat. The effects of these canting errors and other sources of optical performance degradation will be discussed in Test 7.

Conclusions

The results of this test provided an identification of the mirror alignment condition for each heliostat tested. This alignment condition was used during the HELIOS analysis of BCS beam quality measurements (Test 7). The results of this test also provided an estimate of the degree of alignment (canting) error associated with the canting procedures used during testing at the CRTF.

Although the canting procedures used at the CRTF were not totally representative of the procedures that would be used during mass production of the heliostats, it is believed that they were still representative. In that there is probably slightly more canting error associated with the techniques used at the CRTF than a production technique, there may be a slight degree of conservatism in the beam quality assessments made in Test 7.

Test A-3: Mirror Realignment

Objective

After installation of a heliostat in the field it may be necessary to replace one or more mirror modules. In this event, a field tool will be required to realign (cant) the mirrors that are replaced. The objective of this test was to demonstrate the acceptability of this tool and/or procedure.

Description

The procedure used for determining the acceptability of the recanting procedure involved the use of the BCS. A beam quality measurement was made using the BCS before and after mirror recanting. This test was accomplished by switching mirror Modules 6 and 12 on the test heliostat and then using the recanting procedure to align the two mirrors.

On 7/12/79 Mirrors 6 and 12 on MDAC Heliostat #1 were exchanged as shown in Figure A-3.1. The MDAC approach to mirror replacement involved relying on strict manufacturing tolerances on mirror module dimensions between the mounting cups and the mirror face. Recanting then only involved the switching of predetermined spacers from the mirror being replaced to the replacement mirror. This procedure was used during testing at the CRTF.

Figure A-3.1. Mirror Modules Being Exchanged on MDAC Heliostat #1

Figure A-3.2 shows the spacers being exchanged from one mirror module to the other. This test was performed while the heliostat was in an on-axis mirror alignment, as defined earlier in Table A-2.I.

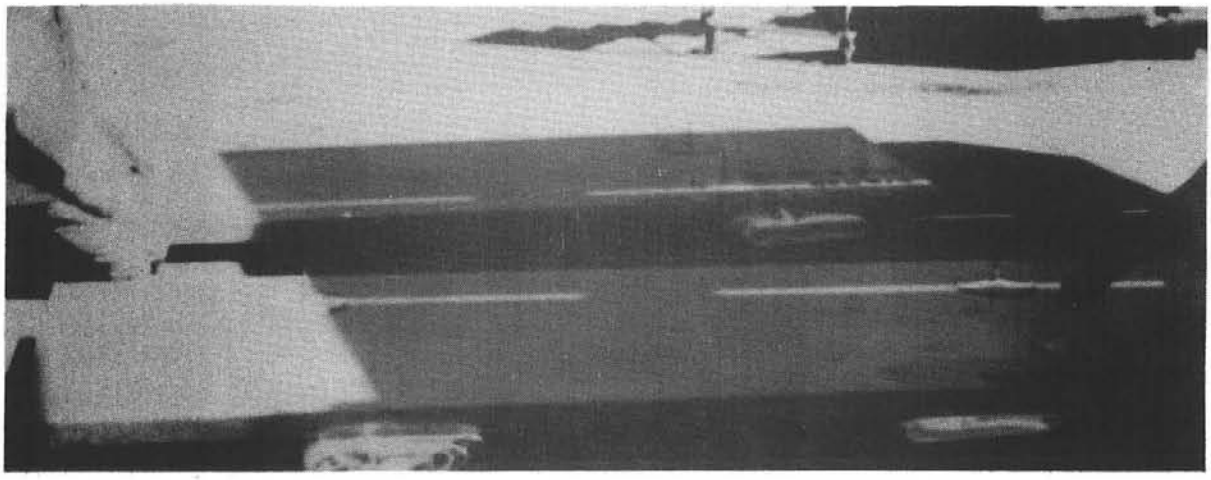

Figure A-3.2. Transfer of Canting Spacers to the Replacement Mirror Module

On 8/10/79, Mirrors 6 and 12 on MMC Heliostat #1 were exchanged. The MMC replacement approach makes use of a field canting tool. The tool consists of four electronic inclinometers, two each mounted at 90 degrees to each other on two triangular (3-point mount) bases. The triangular base units with the associated inclinometers are shown in Figure A-3.3. The inclinometers are housed inside the unit with one inclinometer oriented along the long axis of the mirror module and the second at 90 degrees to the first.

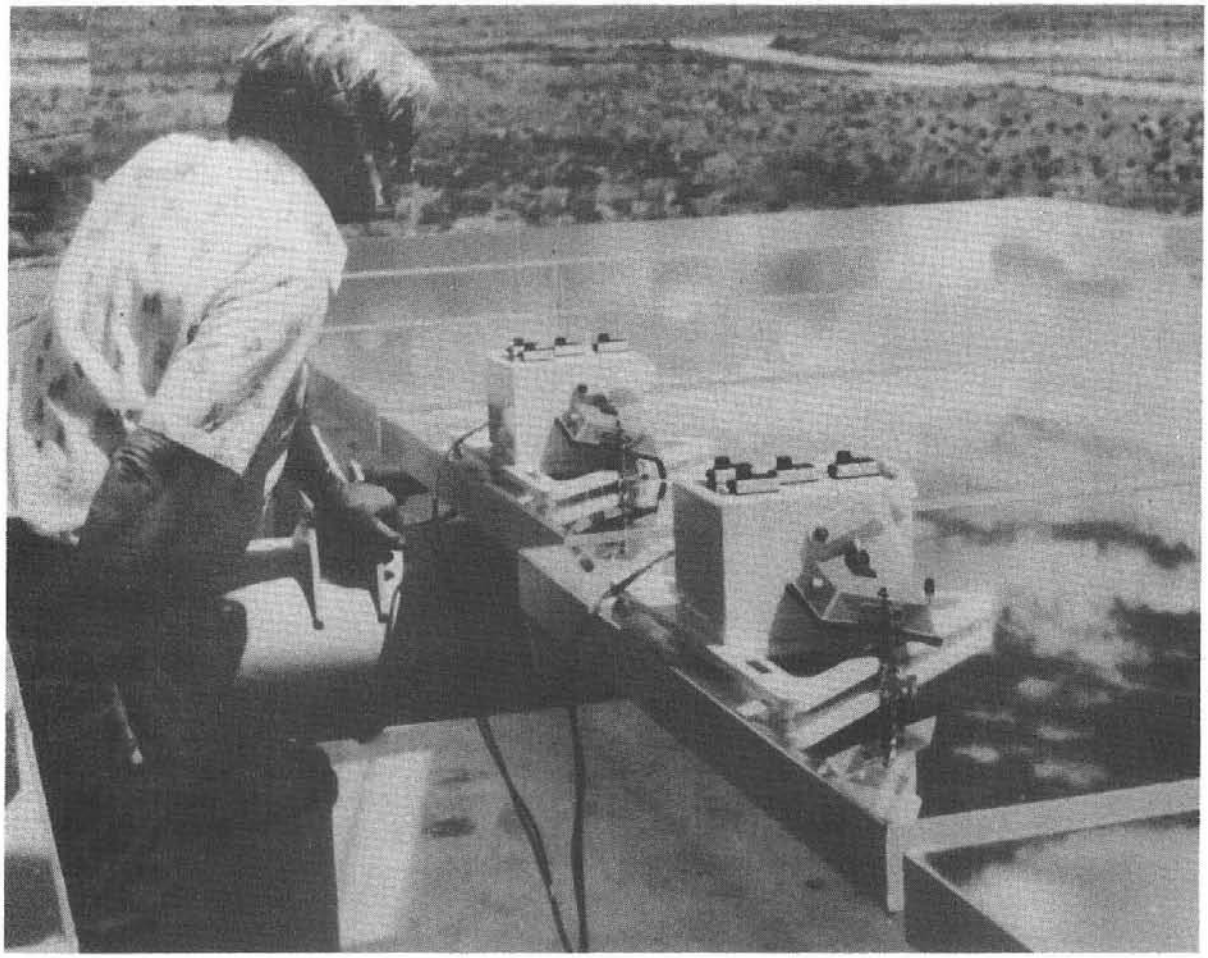

Figure A-3.3. Base Units Associated with the MMC Recanting Tool

After mirror replacement, the heliostat was rotated in elevation to a horizontal (mirror face up) orientation. One of the recanting tool base units was placed on the heliostat reference mirror (typically Number 5) and the second unit was placed on the mirror to be aligned. The angular orientation of any mirror with respect to the reference mirror was predetermined. Therefore, two predetermined angles for the replacement mirror were set on the digital dials on the top of the inclinometer housing, as shown in Figure A-3.4. The

three mirror mounting adjustment bolts were adjusted until the meters were nulled and then the bolts were tightened. This test was performed for an off-axis mirror alignment as previously defined in Table A-2.I.

Figure A-3.4. MMC Recanting Tool in Use During MMC Mirror Module Exchange

Results

On 7/12/79 the MDAC mirror exchange was completed in approximately 30 minutes using three personnel. Figure A-3.5 shows the BCS measured beam quality data on MDAC Heliostat #1 prior to mirror exchange. Figure A-3.6 gives the BCS data following the mirror exchange. The multiple isoflux density contours shown represent 5, 10, 40, 60, and 80 percent of the measured peak flux density.

On 8/10/79 the MMC mirror exchange was completed in approximately 45 minutes, also using three personnel. Figure A-3.7 shows the BCS measured beam quality data on MMC Heliostat #1 prior to mirror exchange, and Figure A-3.8 gives the BCS data following the mirror exchange.

In assessing the degree of success of the recanting technique in terms of beam quality measurements before and after recanting, it is not acceptable to compare the before and after beam shapes directly. This is because the

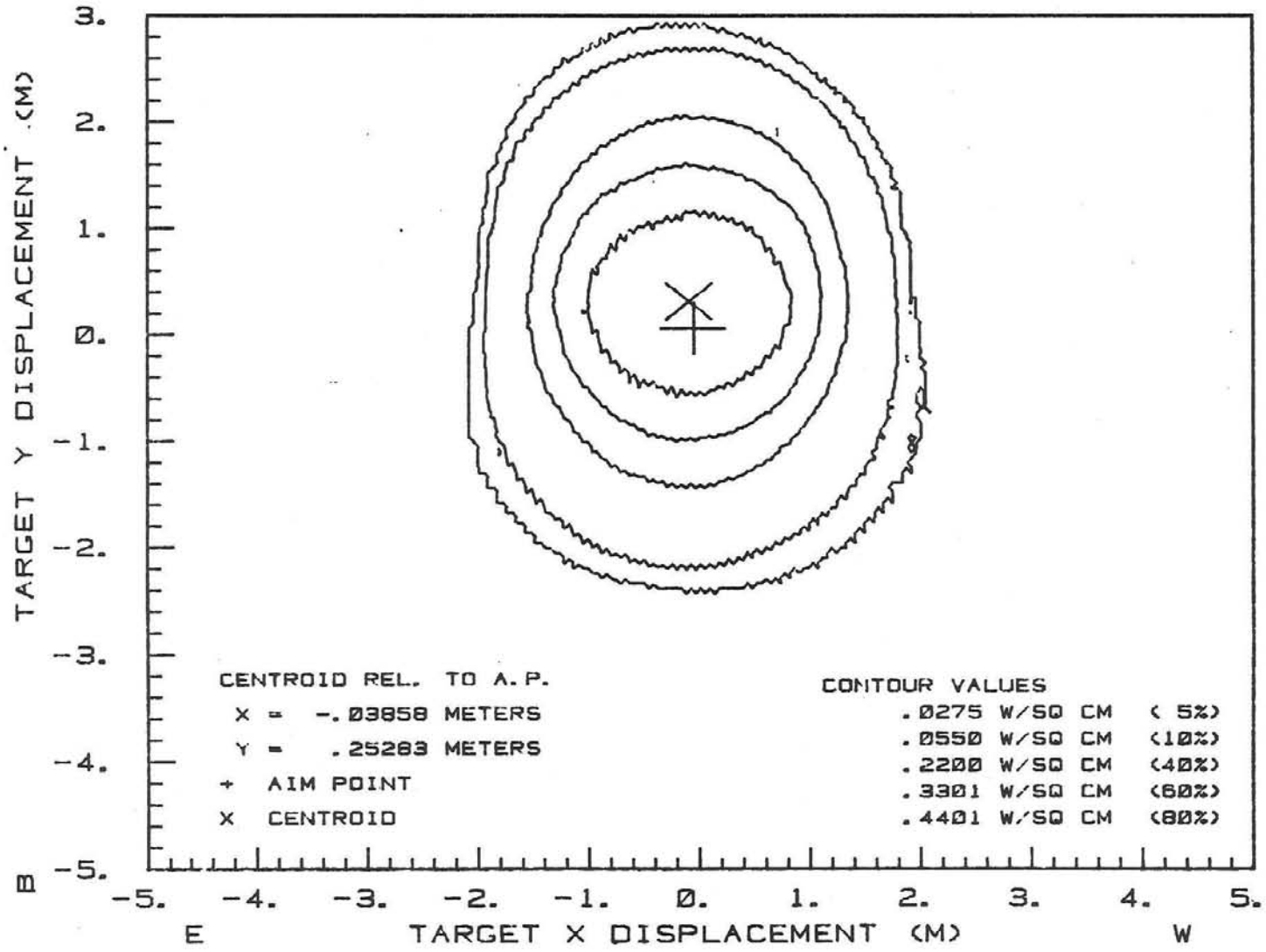

Figure A-3.5. MDAC Heliostat #1 Beam Quality Measurement Prior to Mirror Exchange

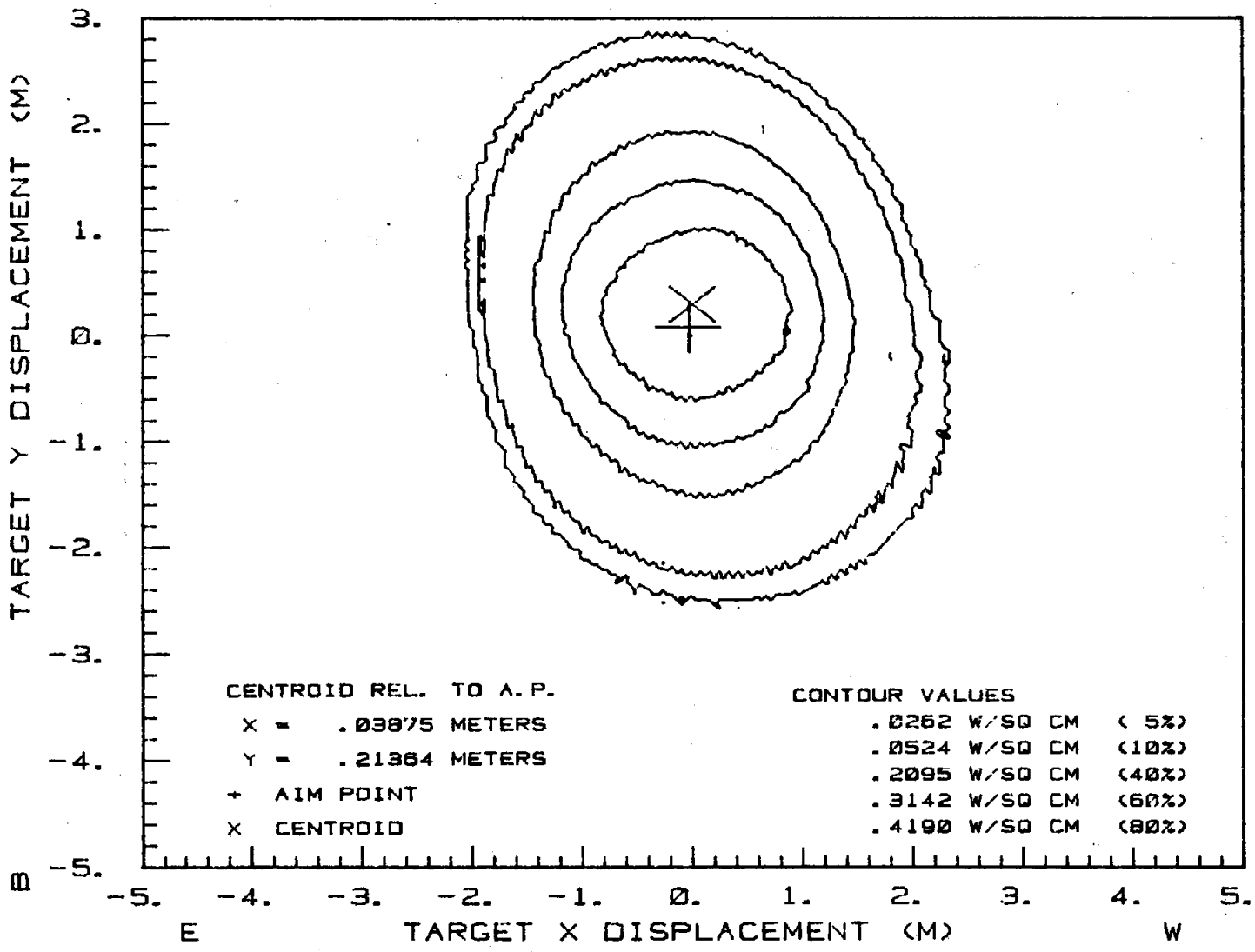

Figure A-3.6. MDAC Heliostat #1 Beam Quality Measurement Following Mirror Exchange and Recanting

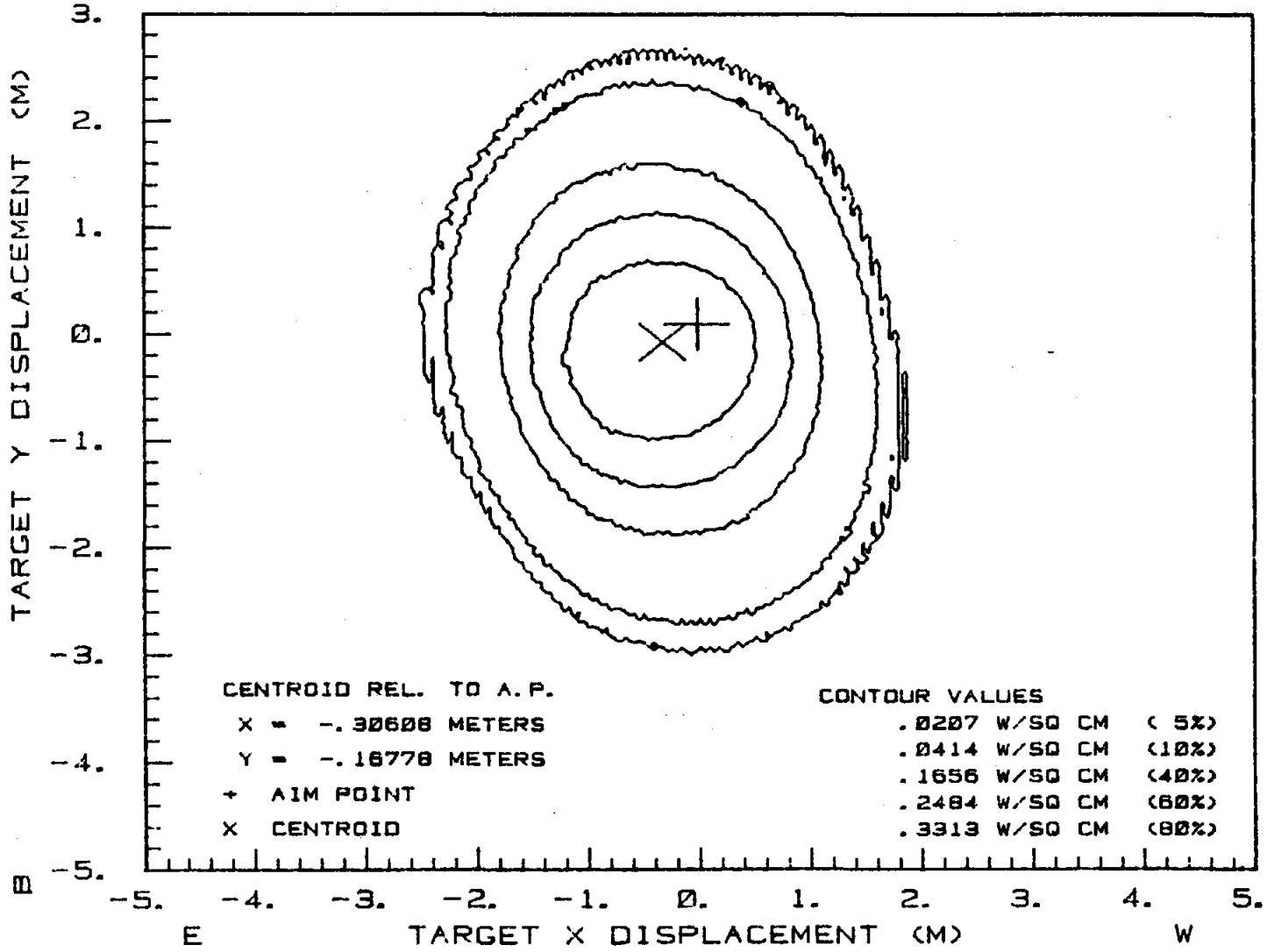

Figure A-3.7. MMC Heliostat #1 Beam Quality Measurement Prior to Mirror Exchange

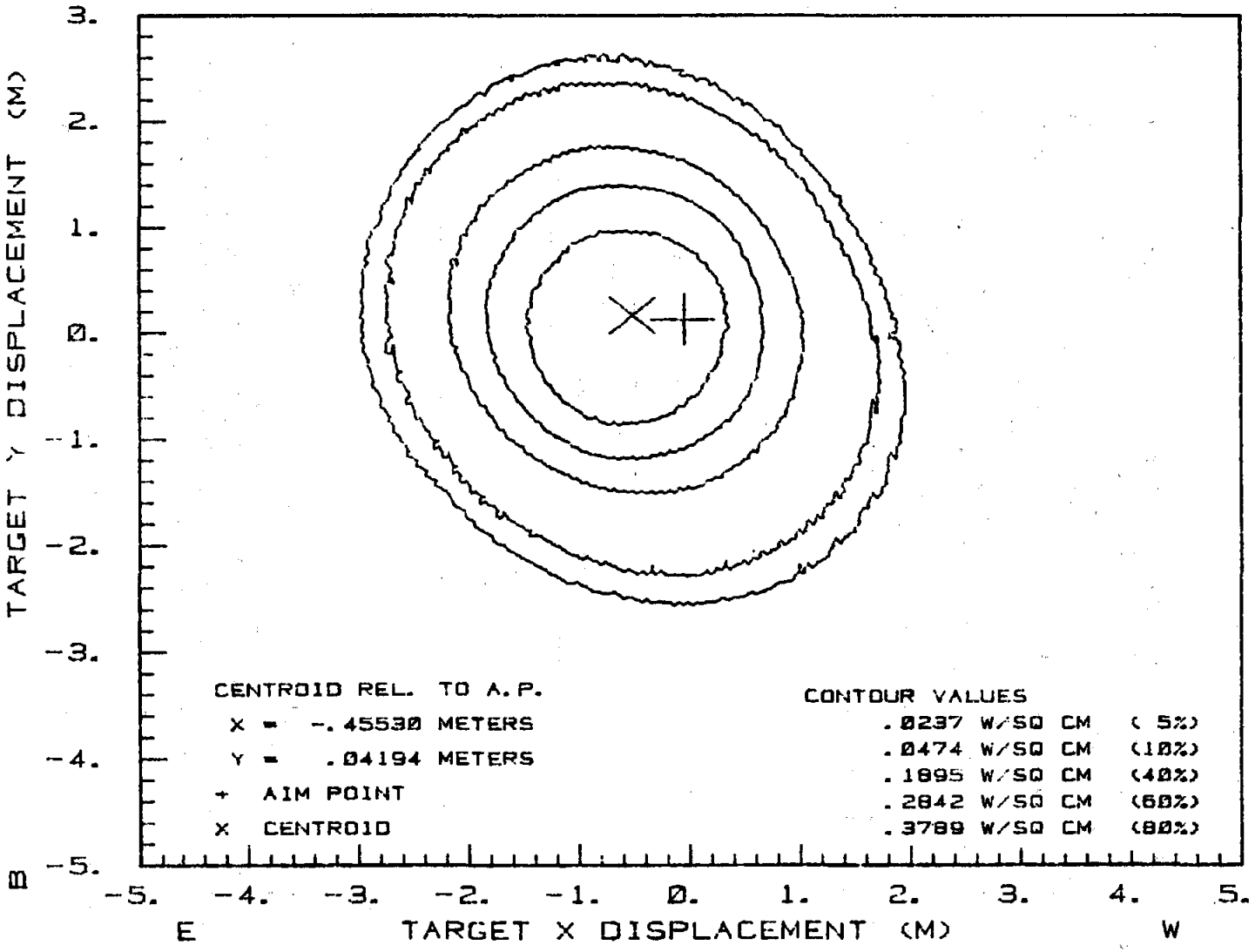

Figure A-3.8. MMC Heliostat #1 Beam Quality Measurement Following Mirror Exchange and Recanting

beam measurements were conducted on different days and at slightly different times of day. The resulting changes in sun position and heliostat geometry will produce a change in optical response even if no additional mirror canting error was introduced by the recanting procedure. It is evident from the measurements, however, that neither procedure introduced a large degradation in beam quality.

The procedure used in analyzing the measured beam data involved the use of the heliostat optical model HELIOS. HELIOS was used to match the measured beam data prior to recanting by unfolding an error distribution that was representative of the heliostat optical response prior to mirror exchange. Similarly, HELIOS was also used to unfold an error distribution that was representative of the optical response following mirror exchange and recanting. The results of this HELIOS beam analysis are given in Table A-3.I. The values in the table represent the standard deviation of the circular normal error distribution in the reflected ray reference system that, when convolved with the optical response of an error-free heliostat, gives the best match to the measured beam data. A more detailed discussion of this HELIOS beam analysis approach will be given later in this report (Test 7).

TABLE A-3.I

RESULTS OF HELIOS/BCS EVALUATION OF RECANTING PROCEDURES

Heliostat	Initial σ_R (mr)	Following Recant σ_R(mr)
MDAC #1	1.35	1.35
MMC #1	1.55	1.65

Conclusions

Both mirror recanting procedures were performed with little difficulty during CRTF testing. The MDAC approach that involved simply exchanging spacers required slightly less time to perform; however, it does rely on strict mirror module dimensional tolerances being maintained during fabrication. The MMC approach does not rely on strict tolerances and appears to be a more dependable and versatile technique.

The HELIOS analysis of the BCS-measured beam data indicated that both procedures provided acceptable means for mirror relacement and recanting in the field.

Test A-4: Operational Modes

Objective

Successful operation of a field of heliostats in a dependable, predictable, versatile, and safe manner places several demands on the overall control system capability. The objective of this test was to demonstrate that the control system was capable of performing all typical modes of operation that could occur at the pilot plant. In addition to common modes of operation, communication loss scenarios were also to be evaluated in order to ensure predictable behavior of the heliostats in the event that communication is lost.

Description

The control system that was evaluated at the CRTF was intended to be configured in a manner such that it was capable of controlling the entire field of heliostats that would be installed at the pilot plant. Only two heliostats for each contractor were installed at the CRTF, however the control system behaved as if it was controlling a full field. The two heliostats were operated in each of two control configurations, as shown in Figure A-4.1. The hierarchy of control descends from the Heliostat Array Controller (HAC) to the Heliostat Field Controller (HFC) to the Heliostat Controller (HC). The HAC is capable of individually controlling all the heliostats in the field. This is done via messages sent to the HFCs. Each HFC in the full field configuration is capable of controlling up to 32 heliostats that are equipped with only HC electronics. Testing both the dual and single HFC configurations (Figure A-4.1) verified that the HAC was capable of controlling multiple heliostats through a single HFC and multiple HFC-equipped heliostats. The HFCs are physically located in one of the 32 heliostats along with the HC electronics. The HAC is located in the control building (trailer at CRTF). The HAC provides the man-machine interface, timing (WWV receiver), and status and error logging. It also translates operator commands and sends them to the HFCs for eventual action by the heliostat. The general control configuration for the MDAC and MMC heliostats were the same. However, the actual functions performed by the HAC, HFC, and HC in the two designs differ significantly.

MMC Control System

In the MMC design, the computational requirements are shared by the HAC and the HC. The HAC calculates the sun position and sends this information via the HFC to the HC. The HC uses the sun position to calculate the required azimuth and elevation position. The required position is compared with the actual position from the incremental encoders on the heliostat and the motors are turned on as needed to reach the desired position. The encoders have a 13-bit or 0.76-mR resolution. The heliostat absolute position is determined from a separate, single-encoder bit. This bit or mark is located a few degrees from the normal, face-down stow position. The absolute position is corrected when the heliostat encounters this bit.

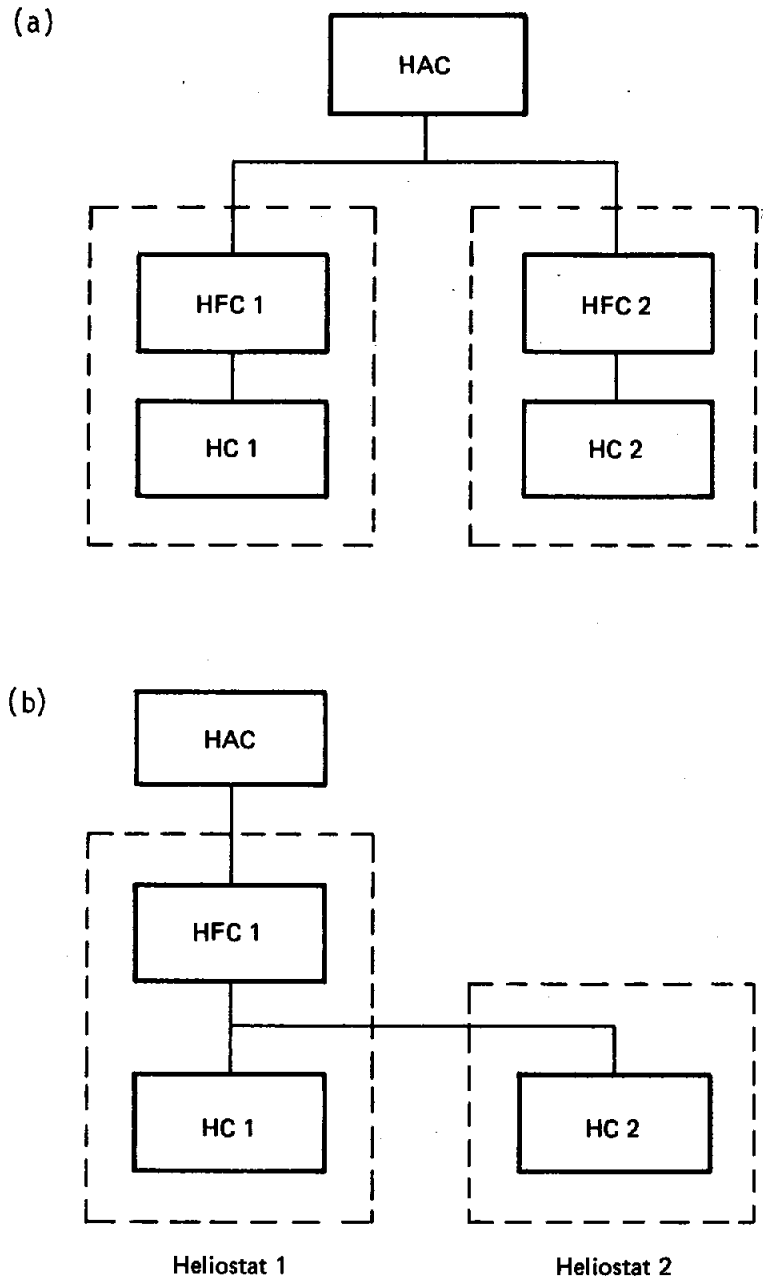

Figure A-4.1. Heliostat Control Configurations Used at the CRTF during Testing. (a) Dual HFC and (b) Single HFC.

Microswitch limit switches on each axis interrupt motor current and prevent mechanical damage in the event of control or operator error. Power to the heliostat is 120 volts a.c. single phase and consumes about 382 watt-hours in a typical 10-hour day. The motors, one on each axis, operate on 120 or 18 volts d.c. provided by rectifiers in the HC.

MDAC Control System

The tracking computations in the MDAC design are centered in the HFC. The HAC provides the timing, monitors status, and communicates with the HFC. The HFC calculates the sun position, heliostat position, and heliostat rate of movement. The HFC sends the heliostat position in motor turns and the rate to the HC. The HC activates the motors to satisfy the position (first) and then the rate received from the HFC. The HFC also does tilt and nonorthogonality corrections to the gimbal angle positions, wire walk control, status monitoring, and reporting. The HC monitors the motor turn sensors and the absolute encoders and sends this information to the HFC when requested. The motor turn count gives about 0.14-mR resolution in azimuth and about 0.13- to 0.19-mR resolution in elevation. The heliostat elevation motion is a nonlinear function of motor turns because of the linear actuator (jack) used. Separate absolute encoders on each output axis have a 4-bit or 392.6-mR (22.5 degrees) resolution. The absolute position of the heliostat is determined by these encoders.

Magnetic limit switches on each axis operate a relay that interrupts motor current and prevents mechanical damage in the event of control or operator error. Power to the heliostat is 208 volts a.c. three phase and consumes about 523 watt-hours in a typical 10-hour day. The motors, one azimuth and two elevation, operate on 208 volts three phase. The controller, HC, and HFC operate on 120 volts a.c. single phase.

Test Description and Results

The tests were divided into four basic categories: standard modes, special modes, simulated communication loss, and south field singularity resolution. Each test was performed early in the test program and again in abbreviated form near the end.

Each test step was initiated by issuing the appropriate command to the HAC terminal. The results of the commands were recorded for later analysis. Each contractor provided a heliostat status recording capability for the test. Information that was recorded included date, time, command, alarm and log reported heliostat position. The data recording interval was 8 to 30 seconds depending upon the test. Actual and calculated reflected beam angles were also available.

Standard Modes Tests

The standard modes are those functions that are typical of actual operating conditions. The heliostats were required to independently move from a stow position (mirror face down) to a tracking standby position to a tracking target position and back again to standby and stow. Table A-4.I shows the sequence of tests.

TABLE A-4.I

STANDARD MODES TESTS

Test	Heliostat 1	Heliostat 2	Data
1	Stow to standby*	Stow	Encoder position
2	Standby to target*	Stow	Encoder position Beam centroid
3	Target	Stow to standby	Encoder position
4	Target	Standby to target	Encoder position
5	Target to standby	Target	Encoder position Beam centroid
6	Standby to stow	Target	Encoder position
7	Stow	Target to standby	Encoder position
8	Stow	Standby to stow	Encoder position
9	Stow to standby	Stow to standby	Encoder position
10	Standby to target	Standby to target	Encoder position
11	Target to standby	Target	--
12	Standby to fixed Position 1** -90° azimuth 0° elevation	Target	Encoder position

*Standby position and target position were SB and A1 as defined in Figure A-4 for all tests in this table. Tracking these points was required.

**Fixed Position 1 was a stationary azimuth and elevation encoder position with heliostat vertical and facing south for MMC and west for MDAC.

MMC--The heliostats responded correctly to the commands issued to the HAC. Table A-4.II summarizes the times required to complete the various commands. Note that in the case of the wire walks there are fixed delays built in at the bottom of the wire to allow all heliostats time to reach the point before starting up the wire.

While the heliostat is tracking, the HAC logged heliostat beam position and the error from the HAC-calculated position. The BCS was directed to record centroids at the same time. Figures A-4.2 and A-4.3 show the HAC and BCS errors. The cause of the offset in the elevation data is not known.

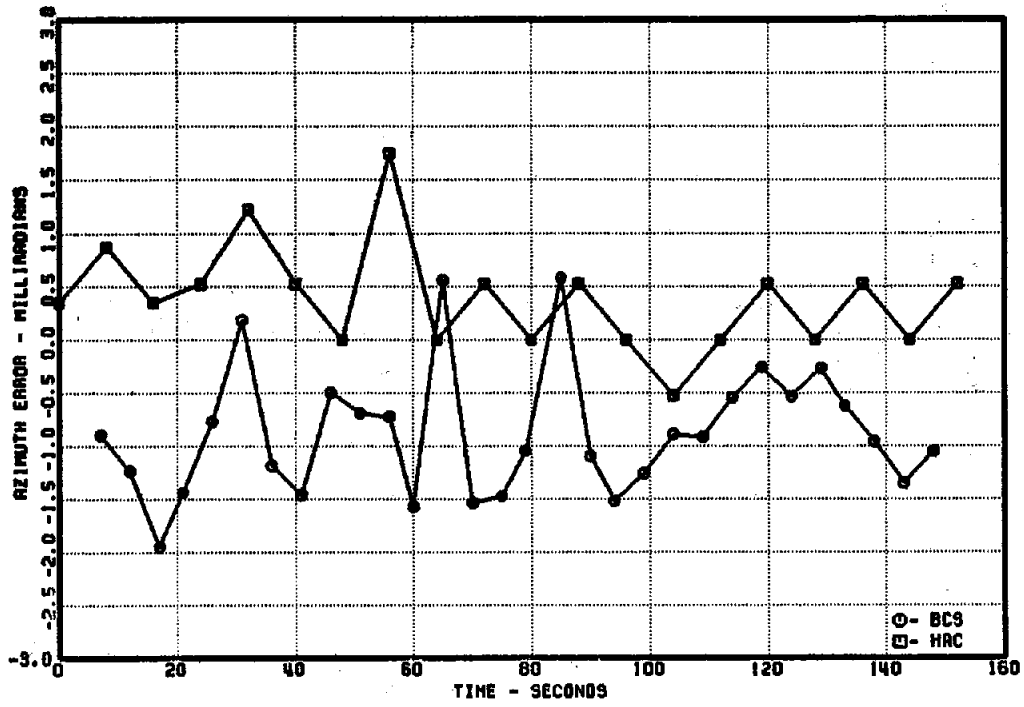

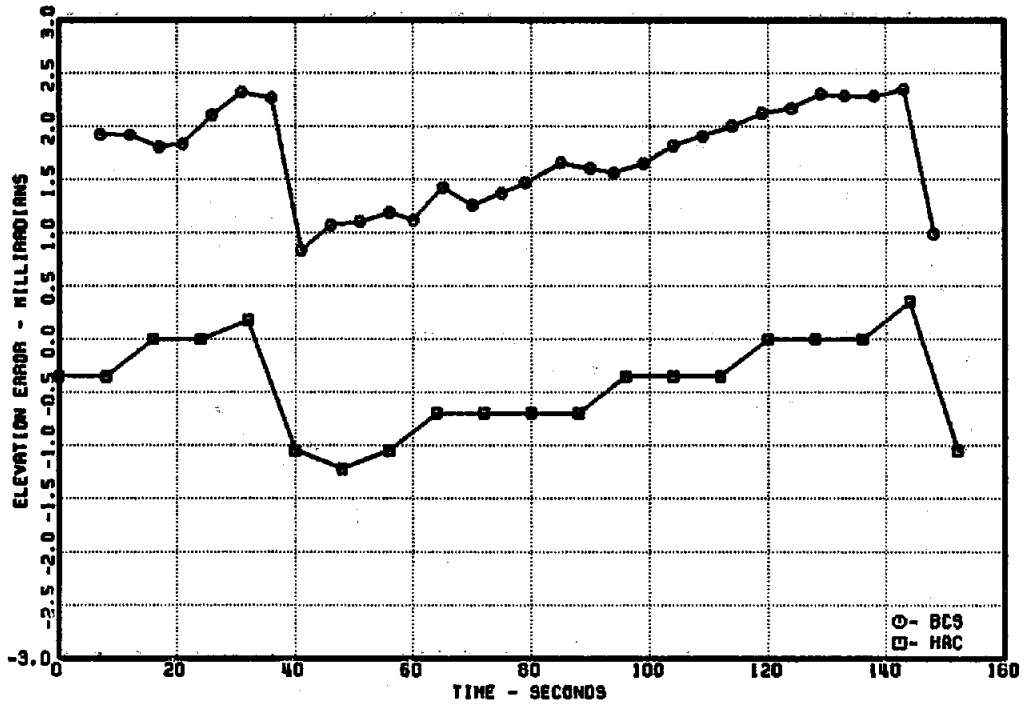

Figure A-4.2. MMC 1 Tracking Error

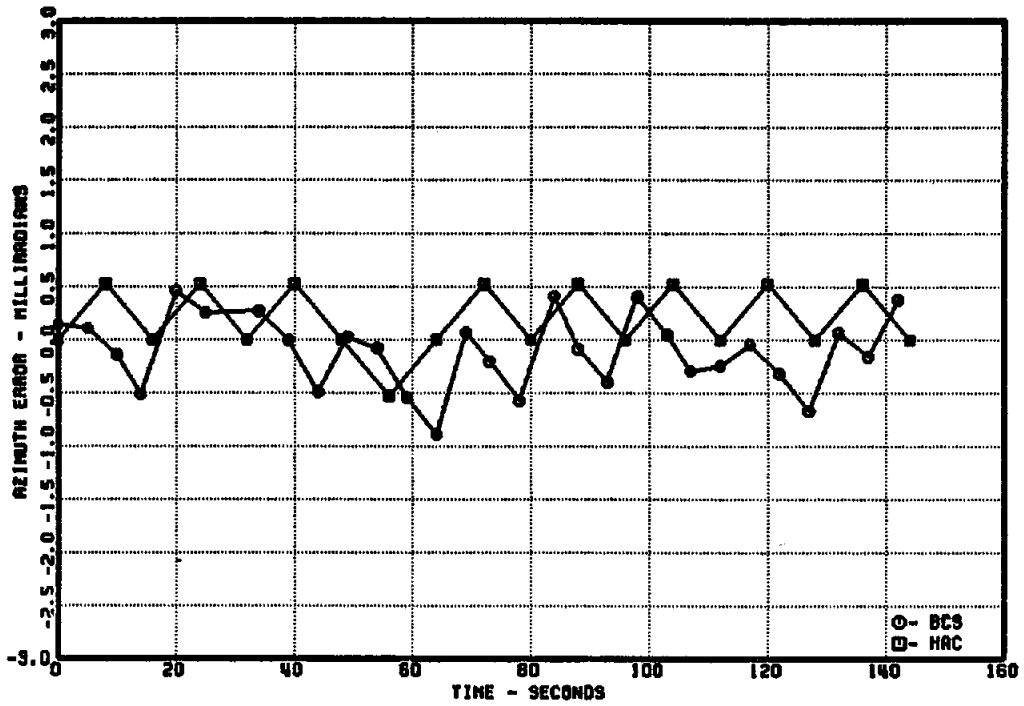

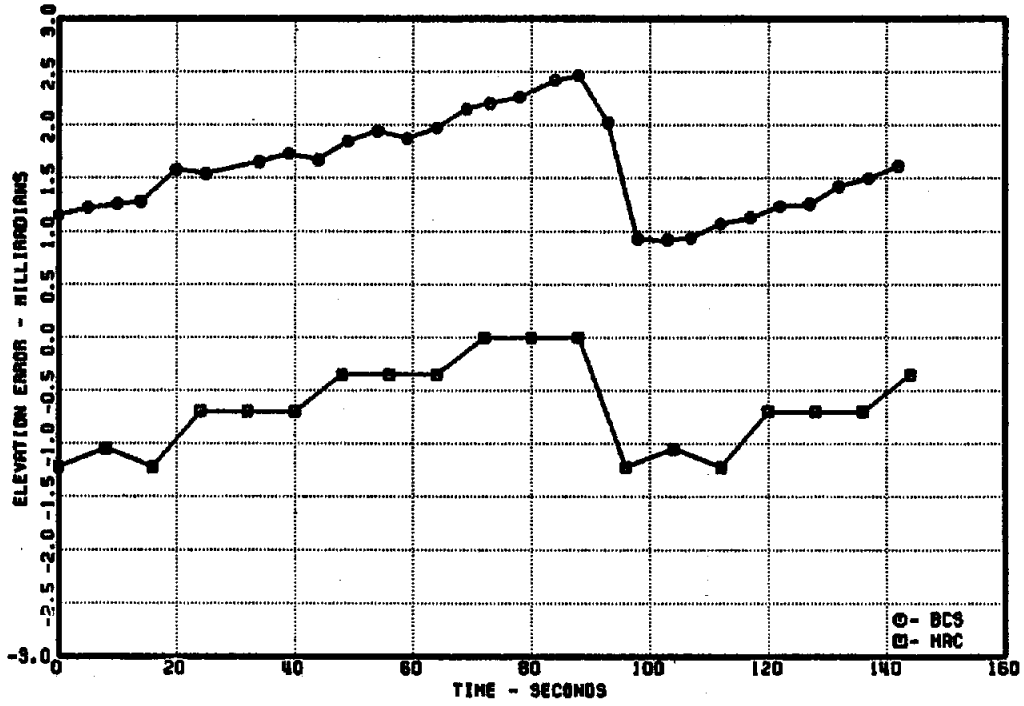

Figure A-4.3. MMC 2 Tracking Error

TABLE A-4.II

STANDARD MODES, AVERAGE TIMES

Operation	MMC	MDAC
	474 sec 7.9 min	786 sec 13.1 min
Unstow	13 sec	27 sec
Standby to track	16 sec	41 sec
Stow	386 sec 6.4 min	711 sec 11.9 min

MDAC--The heliostats responded correctly to the commands issued to the HAC. Table A-4.II summarizes the times required to complete the various commands. The dual HFC test was conducted two weeks after the single HFC test because of an HC failure.

The simultaneous BCS and HAC tracking error test was not conducted because there was insufficient sunlight during this part of the testing. Figures A-4.4 and A-4.5 show the HAC tracking error recorded.

Special Modes

This sequence of tests demonstrated the heliostats' ability to move to various positions and to determine the azimuth and elevation slew rates. Table A-4.III summarizes the tests.

MMC--The sequence of tests was completed satisfactorily. During the transition of Test 23b the HFC lost communication with both HCs. One heliostat stopped and the other continued to the azimuth limit. The heliostats had already reached the commanded elevation position. The failure was believed to be caused by the stack overflow problem in the HC.

The heliostat slew rates are shown in Table A-4.IV. Note, the elevation rate of Heliostat 1 is higher because the motor used was actually an azimuth motor that had a different gear ratio.

MDAC--The heliostats did not respond to all the commands properly; Table A-4.V summarizes the results. When commanded from 0 to 90 degrees in elevation (Test 4) each heliostat failed to reach the commanded azimuth position. This was caused by the tilt and nonorthogonality correction in the HFC. The HFC did a tilt correction on the position and then tried to command the

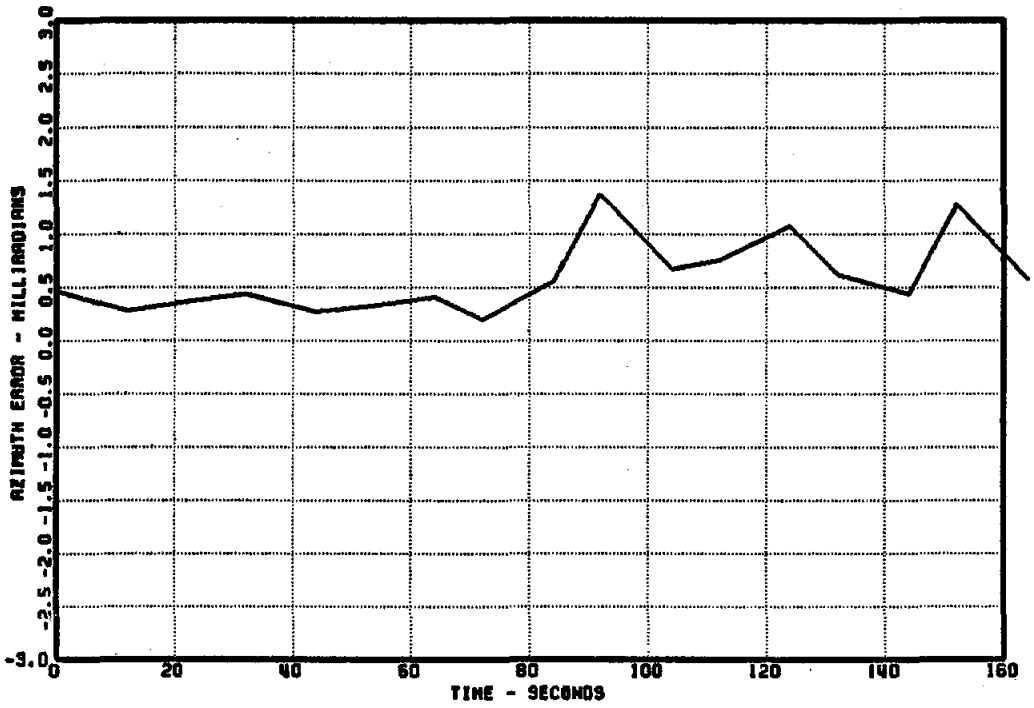

Figure A-4.4. MDAC 1 Tracking Error

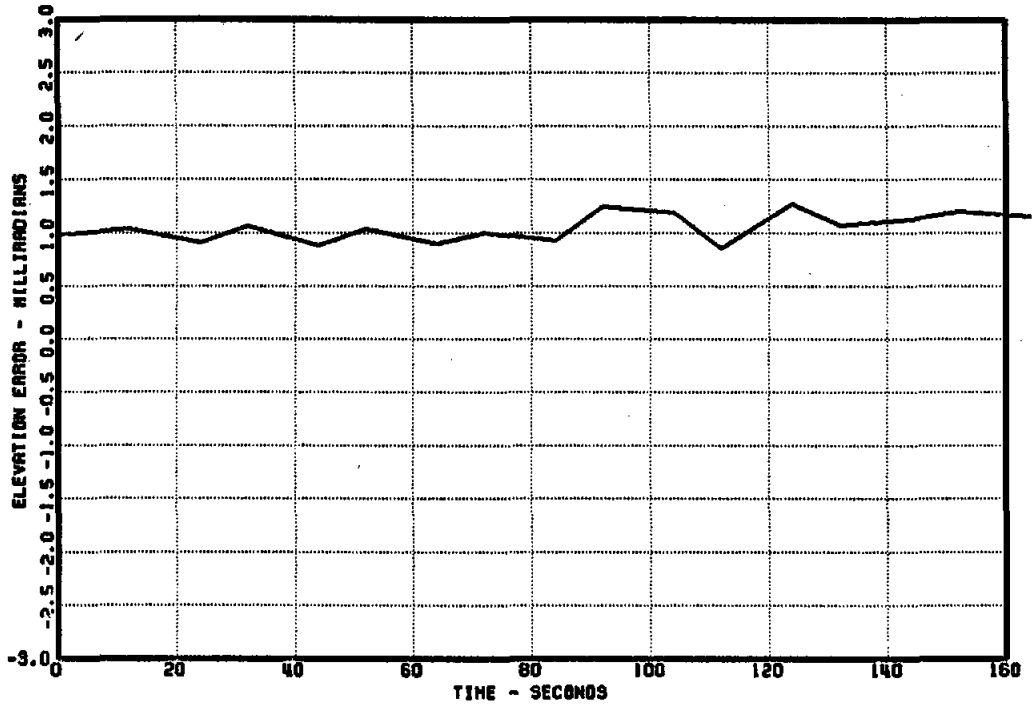

Figure A-4.5. MDAC 2 Tracking Error

TABLE A-4.III

SPECIAL MODES

Test	Heliostat 1 AZ	Heliostat 1 EL	Heliostat 2 AZ	Heliostat 2 EL	Data	Remarks
1	Track standby		Track target		-	Omitted
2	- 90°	0°	Track		-	Initial conditions
3	-180	0	Track		Heliostat position	Azimuth slew rate
4	-180	0	Track		-	-
5	-180	90	Track		Heliostat	Elevation slew rate
6	0	0	Track		-	Initial conditions
7	- 90	90	Track		Heliostat position	Combined azimuth and elevation slew rate

References

	Martin Marietta	McDonnell Douglas
Elevation		
0° Positive rotation	Mirror vertical Up	Mirror vertical Up
Azimuth		
0° Positive rotation	Mirror facing east CCW	Mirror facing south CCW

TABLE A-4.IV

MMC HELIOSTAT SLEW RATES

Heliostat	Heliostat Rate (mR/sec) Azimuth	Elevation	Conditions
1	6.42	7.80	AZ motor only or EL motor only
1	6.37	7.60	Both AZ and EL motors running at the same time
2	6.58	7.57	AZ motor only or EL motor only
2	6.46	7.30	Both AZ and EL motors running at the same time

TABLE A-4.V

MDAC HELIOSTAT SLEW RATES

Heliostat	Heliostat Rate (mR/sec) Azimuth	Elevation	Conditions
1	4.14	x.xx	AZ motor only or EL motor only
1	4.14	4.03	Both AZ and EL motors running at the same time
2	4.15	4.12	AZ motor only or EL motor only
2	4.08	4.09	Both AZ and EL motors running at the same time

heliostat to the correct elevation. Since the elevation was 90 degrees, the heliostat was commanded to move in azimuth in order to minimize the elevation error. The resulting azimuth angle was 37 degrees off. The test was repeated with a command of 89 degrees. The heliostat moved to the correct azimuth and elevation position. This confirmed the cause of the problem. When this test was run a second time one month later, the problem had been fixed. The fixed-position commands (non-tracking) are not corrected for tilt and the correct position is achieved.

When the heliostat was commanded from -180 degrees azimuth to 0 degrees, it moved in the wrong direction. The heliostat would have hit a limit switch. This problem was not fixed by the end of the testing.

When the heliostat moved in the wrong azimuth direction, another problem was encountered. At about 264 degrees the heliostat stopped moving clockwise and reversed direction moving counterclockwise. The heliostat was cycling around this position. This was diagnosed as a motor-turn count overflow problem. This problem was not fixed by the end of the testing.

Communication Loss

This test was to determine the heliostat response to loss of communication between the HAC and HFC and between the HFC and HC.

MMC--Upon loss of HAC/HFC communication, the heliostat or heliostats wait about 10 seconds then move from track to standby, down the wire, and then to the stow position. A suitable alarm was displayed at the HAC.

Upon loss of HFC/HC communication, the heliostat stops at the last commanded position.

MDAC--Upon loss of HAC/HFC communication, the heliostat or heliostats continue to track for about 15 minutes then move from track to standby, down the wire, and then to the stow position. A suitable alarm was displayed at the HAC.

Upon loss of HFC/HC communication, the heliostat continues to move at the last commanded rate until the heliostat hits a limit switch. This can take considerable time if the rate is low.

Singularity Test

The singularity point occurs when the elevation angle of the sun is equal to the elevation angle of the reflected beam from the heliostat and the sun, heliostat, and target are in line. This condition occurs in the south field and some on the east and west sides. At the singularity the heliostat mirrors are horizontal, face up; and the azimuth angle becomes undefined in the sense that the reflected beam location is independent of the azimuth angle of the heliostat for that one condition. The approach to and departure from the singularity point is influenced by the control design and the available angle of travel of the heliostat. As the heliostat approaches the singularity point (90 degrees in elevation) the elevation angle approaches 90 degrees. Beyond the point the elevation angle must go beyond 90 degrees to continue tracking. Both MMC and MDAC heliostats cannot travel much past horizontal (90 degrees) in elevation. This prevents the heliostat from tracking in the "over the shoulder" configuration. In order to resolve this singularity condition the heliostat is required to rotate about 180 degrees in azimuth so that the elevation drive of the heliostat can then track back down the other side of the singularity point.

The heliostat is unable to accurately track during the 180-degree rotation because of the slew rate limitation of the heliostat. The specification requirement is 15 minutes to resolve the condition and return to accurate track.

This maneuver is complicated by the changing sun/heliostat/receiver geometry and the slew rate capability of the heliostat. The heliostat control system must determine the direction of rotation to ensure that there is sufficient azimuth travel left to resolve the singularity and also be able to complete the day's tracking. If the heliostat turns in the wrong azimuth direction, a limit switch will be reached (gimbal lock).

A singularity condition could occur during the wire walk. The control system should be able to provide wire walk capability during these conditions without losing control of the heliostats. The singularity during wire walk was not evaluated.

The singularity tests performed at the CRTF were done by having both heliostats in a tracking mode using a contrived aimpoint north of the heliostats. At a particular time of day one of the heliostats would experience the singularity condition. By recording encoder position data as discussed earlier, it was possible to determine if the test heliostat resolved the condition correctly within the required 15 minutes. The singularity tests were run for both the single and dual HFC control configuration.

MMC--The single HFC test was conducted 7/9/80 (MMC Test 43). The singularity passed through Heliostat 2. Figures A-4.6 through A-4.9 show the azimuth and elevation positions for each heliostat. Figures A-4.10 through A-4.13 show the azimuth and elevation rates for each heliostat. Heliostat 1 continued to track while Heliostat 2 rotated 177.6 degrees in 8.6 minutes to resume tracking.

The dual HFC test was conducted on 7/9/80 (MMC Test 44). The singularity passed through Heliostat 2. Figures A-4.14 through A-4.17 show the azimuth and elevation positions for each heliostat. Figures A-4.18 through A-4.21 show the azimuth and elevation rates for each heliostat. Heliostat 1 continued to track while Heliostat 2 rotated 176.8 degrees in 8.0 minutes to resume tracking.

On 9/6/80 a second dual HFC singularity test was conducted (MMC Test 83). The second single HFC test was deleted from the test plan. The singularity passed through Heliostat 2. Figures A-4.22 and A-4.23 show the azimuth and elevation positions for Heliostat 2. Figures A-4.24 and A-4.25 show the azimuth and elevation rates for Heliostat 2. Heliostat 1 continued to track while Heliostat 2 rotated 177.2 degrees in 8.2 minutes to resume tracking.

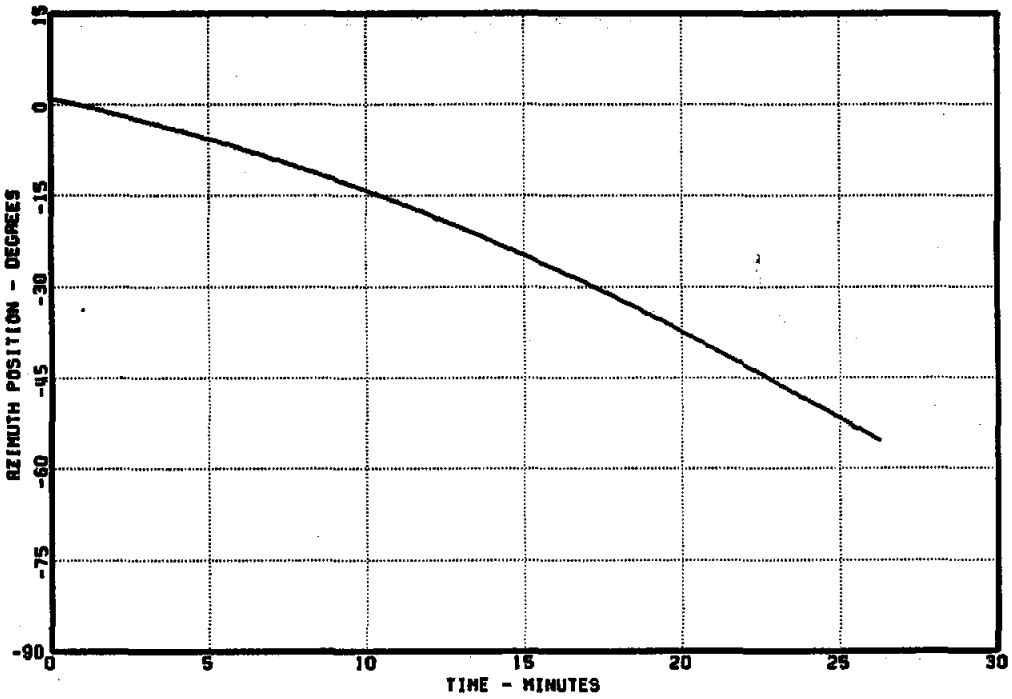

Figure A-4.6. MMC 1 Singularity T43

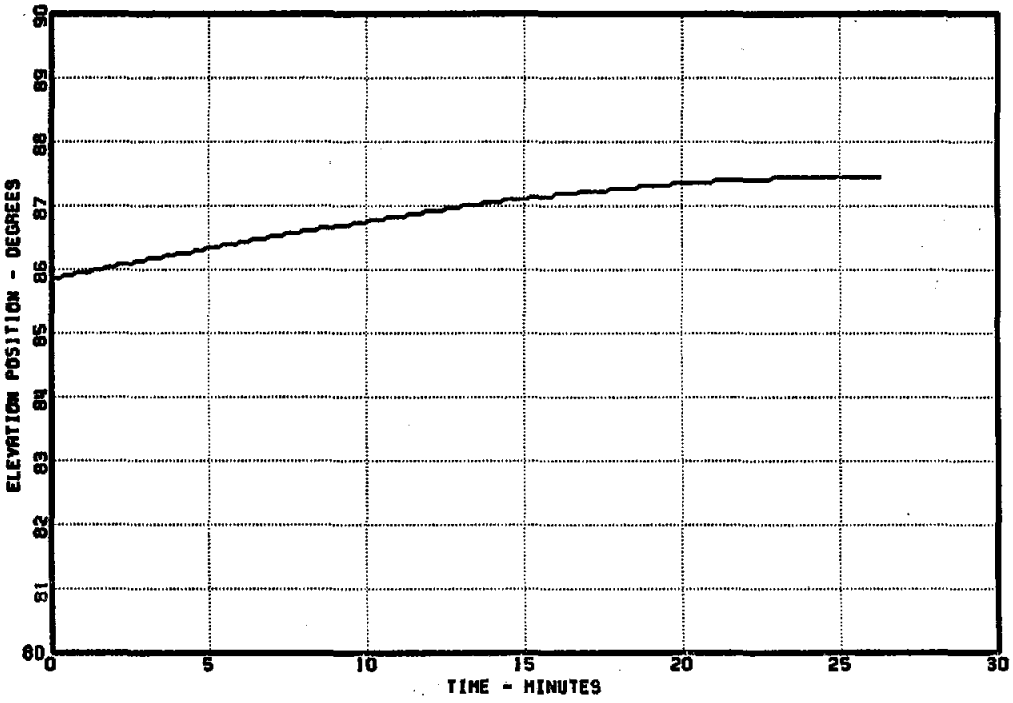

Figure A-4.7. MMC 1 Singularity T43

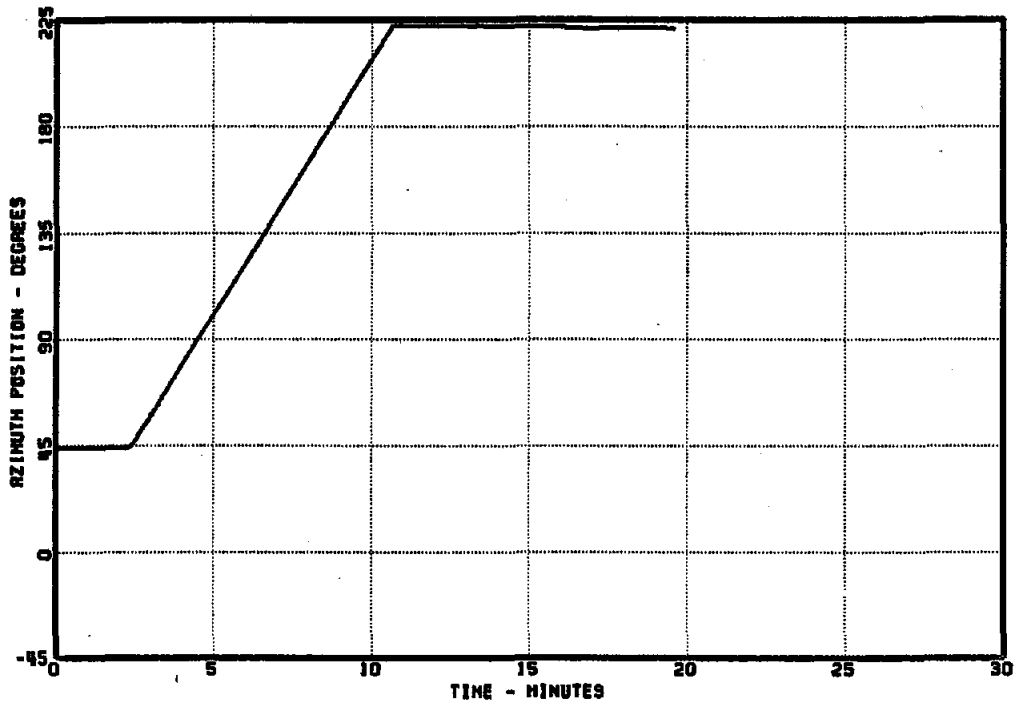

Figure A-4.8. MMC 2 Singularity T43

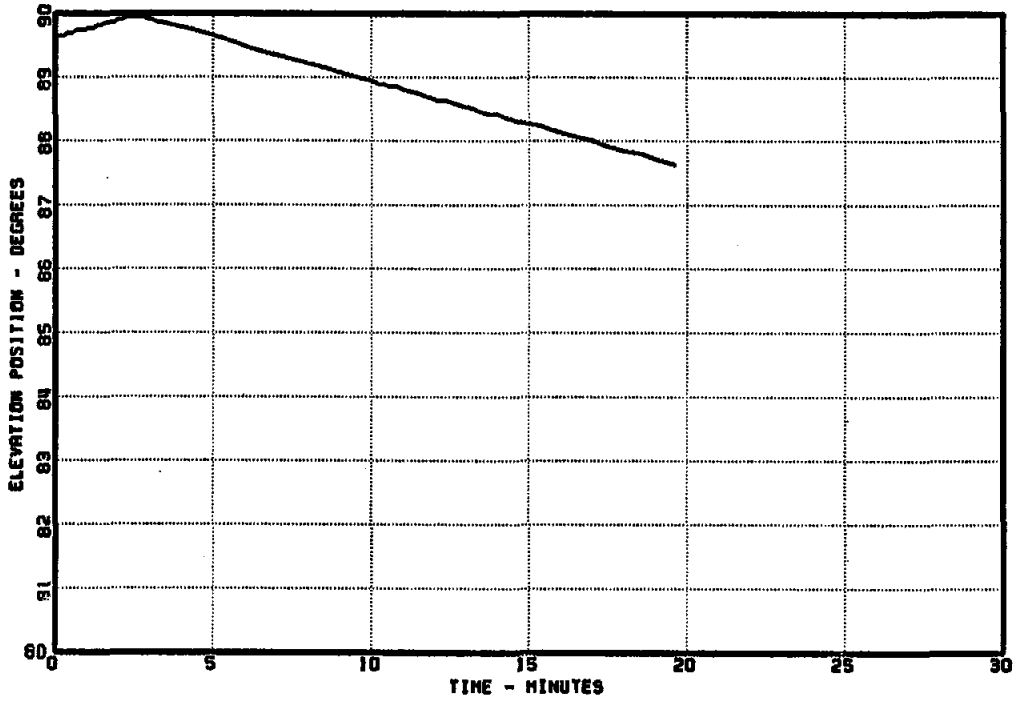

Figure A-4.9. MMC 2 Singularity T43

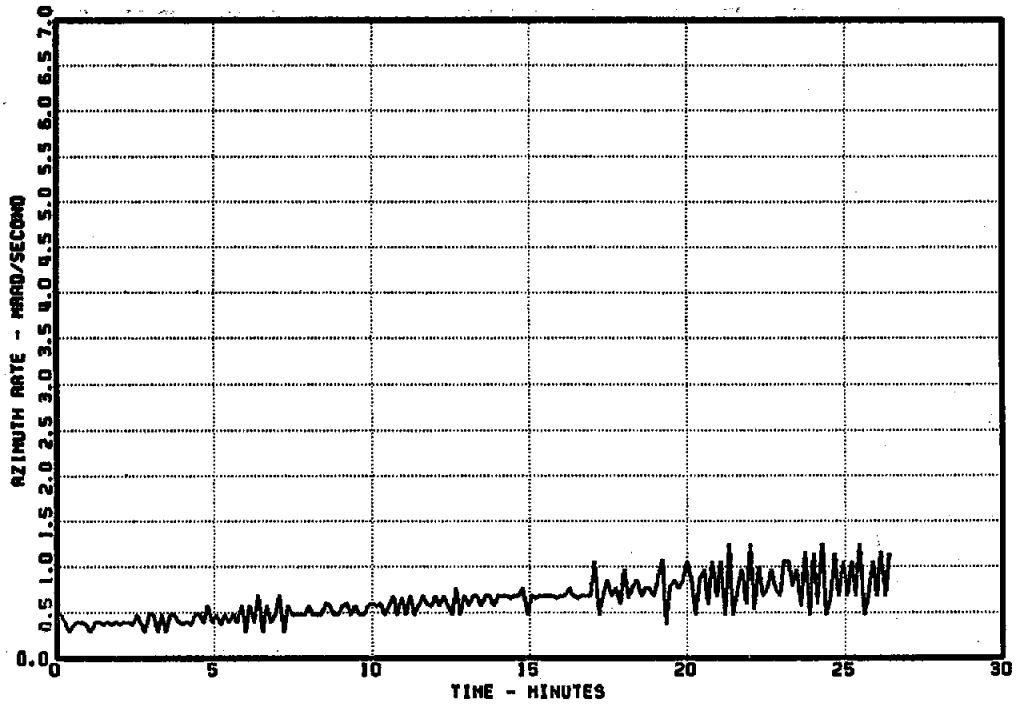

Figure A-4.10. MMC 1 Singularity T43

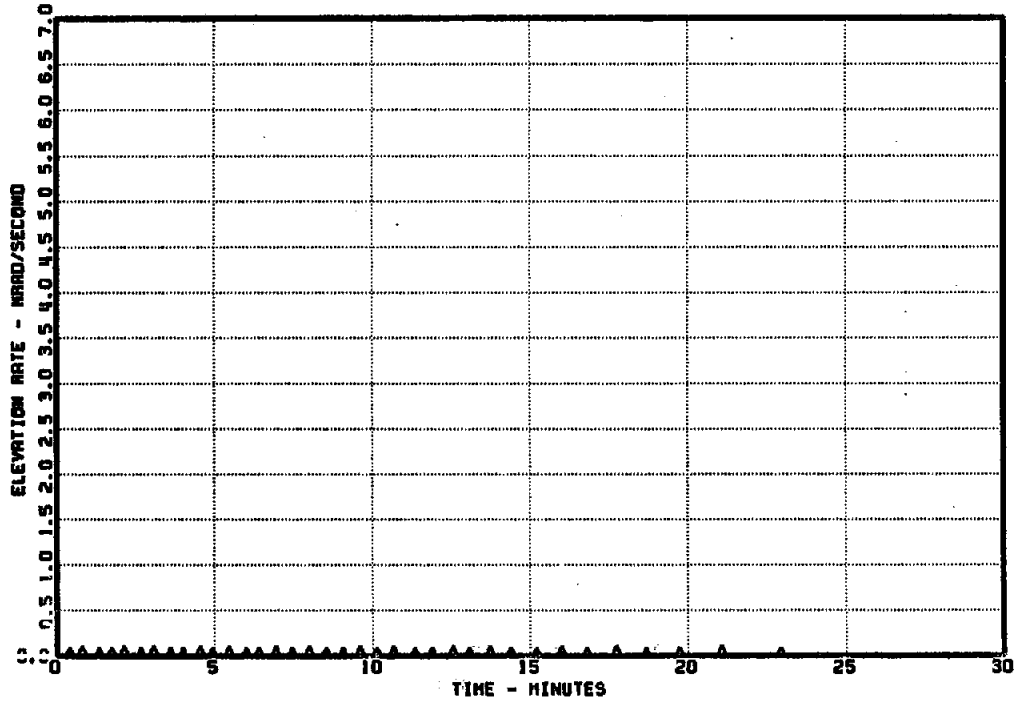

Figure A-4.11. MMC 1 Singularity T43

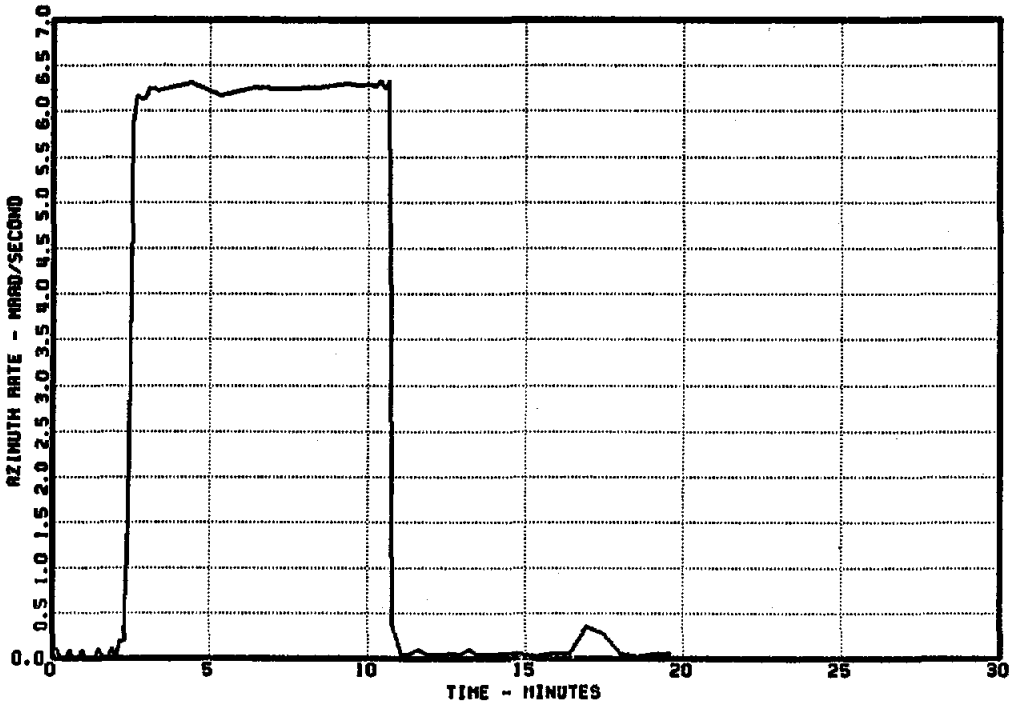

Figure A-4.12. MMC 2 Singularity Rate T43

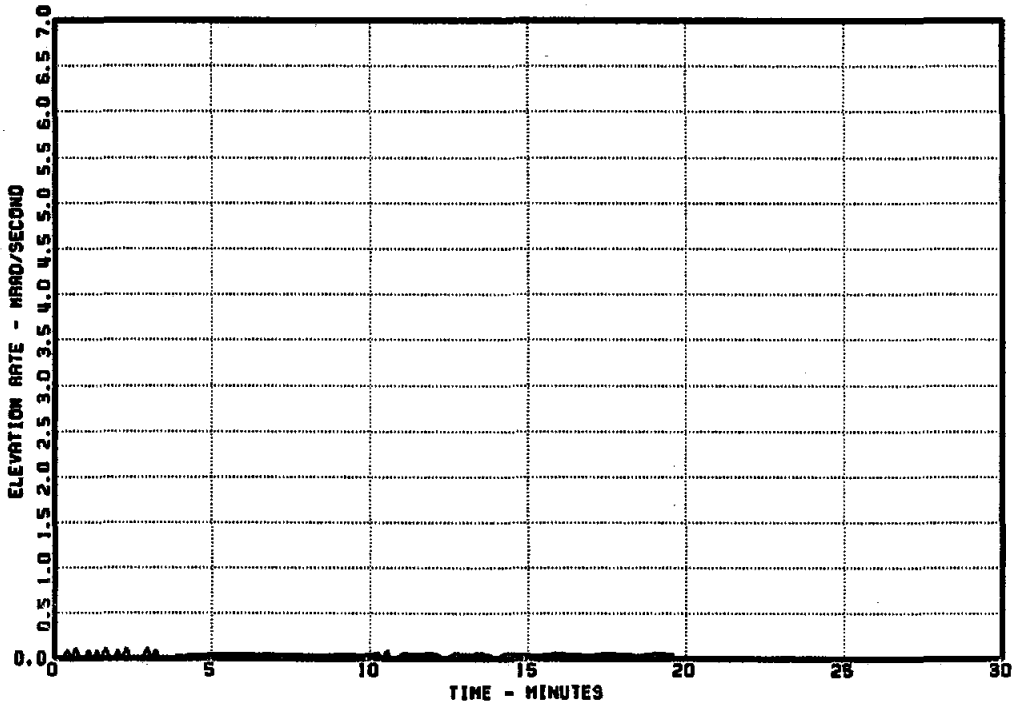

Figure A-4.13. MMC 2 Singularity Rate T43

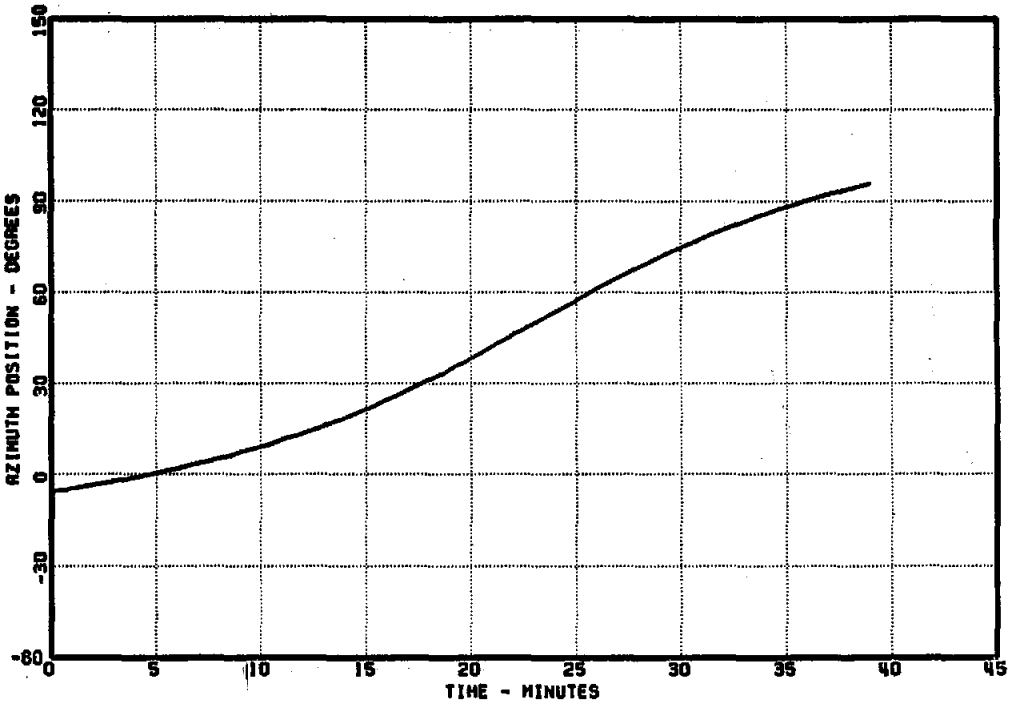

Figure A-4.14. MMC 1 Singularity Rate T44

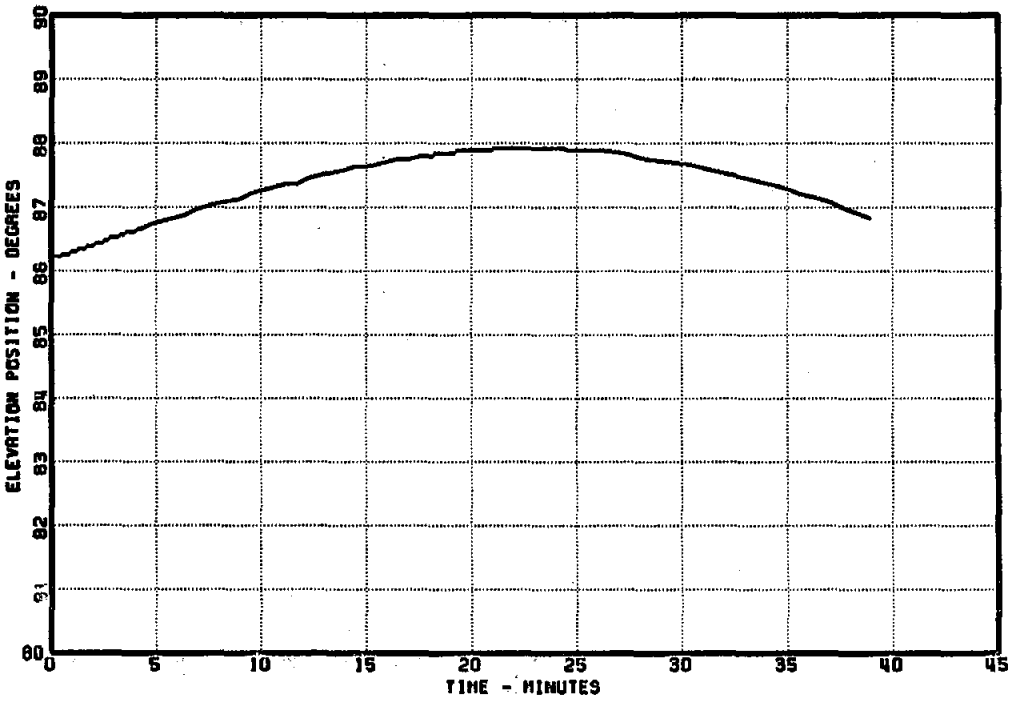

Figure A-4.15. MMC 1 Singularity Rate T44

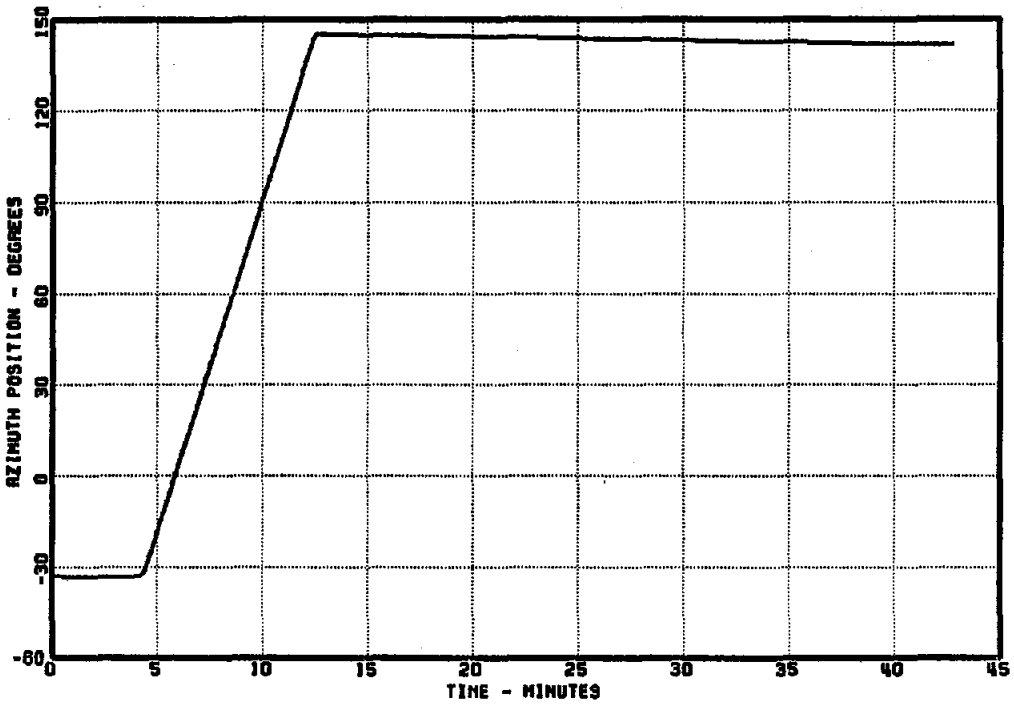

Figure A-4.16. MMC 2 Singularity Rate T44

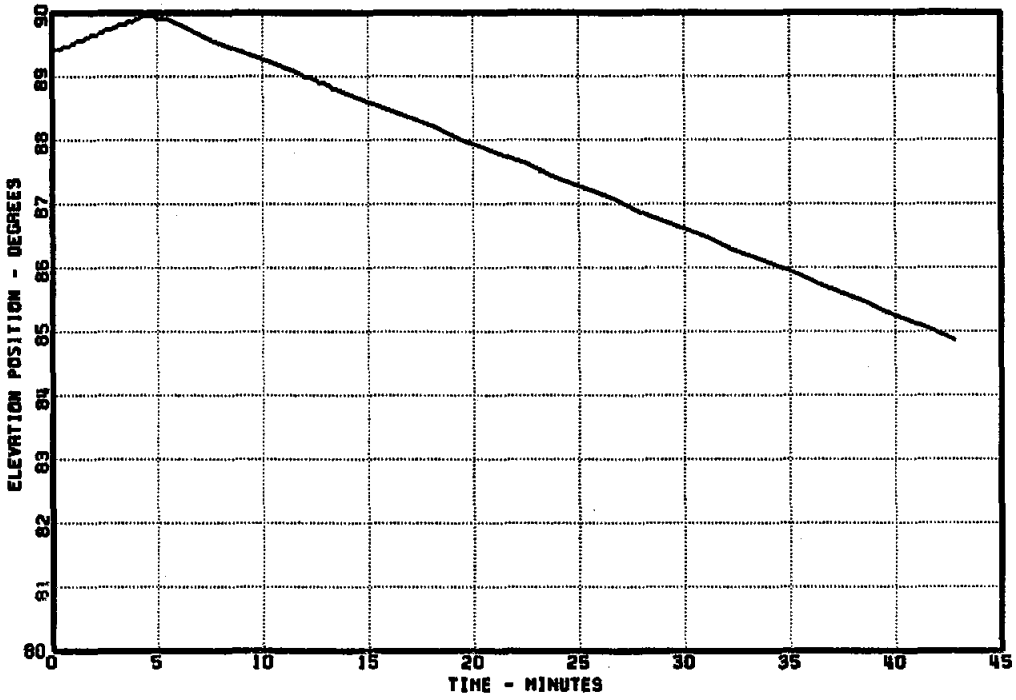

Figure A-4.17. MMC 2 Singularity Rate T44

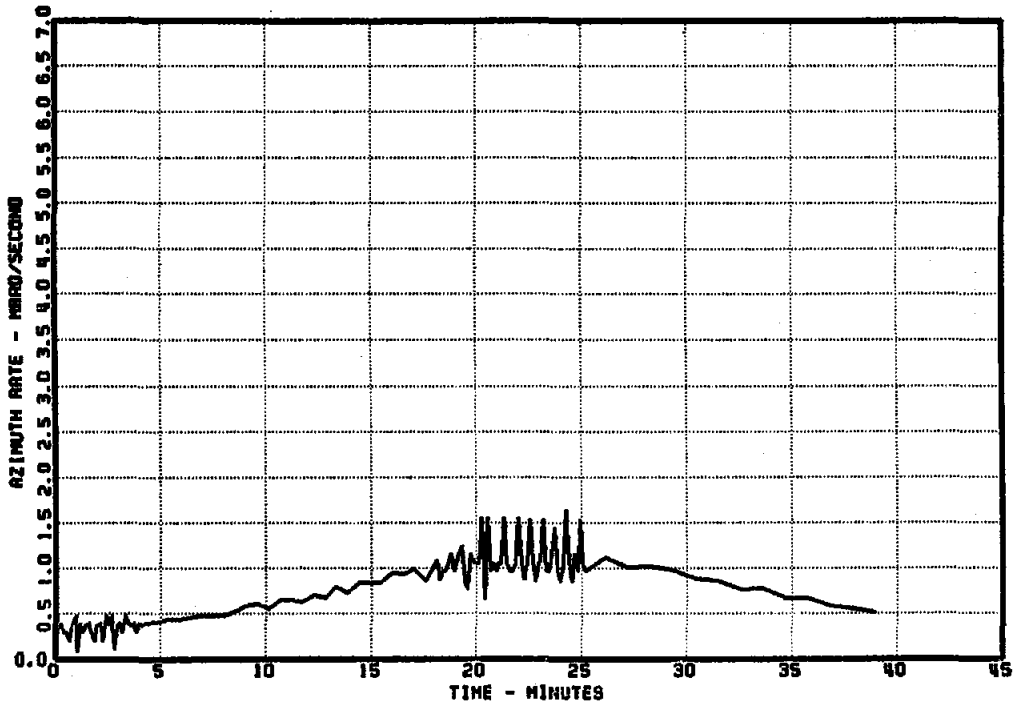

Figure A-4.18. MMC 1 Singularity Rate T44

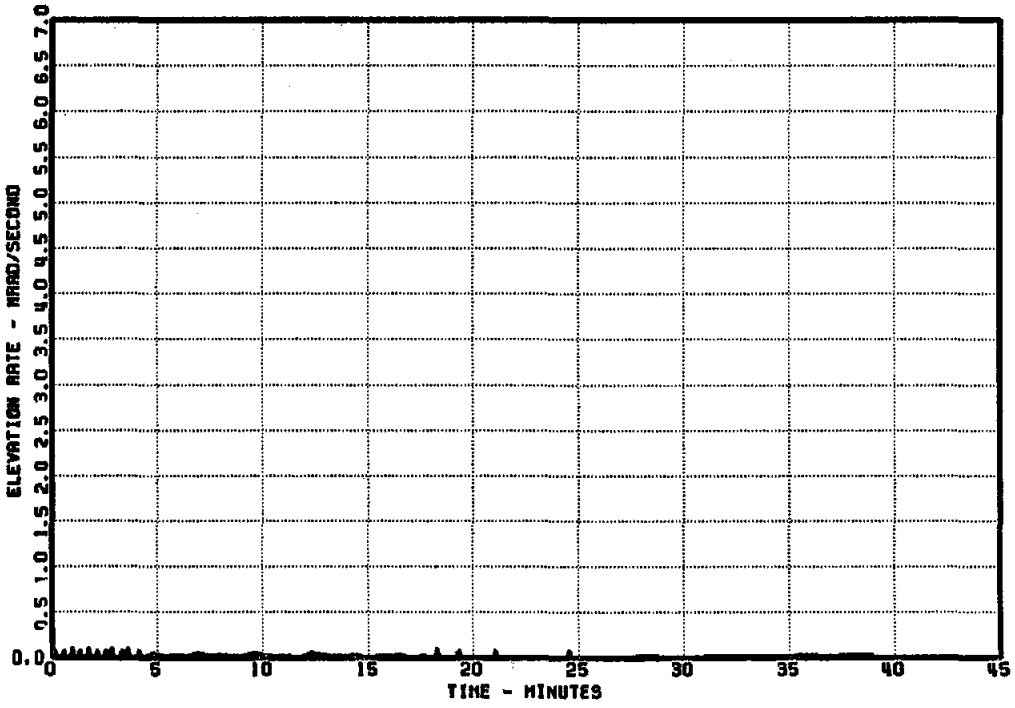

Figure A-4.19. MMC 1 Singularity T44

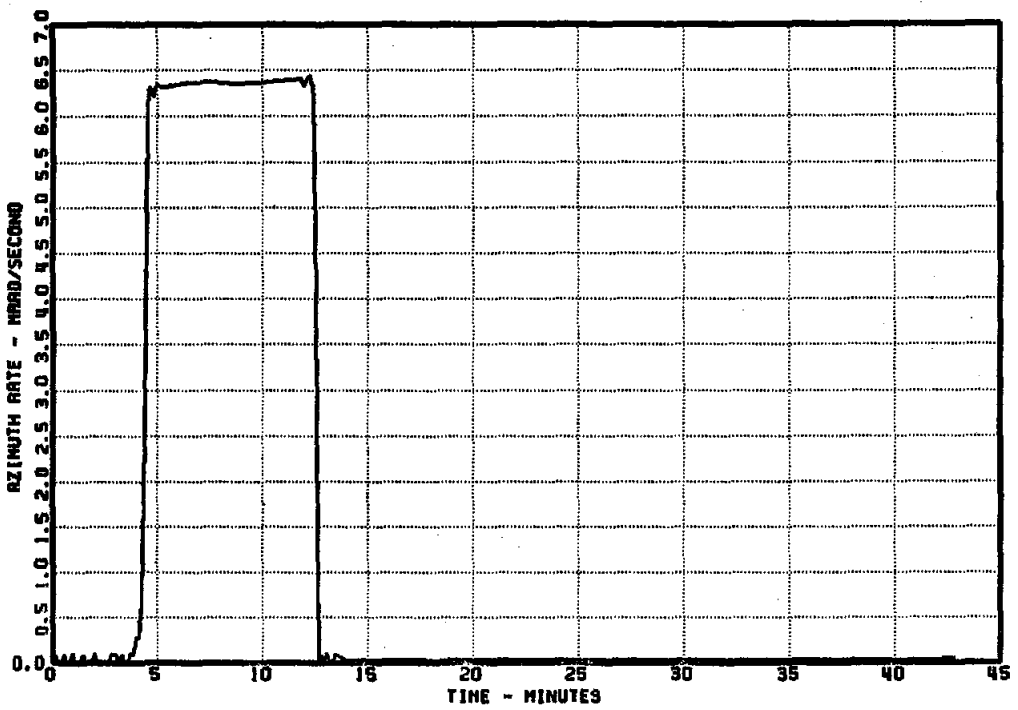

Figure A-4.20. MMC 2 Singularity Rate T44

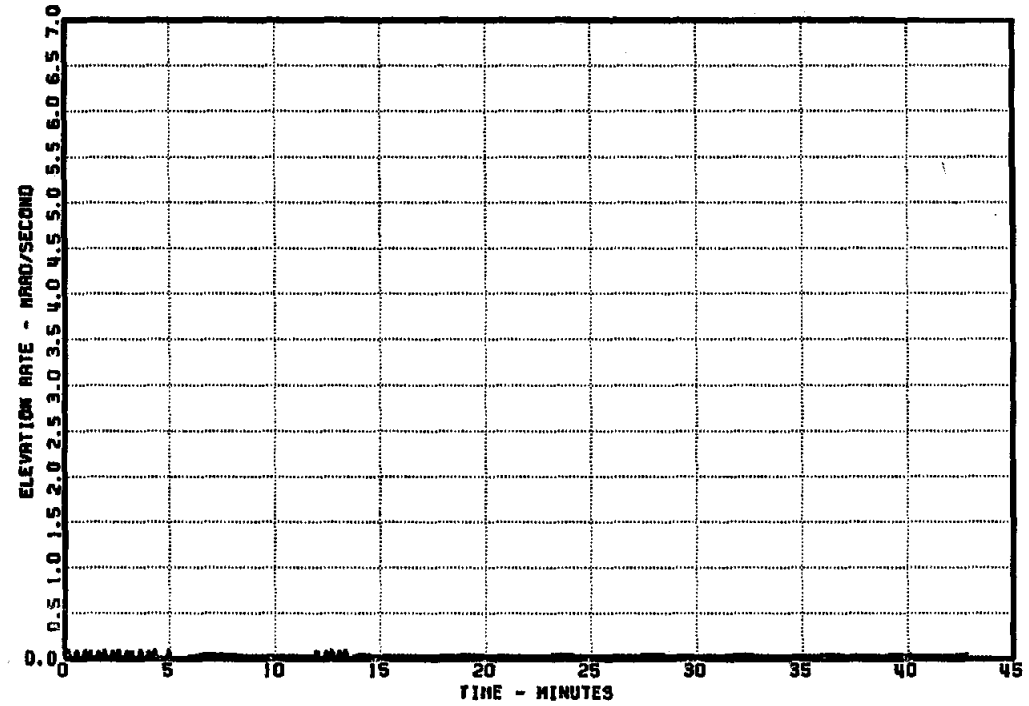

Figure A-4.21. MMC 1 Singularity T44

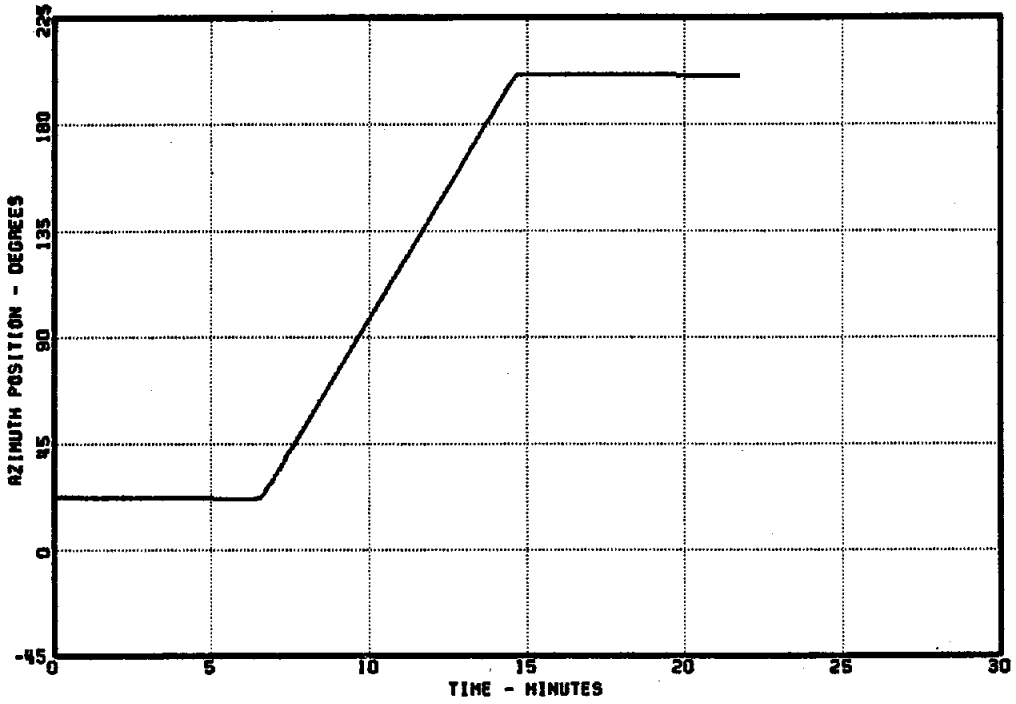

Figure A-4.22. MMC 2 Singularity T83

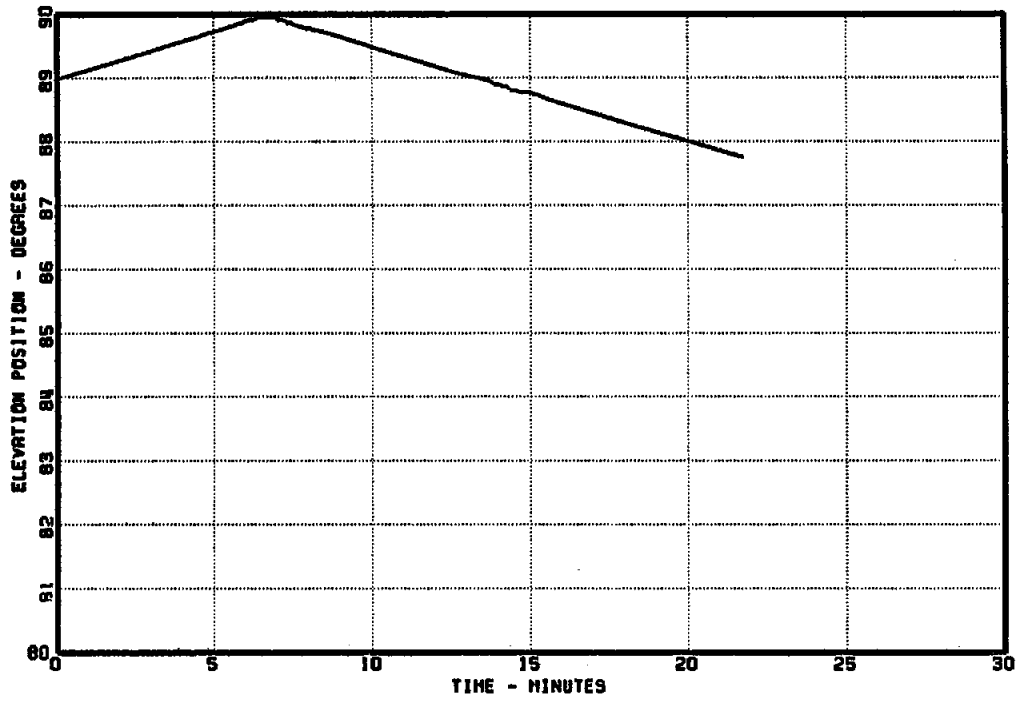

Figure A-4.23. MMC 2 Singularity T83

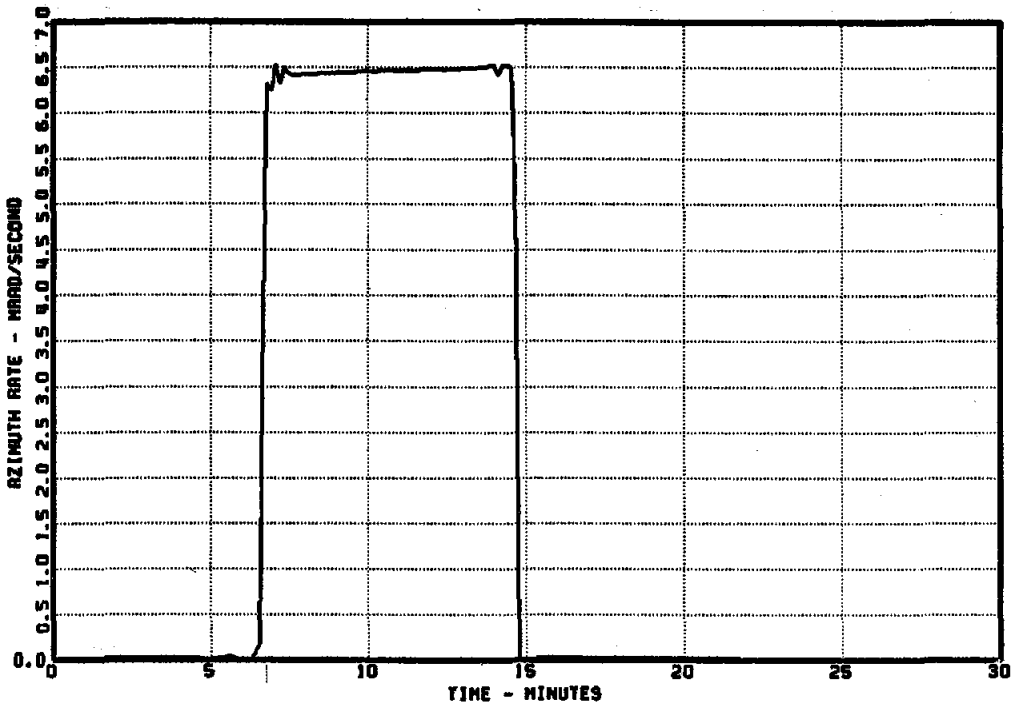

Figure A-4.24. MMC 2 Singularity T83

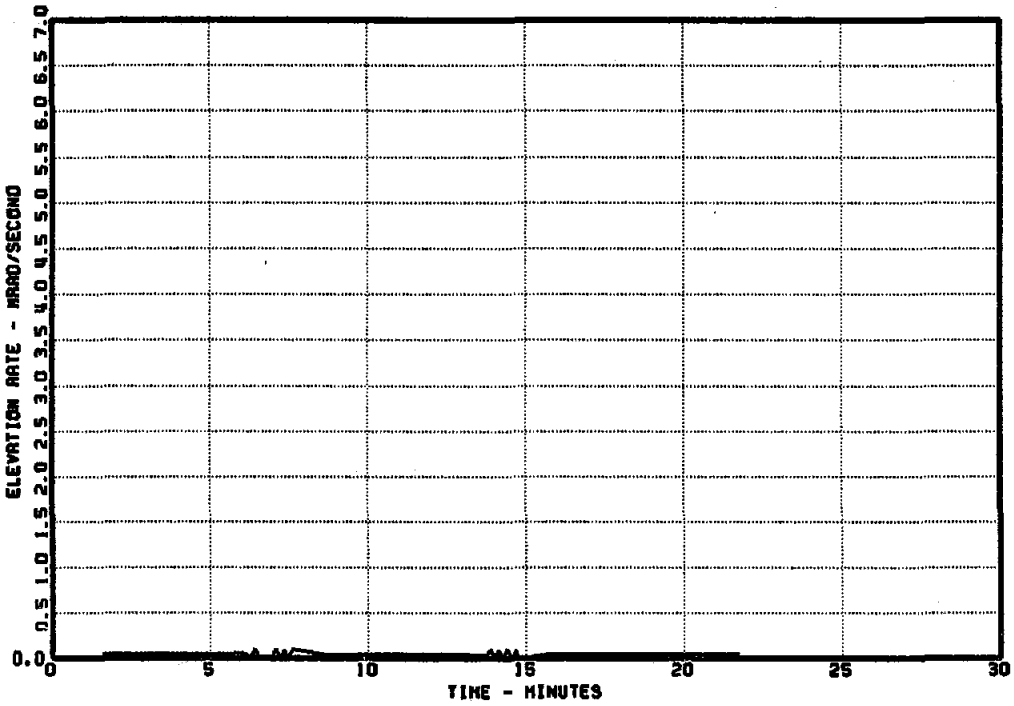

Figure A-4.25. MMC 2 Singularity T83

MDAC--Control system hardware and software problems prevented completion of the singularity test in the first round of operational modes tests. A singularity test in the single HFC mode was completed on 8/30/79. The singularity passed through Heliostat 1. Figures A-4.26 through A-4.29 show the azimuth and elevation positions for each heliostat. Figures A-4.30 through A-4.33 show the azimuth and elevation rates for each heliostat. Heliostat 2 continued to track while Heliostat 1 rotated 181.4 degrees in 13.7 minutes to resume tracking.

On 9/14/79 the singularity test with the dual HFC configuration was conducted. The singularity passed through Heliostat 1. The heliostat moved in the wrong direction and would have hit an azimuth limit switch. The singularity point will pass either on one side or the other side of the heliostat. It appears that the heliostat was able to resolve the singularity only on one side. On the other side it moves in the wrong direction and locks up at a limit or at the motor turns count overflow point. This condition had not been resolved by the end of testing.

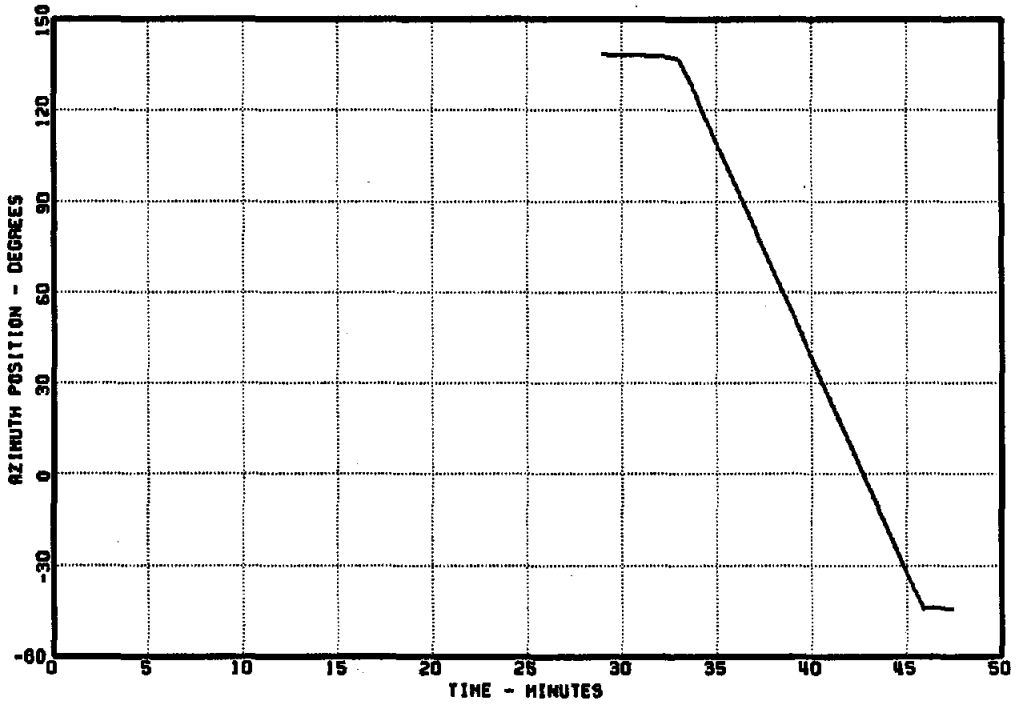

Figure A-4.26. MDAC Heliostat 1 Singularity

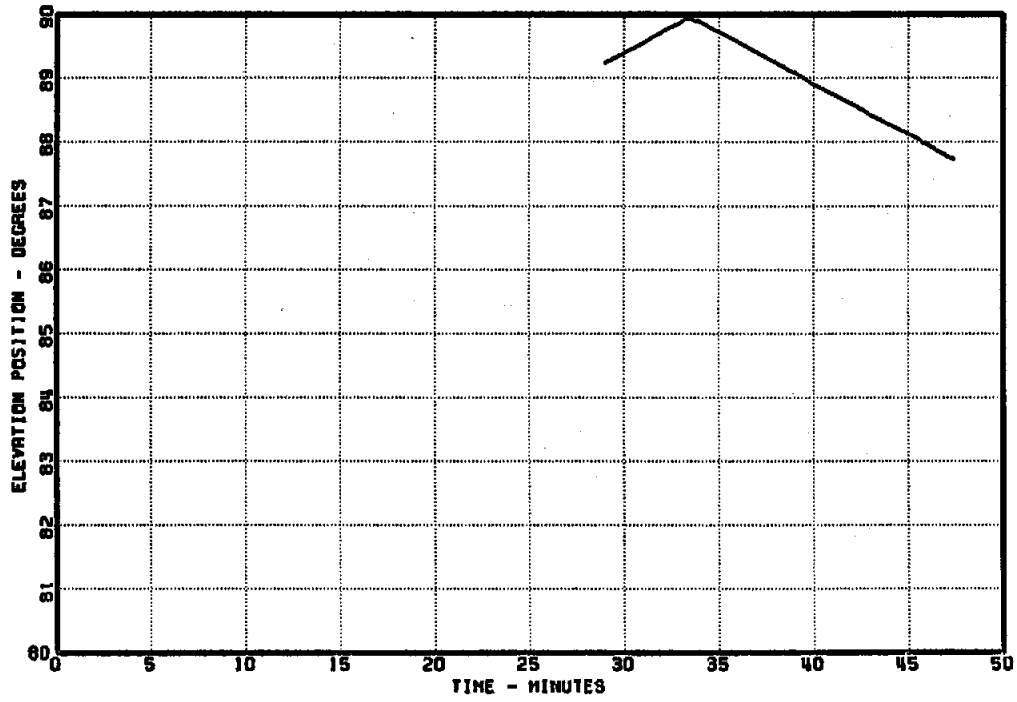

Figure A-4.27. MDAC Heliostat 1 Singularity

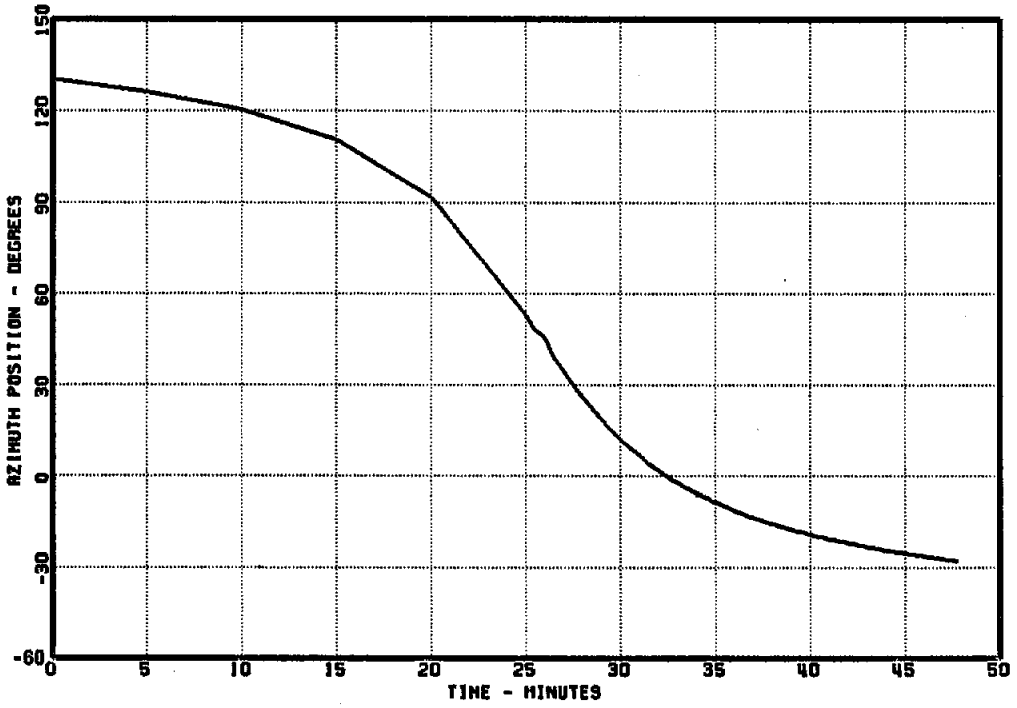

Figure A-4.28. MDAC Heliostat 1 Singularity

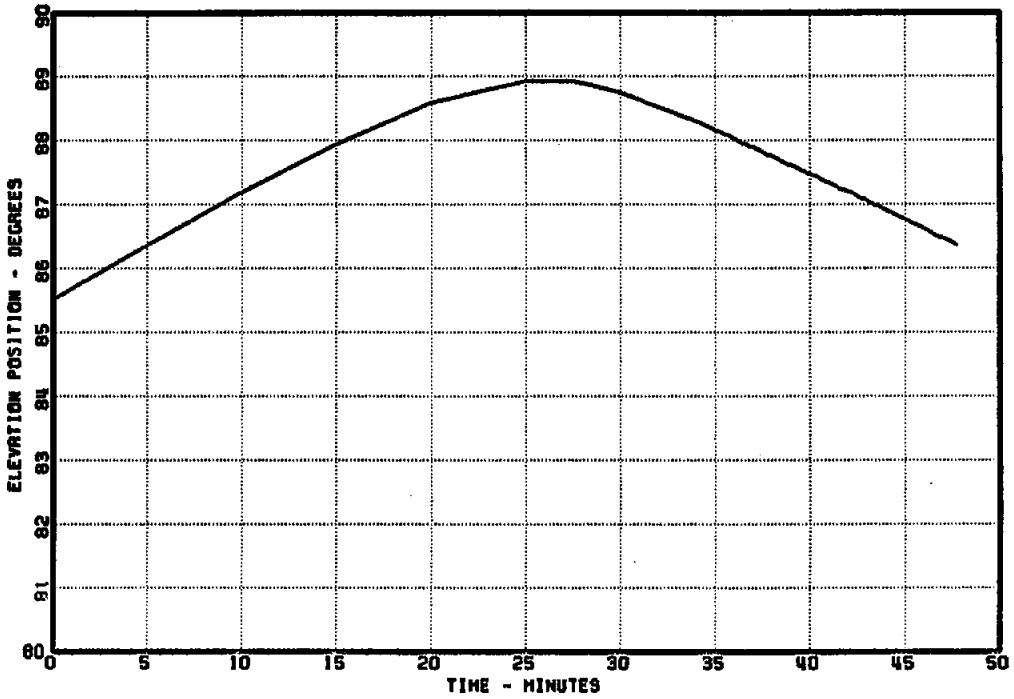

Figure A-4.29. MDAC 2 Singularity

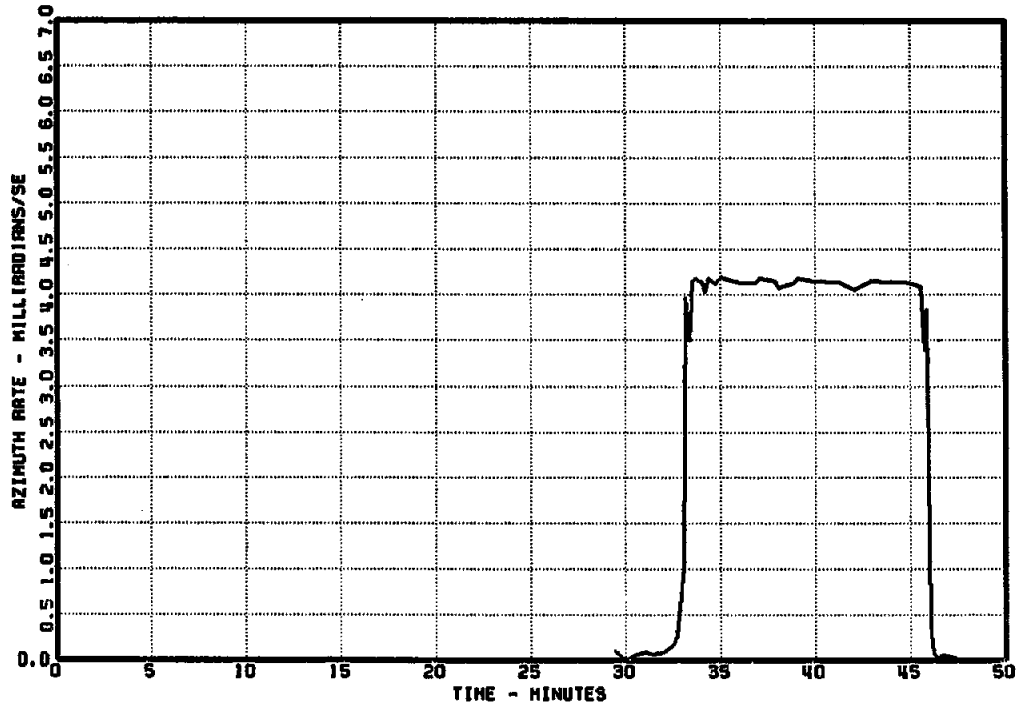

Figure A-4.30. MDAC 1 Singularity Rate

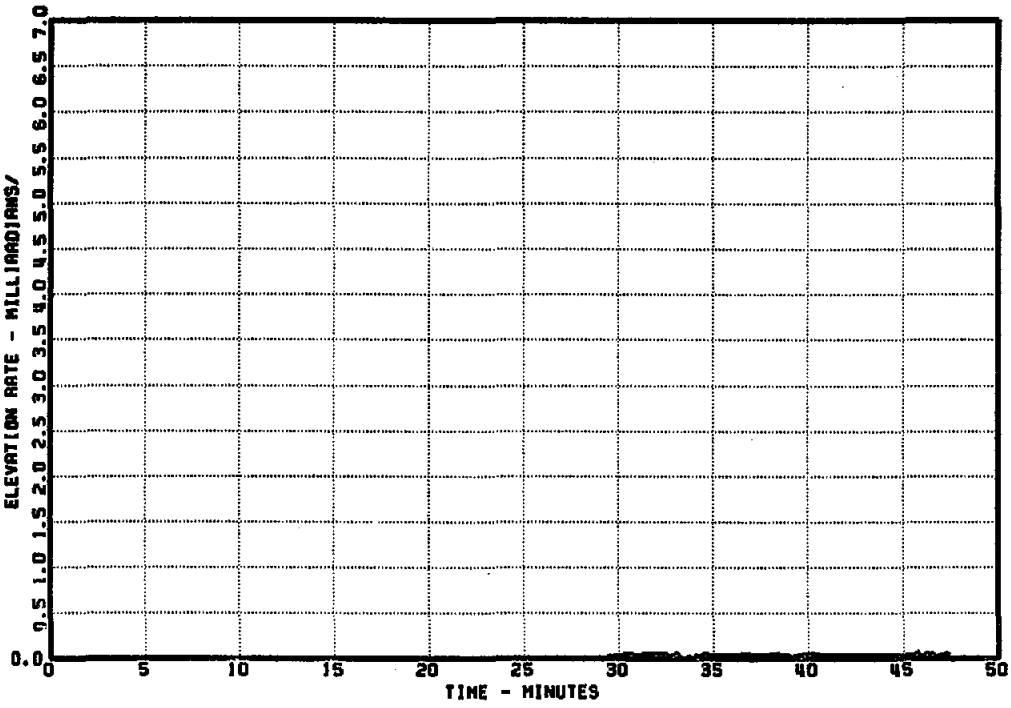

Figure A-4.31. MDAC 1 Singularity Rate

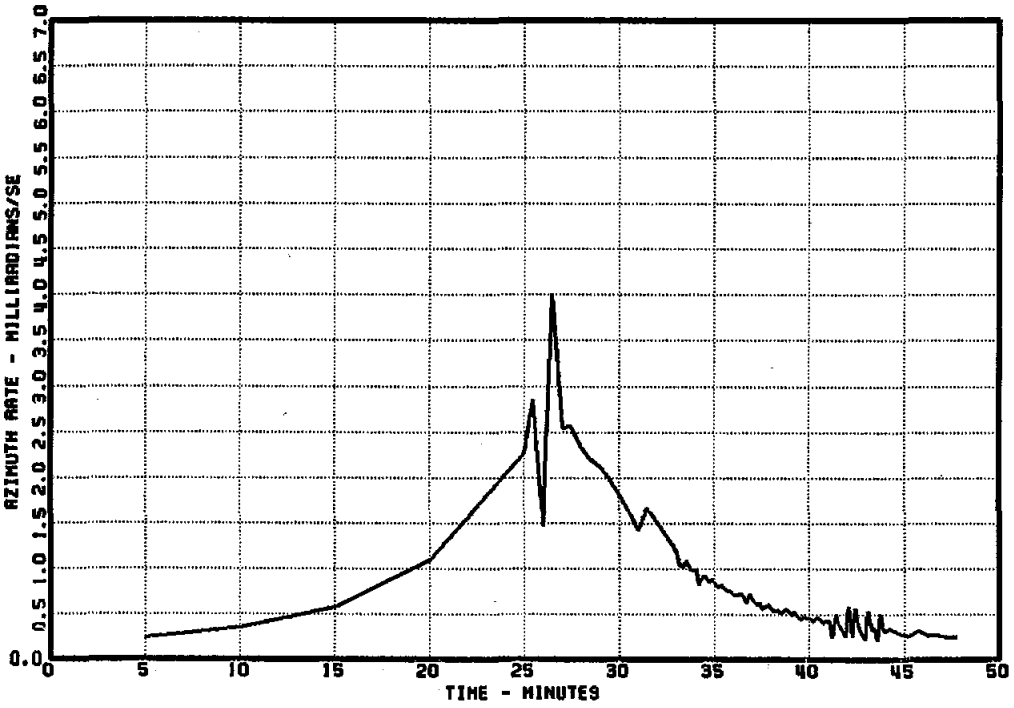

Figure A-4.32. MDAC 2 Singularity Rate

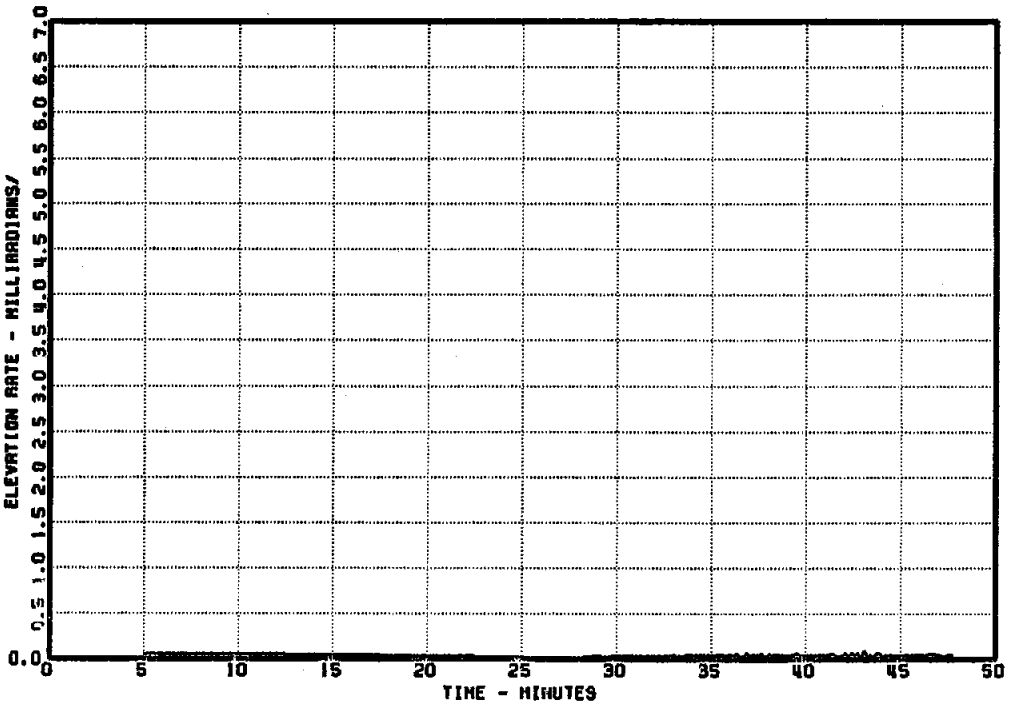

Figure A-4.32. MDAC 2 Singularity Rate

Conclusions

The general level of sophistication and completeness of the MMC control system was good. With the exception of a few occurrences of random failures caused by the stack overflow problem in the HFC, the control system and heliostats performed all the operational modes tests successfully.

The level of completeness of the MDAC control system was generally not as polished as the MMC system. Software debugging and refinement continued through the greater part of the test program at the CRTF. Motor controller failures also caused considerable problems. After software modifications the control system successfully completed the standard modes tests, most of the special modes tests, and the communication loss tests. However, the heliostat was able to resolve the singularity only on one side and there were some position commands that caused the heliostat to operate incorrectly.

Test A-5: Control/Drive Pointing

Objective

The objective of this test was to evaluate the repeatability and stability of the heliostat control system and drive mechanism. The use of the laser system described earlier and shown in Figures A-7 and A-8 made it possible to isolate heliostat gimbal angle pointing from the structural and optical response of the entire heliostat.

Description

The test setup involved mounting a 5-mW Spectra-Physics laser equipped with a focusing telescope as near as possible to the intersection of the test heliostat's azimuth and elevation axes. The laser and mounting arrangement used during evaluation of the MDAC Heliostat 2 is shown in Figure A-5.1. During the test the laser target was located approximately 30 meters south of each heliostat.

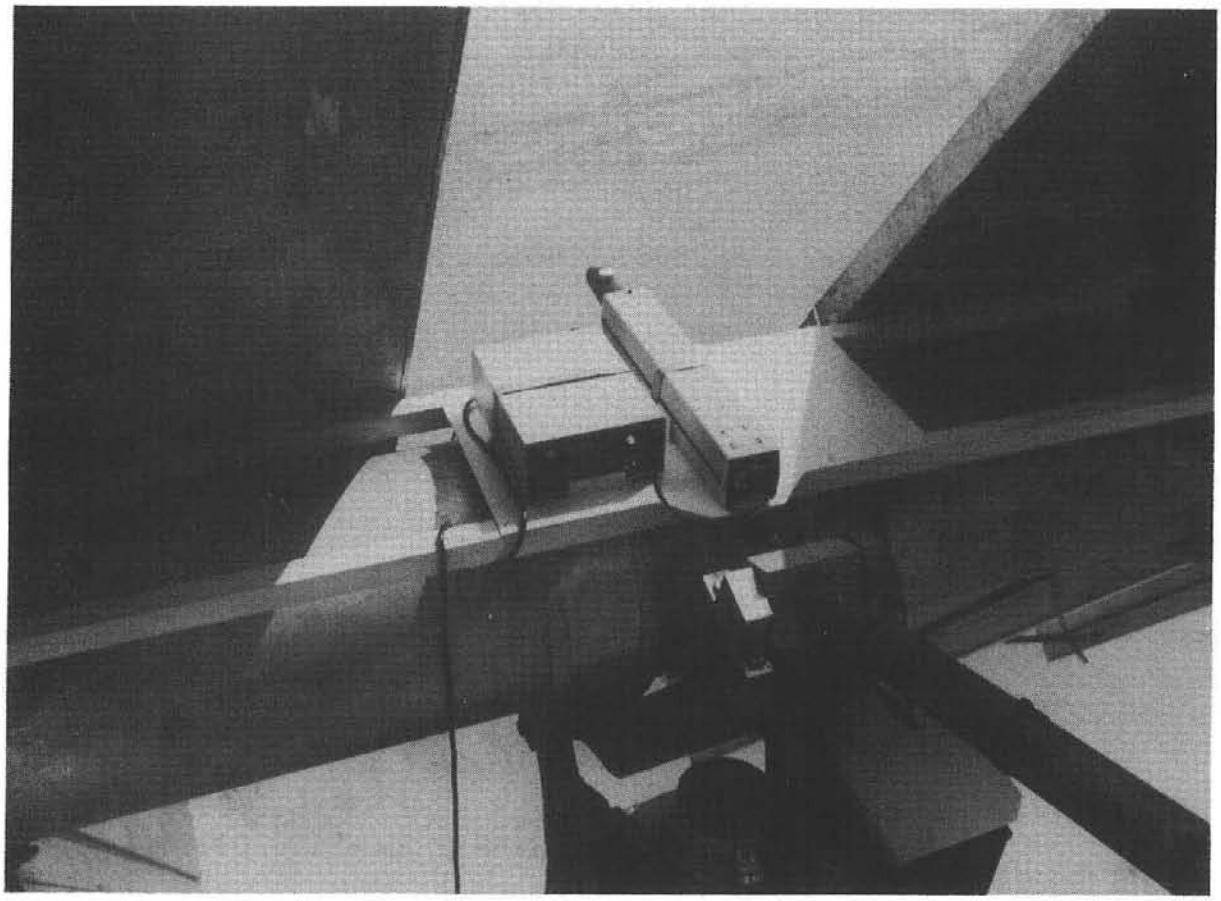

Figure 5.1. Laser Mounted in MDAC Heliostat during Control/Drive Pointing Tests

The repeatability portion of this test involved moving the heliostat through a prescribed series of gimbal angle movements. With the laser mounted in the heliostat the heliostat was moved until the laser spot was located approximately in the center of the target. With the heliostat in this position the gimbal angle (encoder) positions were recorded as the reference location. The prescribed gimbal angle movements were then made relative to this reference location. As indicated in Figure A-7 a series of eight different laser paths were used. For instance, moving the laser from Point 0 to Point 1 in Figure A-7 involved driving the heliostat azimuth drive a fixed angular distance. The path from Point 0 to Point 2 involved driving both azimuth and elevation drives. The movement along each path was repeated five times and the degree of repeatability was assessed in terms of the proximity of the laser to Point 0 on returning from each of the eight directions.

Concern that the laser could present an eye safety hazard dictated that the laser beam be kept on the 1.22x1.22-meter laser target. Therefore, the actual angular movements used during the test were relatively small. Typical movements were approximately 1 degree (17.4 mR) either side of the reference location. Both heliostats from each contractor were evaluated in this manner.

The stability portion of this test involved commanding the heliostat gimbal angles to the reference location described earlier and maintaining this commanded position for a 30-minute period. By recording laser movement during this period, the intent was to observe the results of any control system instability, electronic drift, etc.

An additional test was also performed with the laser system on one of the MMC heliostats to assess the ability of the MMC heliostats to self-compensate for steady wind loads. The angular encoders on the MMC heliostats have an angular resolution of 0.76 mR and are located on the output shafts (azimuth and elevation) of the drive unit. Thus, they sense angular movements as a result of wind loading of the mirror assembly. Using a weight and pulley system the heliostat was loaded to produce moments about the elevation axis and then about the azimuth axis. The heliostat was vertical during loading. Elevation moments were produced by pulling at the bottom of the inside two heliostat crossbeams, and azimuth moments were produced by pulling on the end of the elevation (torque) tube. Laser deflections under load were recorded with the control system active and inactive in order to obtain deflection measurements with and without control system compensation. An equivalent test was not run on a MDAC heliostat since the encoders on the MDAC design are not located on the output of the drive system and, consequently, do not sense angular deflections as a result of wind loading.

Results

During the repeatability testing a total of 40 angular movements were recorded on video tape for each heliostat. Subsequent analysis of these video tapes indicated that the MMC heliostats and the MDAC heliostats returned to the reference location following each prescribed movement to within less than 0.7 mR. Marginal angular resolution of the laser system, slight blooming of the laser spot on the vidicon tube, slight video geometric distortion, and difficulty in scaling the data from a video monitor made it difficult to determine the repeatability to any better than approximately 0.3 mR. As a

result of this relatively poor measurement resolution no attempt was made to statistically analyze the measured data. Future repeatability testing with this system will use much larger heliostat angular movements and the measurement resolution will be increased.

Analysis of the video recordings taken during the 30-minute stability tests indicated no system instability or tendency to drift for either the MMC or the MDAC heliostats. The laser spot remained in the same location on the target during the 30-minute test interval to within less than 0.5 mR.

Table A-5.I gives the results of the additional simulated wind loading test on the MMC heliostat. The table gives the moment applied to each drive axis and the resulting measured angular deflection with and without the control system actively compensating for the deflection. Also given are the times required for the control system to complete angular compensation. The time required is measured from the moment the load was applied. Each deflection value given in Table A-5.I is the average of three measurements.

TABLE A-5.I

MEASURED ANGULAR DEFLECTIONS ABOUT MMC DRIVE AXES
WITH AND WITHOUT CONTROL SYSTEM COMPENSATION

Moment (kg-m)	Axis	Deflection (mR)	With Compensation	
			Deflection (mR)	Time Required (s)
155	Elev	0.7	0.6	1.6
270	Elev	1.5	0.9	3.0
310	Elev	1.6	0.9	3.5
140	Azm	2.6	0.7	3.9
245	Azm	3.5	0.9	8.5
275	Azm	2.6	0.9	8.8

Conclusions

For the small angle movements considered during the repeatability testing both the MDAC and the MMC heliostats were repeatable to within measurement resolution with all cases repeating to within less than 0.7 mR. The MDAC heliostats did however have repeatability problems that did not manifest themselves during the small angle movements of this test. These problems will be discussed later in this report during the discussion of tracking accuracy testing (Test A-6).

The 30-minute stability testing indicated no inherent control instability or electronic drift associated with either the MDAC or the MMC heliostat design.

Evaluation of the ability of the MMC heliostat control system capability to compensate for mirror assembly angular deflections caused by steady wind loads indicated that the control system did provide significant correction. For applied moments approximately equivalent to 11-m/s (25-mph) winds, the control system was able to correct gimbal angle pointing to within 0.9 mR of the no-load position. 0.9 mR is just slightly more than the encoder resolution of 0.76 mR. It should be noted however that the time required for the control system to correct for wind loading is by design relatively long in order to avoid control system instability that would occur if the control system attempted to make more rapid corrections. This capability for wind load compensation is therefore most useful only for steady wind conditions since the drive rate limitation will not allow correction for rapidly changing wind gust loads. A second advantage of the MMC approach is that the elevation encoder tends to self-compensate for angular deflections that occur about the elevation axis of the heliostat as a result of gravity-induced moments at different elevation angles of the heliostat.

Test A-6: Beam Centroid Pointing (Tracking Accuracy)

Objective

In order to assess the ability of a heliostat to maintain its reflected beam on a desired aimpoint on a target (receiver) it is necessary to determine the beam location relative to the aimpoint at different times of the day and year. The objective of this test was to provide actual heliostat tracking accuracy data in terms of the deviation of the beam centroid location from the desired aimpoint. Evaluation of time of year variation in tracking and the effect of accelerated life cycling on tracking accuracy were also to be evaluated to the extent possible in a three-month test period.

Description

The heliostat locations and beam aimpoint used during this testing were as indicated previously in Figures A-2 and A-4. The BCS was used to determine the beam centroid location relative to the desired aimpoint as the heliostat was tracking its beam on the BCS target. Typically, 30 samples of centroid location were taken at approximately 4-second intervals, as illustrated by a typical 30-point sample in Figure A-6.1. As can be seen in this figure, during the period that these data were taken the heliostat control system initiated several gimbal angle tracking updates. If the heliostat had been tracking perfectly the mean value of the vertical and horizontal errors indicated in Figure 6.1 would be zero, in which case the sawtooth pattern would be centered along the zero error line.

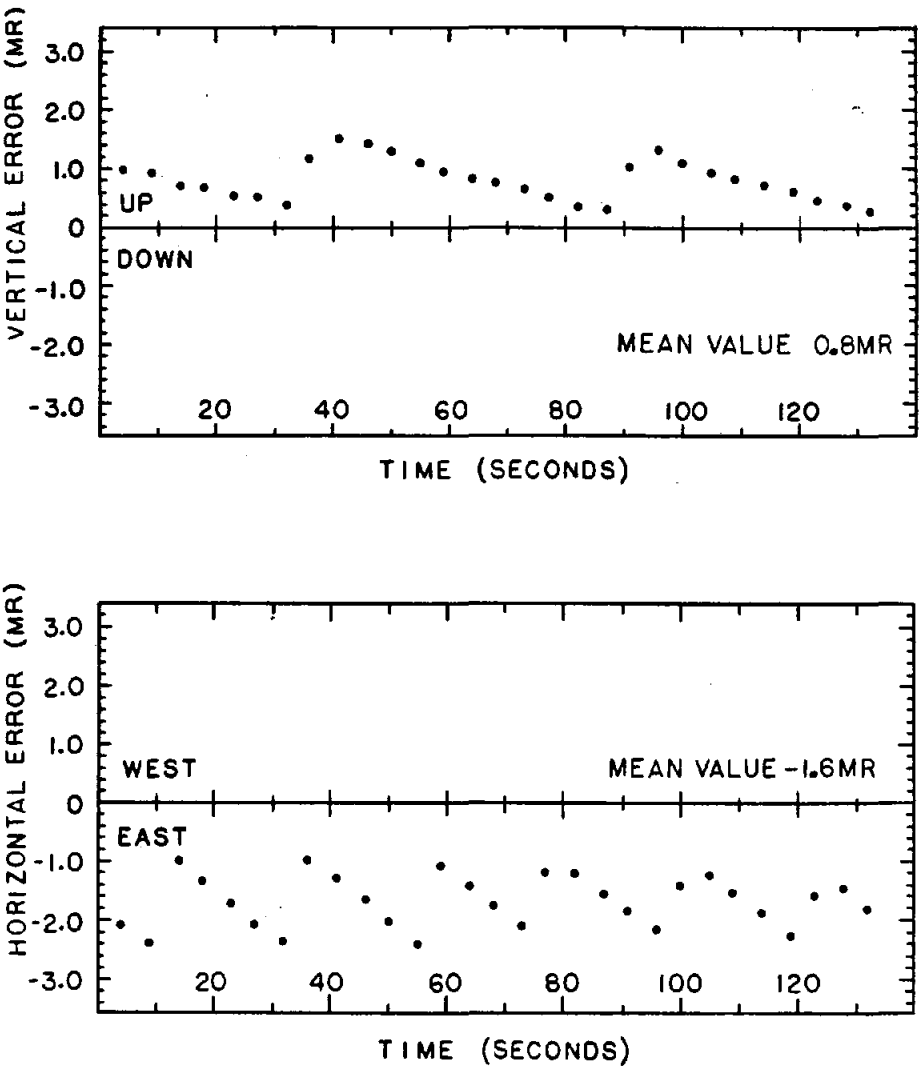

Figure A-6.1. Typical Rapid Sampling of Reflected Beam Error

In order to evaluate tracking error over an entire day these 30-point samples were repeated every 20 to 30 minutes. The mean values of these sample intervals were assumed to be representative of where the heliostat beam was located during the two-minute period required to take the data. Successive mean values were then used to obtain a statistical assessment of the day-long tracking accuracy.

In order to obtain day-long data on both of a contractor's heliostats during the same day, both heliostats were held at a standby location to the east of the BCS target. The heliostats were cycled on and off the target at 20-to 30-minute intervals during an approximate eight-hour period. In order to evaluate the effects on tracking accuracy of time of year and mechanical aging, the day-long tracking error measurements with the BCS were repeated following simulated life cycling and after as long a time delay as was consistent with completing all testing within the June through September 1979 time frame.

Prior to presenting the results of the tracking accuracy tests it is necessary to briefly describe several potential sources of tracking error. This description will be useful in understanding the different philosophies and techniques used by MDAC and MMC in compensating for these errors.

Heliostats are typically two-axis tracking devices using an open loop control system to operate separate drive mechanisms for azimuth and elevation movement. Figure A-6.2 illustrates several potential sources of heliostat tracking error that can result from hardware tolerances or assembly and installation procedures. Due to hardware peculiarities and/or field installation procedure the effective azimuth axis of the heliostat may be tilted with respect to an ideal vertical axis.

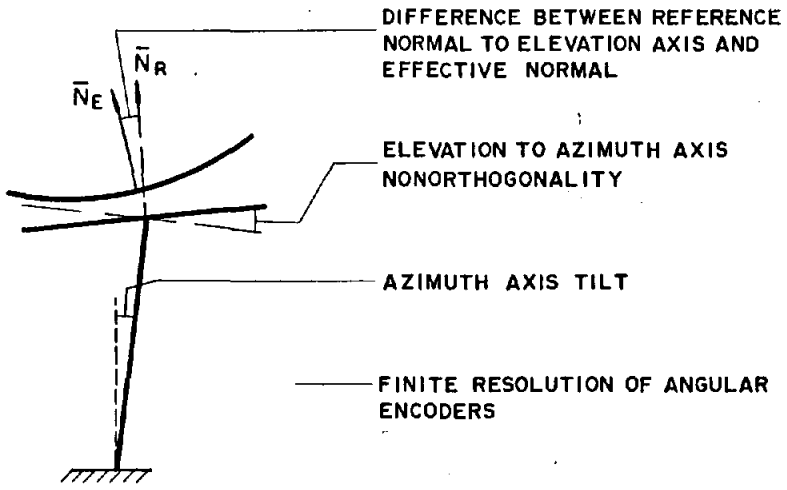

Figure A-6.2. Potential Heliostat Hardware Tracking Error Sources

Manufacturing tolerances and/or fabrication procedures may also result in the effective elevation axis being nonorthogonal to the azimuth axis. For the same reasons, the effective normal vector to the composite of mirrors mounted on the heliostat structure may deviate from the ideal reference normal vector that is perpendicular to the elevation axis. The mirror canting procedure used can therefore influence tracking accuracy in that the composite canted assembly may be at an angle to the reference normal.

Gravity loading of the structure may also influence tracking in that the mass of the composite mirror assembly may produce moments that are high enough in relation to the structural compliance of the drive unit/mirror support assembly to produce an angular displacement of the effective mirror normal relative to the reference normal. The effect of this gravitational influence depends on the heliostat design but, typically, varies as a function of the elevation angle of the heliostat.

The finite angular resolution of the angular encoders used on the heliostat also contribute to the overall tracking error in that the heliostat can only be positioned to within the angular resolution of the encoder. In

addition, the encoders on each heliostat axis must be physically attached and referenced to the heliostat structure. The zero readings of the encoders must be accurately referenced to a known orientation of the heliostat reflective surface. An error in this referencing will result in tracking error. Geographical survey errors in the location of the heliostat relative to the target (receiver) can also contribute to tracking error.

The tracking errors previously mentioned might be termed hardware errors. In addition to heliostat hardware errors, there are several sources of tracking error that could be termed computational errors. Heliostat azimuth and elevation angles are calculated from vectors that define the position of the sun and the position of the target (receiver) relative to the heliostat. The location of the heliostat relative to the target can be surveyed to a high degree of accuracy so a potential source of error remaining is the determination of the position of the sun relative to the heliostat.

Tabular solar ephemeris data[7] are typically regarded as providing the "correct" position of the sun and different computational models have been derived that closely approximate the tabular ephemeris data. These sun position models typically include the effects of precession and nutation of the earth"s axis and are capable of providing the actual position of the sun to within approximately one second of arc (.0048 mR) of the ephemeris data. Minicomputer round-off error and compromises that reduce computational time may result in a calculated sun position with a much larger degree of error. It should also be noted that a heliostat control system must be capable of calculating the apparent position of the sun in addition to the actual position of the sun. The apparent position of the sun differs from the actual position of the sun due to the refraction of the sun's rays as they pass through varying thicknesses of the earth's atmosphere. Atmospheric refraction results in the apparent elevation of the sun differing from the actual elevation by greater than 1 mR for sun elevation angles of less than 0.26 radian (15 degrees). Consequently, an atmospheric refraction correction must be included in the sun position determination. Changing atmospheric conditions, such as humidity, can also result in a change of 0.1 to 0.2 mR in the apparent position of the sun. However, these effects are typically not considered in the control system.

If the heliostat manufacturer has chosen not to reduce the hardware errors (tilt, nonorthogonality, gravity influence, etc.) to a negligible level then the heliostat computational system must contain algorithms that will compensate for these errors. Errors in the determination of the necessary input parameters to these compensating algorithms will ultimately result in tracking error of the heliostat. MMC and MDAC treated these potential hardware and computational tracking error sources in different ways, which will be discussed later.

The approach used by MMC was to minimize hardware error sources, and thus be able to avoid the necessity of control system compensation for azimuth axis tilt and azimuth axis to elevation axis nonorthogonality. This was accomplished by a field installation and leveling procedure that reduced azimuth axis tilt to less than 0.14 mR (30 seconds of arc). Nonorthogonality of the elevation

axis with respect to the azimuth axis was minimized by maintaining stringent production tolerances in the drive unit and in the arms that link the elevation drive shaft to the elevation (torque) tube.

During the off-axis alignment of the MMC heliostats, as discussed earlier in Test A-2, the reference mirror module was oriented with respect to the elevation axis only visually. Since the remainder of the mirror modules were canted with respect to the reference module, some degree of tracking error could have been introduced in that the effective normal to the mirror assembly may have deviated from the reference normal assumed by the control system. The potential introduction of tracking error during this mirror canting procedure can partially be attributed to the fact that the procedures used at the CRTF were not totally representative of procedures that would be used during heliostat mass production and installation. A production mirror canting tool proposed by MMC could minimize the possibility of tracking error being introduced by the mirror canting procedure.

The plane defined by the mirror module assembly on the MMC heliostat has a relatively small displacement ($\sim$ 0.11 meter) from the output shaft of the drive unit, therefore moments inroduced by the mirror assembly at different elevation angles are relatively small. MMC does not use software compensation for gravity-introduced moments on the elevation shaft of the drive unit. However, location of the elevation encoder on the output shaft of the drive unit tends to self-correct for angular deflections as a result of compliance in the drive unit.

Referencing of the MMC encoders to the heliostat structure was accomplished in a three-step process. Initially, the encoders were installed and located visually to within approximately 5 degrees of the desired location. The offset or "bias" angle that will complete the referencing is determined by utilizing the reflected beam from the heliostat. A first-order bias is obtained by attempting to track the beam on a desired aimpoint on the target. While visually observing the reflected beam location, the azimuth and elevation encoder biases are iterated until the beam is centered on the aimpoint. The first-order biases are recorded and then a final refined set of biases are determined with the BCS. The final biases are determined by measuring the beam location with the BCS at three different times during the day. A best-average encoder bias is then derived from the three measured values. This final encoder bias tends to compensate for tracking error variation with time of day. The final encoder biases are stored in the control system data base and can be periodically updated if necessary by repeating the biasing procedure.

The approach used by MDAC in dealing with hardware tracking error sources was based on a different philosophy than that employed by MMC. MDAC chose to utilize control system compensation for azimuth axis tilt and azimuth axis to elevation axis nonorthogonality. It was their belief that tracking accuracy could be improved and heliostat installation and manufacturing costs could be reduced. Installation could be simplified in that the drive system need only be approximately leveled. Field leveling at the CRTF was to less than 4 mR of azimuth axis tilt versus less than 0.14 mR for MMC. Manufacturing costs could be saved by reducing tolerances on the drive unit casting since nonorthogonality was also to be compensated for in the control system.

As described in Test A-2, the MDAC mirror canting procedure used a small reference plane on the elevation tube with respect to all the other canted mirror modules. This procedure was intended to minimize tracking error introduced by the effective normal to the composite of mirror modules deviating from the ideal reference normal; therefore, no control system compensation was used for this error source. It should be noted that when tilt and nonorthogonality compensation are to be handled in the control system, it is necessary to accurately determine for each heliostat in the field what the angles and directions associated with tilt and nonorthogonality are.

While at the CRTF, MDAC used two different techniques for determining tilt and nonorthogonality parameters that were needed in their control system. The first procedure, and the one used to obtain the parameters for each heliostat during this test, involved rotating the heliostat in elevation to a mirror face-up orientation. A two-axis electronic inclinometer was placed on the small reference plane in the center of the elevation tube with one axis parallel to the elevation tube and the other at 90 degrees to the elevation tube. The heliostat was rotated in azimuth and angles measured by the inclinometer were recorded every 40 degrees of azimuth rotation. These data were then used to unfold the tilt and nonorthogonality parameters that were stored in the control system data base.

The second procedure, and the one used during tracking accuracy tests before and after simulated wind load testing (Test A-9) involved obtaining day-long BCS tracking accuracy data with no control system compensation for tilt and nonorthogonality. A MDAC procedure was then used to unfold tilt and nonorthogonality parameters from the measured BCS data. The procedure used by MDAC to reference their angular encoders to the heliostat structure was accomplished in the following manner. Initially, a small flat reference mirror was attached to the center of the elevation tube on the reference plane. A theodolite was set up directly over survey Monument B to define a point in space relative to the reference mirror. The heliostat was then manually rotated until the normal to the reference mirror intersected the point defined by the theodolite. From this known orientation the heliostat was rotated in azimuth and elevation until the normal to the mirror was horizontal and pointing south. The turns counts for the incremental encoders on each axis were recorded and the 4-bit absolute encoders on each axis were manually rotated until a signal transition was observed. The absolute encoders were then secured. The turns counts recorded for each incremental encoder were then stored in the control system data base.

Results

The results of the day-long BCS tracking accuracy evaluations before and after life cycling the heliostats will be presented in three different ways. The first will be the X,Y positions of the beam centroid locations on the BCS target plane that are determined by the BCS during the day. The X,Y positions of the beam centroids are used to determine the corresponding horizontal and vertical reflected beam angular errors used to determine compliance with the tracking accuracy specification, and the X,Y position data in conjunction with a sun position program are used to calculate the corresponding mirror normal angular errors.

Figure A-6.3 gives the measured beam centroid positions of MMC Heliostat 1 beam during the day. The X and Y axes are in the plane of the BCS target with positive X to the west and positive Y in the upward direction. The data plotted were measured in July and then again in September following simulated life cycling of the heliostat. The time arrow in the figure indicates the general path that the locus of centroid locations followed during the day.

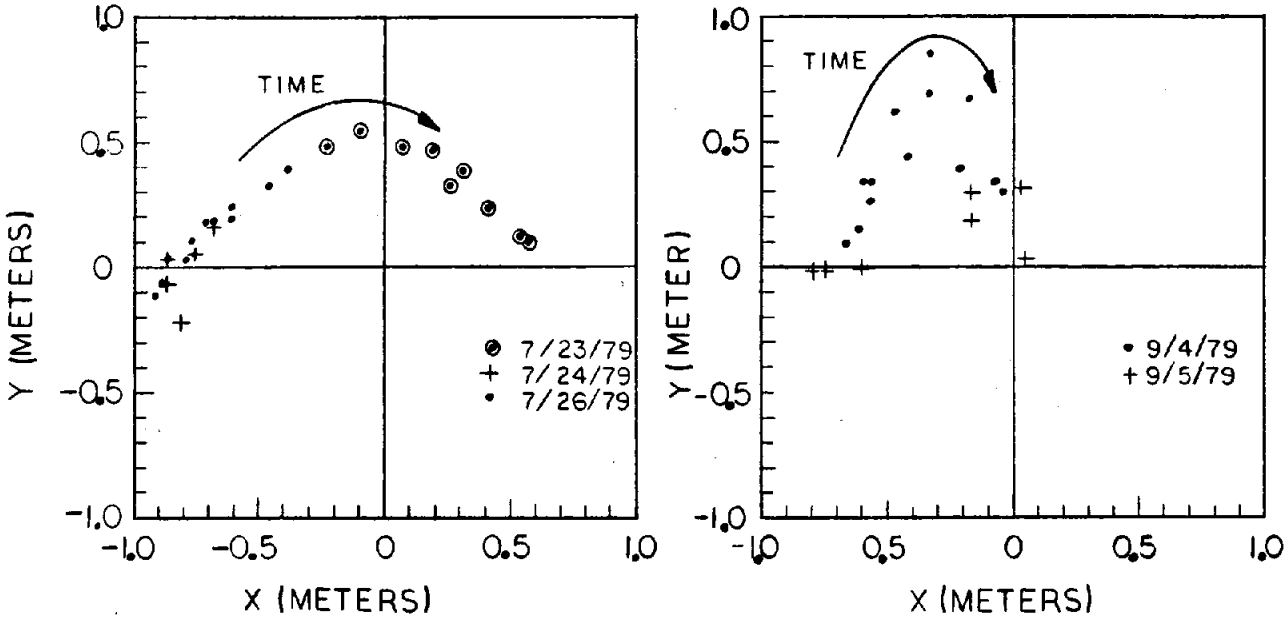

Figure A-6.3. MMC Heliostat 1 Day-Long Centroid Location Data during Initial and Final Tests

Figure A-6.4 gives similar data for MMC Heliostat 2. Interruptions due to cloud cover or other simultaneous testing often resulted in BCS tracking data being obtained on succeeding days, as indicated in Figures A-6.3 and A-6.4.

The necessity of obtaining tracking data on succeeding days also proved to be a good means of assessing the day-to-day repeatability of the heliostat control system. The final tracking data taken on the MMC heliostat on 9/4 and 9/5/79 were obtained during wind conditions of from 4.5 to 6.7 m/s (10-15 mph) with occasional gusts to 8.9 m/s (20 mph). Typically, all other tracking data were taken during wind conditions of less than 3.1 m/s (7 mph).

Similar centroid location data for the two MDAC heliostats are shown in Figures A-6.5 and A-6.6. Repeated electronic control failures in the MDAC heliostats resulted in the first set of tracking data not being taken until 9/1/79. Twenty-four-hr/day life cycling of the MDAC heliostats was initiated in order to obtain an equivalent number of life cycles with MMC heliostats

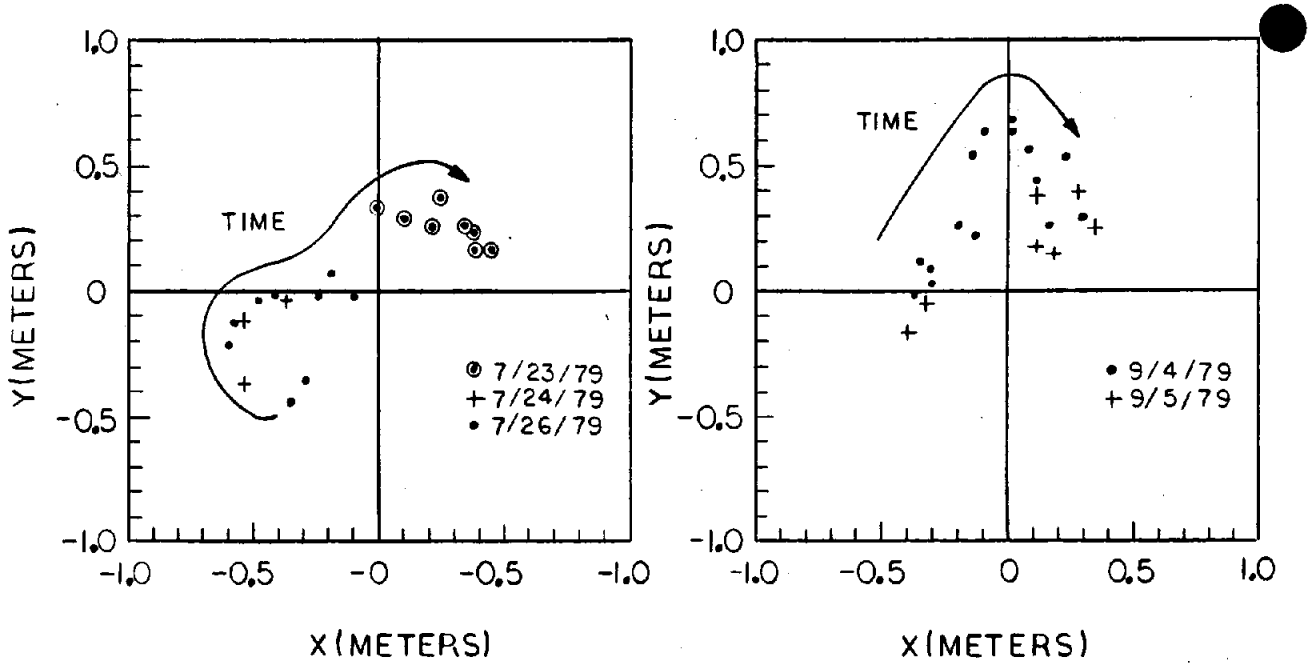

Figure A-6.4. MMC Heliostat 2 Day-Long Centroid Location Data during Initial and Final Tests

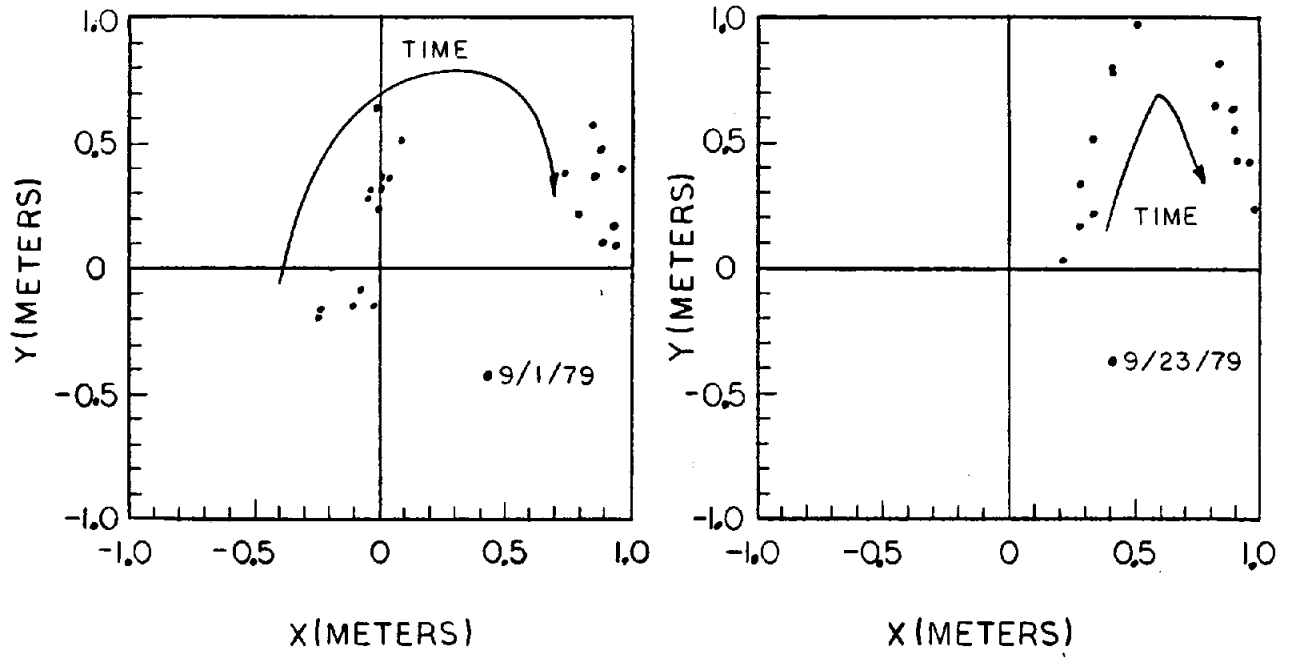

Figure A-6.5. MDAC Heliostat 1 Day-Long Centroid Location Data during Initial and Final Tests

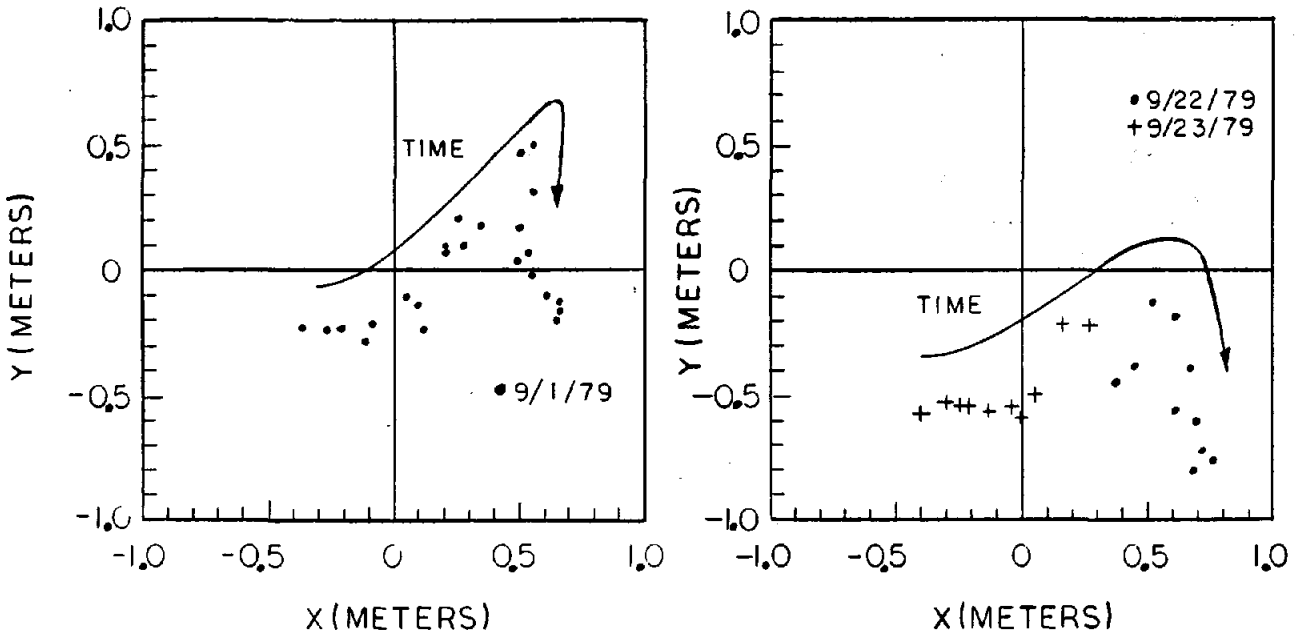

Figure A-6.6. MDAC Heliostat 2 Day-Long Centroid Location Data during Initial and Final Tests

prior to the final tracking assessment on 9/23/79. The shortened time period between initial and final tracking assessment of the MDAC heliostats also made it more difficult to observe tracking accuracy variation with time of year sun position variation.

Day-to-day repeatability of the MDAC heliostats during the CRTF testing proved to be relatively poor due to two things. The dual linear screw jacks used for elevation movement exhibited an unrepeatable transfer of movement when the stow jack stopped moving and the tracking jack continued the elevation movement. This transfer resulted on occasion in a 1- to 2-mR difference in the elevation location of the beam from one day to the next.

The second problem encountered was observed primarily in the MDAC Heliostat 1. The absolute encoder on this heliostat would cause undesired updates of the azimuth incremental encoder and result in an undesired horizontal movement of the reflected beam. This discontinuity can be seen in Figure A-6.5 for the initial and final tracking data of the MDAC Heliostat 1.

The 10-MW_e pilot plant beam tracking accuracy specification was written in terms of a maximum allowable one standard deviation of the reflected beam angular error distribution for each tracking axis. The reflected beam angles for each axis were expressed in terms of the horizontal and vertical displacements of the beam centroid location from the desired aimpoint on the BCS target.

The X,Y centroid location data, presented in Figures A-6.3 through A-6.6, were used to calculate horizontal and vertical angular errors of the reflected

beam relative to the heliostat location. Strictly speaking, it is not correct to think of these angular errors as corresponding directly to heliostat azimuth and elevation errors since in the reflected ray system heliostat azimuth and elevation movements are coupled. A movement in azimuth only at the heliostat will result in a horizontal and a vertical movement of the reflected beam. The magnitude of this coupling varies as a function of sun position. Figures A-6.7 and A-6.8 give the reflected beam angular error data for MMC Heliostats 1 and 2, respectively, for the initial and the final tracking evaluation. Also shown in the figures are the root mean square (rms) values of the tracking error data presented in each figure.

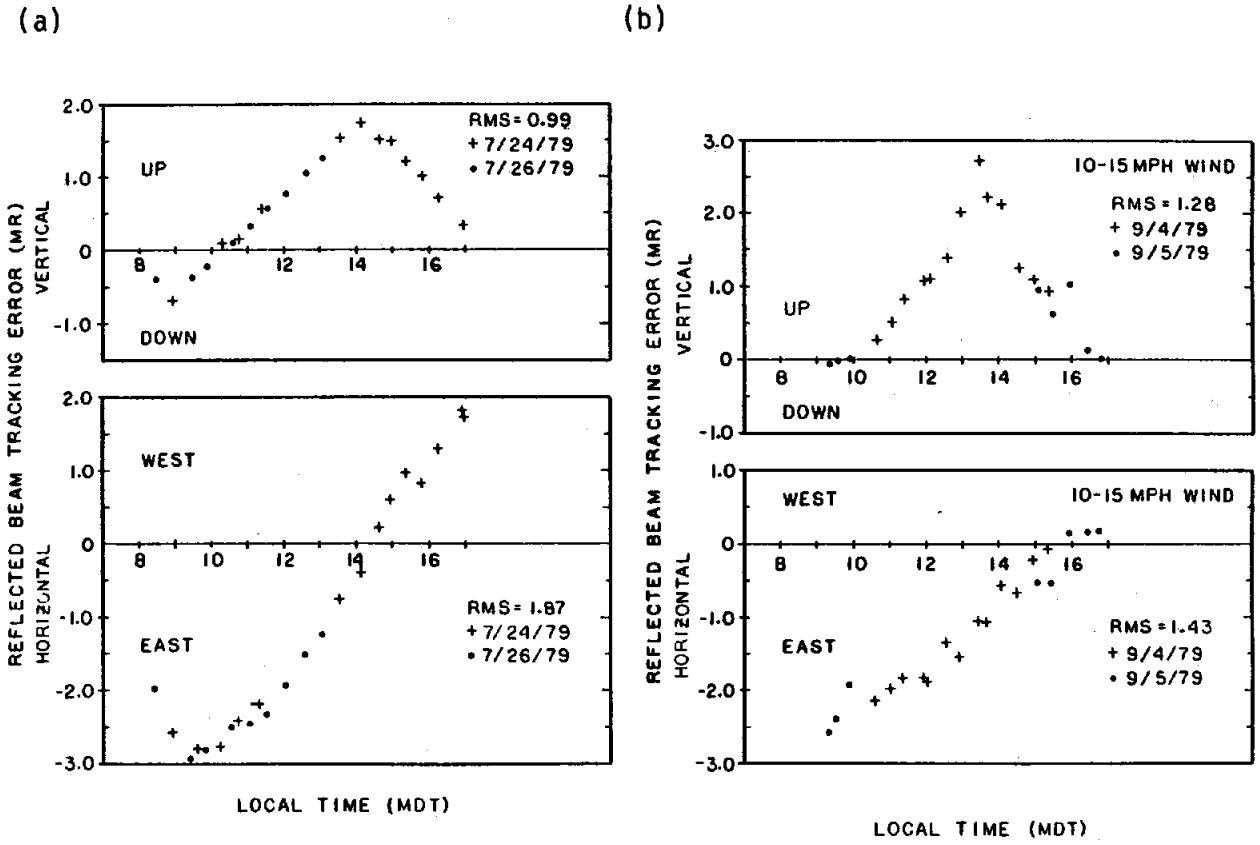

Figure A-6.7. MMC 1 Reflected Beam Angular Tracking Errors during (a) Initial Test and (b) Final Test

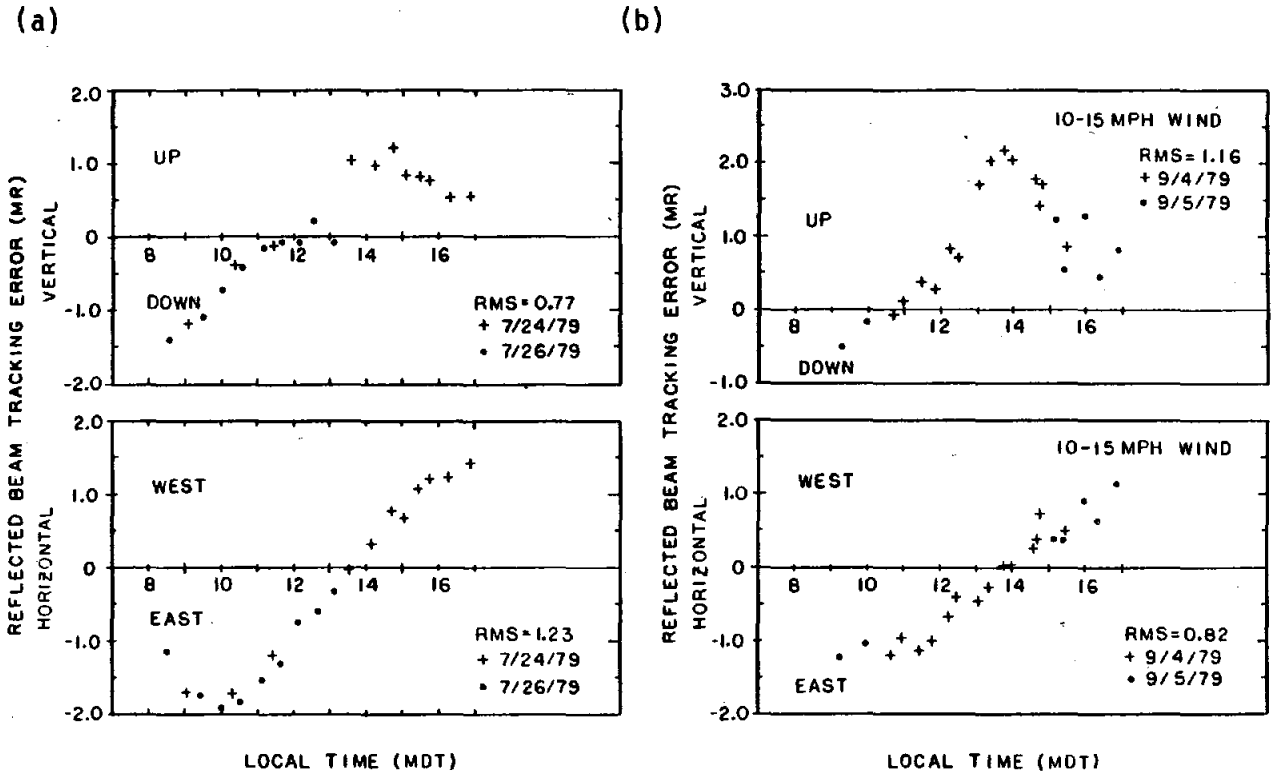

Figure A-6.8. MMC 2 Reflected Beam Angular Tracking Errors during (a) Initial Test and (b) Final Test

The corresponding reflected beam tracking error data for the MDAC heliostats are given in Figures A-6.9 and A-6.10. The azimuth encoder update problem mentioned previously is evident in the MDAC Heliostat 1 data in Figure A-6.9. Table A.6.I gives a summary of the root mean square tracking error values obtained from the day-long tracking error data for the MMC and MDAC heliostats. Typically, the reflected beam angular error data were not always equally spaced in time. A linear interpolation was used between measured data points in order to obtain a set of equally spaced (in time) data. The RMS values in Table A-6.I were then calculated from the equally spaced data. This approach avoided weighting the RMS values more heavily during times of the day when more measured data were taken. The data in the final column of this table were obtained after completing approximately 120 simulated daily tracking cycles.

Analytical models for the behavior of a large field of heliostats, such as HELIOS, DELSOL, and MIRVAL,[5,8,9] treat field tracking errors in terms of separate Gaussian error distributions associated with the heliostat azimuth and elevation axes. Since a large number of heliostats are being considered in these models the mean value of the tracking error distribution associated with each axis is assumed to be zero. Consequently, the input parameters to the codes are only the standard deviations describing the Gaussian distributions.

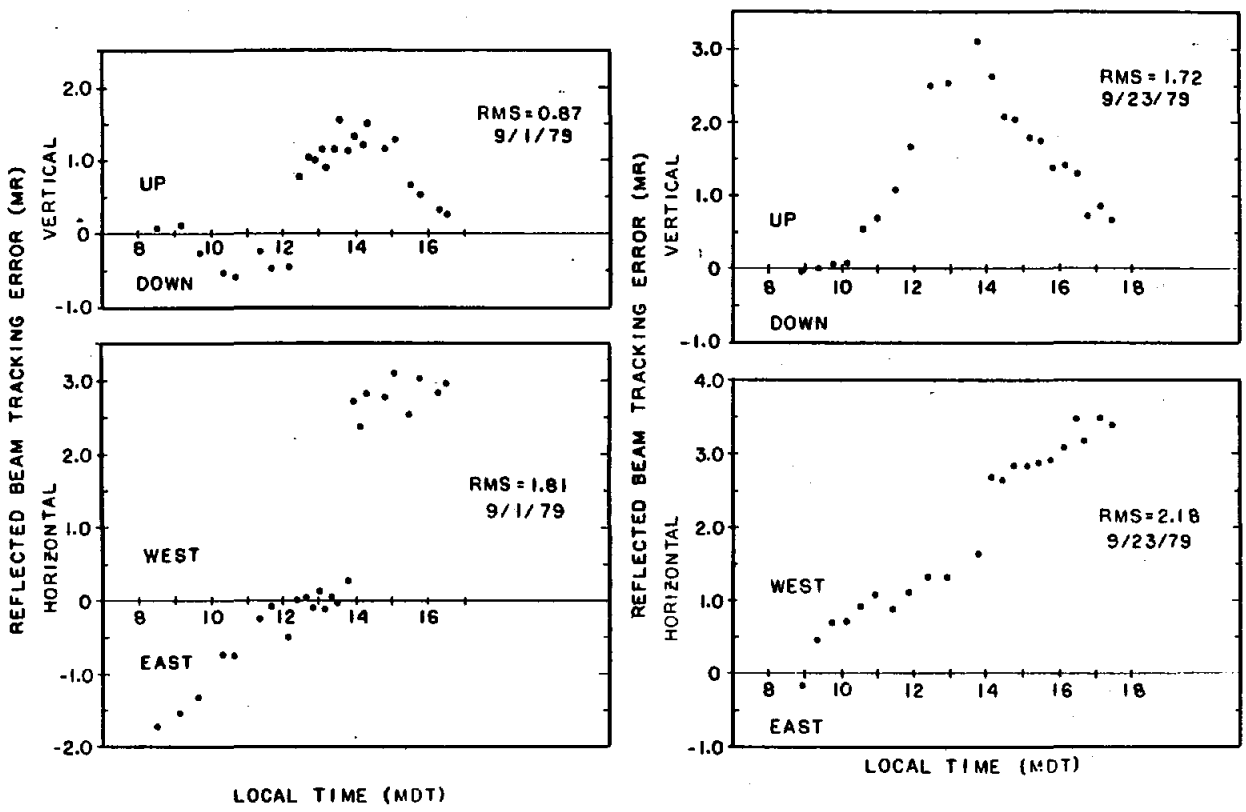

Figure A-6.9. MDAC 1 Reflected Beam Angular Tracking Errors during (a) Initial Test and (b) Final Test

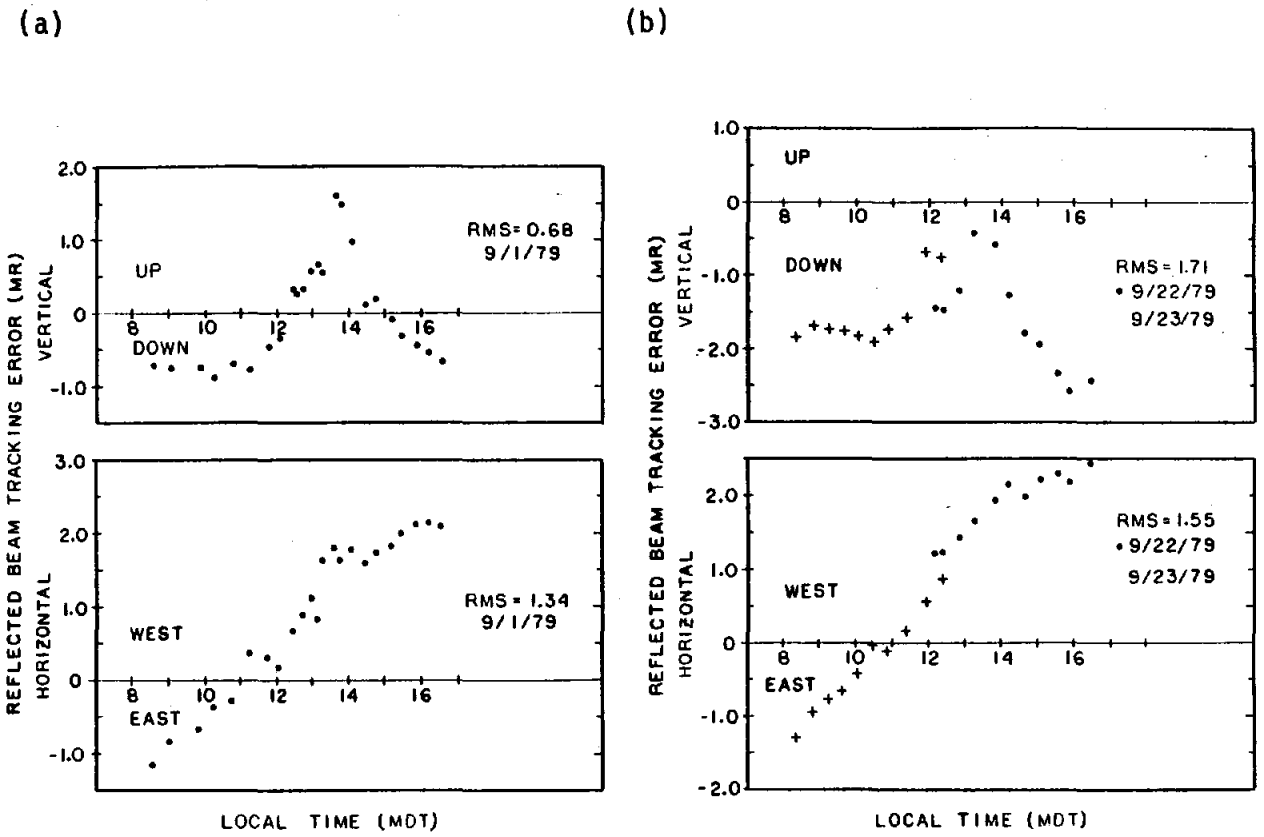

Figure A-6.10. MDAC 2 Reflected Beam Angular Tracking Errors during (a) Final Test and (b) Initial Test

TABLE A-6.I

REFLECTED BEAM ROOT MEAN SQUARE TRACKING ERRORS (mR)

	Initial	Final
MMC 1 Vertical	0.99	1.28
Horizontal	1.87	1.43
MMC 2 Vertical	0.77	1.16
Horizontal	1.23	0.82
MDAC 1 Vertical	0.87	1.72
Horizontal	1.81	2.18
MDAC 2 Vertical	0.68	1.71
Horizontal	1.34	1.55

The beam centroid location data presented in Figures A-6.3 through A-6.6 can also be used to determine the mirror normal (heliostat tracking axis) errors that correspond to the centroid location data. This was done for the tracking data obtained on both the MMC and MDAC heliostats. The resulting mirror normal azimuth and elevation errors versus time of day are given in Figures A-6.11 through A-6.14.

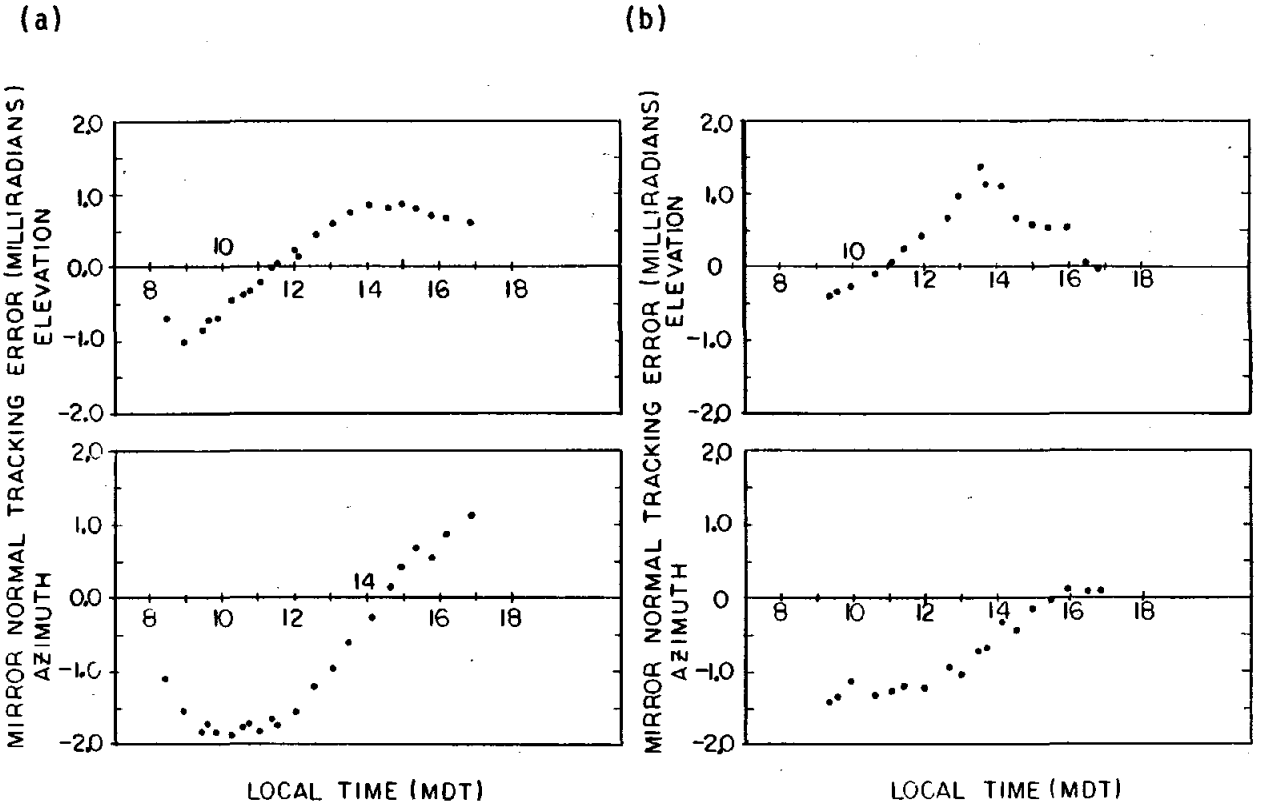

Figure A-6.11. MMC Heliostat 1 Mirror Normal Tracking Error during (a) Initial and (b) Final Tests

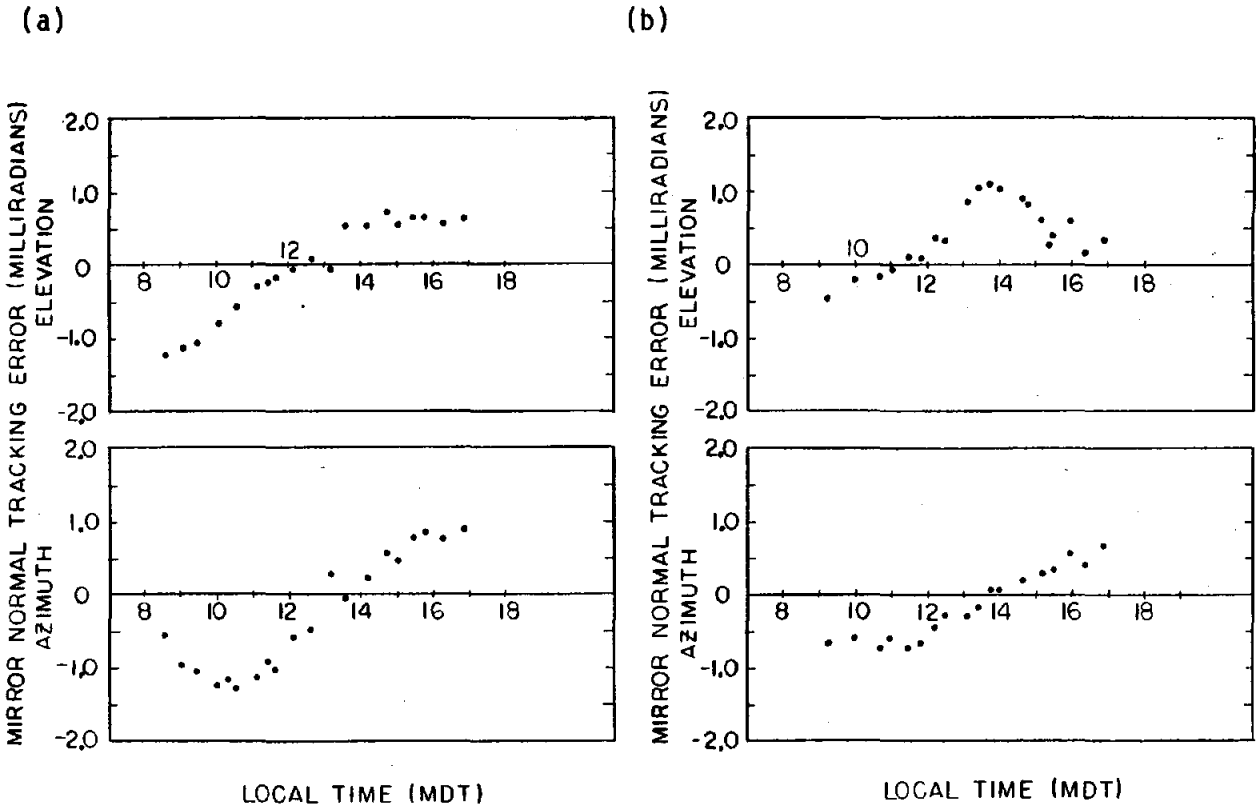

Figure A-6.12. MMC Heliostat 2 Mirror Normal Tracking Error during (a) Initial and (b) Final Tests

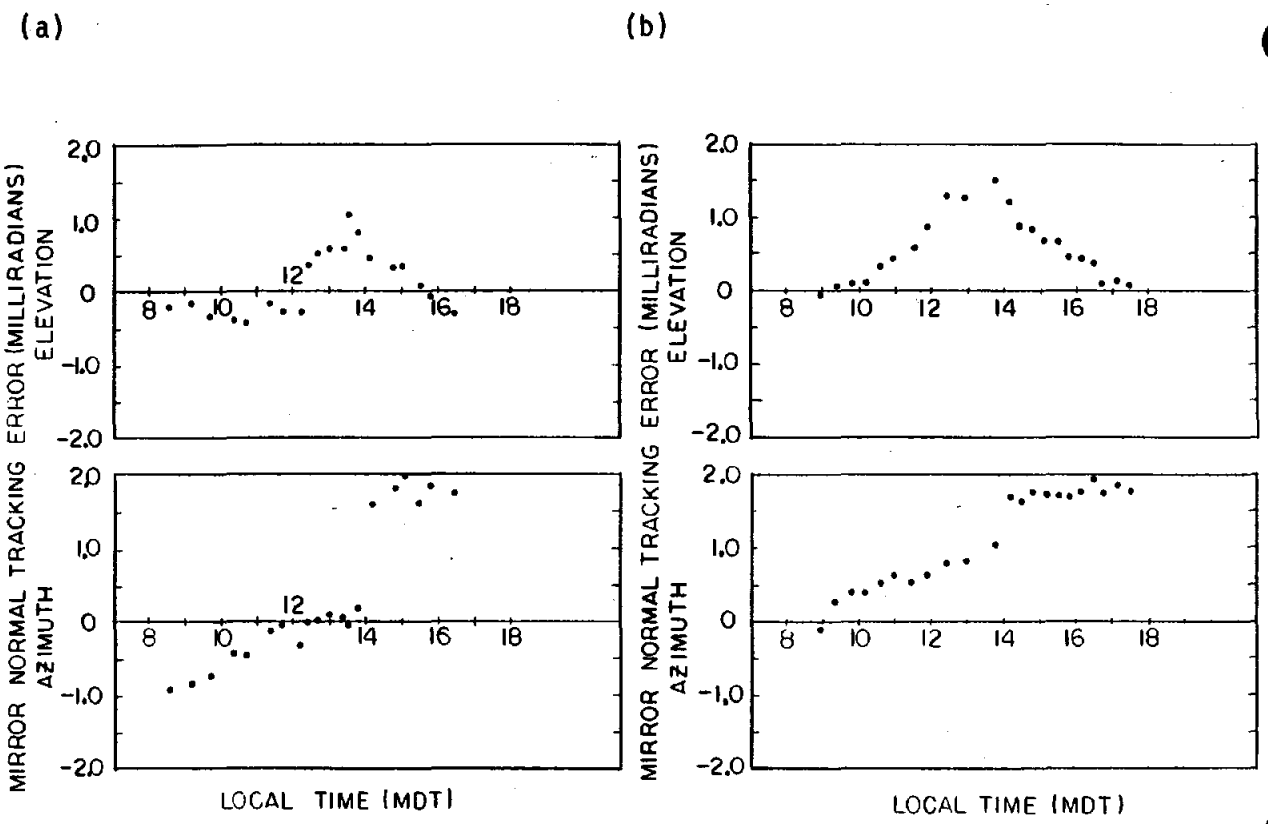

Figure A-6.13. MDAC Heliostat 1 Mirror Normal Tracking Error during (a) Initial and (b) Final Tests

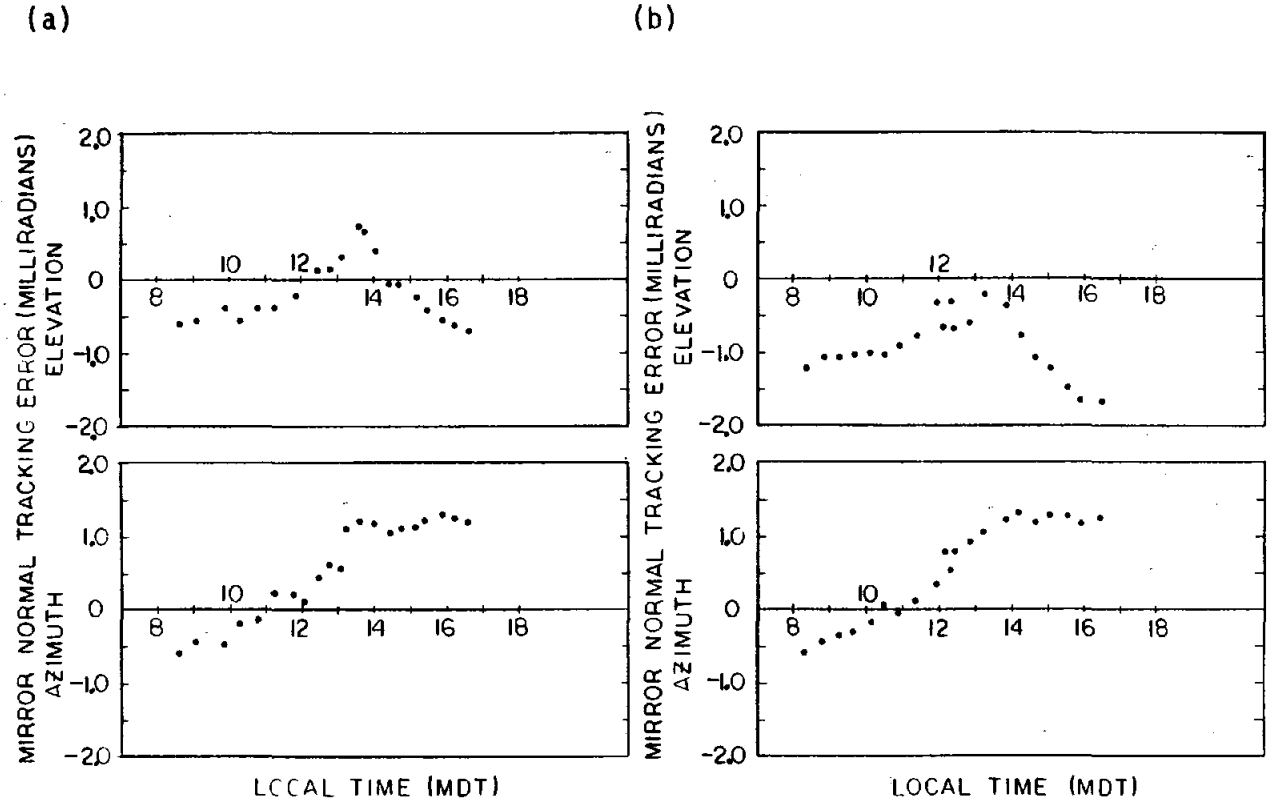

Figure A-6.14. MDAC Heliostat 2 Mirror Normal Tracking Error during (a) Initial and (b) Final Tests

Table A-6.II gives a summary of the mean, standard deviation and root mean square (rms) error associated with each set of day-long mirror normal error data. The data presented in this table represent data from only two heliostats for each contractor. It is therefore difficult to estimate with certainty the tracking error distribution that is representative of an entire field of heliostats. Since the analytical codes previously mentioned assume a normally distributed tracking error distribution with zero mean, perhaps a reasonable estimate of the full field tracking error standard deviation for each axis would be the average of the four rms values given in Table A-6.II for each axis. Thus, for a field of MMC heliostats, an estimate of the standard deviations that define elevation and azimuth mirror normal tracking error would be 0.63 and 0.90 mR, respectively. Similarly, for a field of MDAC heliostats, the estimate would be 0.65 and 1.02 mR for elevation and azimuth, respectively.

TABLE A-6.II

TRACKING ERRORS IN TERMS OF MIRROR NORMAL (TRACKING AXIS) ERRORS (mR)

	Initial			Final		
	Mean	Std. Dev.	RMS	Mean	Std. Dev.	RMS
MMC 1 Elev.	0.11	0.63	0.63	0.41	0.53	0.66
Azm.	-.84	1.09	1.35	-.71	0.57	0.90
MMC 2 Elev.	-.07	0.66	0.65	0.34	0.44	0.56
Azm.	-.28	0.81	0.83	-.13	0.48	0.50
MDAC 1 Elev.	0.13	0.43	0.45	0.57	0.46	0.72
Azm.	0.36	1.01	1.04	1.14	0.66	1.31
MDAC 2 Elev.	-.19	0.39	0.43	-.91	0.41	1.00
Azm.	0.56	0.67	0.86	0.54	0.67	0.85

Conclusions

The data given in Table A-6.I were used to determine the compliance of each heliostat tested with the tracking accuracy specification. To comply with the specification the values in the table had to be less than 1.5 mR. The MMC heliostats failed to meet this specification in only one of the eight cases shown, while the MDAC heliostats failed to meet the specification in five out of eight cases.

For the one case in azimuth that MMC Heliostat 1 failed to meet the specification it can be seen from the mean values of mirror normal error in Table A-6.II that an encoder bias one position (.76 mR) different from that used would have met specification. The mirror normal data on this same heliostat seven weeks later during the final assessment are consistent in that they also indicate that the same change in encoder bias would improve the data. Tracking data obtained on the MMC heliostats indicate that they were very repeatable from one day to the next.

The failure of the MDAC heliostats to meet the tracking accuracy specification was the result of several factors. Both heliostats exhibited poor day-to-day repeatability in elevation due to inconsistency of the mechanical transfer from the stow jack to the elevation jack. Variations of 1 to 2 mR in the vertical location of the reflected beam from one day to the next were attributed to the jack transfer problem.

MDAC Heliostat 1 exhibited undesired absolute encoder updates to the incremental encoder turns count in azimuth during both tracking assessments. Both heliostats also exhibited a general shift and consequent degradation in the reflected beam data from the initial to the final assessment. This was attributed to either mechanical wear during life cycling between assessments or to an incorrect determination of the original tilt and nonorthogonality correction parameters. There are some indications both of these factors may

have influenced the tracking data. Mechanical wear will be discussed later in this report (Test A-8) and additional tracking data obtained using different tilt and nonorthogonality parameters will be given in Test A-9.

A final perturbation in the MDAC heliostat tracking data was the result of pedestal bending due to differential heating by the sun. Near solar noon during CRTF testing, the MDAC pedestals were fully illuminated by the sun. The galvanized coating on the pedestal is a somewhat selective absorber of solar energy. This resulted in a measured temperature gradient of approximately 17°C (30°F) between the shaded and the illuminated sides. During the approximately 1-1/2-hour interval that the pedestal was illuminated a vertical reflected beam error of slightly over 1 mR was observed. This effect is evident in the reflected beam data in Figure A-6.10. It is even more evident in the tracking data that will be presented in Test A-9 using different tilt and nonorthogonality parameters. The MMC heliostats did not display a noticeable thermal influence because they were painted white and had a slightly thicker pedestal wall.

Test A-7: Beam Quality

Objective

In addition to the tracking accuracy of the heliostats, the second primary factor that can influence the overall performance of the heliostat collector system is the quality of the reflected beams from the heliostats themselves. Beam quality refers to the actual flux density distribution of the reflected heliostat beam on a target (receiver), and is thus a measure of the optical performance of the heliostat's reflecting surfaces. The objective of this test was to obtain measured beam quality data for the prototype heliostats and to use these data in conjunction with a HELIOS analysis of the test heliostats to determine the heliostats' compliance with the beam quality performance specification. A second objective of this test was to assess any degradation in beam quality during the three-month test period as a result of life cycling (Test A-8) or general exposure to the environment.

Description

The actual flux density distribution produced by a heliostat beam on a target (receiver) can be influenced by a large number of parameters. Prior to describing the procedure used in obtaining and analyzing measured beam quality data, a brief description of several of these parameters will be given.

The overall size of the heliostat, the size of individual mirror modules on the heliostat, the curvature of the individual mirror modules, and the distance from the heliostat to the target all influence the effective size of the reflected beam on the target.[10] The procedure used in canting (aligning) the individual mirrors on the heliostat, discussed in Test A-2, will also influence beam quality. Insolation and the effective solar reflectance of the mirrors on the heliostat obviously have an influence on the flux density distribution on the target.

Several manufacturing and/or assembly procedures may introduce "errors" that adversely affect the optical performance of the heliostat, and thus influence the beam quality. These errors may include variations in mirror module curvature from the reference (desired) curvature, waviness or nonspecular effects of the mirror surface, and errors in canting (aligning) the mirror modules with respect to each other.

The structural stiffness of the mirror module support structure may also influence beam quality. The weight of the mirror modules may be high enough in relation to the stiffness of the crossbeams that bending of the crossbeams, or of the mirror modules themselves, may occur as a result of gravity or wind loading of the structure. Deflections of the support structure will then introduce additional mirror canting error and the degree of this error may vary as a function of the elevation angle of the heliostat.

Finally, the flux density distribuion on the target is also influenced by the effective size and angular distribution of intensity of the sun (sunshape). Hazy or cloudy atmospheric conditions result in a broadening effect on the sunshape[11] that will result in a broadening of the reflected beam.

As a result of the number of potential influences on measured beam quality, an attempt was made during testing of the MMC and the MDAC heliostats to either minimize or to quantify as many of the potential error sources as possible. It is not necessary to quantify all these optical errors (canting, waviness, nonspecularity, etc.) in order to evaluate the performance of the heliostat relative to a performance specification.[3,4] However, during this test program an attempt was made to quantify as many of these errors as possible in order to understand which error sources produced the largest degradation in beam quality.

A number of tests were run to characterize the behavior of the MMC and the MDAC mirror modules (see Test Section D for a discussion of the mirror module tests). Evaluation of the beam quality of both the MMC and the MDAC mirror modules was complicated by the fact that the curvature of the mirror modules varied considerably with temperature. Differential thermal expansion between the glass mirror and the steel back sheet of the module produced this behavior. The manufacturing procedure used by MMC produced a mirror module with an approximately spherical curvature and that used by MDAC produced an approximately cylindrical curvature with curvature primarily along the long dimension of the module.

Figure A-7.1 gives the inverse radius of curvature for the MMC and MDAC mirror module versus temperature. The data in this figure represent an average of the curvature versus temperature data obtained in Test Section D. Also shown in the figure are the results of measurements made by MMC and MDAC. It can be seen from the figure that reasonably good agreement between MMC and Sandia measurements were obtained, however, this was not the case for the MDAC mirror modules. It can also be seen from the figure that the MDAC mirror modules become convex for temperatures below approximately 7°F (45°F). The data presented were obtained in an environmental chamber with the mirror module at different, but uniform, temperatures across the cross section.

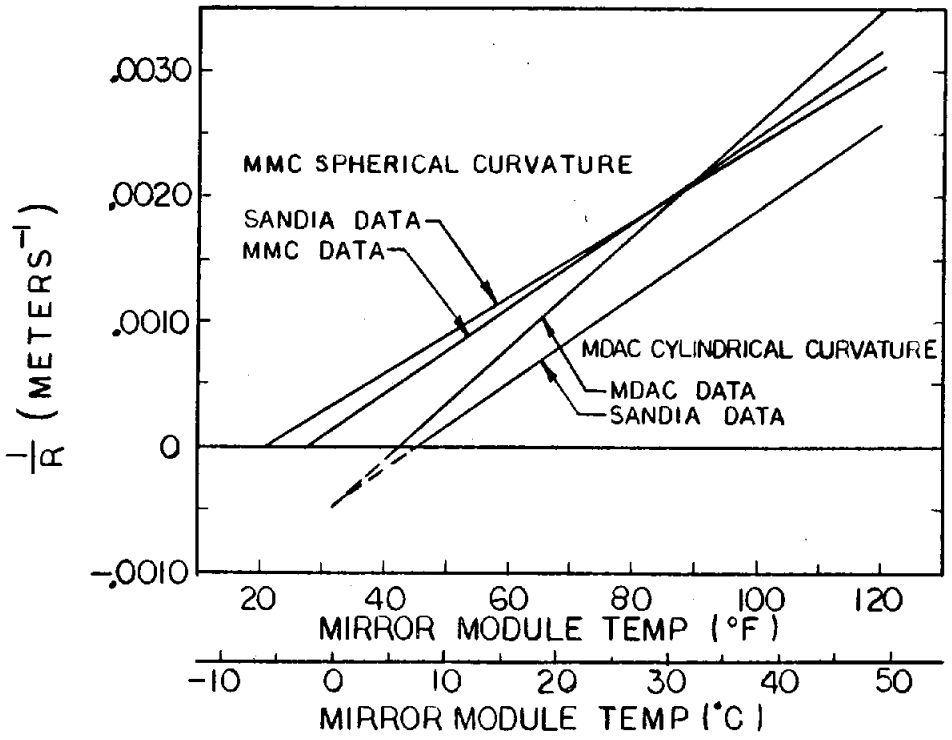

Figure A-7.1. Inverse Radius of Curvature of Test Mirror Modules vs Temperature

Field temperature measurements were made on both the MMC and the MDAC mirror modules that indicated a temperature difference between the glass and the steel back sheet as a result of the sun shining on the heliostat. The mirror modules were also slightly hotter than the ambient air. In the stowed orientation there are relatively large temperature differences between the steel back sheet and the glass mirror.

Figure A-7.2 presents measured temperature data on the MDAC mirror module initially in a stowed orientation and then rotated up into a tracking condition. Figure A-7.3 presents similar data for the MMC mirror module. The high steel temperature on the MDAC module while in a stowed position is a result of the galvanized coating on the module versus white paint on the MMC module. The styrofoam core of the MDAC mirror module also resulted in a larger temperature difference between the glass and the steel back sheet than was observed on the MMC module that has an aluminum honeycomb core. It can also be seen from the data that it takes longer for temperatures to equilibrate following a stow condition in the MDAC module than in the MMC module. During BCS beam quality testing, ambient air temperature was measured and data, such as that in Figures A-7.2 and A-7.3, were used to estimate the average mirror module temperature. The temperature was then used to find the radius of curvature using Figure A-7.1.

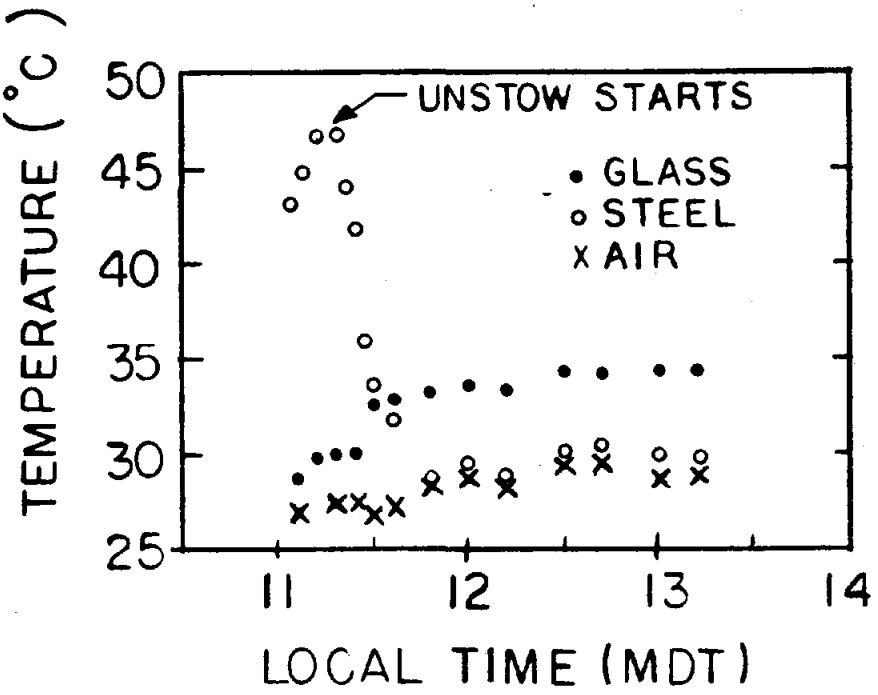

Figure A-7.2. Measured MDAC Mirror Module Temperatures during CRTF Testing

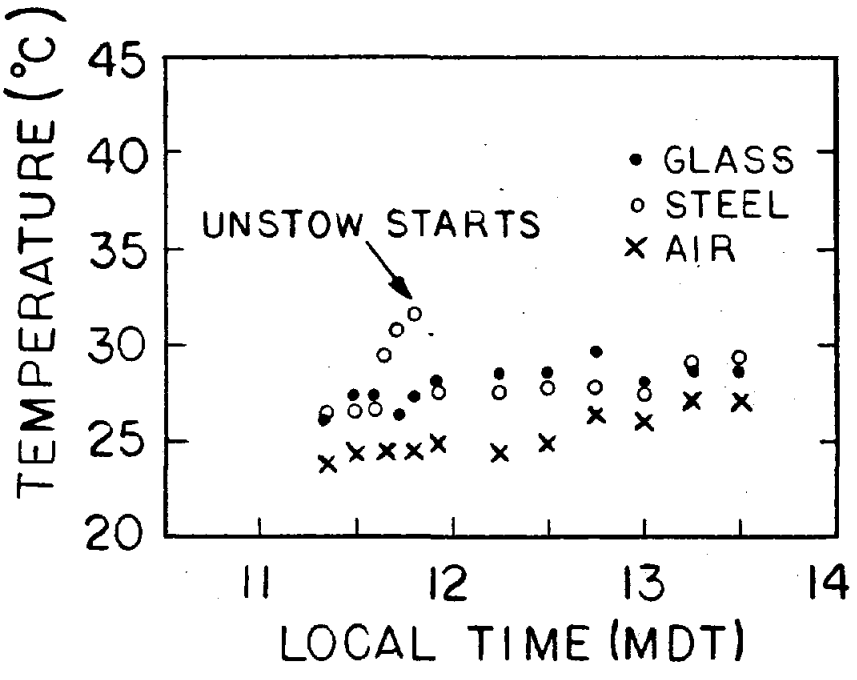

Figure A-7.2. Measured MMC Mirror Module Temperatures during CRTF Testing

Mirror module waviness measurements were made using a laser ray trace technique (Test Section D). The results indicated root mean square (rms) waviness (slope errors) of 0.20 and 0.25 mR for the MDAC mirror modules along the short and long dimensions of the module, respectively. Similar data on MMC modules resulted in rms slope errors of 0.21 and 0.45 mR in the short and the long directions, respectively. The larger waviness errors in the MMC modules were believed to be caused by mill cutting ridges in the tool used during fabrication of the mirror modules.

Reflectance measurements were made on both the MMC and the MDAC mirror modules (Test Section D). The results of these measurements indicated solar averaged reflectance values of between 89 and 90 percent with the MMC mirrors showing slightly higher reflectance than the MDAC modules. The solar-averaged value assumes a Thekaekara model for the solar spectrum at an air mass of 1.5. During BCS beam quality testing of the test heliostats, the heliostats were washed several times during the test period to minimize potential scattering by dust buildup and the reflectance during all BCS measurements was assumed to be 89 percent for both MMC and MDAC. Even though measured sunshape data were obtained from the LBL circumsolar telescope[12] located at the CRTF during BCS measurements, the BCS beam quality measurements were only taken during very clear conditions in order to minimize the influence of sunshape.

A typical measured clear sky sunshape is shown in Figure A-7.4. The data represent the base ten logarithm of the relative intensity of the sun along a vertical slice through the center of the sun. Figure A-7.5 illustrates a measured sunshape during hazy sky conditions.

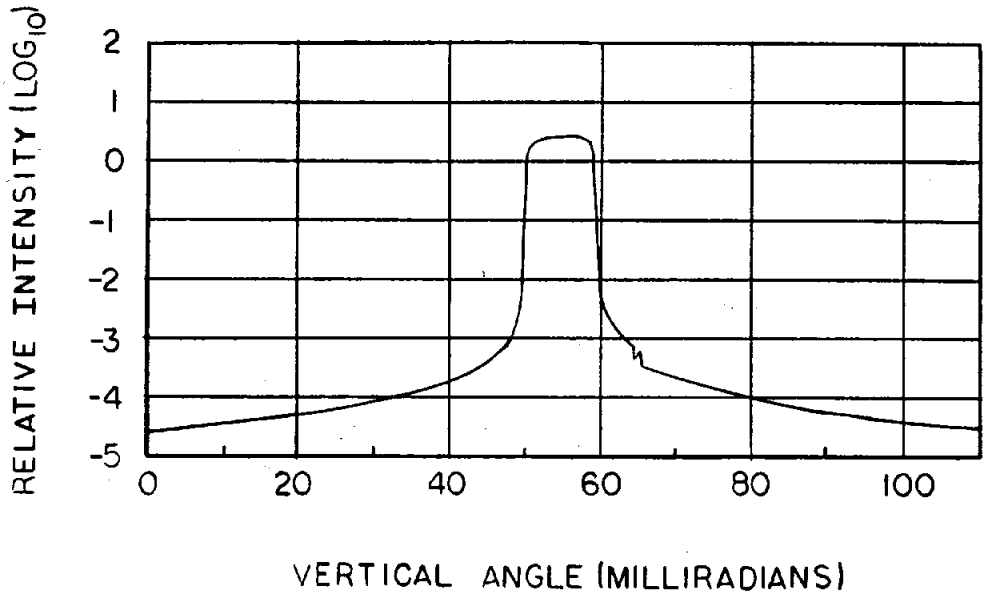

Figure A-7.4. Typical Measured Sunshape under Clear Sky Conditions from LBL Circumsolar Telescope

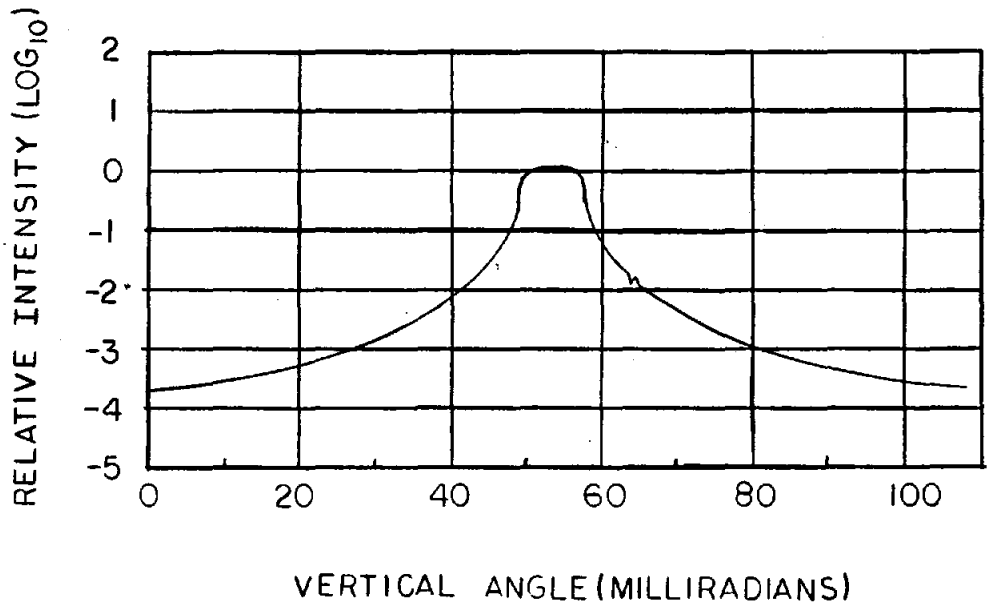

Figure A-7.5. Typical Measured Sunshape under Hazy Sky Conditions from LBL Circumsolar Telescope

A data processing scheme is used to reduce these measured data to the inputs required by HELIOS. The final input that was used was NASTRAN-predicted values of the mirror module canting errors (mirror normal deflections). The errors were introduced by a variation in gravity loading of the mirror support structure at different elevation angles of the heliostat.

Prior to obtaining measured beam quality data with the BCS, the mirror modules on the MMC and the MDAC heliostats were canted (aligned) as described in Test A-2. Beam quality data were obtained for the MMC heliostats for an off-axis canting only. Beam quality data for the MDAC heliostats were obtained for both an on-axis and an off-axis canting condition. The canting conditions are as given in Table A-2.I in Test A-2.

BCS data were obtained on each heliostat being evaluated at three different times during the day--morning, approximately noon, and afternoon. This made it possible to assess the effects of optical aberration of the heliostat beams at large angle of incidence conditions experienced during morning and afternoon conditions. As with the tracking accuracy data in Test A-6, beam quality data were taken before and after life cycling the heliostats.

Results (BCS Measurements)

As discussed in Test A-2, the mirror modules on the MDAC heliostats were initially canted in an on-axis fashion. The decision was made to recant the MDAC mirror modules off-axis using the same procedure used for the MMC heliostats. This was done not because an off-axis alignment was believed to be

preferable, but because the testing was of a competitive nature and it was believed desirable to use a consistent procedure for both contractors during testing.

Prior to recanting the MDAC heliostats off-axis, beam quality measurements of both MDAC heliostats were taken while they were still in an on-axis condition. The results of these BCS measurements of both MDAC heliostats at three different times during the day are given in Figures A-7.6 through A-7.11.

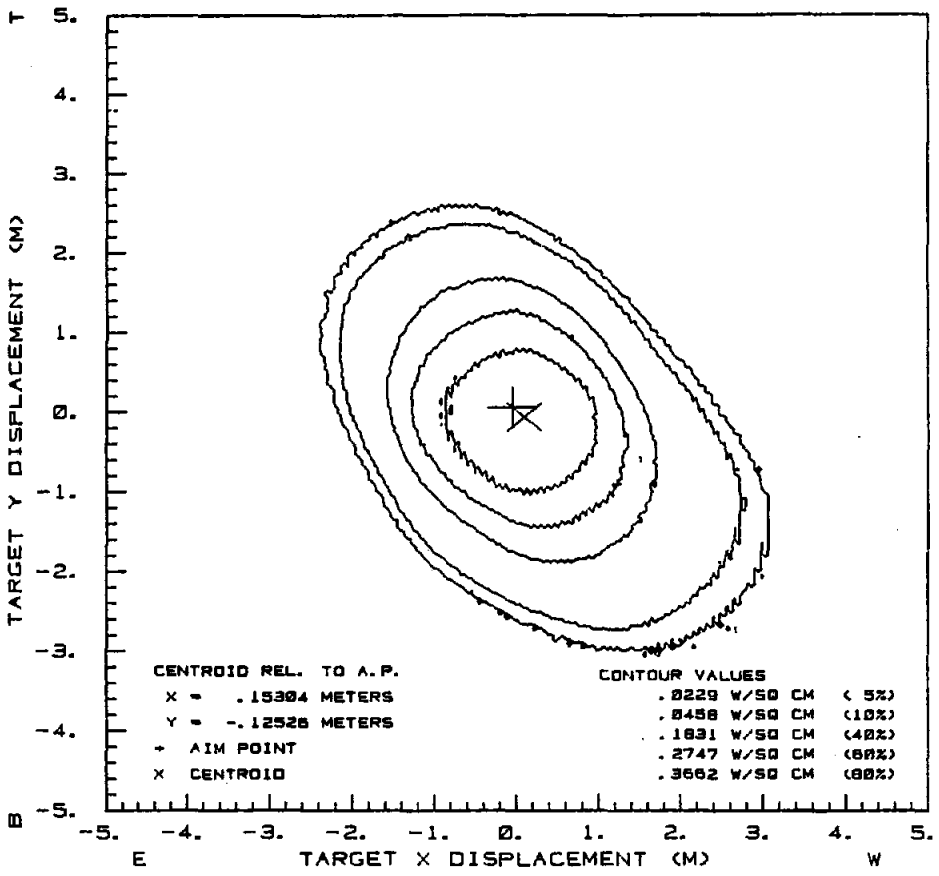

Figure A-7.6. MDAC #1 Beam Quality Data in Morning for an On-Axis Alignment

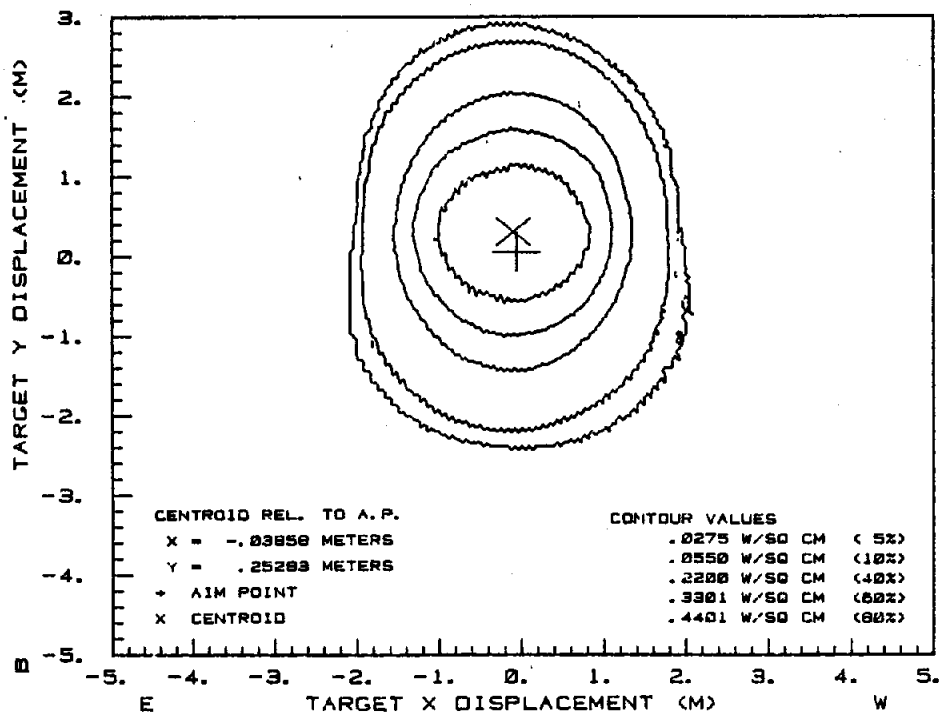

Figure A-7.7. MDAC #1 Beam Quality Data near Solar Noon for an On-Axis Alignment

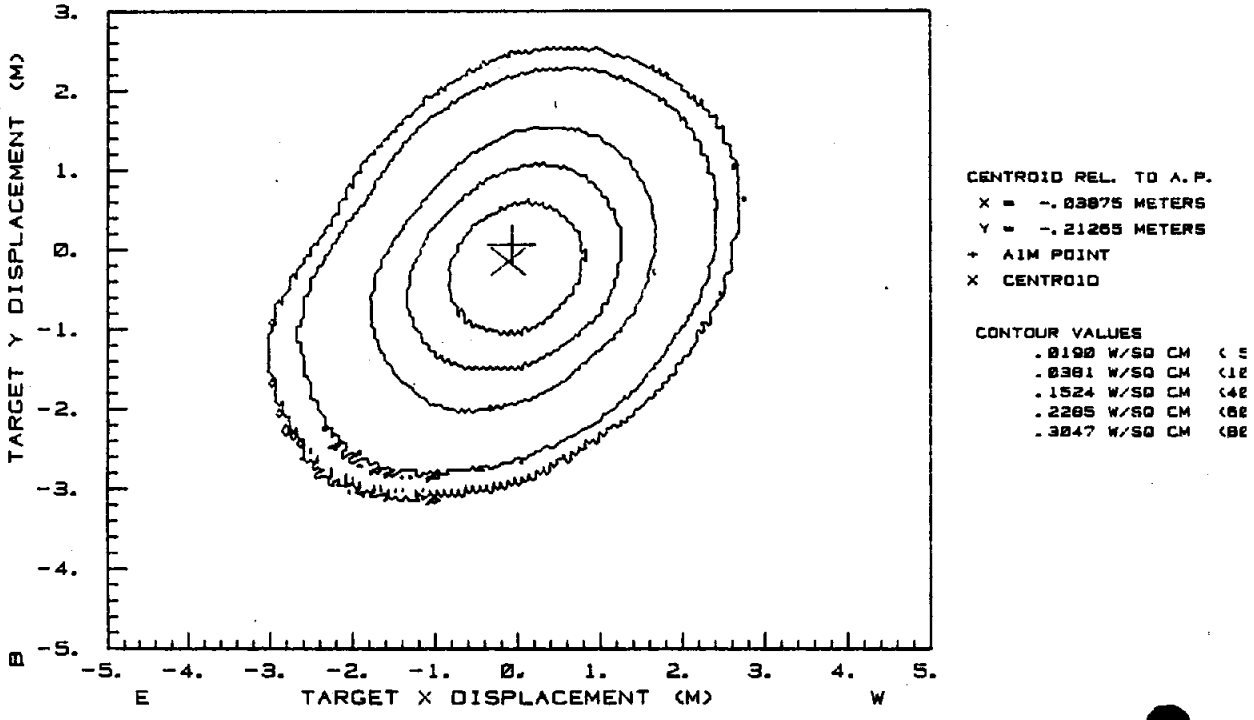

Figure A-7.8. MDAC #1 Beam Quality Data in Afternoon for an On-Axis Alignment

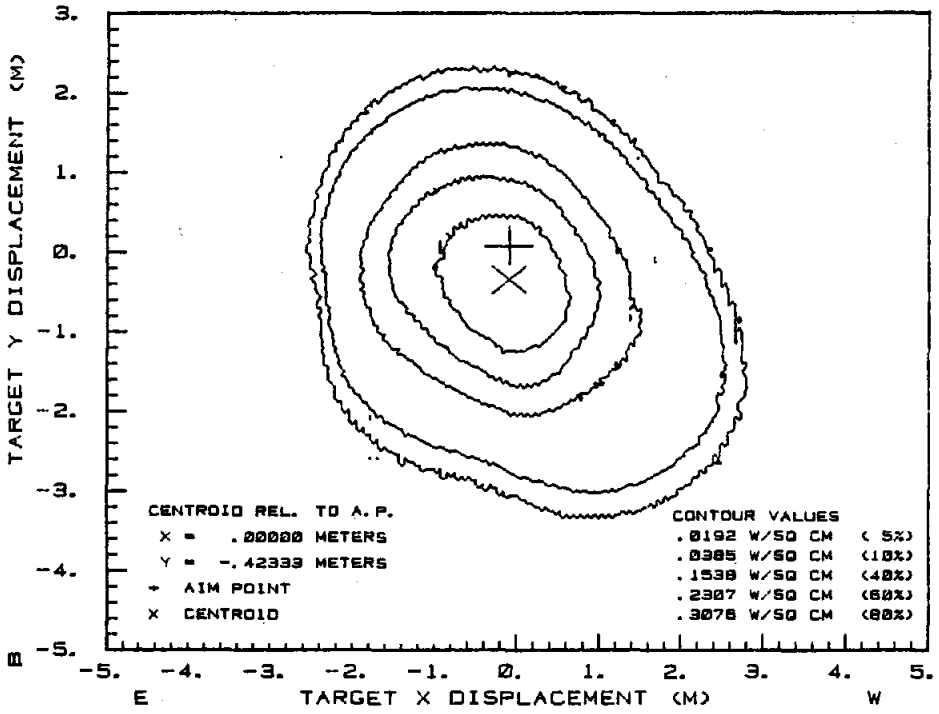

Figure A-7.9. MDAC #2 Beam Quality Data in Morning for an On-Axis Alignment

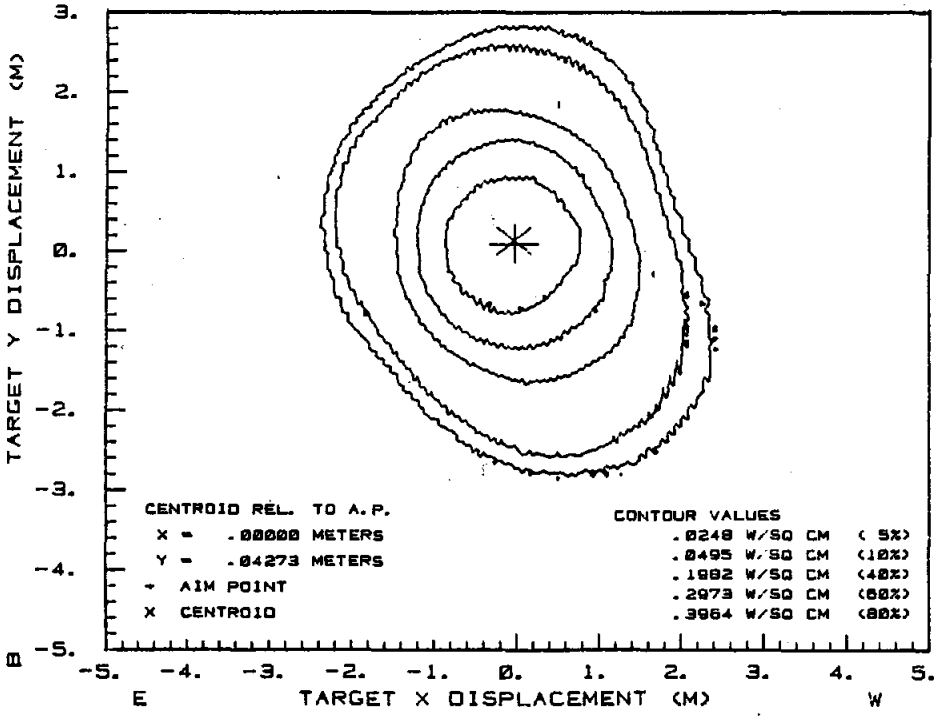

Figure A-7.10. MDAC #2 Beam Quality Data near Solar Noon for an On-Axis Alignment

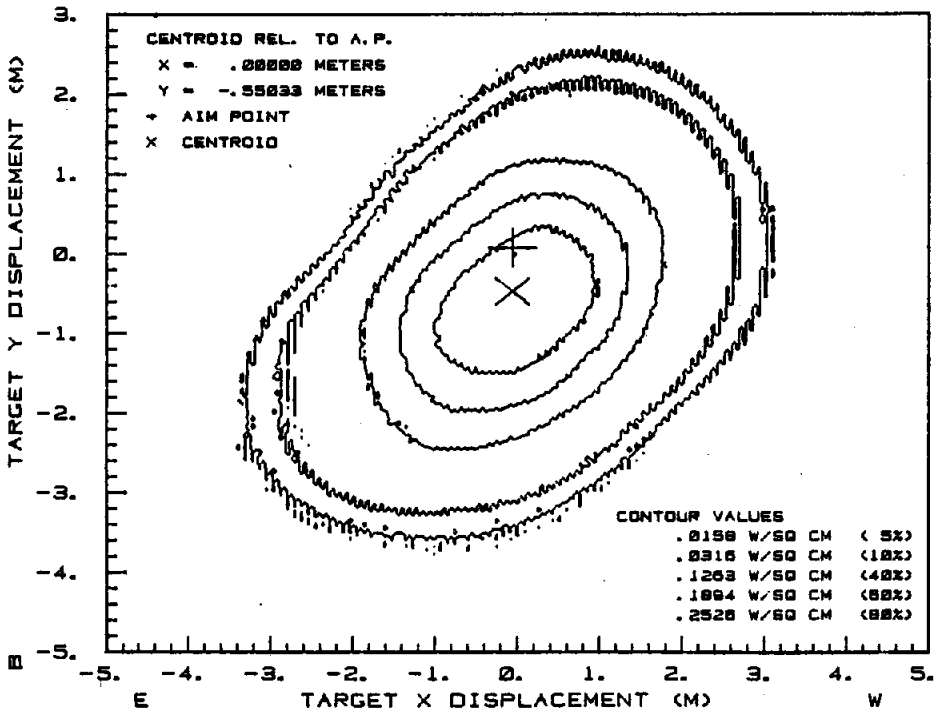

Figure A-7.11. MDAC #2 Beam Quality Data in Afternoon for an On-Axis Alignment

As a result of visual observations that indicated that MDAC Heliostat 2 may have been canted incorrectly in the assembly building, MDAC personnel made several attempts at redoing the on-axis canting after it had been installed in the field. Wind and thermal influences on the pedestal were problems during this recanting and Figure A-7.12 illustrates a BCS measurement with one or more mirror modules canted incorrectly. The measured data previously given for MDAC 2 (Figures A-7.9 through A-7.11) were taken after MDAC personnel were satisfied that it was canted as well as was possible using the inclinometer in the field.

The BCS data in each figure mentioned above give the beam shape in terms of iso-flux density contours on the BCS target. The contours presented are for flux density levels that are at different percentages of the measured peak flux density value.

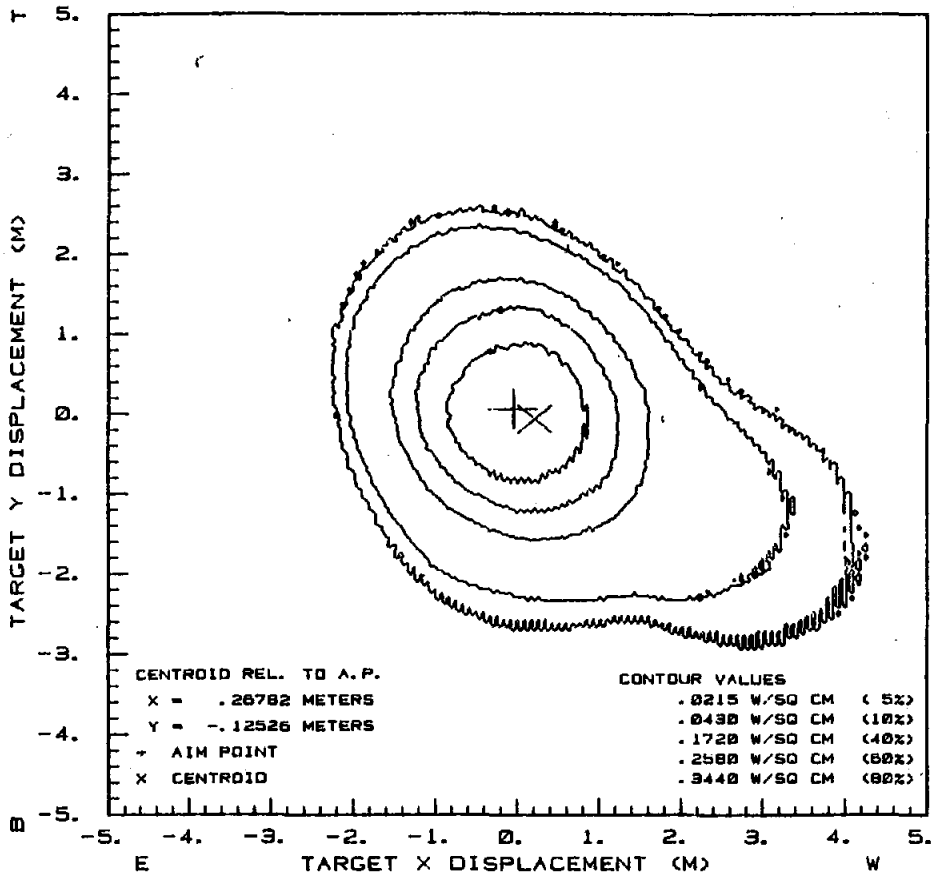

Figure A-7.12. MDAC #2 Heliostat with Mirror Modules Canted Incorrectly

After recanting the MDAC heliostats off-axis as described in Test A-2, BCS beam quality data were again taken at three different times during the day. The results are given in Figures A-7.13 through A-7.18. Additional beam quality data were taken on the MDAC heliostats later in the test period as a means of trying to detect any degradation in beam quality as a result of life cycling and environmental exposure. The results of these BCS measurements are given in Figures A-7.19 through A-7.22.

The MMC heliostats were aligned (canted) in an off-axis manner only, as discussed in Test A-2. A typical beam from one of the MMC heliostats at a time near solar noon can be seen on the BCS target in Figure A-7.23. The results of BCS-measured beam quality data on both of the MMC heliostats at three different times during the day are given in Figures A-7.24 through A-7.29. Additional beam quality data were also taken on the MMC heliostats near the end of the test period in order to assess any performance degradation. These BCS measurements are given in Figures A-7.30 through A-7.33.

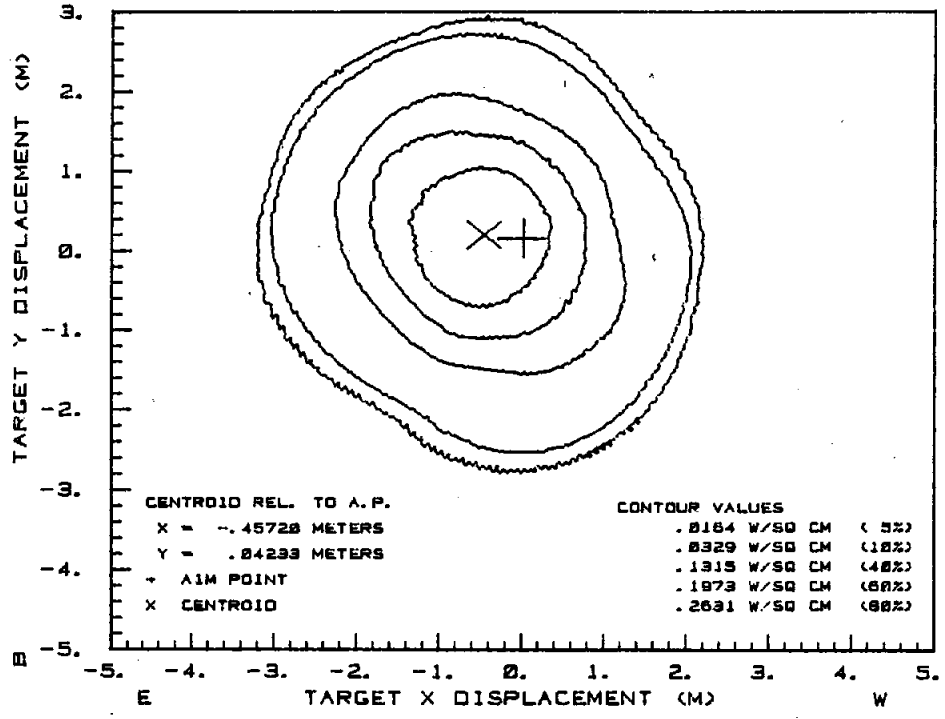

Figure A-7.13. MDAC #1 Beam Quality Data in Morning for an Off-Axis Alignment

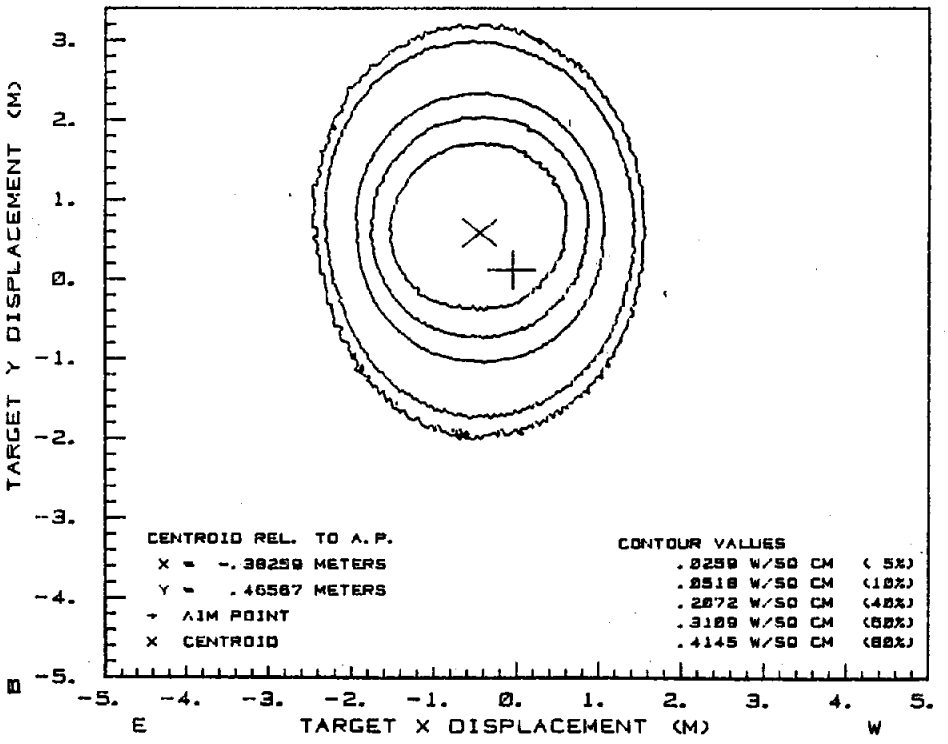

Figure A-7.14. MDAC #1 Beam Quality Data near Solar Noon for an Off-Axis Alignment

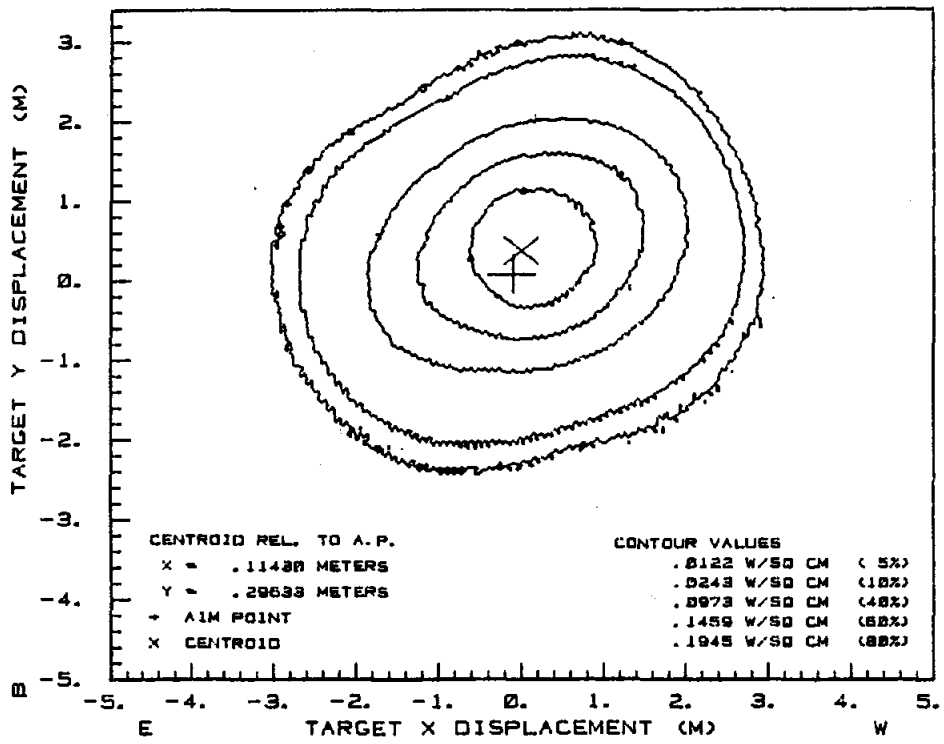

Figure A-7.15. MDAC #1 Beam Quality Data in Afternoon for an Off-Axis Alignment

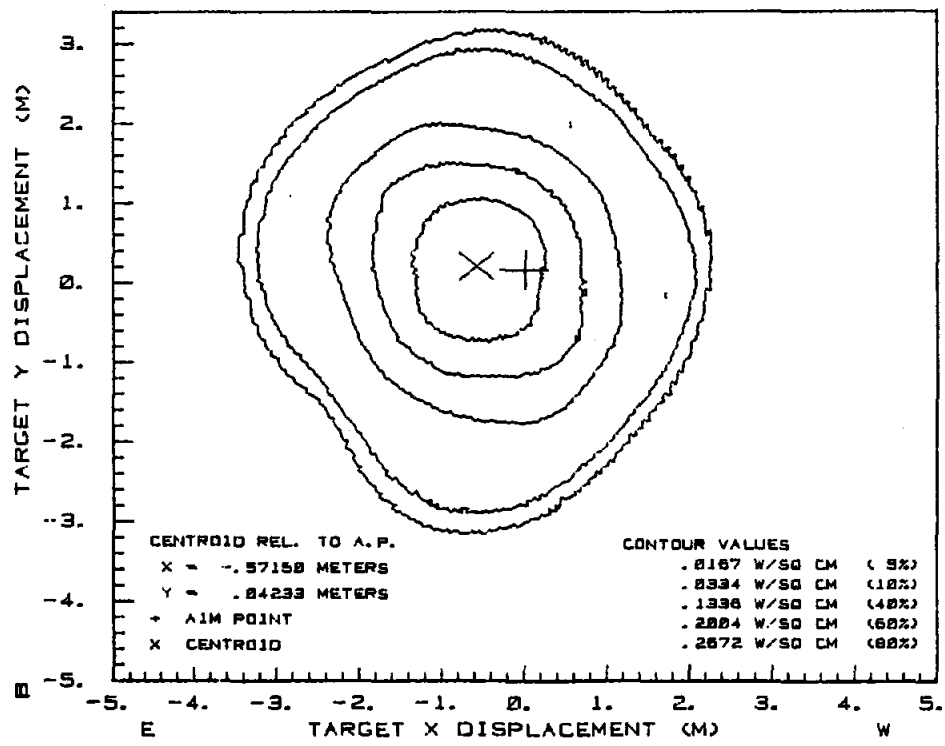

Figure A-7.16. MDAC #2 Beam Quality Data in Morning for an Off-Axis Alignment

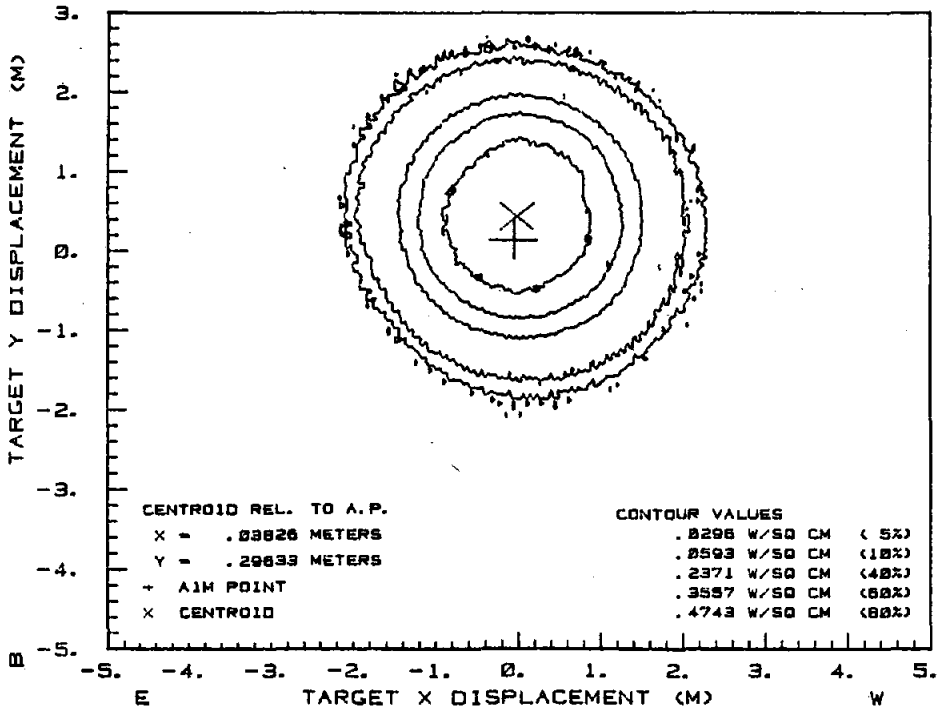

Figure A-7.17. MDAC #2 Beam Quality Data near Solar Noon for an Off-Axis Alignment

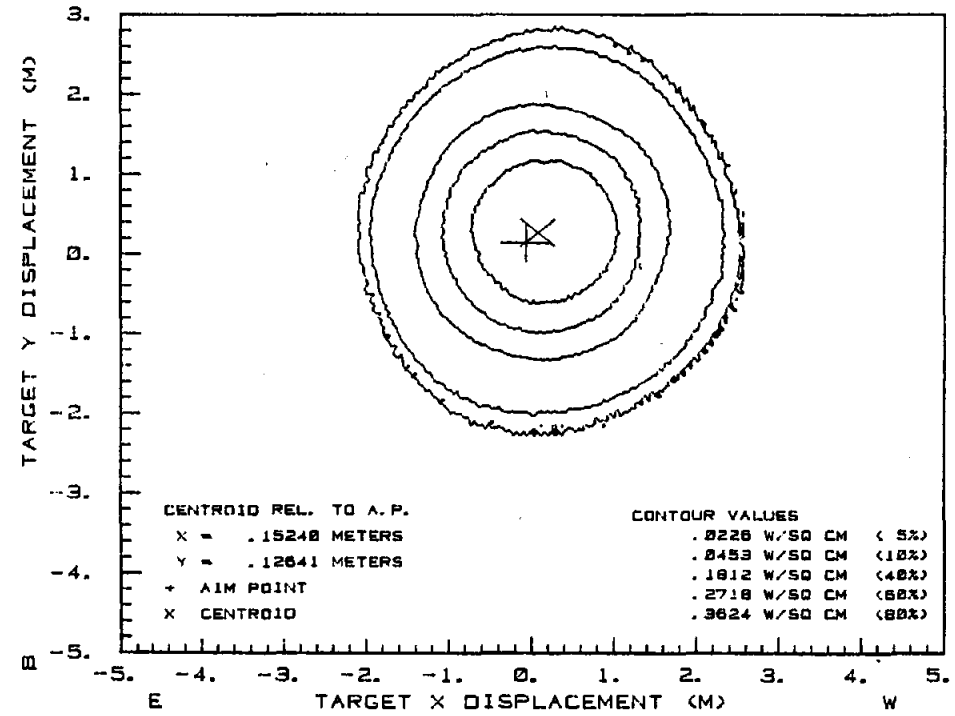

Figure A-7.18. MDAC #2 Beam Quality Data in Afternoon for an Off-Axis Alignment

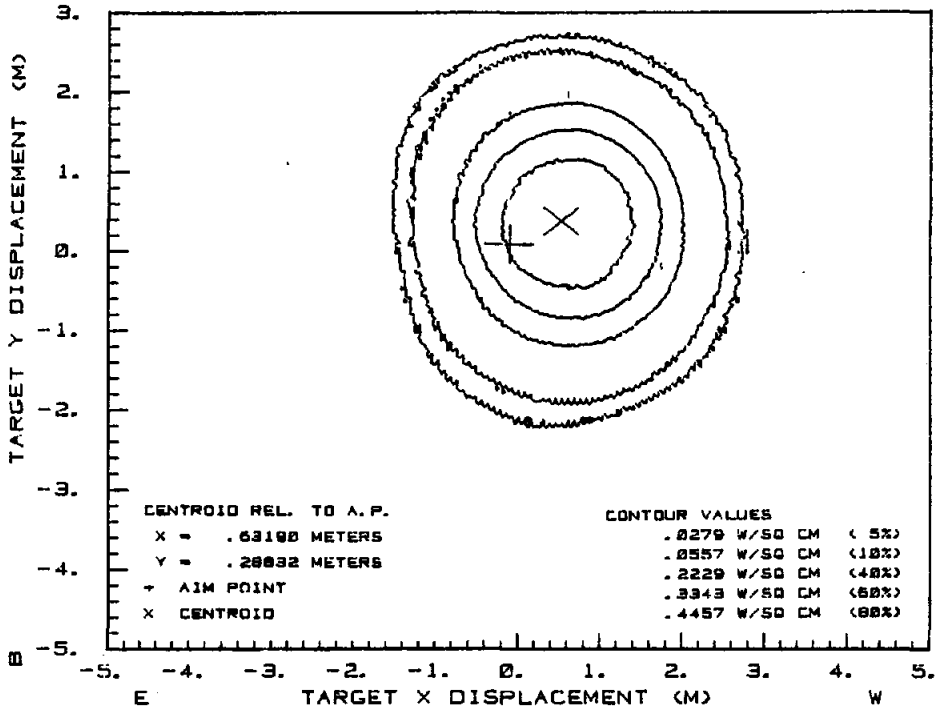

Figure A-7.19. MDAC #1 Beam Quality Data near Solar Noon following Life Cycling

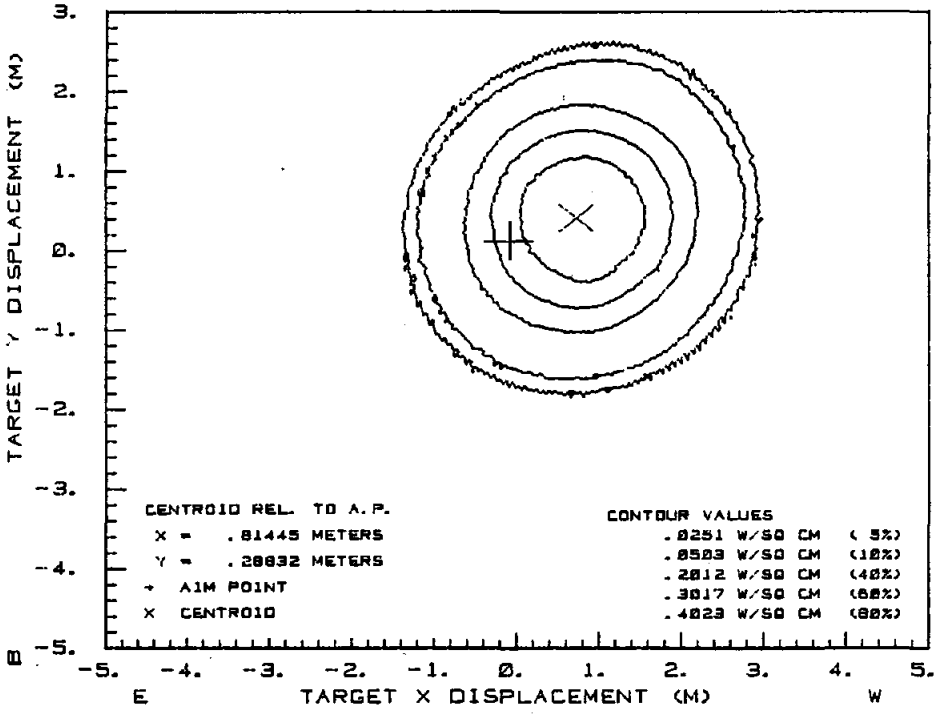

Figure A-7.20. MDAC #1 Beam Quality Data in Afternoon following Life Cycling

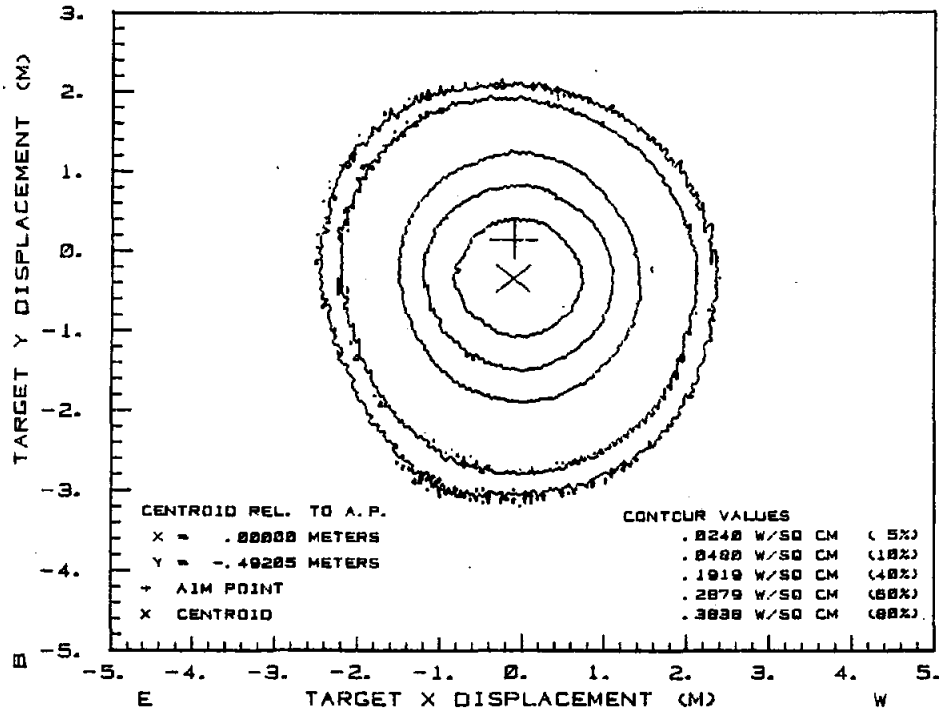

Figure A-7.21. MDAC #1 Beam Quality Data near Solar Noon following Life Cycling

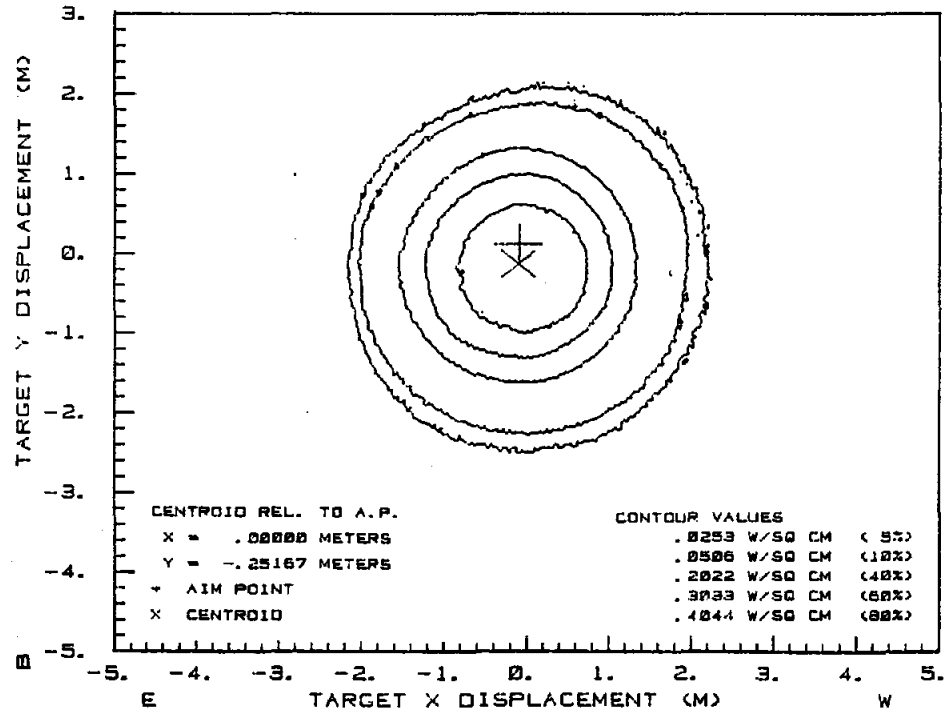

Figure A-7.22. MDAC #2 Beam Quality Data in Afternoon following Life Cycling

Figure A-7.23. Typical Beam from One of the MMC Heliostats near Solar Noon

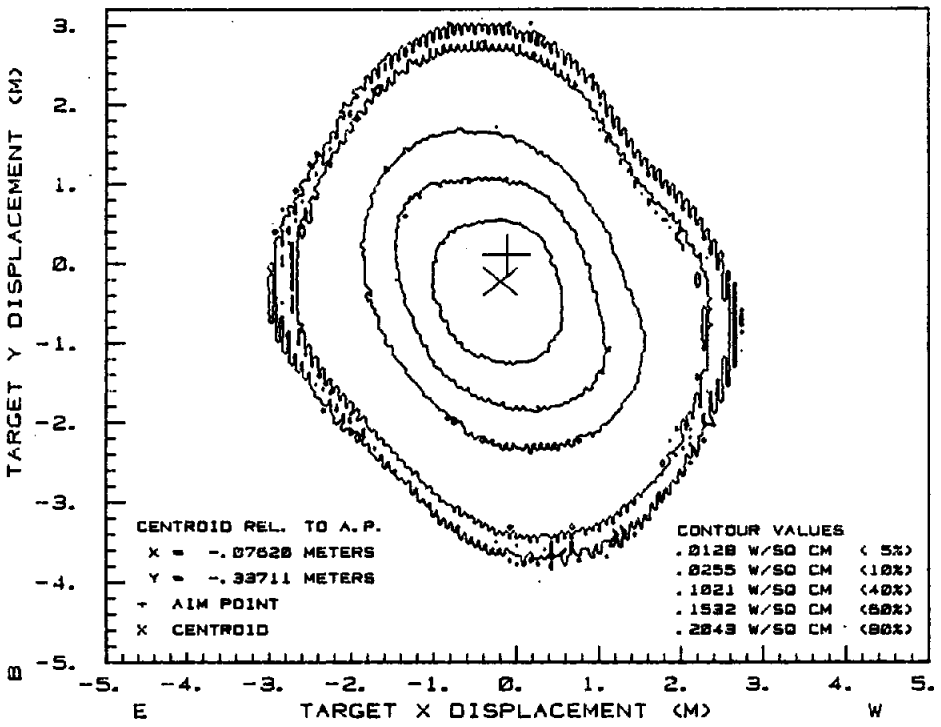

Figure A-7.24. MMC #1 Beam Quality Data in Morning for an Off-Axis Alignment

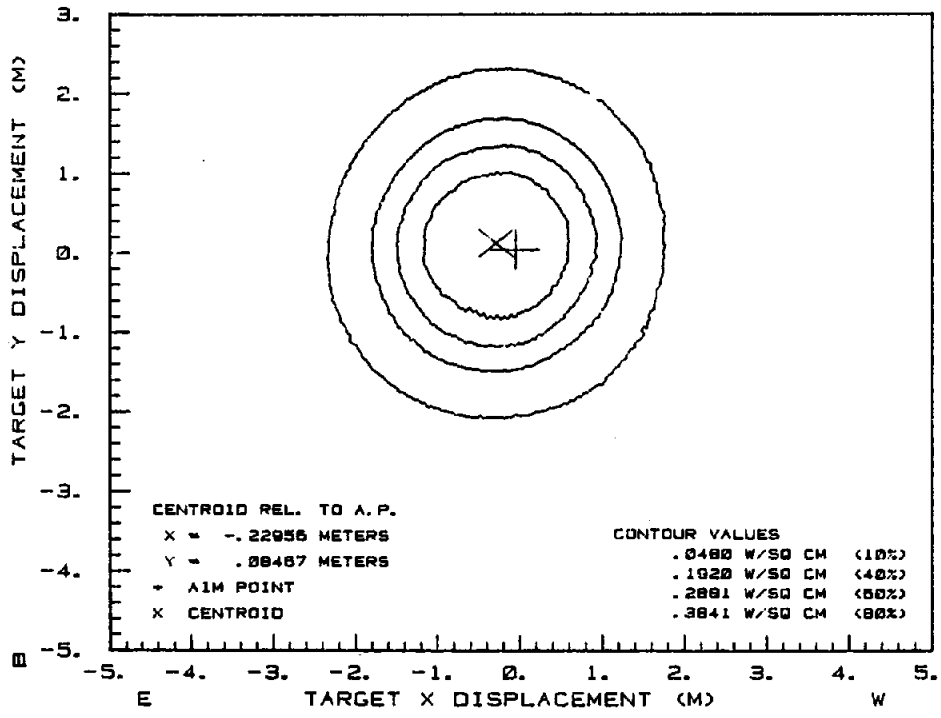

Figure A-7.25. MMC #1 Beam Quality Data near Solar Noon for an Off-Axis Alignment

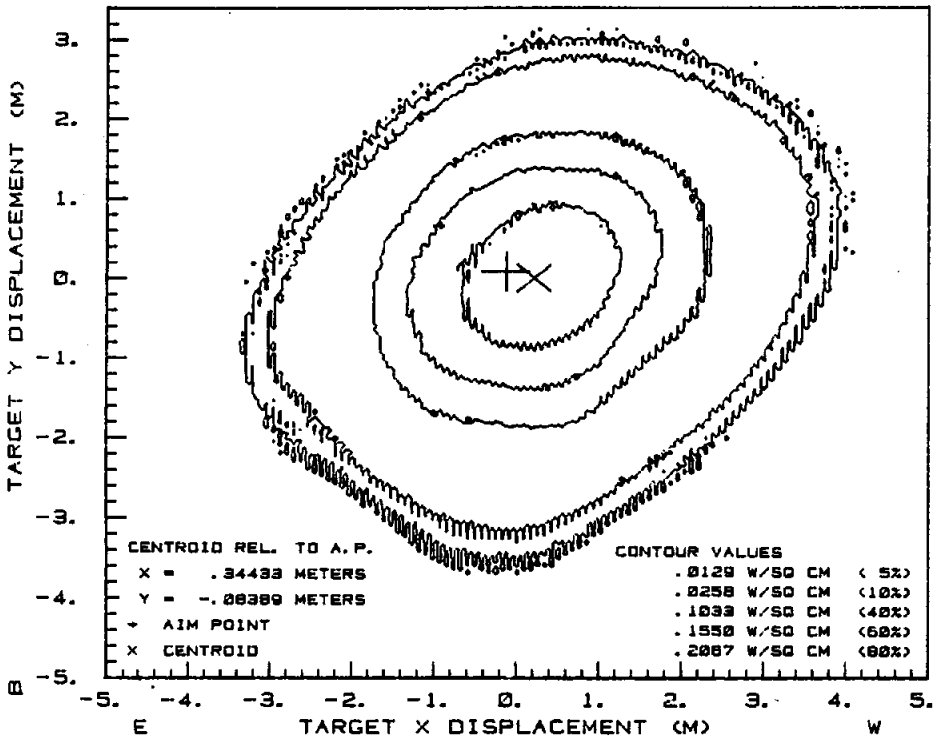

Figure A-7.26. MMC #1 Beam Quality Data in Afternoon for an Off-Axis Alignment

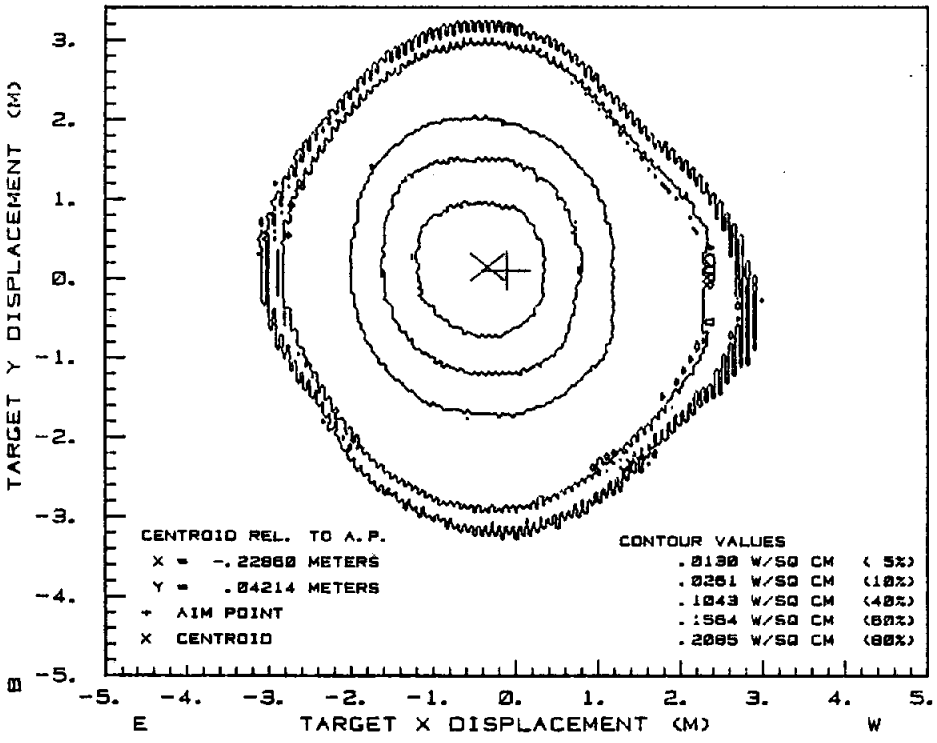

Figure A-7.27. MMC #2 Beam Quality Data in Morning for an Off-Axis Alignment

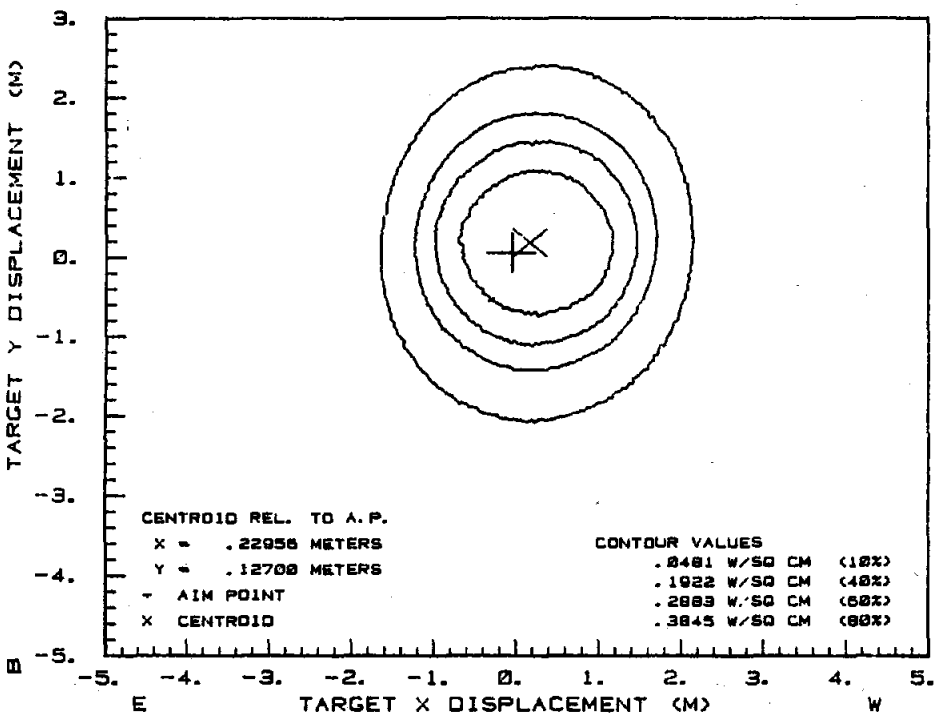

Figure A-7.28. MMC #2 Beam Quality Data near Solar Noon for an Off-Axis Alignment

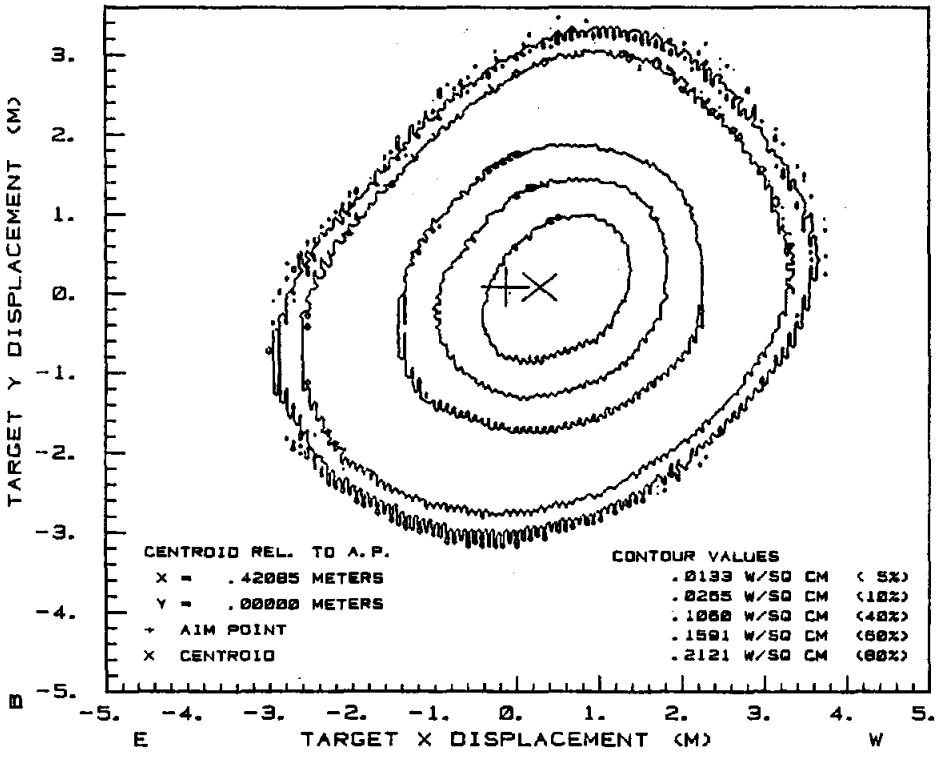

Figure A-7.29. MMC #2 Beam Quality Data in Afternoon for an Off-Axis Alignment

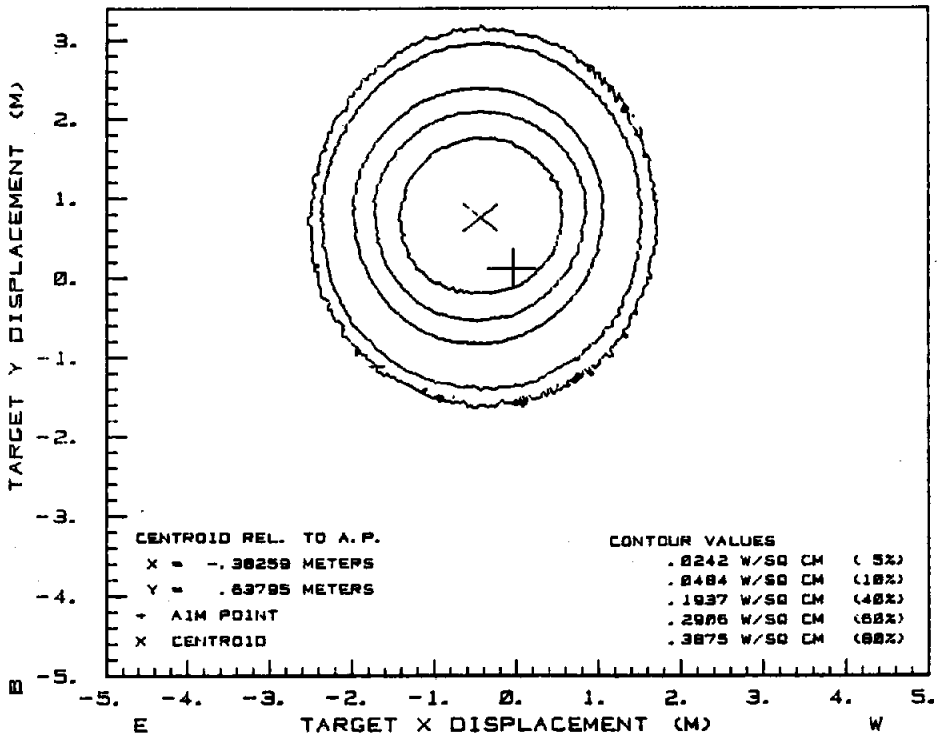

Figure A-7.30. MMC #1 Beam Quality Data near Solar Noon following Life Cycling

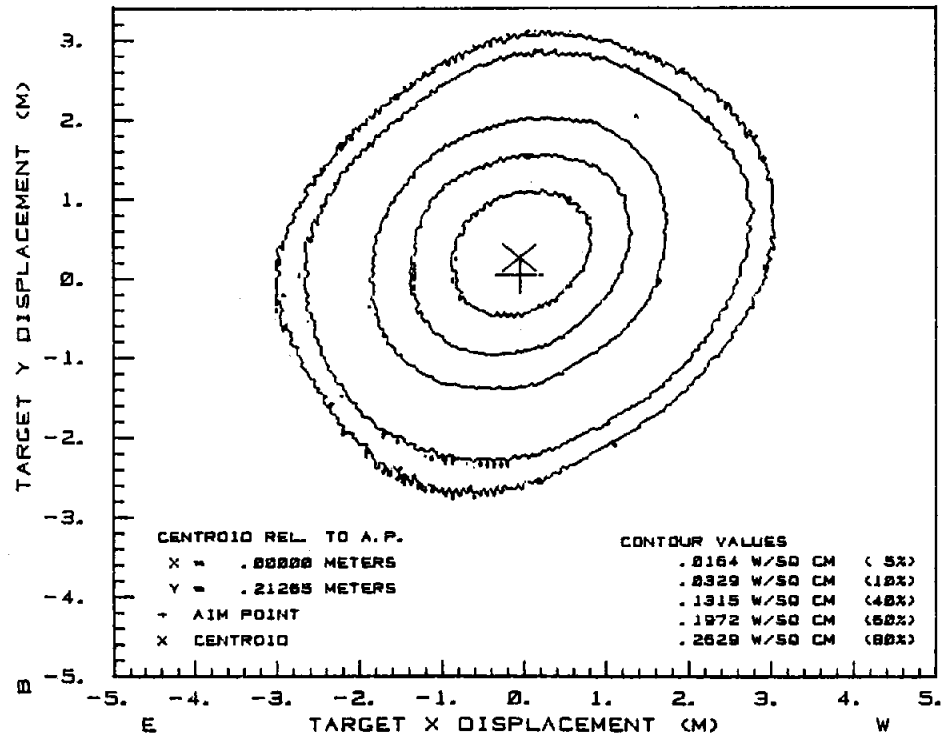

Figure A-7.31. MMC #1 Beam Quality Data in Afternoon following Life Cycling

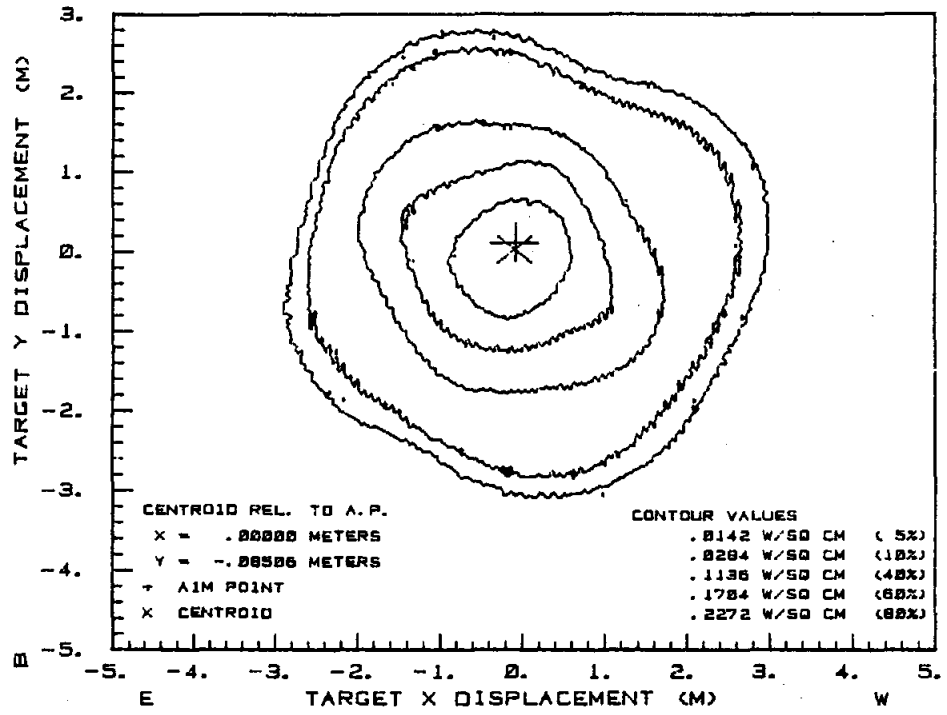

Figure A-7.32. MMC #2 Beam Quality Data in Morning following Life Cycling

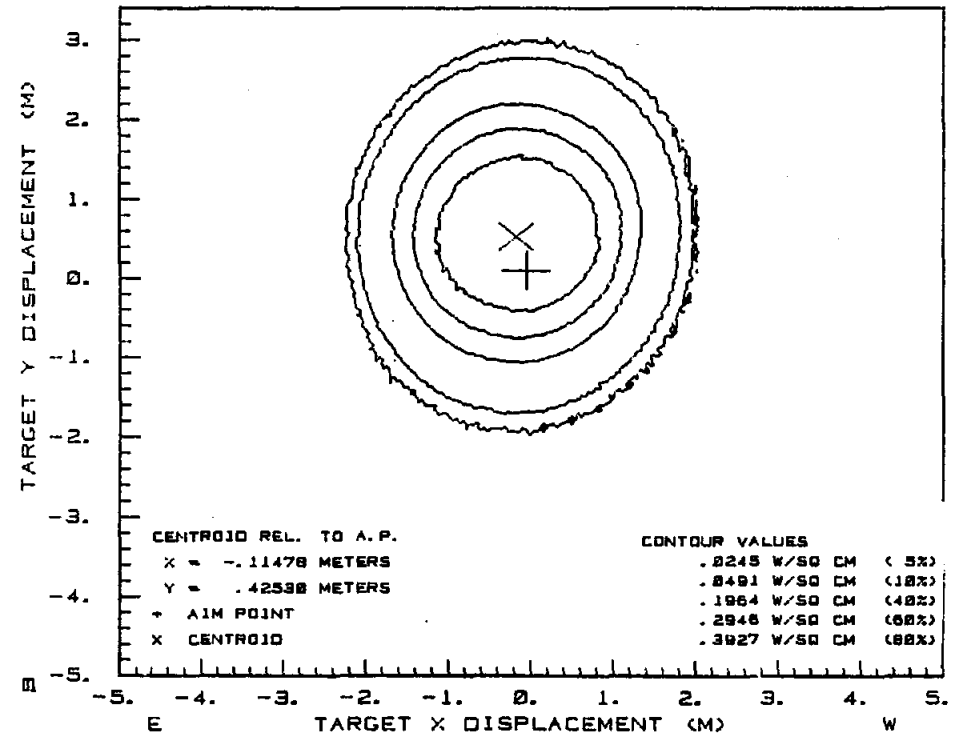

Figure A-7.33. MMC #2 Beam Quality Data near Solar Noon following Life Cycling

In addition to the BCS measurements made during this test, visual observations were also made regarding the optical performance of the test heliostats. During the off-axis canting (Test A-2) of each heliostat, visual observations of the beam quality of individual mirror modules were recorded. The beam images produced by the MMC mirror modules were consistent in size and shape and were well defined spots as can be seen for a typical mirror module in Figure A-2.1 (Test A-2). The aluminum honeycomb core in the MMC mirror modules provided a very stiff mirror module that could not easily be distorted in a manner that would degrade its optical performance.

The beam images produced by the MDAC mirror modules were much less consistent in size and shape and often produced what visually appeared to be separate overlapping images from the same mirror module. This phenomenon was believed to be caused by distortions of the mirror module produced when all four mounting points on each module were bolted to the heliostat crossbeams. The MDAC mirror modules were much more flexible than the MMC modules as a result of the styrofoam core. It was possible to significantly alter the beam size from one of the MDAC mirror modules by selectively pushing on the edges of the module and then tightening the mounting bolts.

Results (HELIOS Analysis)

The beam quality specification, that the MMC and the MDAC heliostats were intended to comply with, was defined in terms of a theoretical contour to which an allowable margin or fringe was added. The theoretical contour was determined with the computer code HELIOS and was defined as the isoflux density contour that contains 90 percent of the power from the heliostat.

The model used in HELIOS to determine the 90-percent contour assumed an error-free heliostat with perfect flat mirror modules of the size supplied by the heliostat manufacturer and the mirror module canting was assumed to be on-axis as planned for the 10-MW_e pilot plant.

A measured clear sky sunshape was used during the determination of the 90-percent contour. The actual specification contour was determined by adding a 1.4-mR fringe to the 90-percent power contour. The size and shape of this specification contour changes for different locations in the heliostat field and for different times of the day or year. The requirement for the pilot plant was that 90 percent of the power from any heliostat in the field be within the specification contour for that heliostat location. This requirement was to be met for any day of the year and for any time of the day when the sun's elevation was greater than 0.26 radian (15 degrees) above the horizon and for ambient temperatures in the range from 0 to 50°C.

When the number of possible combinations of field location, time of year, and ambient temperature conditions at the pilot plant are considered, it can be seen that the beam quality measurements made at the CRTF represented a relatively limited set of conditions. The heliostats at the CRTF were all located essentially north of the receiver at a slant range of approximately 312 meters. Time of year variation was limited to July through September and ambient temperature variation was in the range of 22 to 35°C. As a result of these limitations to the measured beam quality data it was necessary to use the computer code HELIOS, in conjunction with BCS-measured data, in order to

predict heliostat behavior for different field locations, times of the year, and ambient temperatures. A brief description of the analysis technique used is given below.

The HELIOS code is an optical model that treats heliostat characteristics, such as deviations of mirror module curvature from the desired (reference) curvature, mirror waviness, nonspecularity, and mirror canting errors, in a nondeterministic (stochastic) fashion. These parameters are difficult to quantify in a deterministic fashion for an entire heliostat, and an attempt to quantify them for an entire field of heliostats is an impractical task. The HELIOS code lumps these error parameters together in an "error" distribution, that when convolved with the optical response of a "perfect" heliostat, results in a good approximation to the beam images that are measured. Beam measurements can thus be matched with HELIOS by varying the standard deviation of a circular normal error distribution that is statistically convolved in the reflected ray system with the beam distribution produced by the heliostat assuming no errors.

As part of the model in HELIOS each heliostat is defined in terms of its physical dimensions, location relative to the target (use geometry), reference mirror module curvature, mirror module reflectance, and the mirror module canting condition (on-axis or off-axis). For the MMC and the MDAC heliostats the reference mirror module curvature changed with temperature as defined by the data in Figure A-7.1 and the reference mirror module canting conditions for the tests conducted at the CRTF were as given in Table A-2.I (Test A-2).

By obtaining measured beam shapes for as many different time and environmental conditions as possible it was then possible to use HELIOS to determine an error distribution that best characterized the actual optical performance of the heliostat. The error distributions that characterize the actual optical performance of individual heliostats have been found to be reasonably consistent from one heliostat of the same type to the next. The use of this error distribution is therefore a good means for predicting the behavior of the same heliostat for different use geometries, environmental conditions, and times of year. This error distribution can also be used as an estimate of the error distribution that would define the optical response of an entire field of heliostats, provided that tracking error is treated separately from optical performance. This HELIOS analysis technique was used during the analysis of the beam data measured at the CRTF and during the prediction of the performance of the test heliostats under different pilot plant operational conditions.

In matching the BCS-measured data with HELIOS consideration was given to a horizontal slice through the beam, a vertical slice through the beam, and the isoflux density contour that contains 90 percent of the power. This is indicated in the isometric view of one of the measured MMC heliostat beams in Figure A-7.34. A measured beam was considered matched when a good visual comparison between HELIOS and the BCS data was obtained for the two beam slices and the 90-percent contour indicated in this figure. Figure A-7.35 gives the matched data for MMC Heliostat 1 data previously given in Figure A-7.25.

Similar analyses of the other measured cases previously given resulted in the error distribution standard deviations given in Table A-7.I. The values in this table give the standard deviations in milliradians of the circular normal error distributions in the reflected ray reference system that gave a

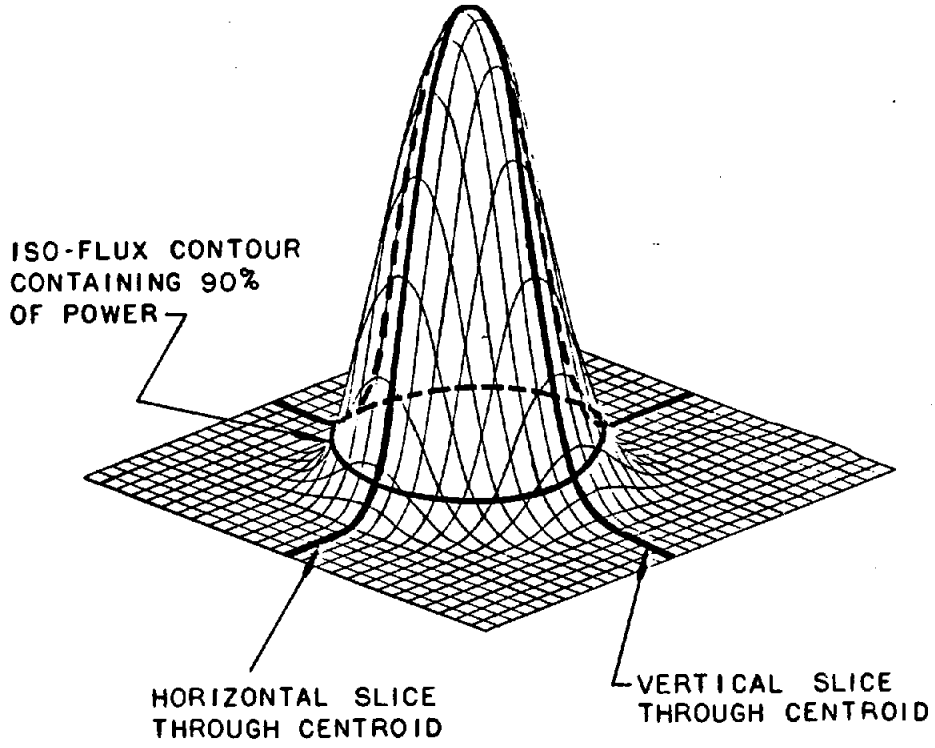

Figure A-7.34. Beam Characteristics Used during BCS/HELIOS Analysis of Measured Data

TABLE A-7.I

HELIOS ERROR DISTRIBUTION STANDARD DEVIATIONS
THAT BEST MATCHED BCS MEASURED BEAM DATA (mR)

Heliostat	On-Axis Cant	Off-Axis Cant
MDAC #1	1.4	1.7
MDAC #2	1.7	1.7
MMC #1	-	1.6
MMC #2	-	1.6

(a)

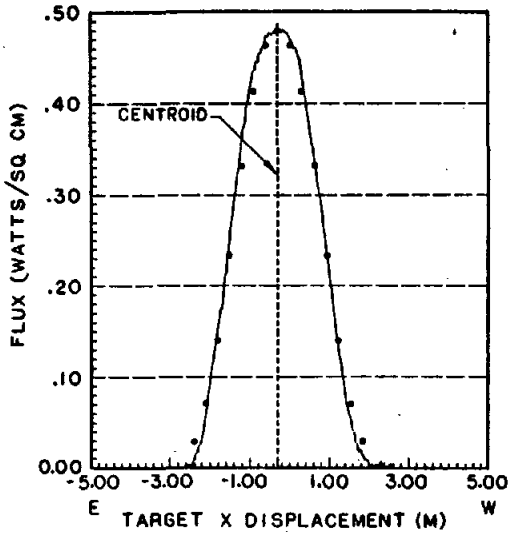

(b)

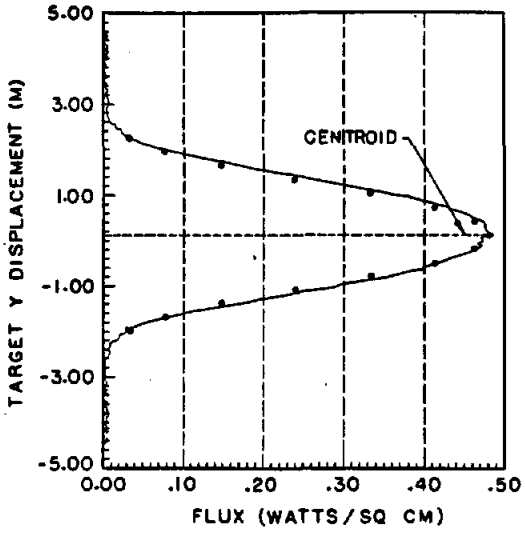

(c)

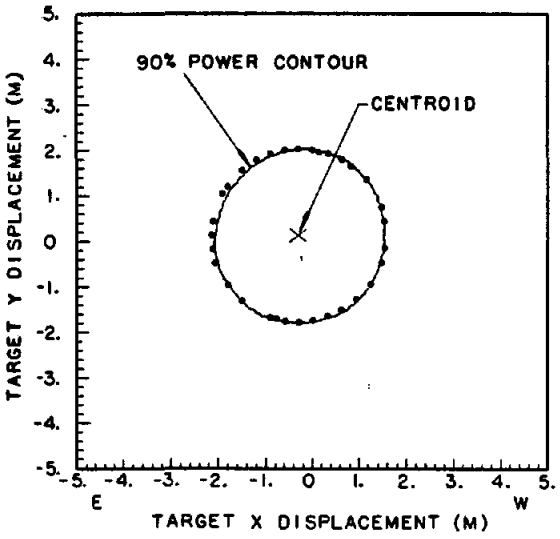

Figure A-7.35. Comparison of MMC #1 BCS and HELIOS Data for (a) a Horizontal Slice and (b) a Vertical Slice through the Beam Centroid, and (c) an Isoflux Density Contour Containing 90% of the Power

reasonable match to the majority of the BCS measured cases for each heliostat. The difference in the standard deviation values for the MDAC 1 vs the MDAC 2 heliostats in the on-axis case are believed to be the result of an attempt by MDAC personnel to recant some of the mirror modules on MDAC 2 in the field by using the same inclinometer procedure used during the initial canting in the assembly building (see Test A-2). Wind and thermal effects that occurred outdoors during canting apparently introduced a higher level of canting error in MDAC 2.

Comparison of the standard deviation values determined for beam measurements before and after life cycling indicated no observable change in beam quality during the three-month test period at the CRTF for either the MDAC or the MMC heliostats.

Since the values in Table A-7.I provided a reasonably good match to the majority of the BCS measurements, it was then possible to predict the behavior of the test heliostats for any desired use geometry, time of year, or environmental condition at the pilot plant. It should also be noted that the values obtained in Table A-7.I were for heliostats canted using the procedures described in Test A-2.

It is believed that a production canting procedure as intended for the pilot plant should be at least as good, if not better than the procedures used at the CRTF. In that sense the values in Table A-7.I may provide slightly conservative predictions. More than 1800 heliostats will be installed at the pilot plant, therefore an attempt to use HELIOS to determine if every heliostat for every location, sun position, temperature, etc. would meet the beam quality specification was impractical. The approach used during HELIOS analysis was to predict performance of the heliostats under what was believed to be worst case conditions. If the predicted performance of the heliostats under these conditions met the specification then it was assumed that they would better than meet the specification for other use conditions.

The worst case location was assumed to be the longest slant range location expected at the pilot plant since the overall beam size from a heliostat at that location would be the largest and result in the highest percentage of spillage off the receiver. For this analysis the longest slant range heliostat was assumed to be 400 meters north of a target (receiver) located 79 meters high and tilted north such that the incoming heliostat beam was perpendicular to the target plane.

For the heliostats tested, the predominant parameter influencing the overall beam size was the curvature of the individual mirror modules and this curvature varied as a function of temperature. The worst case ambient conditions were therefore assumed to be the limits of the specification temperature range 0°C and 50°C. At 0°C the mirror modules have the least curvature (longest focal length) and at 50°C they have the greatest curvature (shortest focal length). Optical aberration and the resulting increase in beam size is most predominant for conditions with a large angle of incidence between the sun's rays and the mirrors on the heliostat. Worst case optical conditions were therefore assumed to occur on the winter solstice and the summer solstice and either in the morning or afternoon.

The NASTRAN predictions (Test A-1) of gravity influence on mirror module canting were also used in this analysis to predict the resulting influence on beam quality. Tables A-7.II and A-7.III give the NASTRAN-predicted unit normal components for the unit normal vector to each mirror module on the MDAC and the MMC heliostats, respectively. The unit vector components are given for different elevation angles of the heliostat and the heliostat is assumed to be pointing south in azimuth. In the NASTRAN model all the mirror modules were assumed to be in the same plane (no mirror canting), therefore, the values in these tables can be used to determine the changes in the mirror module normal vectors as a result of gravity influence at different elevation angles of the heliostat. For example, in Table A-7.II for Mirror Module 1 at an elevation angle of 15 degrees the NASTRAN-predicted components of the unit normal are (0.000318, -0.966016, 0.258483). With no gravity influence and for a mirror module at an elevation angle of 15 degrees the unit normal components can be calculated to be (0., -0.965926, 0.258819). These components are in a coordinate system with x being east, y north, and z vertical. The NASTRAN data thus indicate that the mirror normal has sagged slightly downward and inward to the east. In the NASTRAN analysis gravity sag was assumed to be compensated for at an elevation angle of 45 degrees, as can be seen in Tables A-7.II and A-7.III. Worst case gravity conditions were assumed to occur at the largest and the smallest elevation angles of the heliostat since the effects of gravity at the mid-elevation angles ($\pm$ 45 degrees) are compensated for during the canting procedure. Mirror canting for the pilot plant was assumed to be on-axis with all the heliostats canted for an effective heliostat focal length of 400 meters.

Using the Sandia-measured mirror module vs temperature data in Figure A-7.1 and the error distributions in Table A-7.I that were unfolded from BCS-measured data, several worst case conditions were run using HELIOS for both the MMC and the MDAC heliostats. Figures A-7.36 and A-7.37 give results for the MMC heliostat design.

Each figure shows three isoflux density contours. One of the contours represents the specification contour for the case being considered. The second contour is the HELIOS-predicted contour assuming no gravity influence. The third contour is the HELIOS-predicted contour assuming gravity influence as predicted by the NASTRAN code. The four MMC cases indicated are for a heliostat located 400 m north of a target that is 79 m high and tilted north such that the incident heliostat beam is perpendicular to the target plane. It can be seen from these figures that the predicted performance of the MMC heliostats successfully met the specification for all the worst case conditions considered, except the late afternoon condition on the summer solstice (Day 172) shown in Figure A-7.36. For this large angle of incidence and high temperature condition the focal length of the mirror modules is too short and the resulting beam shape is severely aberrated. The specification was met at noon as also shown in Figure A-7.36. The influence of gravity loading at different heliostat elevation angles in degrading the beam quality of the MMC heliostats can be seen to be relatively small. Either a slight broadening or a narrowing of the beam shape as a result of gravity is possible depending on the elevation angle of the heliostat and the use geometry.

TABLE A-7.II

NASTRAN-PREDICTED GRAVITY INFLUENCE DATA ON THE MDAC HELIOSTAT

Module	Elevation (deg)	Unit Normal x	y	z
1	0.0000MDAC NORM	.486705E-03	-.100000E+01	-.506000E-03
2	0.0000MDAC NORM	-.486207E-03	-.100000E+01	-.505849E-03
3	0.0000MDAC NORM	.447154E-03	-.100000E+01	-.292132E-03
4	0.0000MDAC NORM	-.447256E-03	-.100000E+01	-.292168E-03
5	0.0000MDAC NORM	.420892E-03	-.100000E+01	-.224500E-03
6	0.0000MDAC NORM	-.420860E-03	-.100000E+01	-.224526E-03
7	0.0000MDAC NORM	.402390E-03	-.100000E+01	.903416E-04
8	0.0000MDAC NORM	-.402393E-03	-.100000E+01	.902985E-04
9	0.0000MDAC NORM	.399356E-03	-.100000E+01	.164787E-03
10	0.0000MDAC NORM	-.399250E-03	-.100000E+01	.164751E-03
11	0.0000MDAC NORM	.410135E-03	-.100000E+01	.357839E-03
12	0.0000MDAC NORM	-.410639E-03	-.100000E+01	.358055E-03
1	15.0000MDAC NORM	.318061E-03	-.966016E+00	.258483E+00
2	15.0000MDAC NORM	-.317746E-03	-.966016E+00	.258483E+00
3	15.0000MDAC NORM	.289470E-03	-.965980E+00	.258617E+00
4	15.0000MDAC NORM	-.289535E-03	-.965980E+00	.258617E+00
5	15.0000MDAC NORM	.269150E-03	-.965969E+00	.258657E+00
6	15.0000MDAC NORM	-.269126E-03	-.965969E+00	.258657E+00
7	15.0000MDAC NORM	.252804E-03	-.965918E+00	.258850E+00
8	15.0000MDAC NORM	-.252803E-03	-.965918E+00	.258850E+00
9	15.0000MDAC NORM	.247206E-03	-.965905E+00	.258896E+00
10	15.0000MDAC NORM	-.247139E-03	-.965905E+00	.258896E+00
11	15.0000MDAC NORM	.250523E-03	-.965874E+00	.259012E+00
12	15.0000MDAC NORM	-.250843E-03	-.965874E+00	.259012E+00
1	30.0000MDAC NORM	.152043E-03	-.866103E+00	.499865E+00
2	30.0000MDAC NORM	-.151898E-03	-.866103E+00	.499865E+00
3	30.0000MDAC NORM	.136943E-03	-.866071E+00	.499921E+00
4	30.0000MDAC NORM	-.136973E-03	-.866071E+00	.499921E+00
5	30.0000MDAC NORM	.125581E-03	-.866061E+00	.499938E+00
6	30.0000MDAC NORM	-.125568E-03	-.866061E+00	.499938E+00
7	30.0000MDAC NORM	.115546E-03	-.866015E+00	.500018E+00
8	30.0000MDAC NORM	-.115544E-03	-.866015E+00	.500018E+00
9	30.0000MDAC NORM	.110984E-03	-.866004E+00	.500037E+00
10	30.0000MDAC NORM	-.110952E-03	-.866004E+00	.500037E+00
11	30.0000MDAC NORM	.110624E-03	-.865977E+00	.500084E+00
12	30.0000MDAC NORM	-.110772E-03	-.865977E+00	.500084E+00
1	45.0000MDAC NORM	0.	-.707107E+00	.707107E+00
2	45.0000MDAC NORM	0.	-.707107E+00	.707107E+00
3	45.0000MDAC NORM	0.	-.707107E+00	.707107E+00
4	45.0000MDAC NORM	0.	-.707107E+00	.707107E+00
5	45.0000MDAC NORM	0.	-.707107E+00	.707107E+00
6	45.0000MDAC NORM	0.	-.707107E+00	.707107E+00
7	45.0000MDAC NORM	0.	-.707107E+00	.707107E+00
8	45.0000MDAC NORM	0.	-.707107E+00	.707107E+00
9	45.0000MDAC NORM	0.	-.707107E+00	.707107E+00
10	45.0000MDAC NORM	0.	-.707107E+00	.707107E+00
11	45.0000MDAC NORM	0.	-.707107E+00	.707107E+00
12	45.0000MDAC NORM	0.	-.707107E+00	.707107E+00

Module	Elevation (deg)	Unit Normal x	y	z
1	60.0000MDAC NORM	-.127726E-03	-.499879E+00	.866095E+00
2	60.0000MDAC NORM	.127616E-03	-.499879E+00	.866095E+00
3	60.0000MDAC NORM	-.112046E-03	-.499925E+00	.866069E+00
4	60.0000MDAC NORM	.112068E-03	-.499925E+00	.866069E+00
5	60.0000MDAC NORM	-.990518E-04	-.499937E+00	.866062E+00
6	60.0000MDAC NORM	.990378E-04	-.499937E+00	.866062E+00
7	60.0000MDAC NORM	-.859775E-04	-.499998E+00	.866026E+00
8	60.0000MDAC NORM	.859715E-04	-.499998E+00	.866026E+00
9	60.0000MDAC NORM	-.781980E-04	-.500014E+00	.866017E+00
10	60.0000MDAC NORM	.781733E-04	-.500014E+00	.866017E+00
11	60.0000MDAC NORM	-.738265E-04	-.500047E+00	.865998E+00
12	60.0000MDAC NORM	.739409E-04	-.500047E+00	.865998E+00
1	75.0000MDAC NORM	-.222433E-03	-.258570E+00	.965992E+00
2	75.0000MDAC NORM	.222254E-03	-.258570E+00	.965992E+00
3	75.0000MDAC NORM	-.191559E-03	-.258657E+00	.965969E+00
4	75.0000MDAC NORM	.191594E-03	-.258657E+00	.965969E+00
5	75.0000MDAC NORM	-.164825E-03	-.258677E+00	.965964E+00
6	75.0000MDAC NORM	.164797E-03	-.258677E+00	.965964E+00
7	75.0000MDAC NORM	-.136528E-03	-.258788E+00	.965934E+00
8	75.0000MDAC NORM	.136512E-03	-.258788E+00	.965934E+00
9	75.0000MDAC NORM	-.118282E-03	-.258818E+00	.965926E+00
10	75.0000MDAC NORM	.118241E-03	-.258818E+00	.965926E+00
11	75.0000MDAC NORM	-.105824E-03	-.258875E+00	.965911E+00
12	75.0000MDAC NORM	.106012E-03	-.258875E+00	.965911E+00
1	90.0000MDAC NORM	-.277662E-03	.343046E-03	.100000E+01
2	90.0000MDAC NORM	.277461E-03	.343049E-03	.100000E+01
3	90.0000MDAC NORM	-.233118E-03	.233896E-03	.100000E+01
4	90.0000MDAC NORM	.233157E-03	.233912E-03	.100000E+01
5	90.0000MDAC NORM	-.192835E-03	.212704E-03	.100000E+01
6	90.0000MDAC NORM	.192794E-03	.212697E-03	.100000E+01
7	90.0000MDAC NORM	-.148202E-03	.822767E-04	.100000E+01
8	90.0000MDAC NORM	.148176E-03	.823119E-04	.100000E+01
9	90.0000MDAC NORM	-.117516E-03	.446382E-04	.100000E+01
10	90.0000MDAC NORM	.117469E-03	.446520E-04	.100000E+01
11	90.0000MDAC NORM	-.938104E-04	-.146968E-04	.100000E+01
12	90.0000MDAC NORM	.940242E-04	-.148518E-04	.100000E+01
1	105.0000MDAC NORM	-.289650E-03	.259182E+00	.965828E+00
2	105.0000MDAC NORM	.289476E-03	.259182E+00	.965828E+00
3	105.0000MDAC NORM	-.233891E-03	.259077E+00	.965856E+00
4	105.0000MDAC NORM	.233923E-03	.259077E+00	.965856E+00
5	105.0000MDAC NORM	-.181174E-03	.259063E+00	.965860E+00
6	105.0000MDAC NORM	.181120E-03	.259063E+00	.965860E+00
7	105.0000MDAC NORM	-.120208E-03	.258952E+00	.965890E+00
8	105.0000MDAC NORM	.120167E-03	.258952E+00	.965890E+00
9	105.0000MDAC NORM	-.759559E-04	.258916E+00	.965900E+00
10	105.0000MDAC NORM	.759120E-04	.258916E+00	.965900E+00
11	105.0000MDAC NORM	-.386057E-04	.258877E+00	.965910E+00
12	105.0000MDAC NORM	.387977E-04	.258877E+00	.965910E+00

TABLE A-7.III

NASTRAN-PREDICTED GRAVITY INFLUENCE DATA ON THE MMC HELIOSTAT

Module	Elevation (deg)		Unit Normal x	Unit Normal y	Unit Normal z
1	0.0000MMC	NORM	.315001E-03	-.100000E+01	-.121835E-03
2	0.0000MMC	NORM	-.320677E-03	-.100000E+01	-.129673E-03
3	0.0000MMC	NORM	.373977E-03	-.100000E+01	-.109296E-03
4	0.0000MMC	NORM	-.374317E-03	-.100000E+01	-.117455E-03
5	0.0000MMC	NORM	.465702E-03	-.100000E+01	.116817E-04
6	0.0000MMC	NORM	-.412989E-03	-.100000E+01	.303524E-05
7	0.0000MMC	NORM	.564566E-03	-.100000E+01	.233618E-03
8	0.0000MMC	NORM	-.414669E-03	-.100000E+01	.224980E-03
9	0.0000MMC	NORM	.668542E-03	-.100000E+01	.347856E-03
10	0.0000MMC	NORM	-.468277E-03	-.100000E+01	.339619E-03
11	0.0000MMC	NORM	.734255E-03	-.100000E+01	.342498E-03
12	0.0000MMC	NORM	-.536333E-03	-.100000E+01	.334294E-03
1	15.0000MMC	NORM	.202886E-03	-.965947E+00	.258740E+00
2	15.0000MMC	NORM	-.211814E-03	-.965948E+00	.258736E+00
3	15.0000MMC	NORM	.237171E-03	-.965945E+00	.258749E+00
4	15.0000MMC	NORM	-.241818E-03	-.965946E+00	.258745E+00
5	15.0000MMC	NORM	.296643E-03	-.965922E+00	.258832E+00
6	15.0000MMC	NORM	-.263833E-03	-.965924E+00	.258827E+00
7	15.0000MMC	NORM	.351659E-03	-.965887E+00	.258963E+00
8	15.0000MMC	NORM	-.259283E-03	-.965889E+00	.258959E+00
9	15.0000MMC	NORM	.416544E-03	-.965870E+00	.259027E+00
10	15.0000MMC	NORM	-.294843E-03	-.965871E+00	.259023E+00
11	15.0000MMC	NORM	.454742E-03	-.965872E+00	.259023E+00
12	15.0000MMC	NORM	-.335160E-03	-.965873E+00	.259019E+00
1	30.0000MMC	NORM	.954476E-04	-.866048E+00	.499961E+00
2	30.0000MMC	NORM	-.102439E-03	-.866049E+00	.499959E+00
3	30.0000MMC	NORM	.109617E-03	-.866045E+00	.499966E+00
4	30.0000MMC	NORM	-.114148E-03	-.866046E+00	.499964E+00
5	30.0000MMC	NORM	.137804E-03	-.866023E+00	.500004E+00
6	30.0000MMC	NORM	-.122973E-03	-.866024E+00	.500002E+00
7	30.0000MMC	NORM	.159100E-03	-.865993E+00	.500056E+00
8	30.0000MMC	NORM	-.117850E-03	-.865994E+00	.500055E+00
9	30.0000MMC	NORM	.188522E-03	-.865979E+00	.500080E+00
10	30.0000MMC	NORM	-.135126E-03	-.865980E+00	.500078E+00
11	30.0000MMC	NORM	.204307E-03	-.865981E+00	.500077E+00
12	30.0000MMC	NORM	-.152231E-03	-.865982E+00	.500076E+00
1	45.0000MMC	NORM	0.	-.707107E+00	.707107E+00
2	45.0000MMC	NORM	0.	-.707107E+00	.707107E+00
3	45.0000MMC	NORM	0.	-.707107E+00	.707107E+00
4	45.0000MMC	NORM	0.	-.707107E+00	.707107E+00
5	45.0000MMC	NORM	0.	-.707107E+00	.707107E+00
6	45.0000MMC	NORM	0.	-.707107E+00	.707107E+00
7	45.0000MMC	NORM	0.	-.707107E+00	.707107E+00
8	45.0000MMC	NORM	0.	-.707107E+00	.707107E+00
9	45.0000MMC	NORM	0.	-.707107E+00	.707107E+00
10	45.0000MMC	NORM	0.	-.707107E+00	.707107E+00
11	45.0000MMC	NORM	0.	-.707107E+00	.707107E+00
12	45.0000MMC	NORM	0.	-.707107E+00	.707107E+00
1	60.0000MMC	NORM	-.769509E-04	-.499959E+00	.866049E+00
2	60.0000MMC	NORM	.885210E-04	-.499959E+00	.866049E+00
3	60.0000MMC	NORM	-.842085E-04	-.499965E+00	.866046E+00
4	60.0000MMC	NORM	.928453E-04	-.499964E+00	.866046E+00
5	60.0000MMC	NORM	-.107376E-03	-.500003E+00	.866024E+00
6	60.0000MMC	NORM	.967048E-04	-.500002E+00	.866024E+00
7	60.0000MMC	NORM	-.114798E-03	-.500038E+00	.866003E+00
8	60.0000MMC	NORM	.862339E-04	-.500038E+00	.866003E+00
9	60.0000MMC	NORM	-.136172E-03	-.500050E+00	.865996E+00
10	60.0000MMC	NORM	.101325E-03	-.500050E+00	.865996E+00
11	60.0000MMC	NORM	-.144253E-03	-.500047E+00	.865998E+00
12	60.0000MMC	NORM	.111156E-03	-.500047E+00	.865998E+00
1	75.0000MMC	NORM	-.130163E-03	-.258718E+00	.965953E+00
2	75.0000MMC	NORM	.157094E-03	-.258719E+00	.965953E+00
3	75.0000MMC	NORM	-.137272E-03	-.258731E+00	.965949E+00
4	75.0000MMC	NORM	.158064E-03	-.258732E+00	.965949E+00
5	75.0000MMC	NORM	-.177010E-03	-.258813E+00	.965927E+00
6	75.0000MMC	NORM	.160554E-03	-.258813E+00	.965927E+00
7	75.0000MMC	NORM	-.177472E-03	-.258871E+00	.965912E+00
8	75.0000MMC	NORM	.134977E-03	-.258871E+00	.965912E+00
9	75.0000MMC	NORM	-.210717E-03	-.258884E+00	.965908E+00
10	75.0000MMC	NORM	.161945E-03	-.258885E+00	.965908E+00
11	75.0000MMC	NORM	-.218625E-03	-.258875E+00	.965910E+00
12	75.0000MMC	NORM	.173666E-03	-.258876E+00	.965910E+00
1	90.0000MMC	NORM	-.156007E-03	.160740E-03	.100000E+01
2	90.0000MMC	NORM	.201043E-03	.157015E-03	.100000E+01
3	90.0000MMC	NORM	-.155570E-03	.139077E-03	.100000E+01
4	90.0000MMC	NORM	.191206E-03	.135963E-03	.100000E+01
5	90.0000MMC	NORM	-.204150E-03	.193566E-04	.100000E+01
6	90.0000MMC	NORM	.187190E-03	.172940E-04	.100000E+01
7	90.0000MMC	NORM	-.183745E-03	-.359347E-04	.100000E+01
8	90.0000MMC	NORM	.142903E-03	-.380576E-04	.100000E+01
9	90.0000MMC	NORM	-.218548E-03	-.343962E-04	.100000E+01
10	90.0000MMC	NORM	.177725E-03	-.376025E-04	.100000E+01
11	90.0000MMC	NORM	-.218039E-03	-.205685E-04	.100000E+01
12	90.0000MMC	NORM	.183262E-03	-.238430E-04	.100000E+01
1	105.0000MMC	NORM	-.152721E-03	.259018E+00	.965872E+00
2	105.0000MMC	NORM	.217372E-03	.259011E+00	.965874E+00
3	105.0000MMC	NORM	-.137855E-03	.258991E+00	.965880E+00
4	105.0000MMC	NORM	.190013E-03	.258984E+00	.965881E+00
5	105.0000MMC	NORM	-.186947E-03	.258849E+00	.965918E+00
6	105.0000MMC	NORM	.174800E-03	.258844E+00	.965919E+00
7	105.0000MMC	NORM	-.133190E-03	.258823E+00	.965925E+00
8	105.0000MMC	NORM	.189473E-03	.258818E+00	.965926E+00
9	105.0000MMC	NORM	-.159130E-03	.258851E+00	.965917E+00
10	105.0000MMC	NORM	.147589E-03	.258845E+00	.965919E+00
11	105.0000MMC	NORM	-.142535E-03	.258870E+00	.965912E+00
12	105.0000MMC	NORM	.139292E-03	.258863E+00	.965914E+00

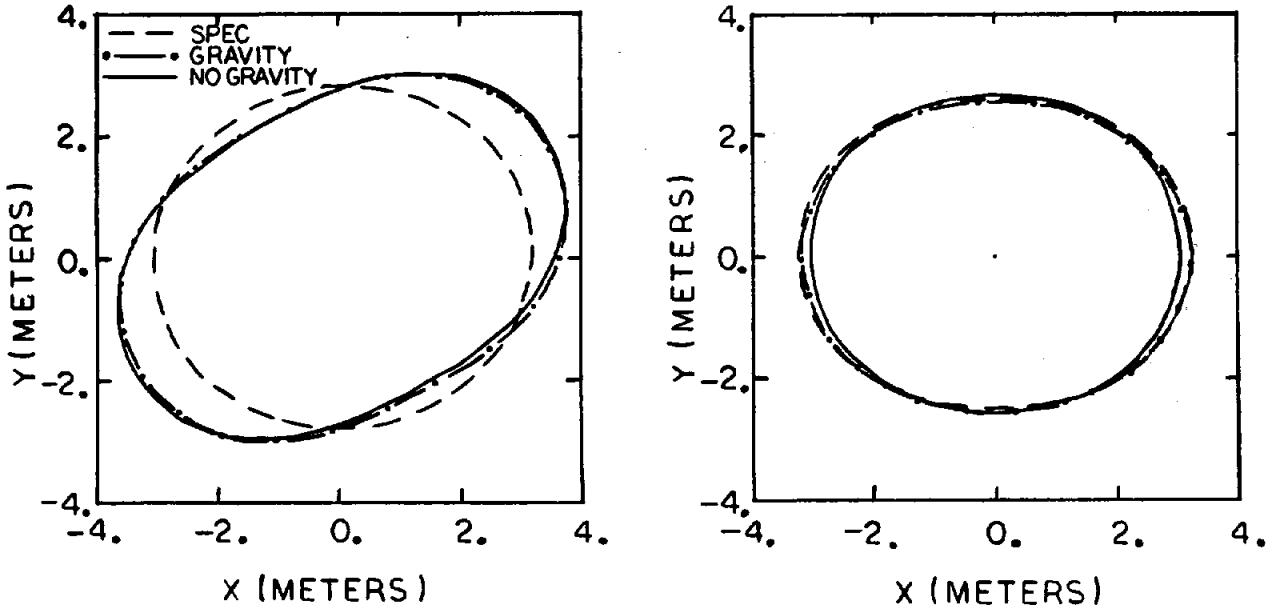

Figure A-7.36. Predicted Performance of an MMC Heliostat that Is 393 m North and 75 m below a Target Oriented Perpendicular to the Incoming Beam. Conditions: On-axis canting for 400 m, Day 172, solar times 0.0 (right) and 4.0 (left), ambient temperature 50°C (122°F), heliostat elevation angles 45.2° and 33.2°, angles of incidence 34.3° and 43.8°.

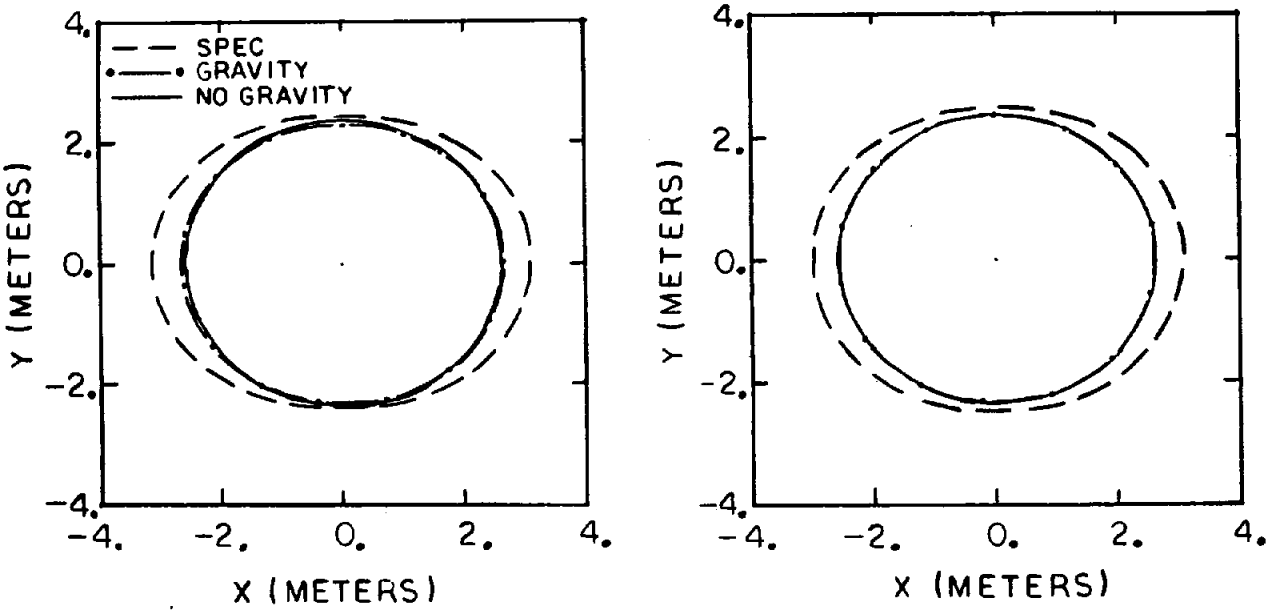

Figure A-7.37. Predicted Performance of an MMC Heliostat that Is 393 m North and 75 m below a Target Oriented Perpendicular to the Incoming Beam. Conditions: On-axis canting for 400 m, Day 335, solar times 0.0 (right) and 4.0 (left), ambient temperature 0°C (32°F), heliostat elevation angles 21.7° and 11.2°, angles of incidence 10.9° and 26.4°.

HELIOS predictions of the performance of the MDAC heliostats for the same worst case conditions are given in Figures A-7.38 and A-7.39. As with the MMC heliostat design, the influence of gravity on beam quality can be seen to be relatively small. The MDAC heliostat, as with MMC, also fails to meet the specifications for large angle of incidence at high temperature conditions (Figure A-7.38). It can also be seen from Figure A-7.39 that the MDAC heliostats failed to meet the specifications at the low temperature (0°C) extreme. A BCS measurement at 0.6°C (33°F) subsequent to the actual test period at the CRTF verified this prediction as shown in Figure A-7.40.

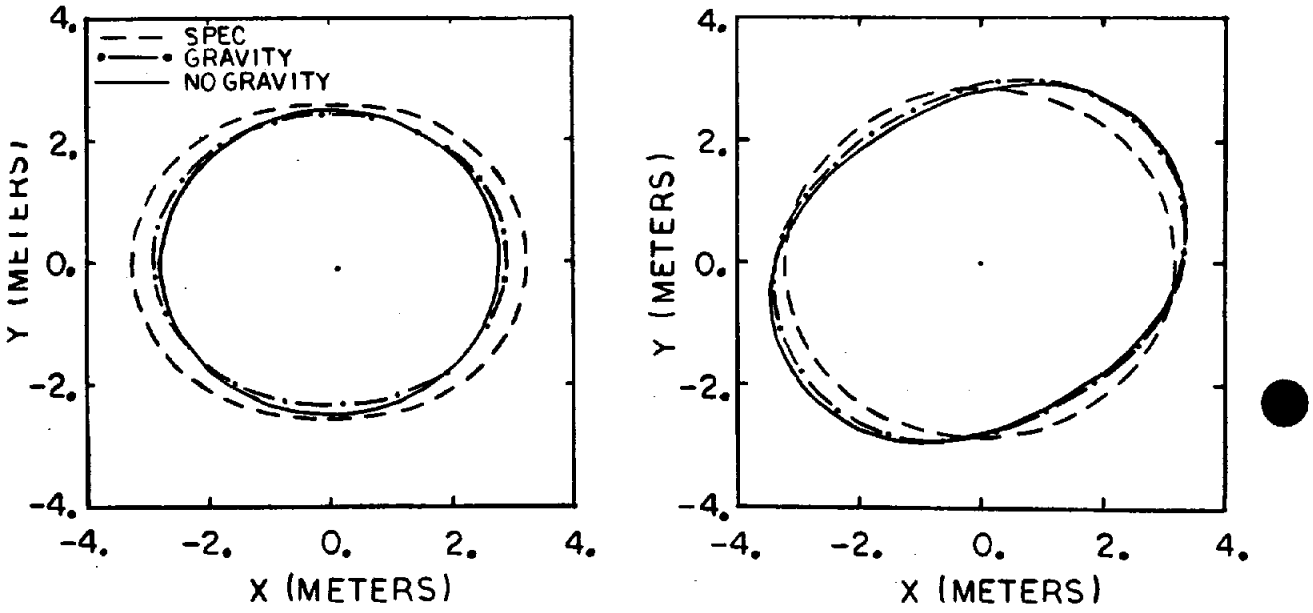

Figure A-7.38. Predicted Performance of an MDAC Heliostat that Is 393 m North and 75 m below a Target Oriented Perpendicular to the Incoming Beam. Conditions: On-axis canting for 400 m, Day 172, solar times 0.0 (right) and 4.0 (left), ambient temperature 50°C (122°F), heliostat elevation angles 45.1° and 33.2°, angles of incidence 34.4° and 43.8°.

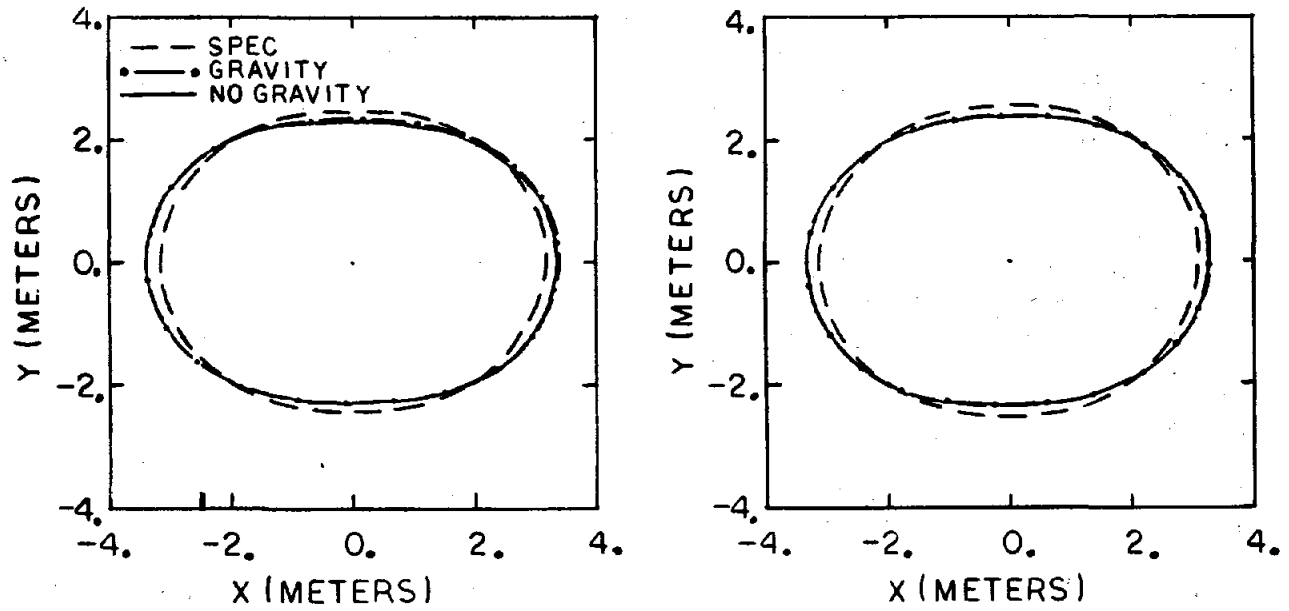

Figure A-7.39. Predicted Performance of an MDAC Heliostat that Is 393 m North and 75 m below a Target Oriented Perpendicular to the Incoming Beam. Conditions: On-axis canting for 400 m, Day 355, solar times 0.0 (right) and 4.0 (left), ambient temperature 0°C (32°F), heliostat elevation angles 21.7° and 11.2°, angles of incidence 10.9° and 26.4°.

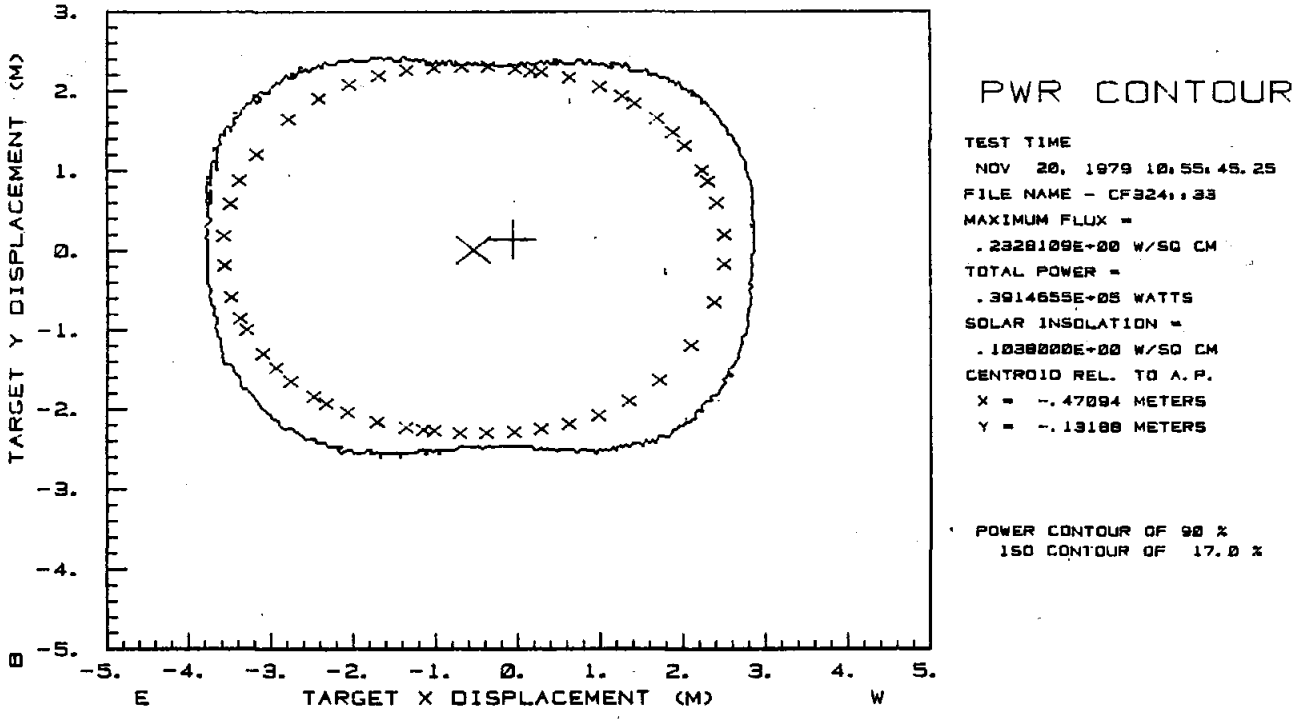

Figure A-7.40. BCS Beam Quality Measurement of MDAC #1 at Ambient Temperature of 0.6°C (33°F) vs Specification (indicated with x's)

Additional HELIOS runs indicated that the beam quality specification was met for temperatures above approximately 4.4°C (40°F). The failure to meet the specification at the low temperature extremes resulted primarily from the fact the mirror modules went beyond flat and became convex for temperatures below approximately 7°C (45°F).

This phenomenon was indicated in the mirror module curvature versus temperature data in Figure A-7.1. The data in Figure A-7.1, and that used in the HELIOS model, assume that the mirror modules smoothly go convex at low temperatures and still maintain an approximately cylindrical curvature. Measurements and visual observation indicated that this was not strictly true. The corners of the mirror modules out past the mounting cups tended to go convex more severely than the area between mounting points. The effect of this behavior can be seen in Figure A-7.40. The curvature of the MDAC mirror modules at high temperature was somewhat uncertain in that Sandia and MDAC measurements differed significantly as indicated in Figure A-7.1. This uncertainty could have resulted from large variations in curvature from one module to the next or from measurement error. If the MDAC curvature at 50°C is used in the HELIOS predictions then the beam quality specification is not met, as indicated in Figure A-7.41, for either noon or late afternoon conditions. Since there appeared to be some uncertainty in the measured MDAC mirror module curvature at high temperatures it was concluded that the MDAC heliostat would marginally meet the specification at high temperatures with the exception of large angle of incidence conditions at the longest slant range.

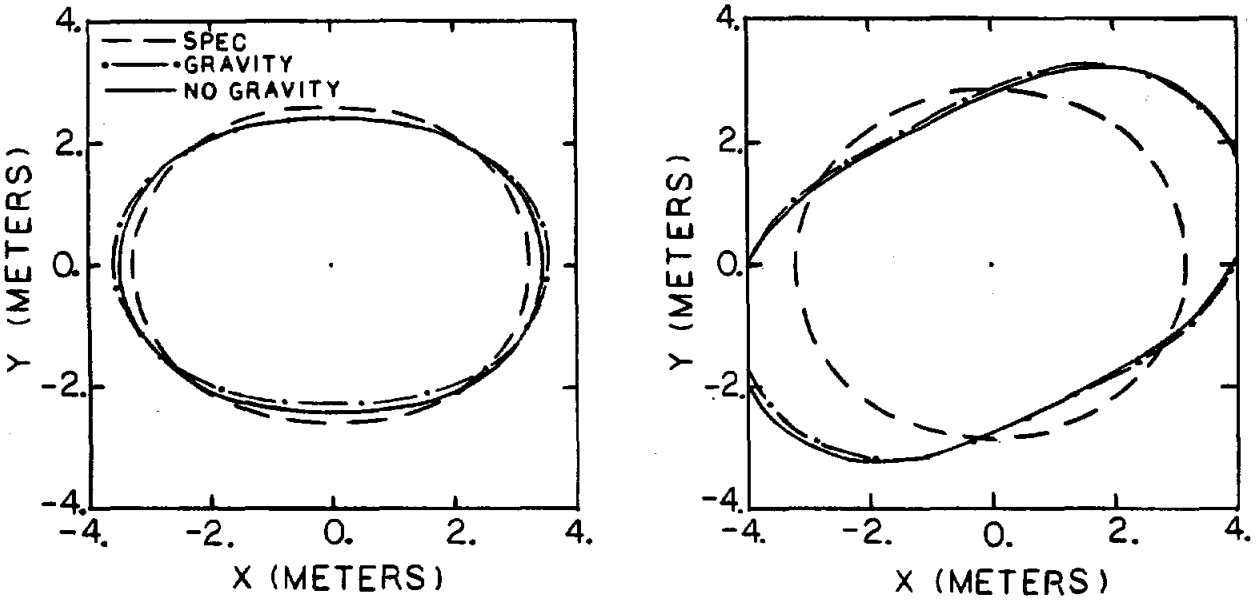

Figure A-7.41. Predicted Performance of an MDAC Heliostat that Is 393 m North and 75 m below a Target Oriented Perpendicular to the Incoming Beam. Conditions: On-axis canting for 400 m, Day 172, solar times 0.0 (right) and 4.0 (left), ambient temperature 50°C (122°F), heliostat elevation angles 45.1° and 33.2°, angles of incidence 34.4° and 43.8°. This case assumes MDAC measured mirror module curvature at 50°C.

Since the canting procedure proposed to be used at the pilot plant involved canting all heliostats on-axis for the longest slant range expected in the field, beam quality predictions for heliostats at short slant ranges were also considered. The reasons for this approach to mirror canting are a potential reduction in production and maintenance costs since all heliostats are canted in the same manner and a more uniform flux density distribution on the receiver from the full field of heliostats.

Figures A-7.42 and A-7.43 illustrate the HELIOS-predicted beam image for one of the MMC heliostats located 75 m north of the target. The target used for this case is 79 m above the base of the heliostat and tilted north such that the beam is perpendicular to the target plane. The specification contour was not originally intended to be used for this type of "under canted" condition; however, for purposes of illustration it is indicated in three of the four cases in Figures A-7.42 and A-7.43. Figure A-7.42 dramatically illustrates the effect of the mirror module curvature at high temperatures relative to the flat (specification) condition.

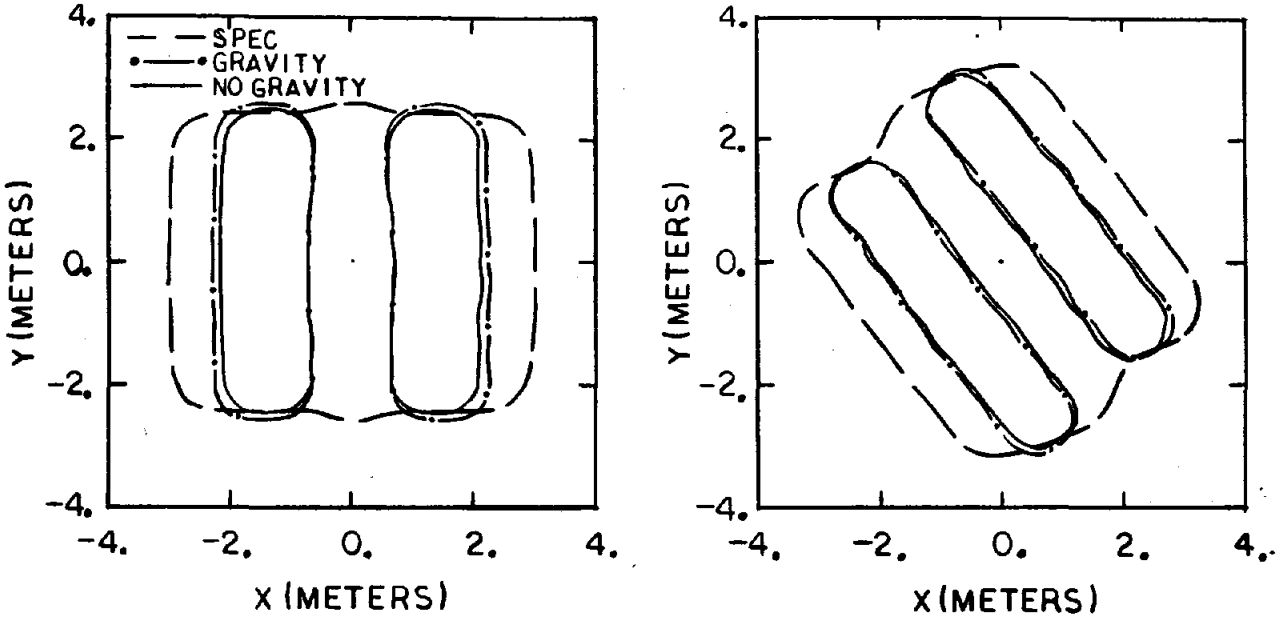

Figure A-7.42. Predicted Performance of an MMC Heliostat that Is 75 m North and 75 m below a Target Oriented Perpendicular to the Incoming Beam. Conditions: On-axis canting for 400 m, Day 172, solar times 0.0 (right) and 4.0 (left), ambient temperature 50°C (122°F).

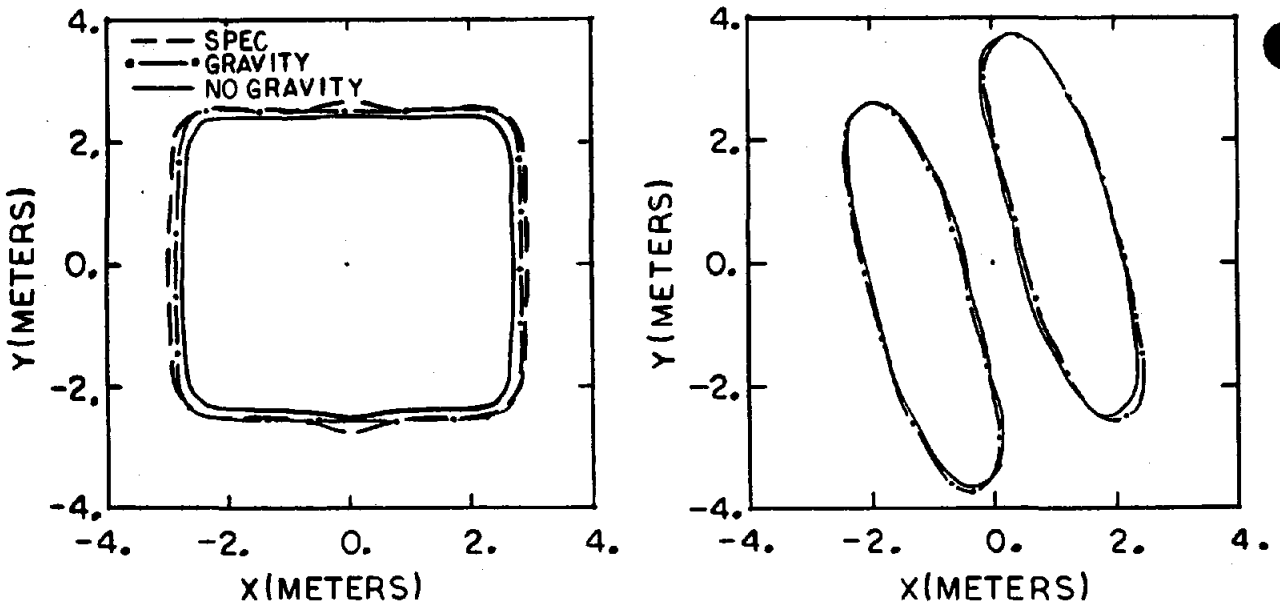

Figure A-7.43. Predicted Performance of an MMC Heliostat that Is 75 m North and 75 m below a Target Oriented Perpendicular to the Incoming Beam. Conditions: On-axis canting for 400 m, Day 355, solar times 0.0 (right) and 4.0 (left), ambient temperature 0°C (32°F).

Conclusions

As a result of beam quality testing at the CRTF several conclusions could be made concerning both the evaluation technique and the performance of the test heliostats. Using BCS-measured beam quality data for a relatively limited set of environmental conditions and use geometries in conjunction with analysis of the measured data with the computer model HELIOS, it was possible to characterize the performance of the test heliostats in terms of an error distribution. This error distribution could then be used to predict the performance of the test heliostats for worst case environmental conditions and different use geometries that could occur at the pilot plant. Using heliostat performance predictions under worst case conditions it was then possible to evaluate the heliostat's compliance with the desired performance specification.

BCS measurements and the HELIOS-predicted performance of the MMC heliostats indicated that their heliostats would meet the performance specification for the majority of possible use geometries and temperature extremes. Predicted performance indicated that at the longest slant range, the highest ambient temperature, and for large angles of incidence the aberration produced as a result of too much mirror module curvature resulted in the performance specification not being met. BCS measurements of beam quality indicated no observable change in beam quality as a result of life cycling and general environmental exposure during the three-month CRTF test period. Subsequent measurements after six months' exposure also showed no degradation in beam quality.

BCS measurements and the HELIOS-predicted performance of the MDAC heliostats indicated that the heliostats failed to meet the pilot plant beam quality specification for low temperature (< 4.4°C) environmental conditions. This was primarily the result of insufficient curvature in the mirror modules at low ambient temperature conditions. The curvature of the MDAC mirror modules at high temperatures (50°C) was not well known as a result of either large variations in curvature from module to module or as a result of measurement error. If Sandia measurements were used to predict performance then the specification was met, except for the same high temperature, long slant range, large angle of incidence conditions for which the MMC heliostat did not meet the specification. If, however, the MDAC measurements of mirror module curvature were used to predict performance, then the heliostat failed to meet specification for a larger number of high temperature conditions.

Test A-8: Life Cycling

Objective

The objective of this test was to obtain limited life-cycle data on the test heliostats. The limitation arose from the DOE schedule restriction that all testing at the CRTF be completed in a three-month period beginning in July 1979. Life cycling was to be initiated at all times during the day (six days per week) when other tests were not being performed. Observations of electronic or mechanical failures were to be recorded and a BCS assessment of tracking accuracy and beam quality were to be done before and after life cycling. Additional life cycle data were to be obtained during environmental testing of individual drive units (Test Section C). The combined life cycle results were to be used to make a subjective judgement of the test heliostats' ability to meet a 30-year life requirement.

Description

The month of June 1979 was intended to be used by the heliostat contractors to assemble and check out their heliostats. The official test schedule was to begin the first of July and life cycle testing was to be done at any time the heliostats were not occupied during other testing.

The test cycle used during life cycling was to simulate a typical operational cycle. The heliostat was moved from a stowed position to a standby position and from there to a tracking position for a period that simulated an 8-a.m.-to-4.p.m. day. After maintaining the tracking condition for the simulated period the heliostat was returned to standby and then to the stowed position. These simulated daily cycles were accomplished at an accelerated pace such that three simulated daily cycles were accomplished in a nine-hour period. Cycling was typically accomplished on a six-day-per-week basis. To prevent beam safety problems during life cycling the elevation movements of the heliostats were limited such that during life cycling the beams from the heliostats were always on the ground in front of the heliostats. The effective gimbal angle movements of the heliostats were then approximately 95 degrees in elevation and 180 degrees in azimuth.

Tracking accuracy and beam quality assessments with the BCS were done prior to and following the life cycle test period. Time of operation, number of cycles, abnormal behavior, and maintenance requirements were recorded during the entire test period.

Results

The installation and checkout of the MMC heliostats at the CRTF went very smoothly and life cycle testing began on July 7, 1979. By the completion of testing on October 1, approximately 120 simulated cycles had been completed by each of the heliostats. The results of the BCS tracking accuracy measurements before and after cycling have been discussed in Test A-6 as have the before and after beam quality measurements in Test A-7. During life cycling of the MMC heliostats no mechanical or electronic failures were recorded; however, eight instances of an HFC communication error problem were recorded. These communication problems were apparently caused by noise or voltage transient sensitivity of the HFC electronics. The communication error problem was rectified by stowing the heliostats and reinitiating the startup sequence.

Assembly of the MDAC heliostats at the CRTF went smoothly; however, control system checkout presented many problems. As a result of repeated control system failures during checkout, life cycling of MDAC Heliostat 2 did not begin until August 15, and cycling of MDAC #1 did not begin until August 21. This approximately six-week slip of the testing schedule by MDAC made it necessary for MDAC personnel to life cycle their heliostats 24 hr/day and 7 days/week in order to complete approximately the same number of cycles (120) as MMC between initial and final assessments of tracking accuracy.

During the period from July 1 to August 20 the control system failures included: five motor control board failures, five encoder failures, apparent limit switch malfunctions, one burned out motor, and a broken motor wire that caused the motor to attempt to run on two-phase power instead of three-phase. It was often difficult to identify the definite cause for several of the failures observed; however, faulty design of the motor control electronics appeared to be the major problem.

In addition to the control system difficulties during checkout, an adhesive failure on one of the mirror mounting cups was recorded. Figure A-8.1 shows the mounting cup that debonded. Later in the test program several more cups debonded and several causes for the failure of the 3M-EC3532 polyurethane adhesive were identified. Moisture accumulation inside the cup coupled with high metal temperatures ($\sim 60°C$) and inadequate preparation of the mirror module back surface were believed to be the primary reasons for the adhesive failure. High metal temperatures were again the result of selective solar absorption by the galvanized finish on the mirror modules.

Subsequent to the start of life cycling on August 15 and through the end of testing in October, four additional control system failures were recorded. These included four motor control board failures, one heliostat control electronics (HC) failure, and one apparent limit switch malfunction that resulted in a burned out motor and a jammed stow jack. Replacement of the damaged jack is shown in Figure A-8.2. Mechanical wear of the jack output shafts caused by a bending moment in the shaft at the location of the shaft

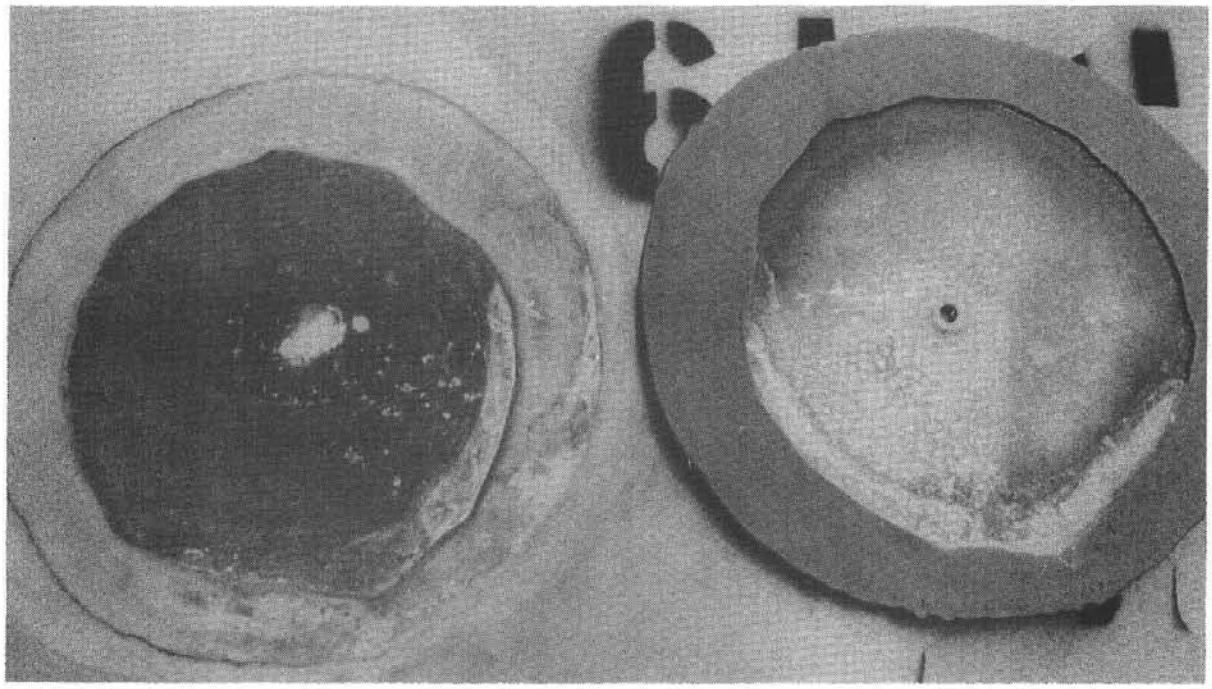

Figure A-8.1. Debonded MDAC Mirror Module Mounting Cup

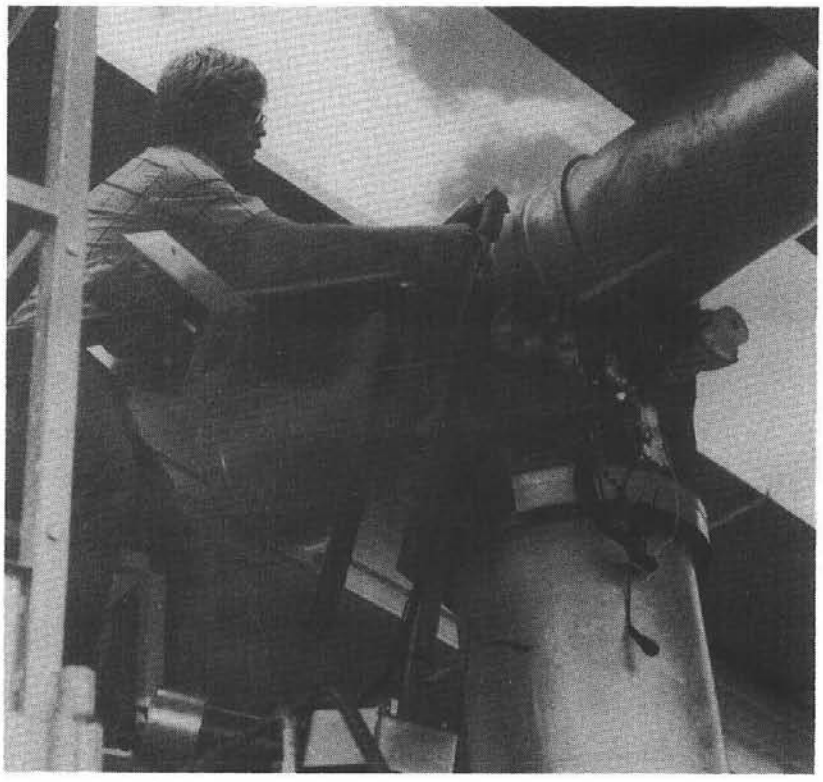

Figure A-8.2. MDAC Damaged Stow Jack Being Replaced

bushing in the pivot collar was observed following cycling. The weight of the drive motor and gear housing near the end of the jack sleeve introduced the bending moment in the jack output shaft as it slid back and forth through the bushing. This same mechanical wear was observed to a much more severe degree during environmental testing of the MDAC drive unit (see Test Section C).

Conclusions

Beam quality and tracking accuracy measurements of the performance of the MMC heliostats following life cycling indicated no degradation as a result of approximately 120 simulated daily tracking cycles. No mechanical failures and no electronic failures were recorded during cycling; however, several instances of communication errors were observed as a result of apparent sensitivity of the HFC to noise and/or voltage transient conditions.

Beam quality performance measurements of the MDAC heliostats indicated no degradation as a result of approximately 120 simulated tracking cycles. Tracking accuracy measurements following cycling did show evidence of degradation during a three-week period of continual cycling. As discussed in Test A-6, it was difficult to decide if this was the result of mechanical wear during cycling, control system nonrepeatability, or incorrect azimuth axis tilt and nonorthogonality parameters. Repeated failures of heliostat control electronics, elevation jack transition repeatability problems, absolute encoder failures, and undesired absolute encoder updates indicated that additional development and refinement of the MDAC control system were required.

Test A-9: 90-mph (40-m/s) Wind Load

Objective

The occurrence of a 40-m/s (90-mph) wind condition at a solar facility would be rare; however, the potential impact such an occurrence would have on the survival of the heliostat field warrants a structural design that can tolerate such wind loading. From a test standpoint the most straightforward approach to verifying that a structure will survive actual wind loads is to simulate the wind loads with statically applied loads.

The objective of this test was to apply loads that approximate a 40-m/s wind load condition with the heliostat mirror plane 10 degrees from the horizontal position. Beam quality and tracking accuracy evaluations were to be made before and after loading to verify that performance had not been degraded. Observations of mechanical failure or slippage were to be recorded during loading. A second objective was to increase the 40-m/s loads by 25 percent and repeat the test in order to investigate the margin of safety available in the heliostat design.

Description

Static loads were analytically determined (for each of the heliostat designs tested) that would produce a moment about the elevation axis that was equivalent to that produced by a 40-m/s wind impacting the mirror plane at a 10-degree angle of attack. The loads were evenly distributed across the heliostat structure at a distance of one-fourth of the overall heliostat dimension from the edge of the outer mirror. Table A-9.I gives the loads and resulting moments for both heliostat designs and for the 40-m/s and the 25-percent overload test.

TABLE A-9.I

LOADS AND CORRESPONDING MOMENTS APPLIED DURING SIMULATED WIND LOADING

	m	ft	kg	lb	kg-m	ft-lb	kg	lb	kg-m	ft-lb
MMC	1.71	5.63	1348	2972	2311	16715	1685	3715	2889	20894
MDAC	1.84	6.04	1461	3222	2695	19493	1826	4027	3369	24336

The loads were applied to the MDAC heliostat on the side of the heliostat that would put the elevation screw jacks in compression, as can be seen in Figure A-9.1. The wooden structures shown in this figure were used to distribute the load evenly into the heliostat crossbeams and thereby avoid localized deformation of the crossbeams that may have occurred otherwise. As a means of detecting movement, dental cement was placed in locations where slippage was likely to occur during loading. On the MDAC heliostat the dental cement was placed on the bolted friction interfaces between the elevation tube and the crossbeams and on bolted interfaces on the elevation drive mechanism.

The elevation tubes on the MMC heliostats are offset in the crossbeams. The loads applied to the MMC heliostat during this test were applied on the side of the heliostat with the longest section of crossbeam from the elevation tube. The loading fixture and test setup on an MMC heliostat can be seen in Figure A-9.2. Dental cement was also applied to the MMC heliostat at the bolted interfaces of the crossbeams to the elevation tube and on bolted interfaces on the arm between the drive unit and elevation tube.

During the loading of the heliostats the loads were applied and then released for 10 repetitions. Data taken during each test included BCS measurements of tracking accuracy, and beam quality before and after loading, and angular deflection measurements at the pedestal base flange. Angular deflection measurements taken on the pedestal base flange were taken to ensure no permanent deflection of the foundation occurred during loading.

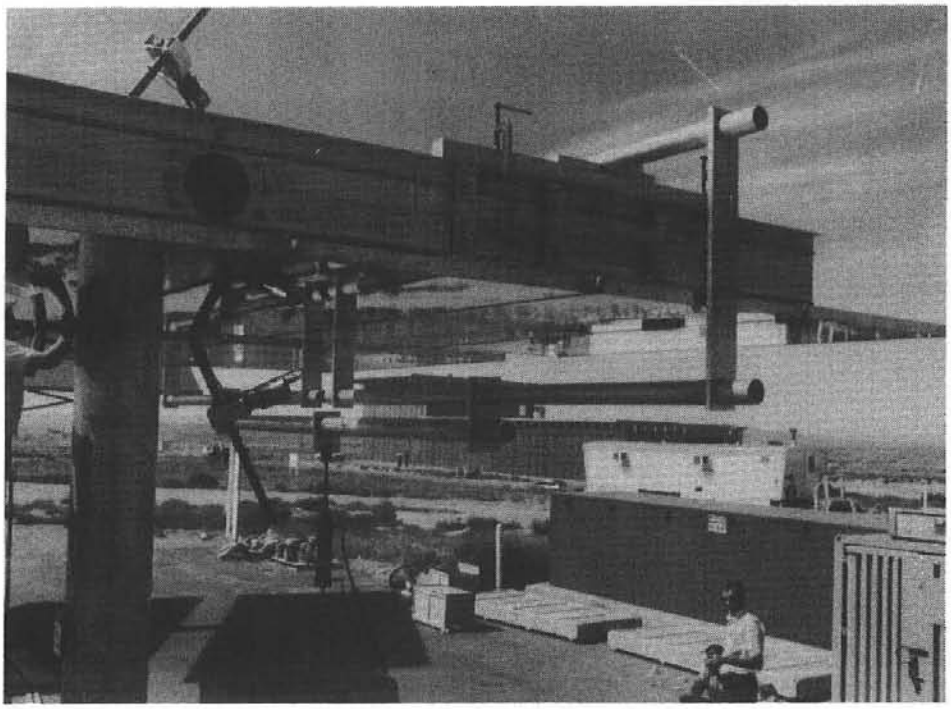

Figure A-9.1. Simulated 40-m/s (90-mph) Wind Load Test Setup on MDAC Heliostat

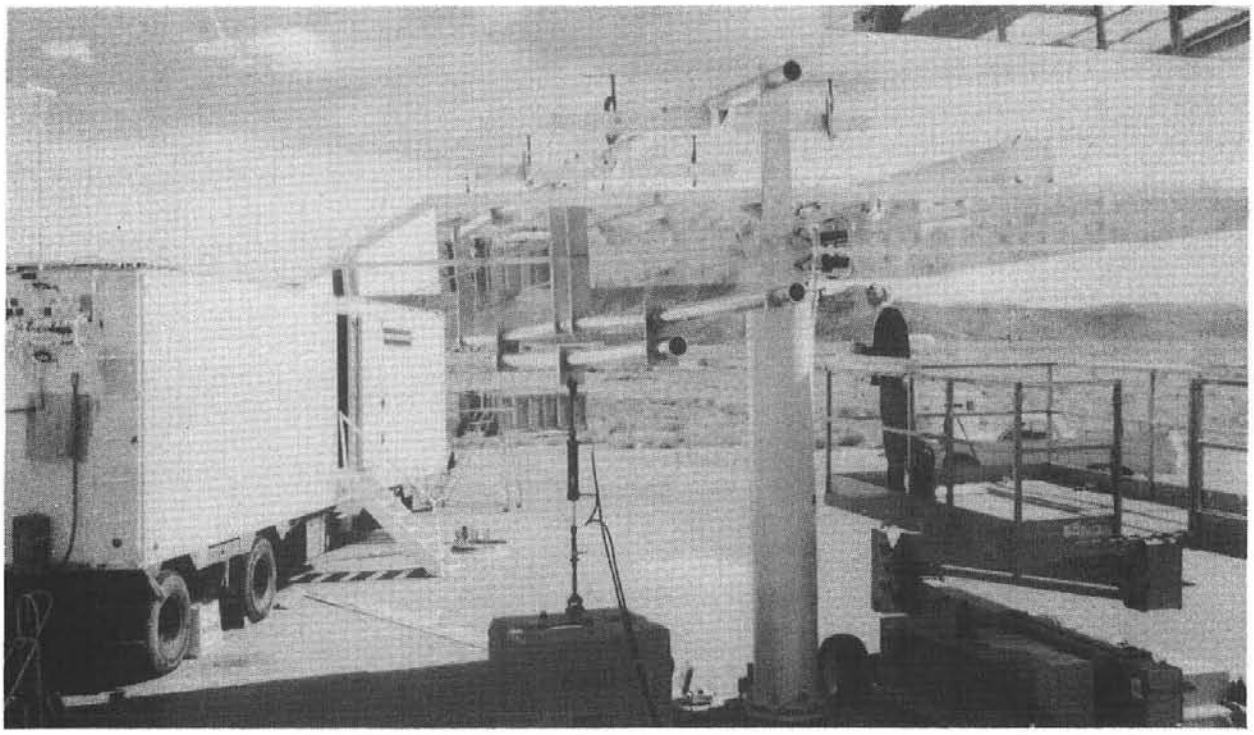

Figure A-9.1. Simulated 40-m/s (90-mph) Wind Load Test Setup on MMC Heliostat

Results

The 40-m/s (90-mph) loading of MMC Heliostat 2 was conducted on September 19. Tracking data prior to the loading are shown in Figure A-6.8 (Test A-6), and tracking data following the 40-m/s loading are shown in Figure A-9.3. Beam quality data prior to loading are given in Figure A-9.4. Beam quality data following the 40-m/s wind load were significantly degraded; however, BCS-measured beam data were not obtained.

It is evident from the tracking accuracy data in Figure A-9.3 that significant degradation of tracking performance resulted from this 40-m/s simulated wind load. Angular deflection mesurements on the pedestal base flange indicated a maximum deflection under load of 0.3 mR and a residual deflection after removal of the load of less than 0.04 mR. This indicated that a permanent deflection had occurred somewhere in the MMC heliostat assembly probably within the drive unit. Examination of the dental cement on the bolted interfaces between the crossbeams and the elevation tube indicated that the bolted interfaces had slipped as a result of the loading. This slip caused a mirror canting distortion and the resulting degradation in beam quality.

After the BCS tracking and beam quality data were retaken, the heliostat was manually jerked in an attempt to get rid of the residual deflection. This jerk resulted in an audible "snapback" that visually restored the lost beam quality and also reduced part of the tracking error, as can be seen in Figure A-9.3. No modifications were made to the heliostat.

On September 23 the load test was repeated at load levels that were 25 percent higher than those used during the 40 m/s test. The tracking accuracy data following this 25-percent overload test are shown in Figure A-9.5. Again the tracking error was significantly degraded as was the beam quality (Figure A-9.6). Slippage again occurred at the bolted interface between the crossbeams and the elevation tube and a residual deflection occurred in the drive unit.

Manually jerking the heliostat again resulted in an audible "snapback" and visually restored the beam quality. Approximately 4 mR of the vertical angular error were also eliminated by jerking the heliostat, as can be seen in Figure A-9.5. Measurements on the base flange of the pedestal during loading indicated a maximum angular deflection under load of 0.35 mR and a residual deflection after removal of the load of less than 0.04 mR.

The 40-m/s (90-mph) simulated wind load testing of the MDAC Heliostat 2 was conducted on September 26. The loads, given in Table A-9.I, were applied and then released 10 times. The reflected beam tracking accuracy data and the beam quality data prior to loading are shown in Figures A-9.7 and A-9.8, respectively.

As mentioned in Test A-6, the tracking accuracy data obtained during this wind load testing were taken using different tilt and nonorthogonality parameters in the MDAC control system than those used during Test 6. The new set of parameters were derived by MDAC personnel from previous BCS-measured tracking data.

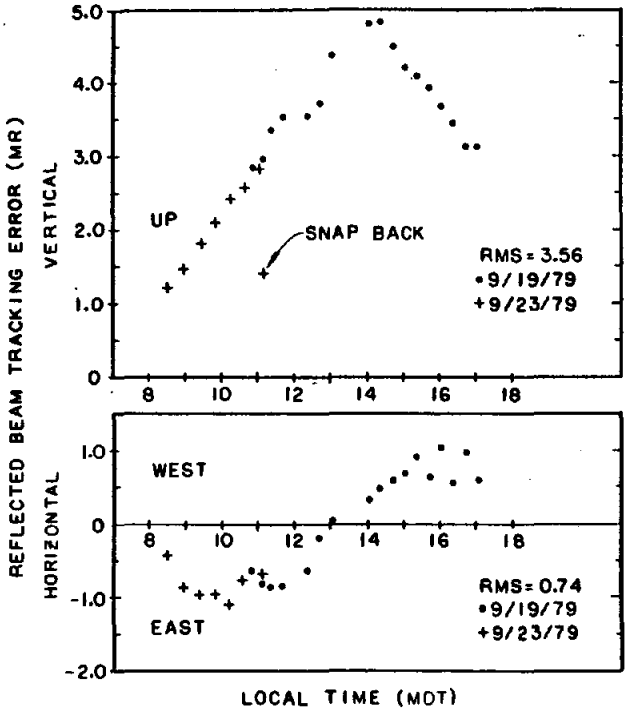

Figure A-9.3. MMC #2 Reflected Beam Angular Tracking Error (mR) following 40-m/s (90-mph) Simulated Wind Load

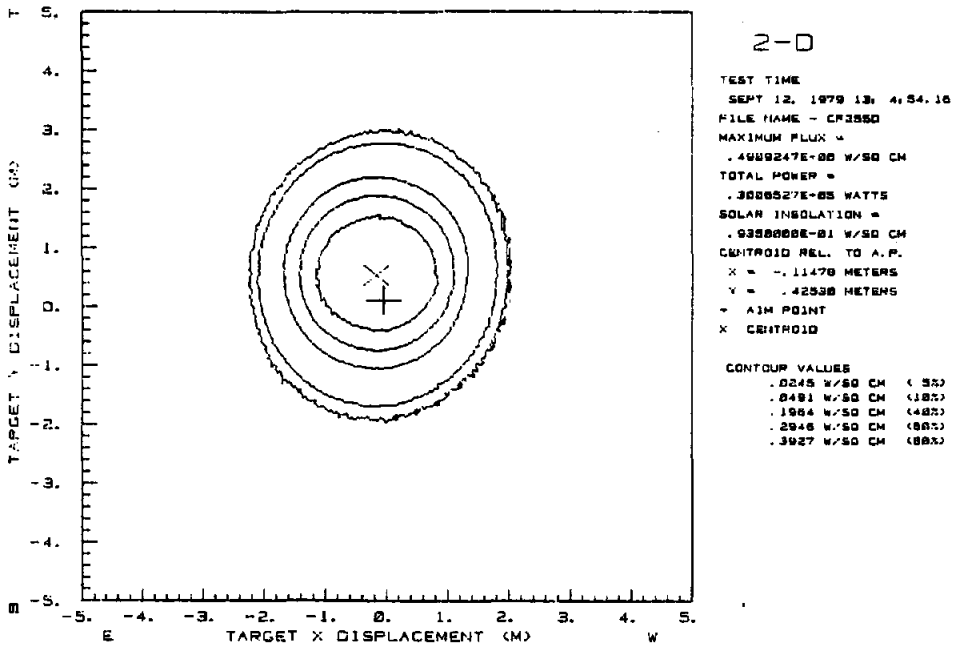

Figure A-9.4. Beam Quality Data on MMC #2 prior to 40-m/s Wind load Test

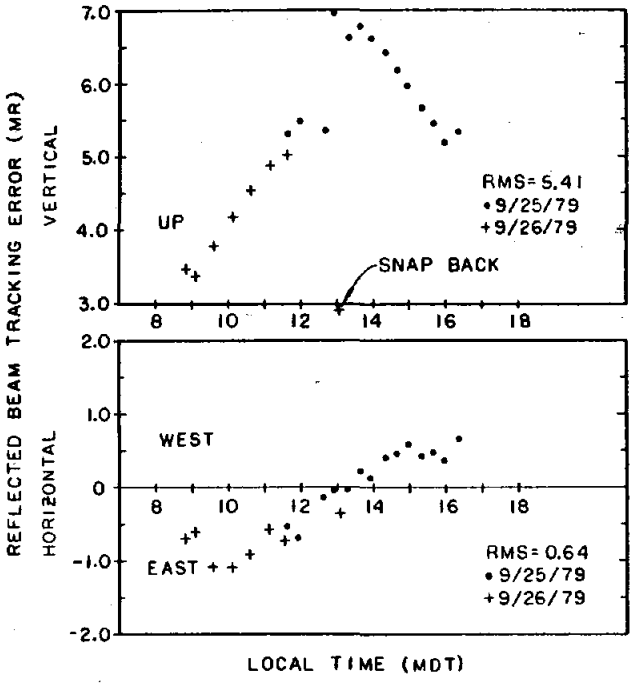

Figure A-9.5. MMC #2 Reflected Beam Angular Tracking Error (mR) following 25% Overload Test

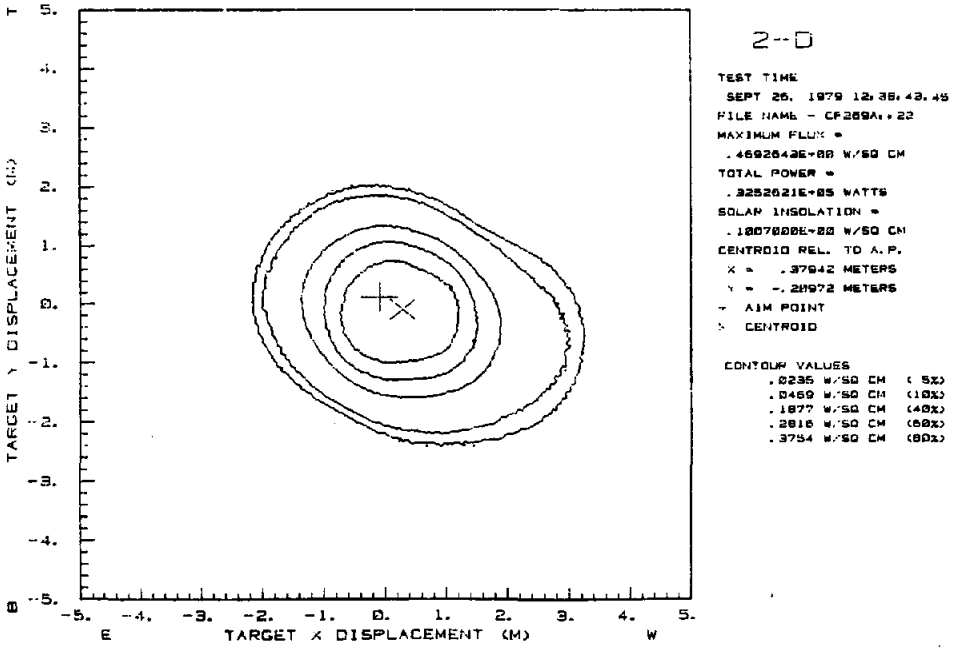

Figure A-9.6. Beam Quality Data on MMC #2 following 25% Overload Test

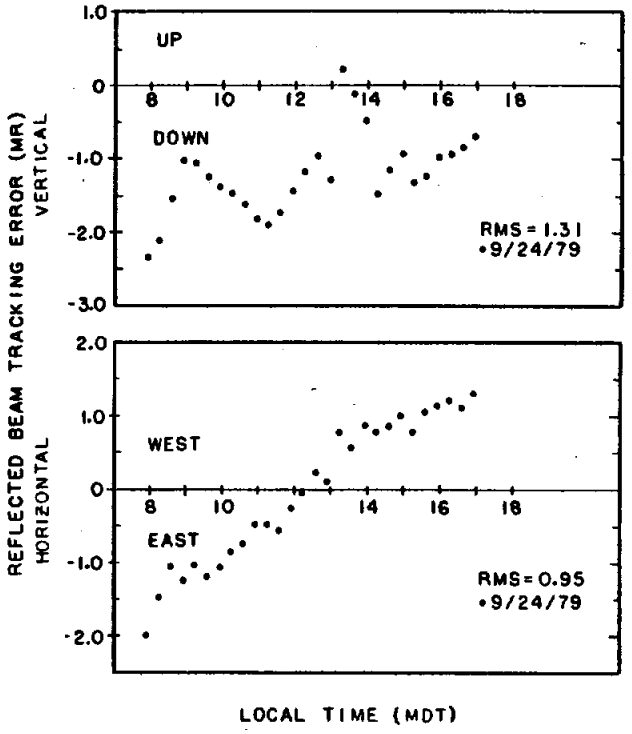

Figure A-9.7. MDAC #2 Reflected Beam Angular Tracking Error (mR) prior to 40-m/s (90-mph) Simulated Wind Load

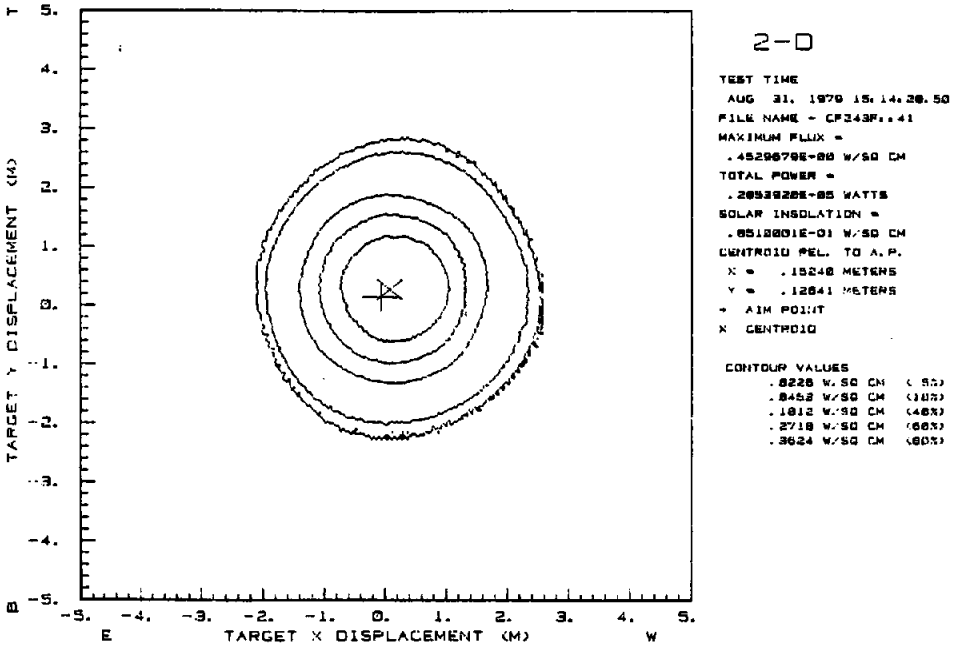

Figure A-9.8. Beam Quality Data on MDAC #2 prior to 40-m/s Wind load Test

The tracking accuracy data following the 40-m/s wind load test are shown in Figure A-9.9. The maximum angular deflection of the pedestal base flange was 0.08 mR under load. The residual deflection after removal of the load was less than 0.03 mR. The dental cement on the bolted interfaces showed no signs of slippage.

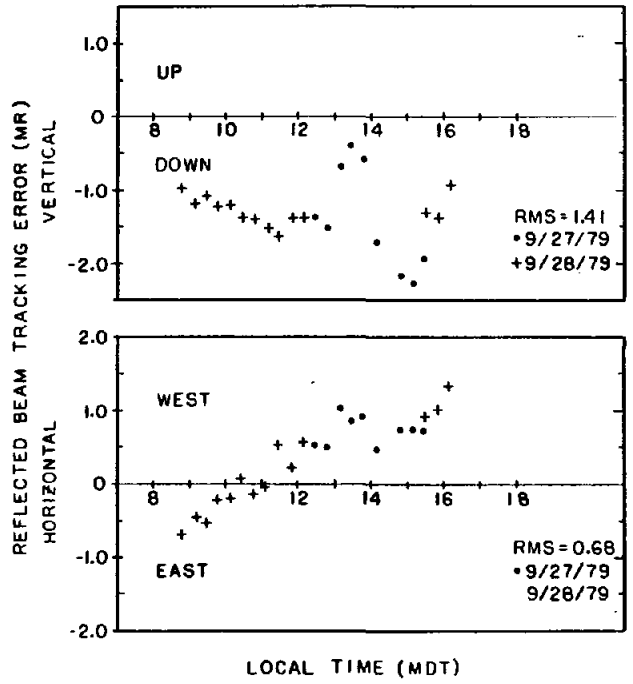

Figure A-9.9. MDAC #2 Reflected Beam Angular Tracking Error (mR) following 40-m/s (90-mph) Simulated Wind Load

On October 2 the load test was repeated at load levels that were 25 percent higher than those used during the 40-m/s test. The tracking accuracy data following this 25-percent overload test are shown in Figure A-9.10. The beam quality data following the test are shown in Figure A-9.11. The results of the simulated wind load testing on the MDAC heliostat indicated that there was no significant change in beam quality or in tracking accuracy as a result of simulated wind load testing. The apparent slight change in elevation tracking error from Figure A-9.9 to A-9.10 can as easily be attributed to a nonrepeatability of the elevation jacks as to a structural change following the 25-percent overload test.

As a result of the failure of the MMC heliostat to pass the simulated 40-m/s wind load testing both in terms of tracking accuracy and beam quality, the heliostat was modified and the test was repeated on October 19. The modifications included increasing the preload on the azimuth bearings in the drive unit and welding all interface joints between the crossbeams and the elevation tube.

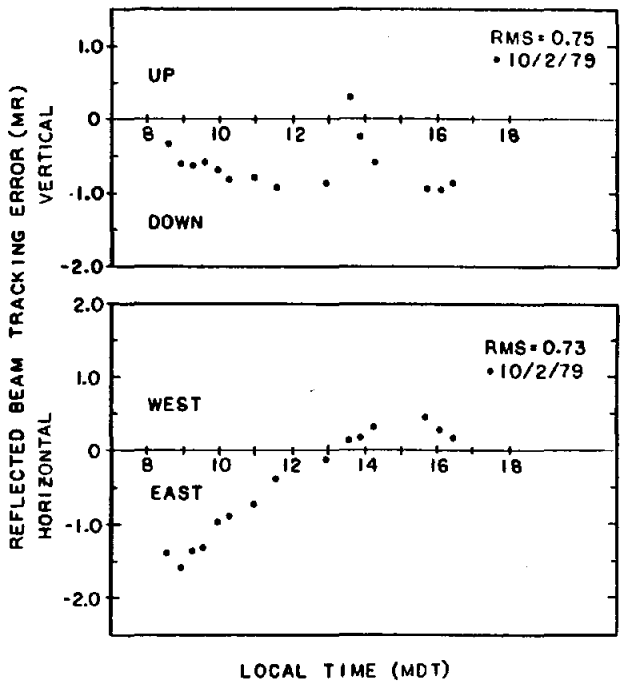

Figure A-9.10. MDAC #2 Reflected Beam Angular Tracking Error (mR) following 25-Percent Overload Test

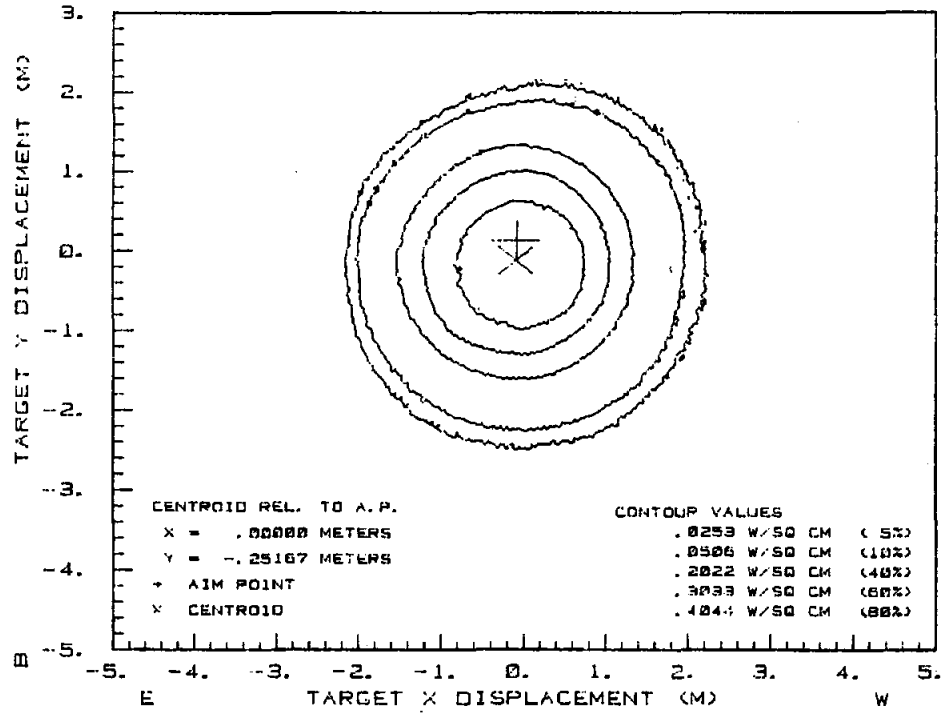

Figure A-9.11. MDAC #2 Beam Quality Data following 25-Percent Overload Test

Tracking accuracy data prior to the test are shown in Figure A-9.12. The same data following the test are shown in Figure A-9.13. Beam quality data before and after the retest are given in Figures A-9.14 and A-9.15, respectively. Analysis of these data indicated that welding the crossbeam to elevation tube joints stopped the degradation of beam quality due to simulated wind load; however, the tracking accuracy problem had not been rectified.

On October 22 the same test was again repeated at load levels 25 percent above the 40-m/s case. Beam quality data following the 25-percent overload test are given in Figure A-9.16. These data also indicated that welding the crossbeam to elevation tube interfaces rectified the beam quality degradation problem seen prior to welding the interfaces. Tracking accuracy data following this 25-percent overload test are given in Figure A-9.17.

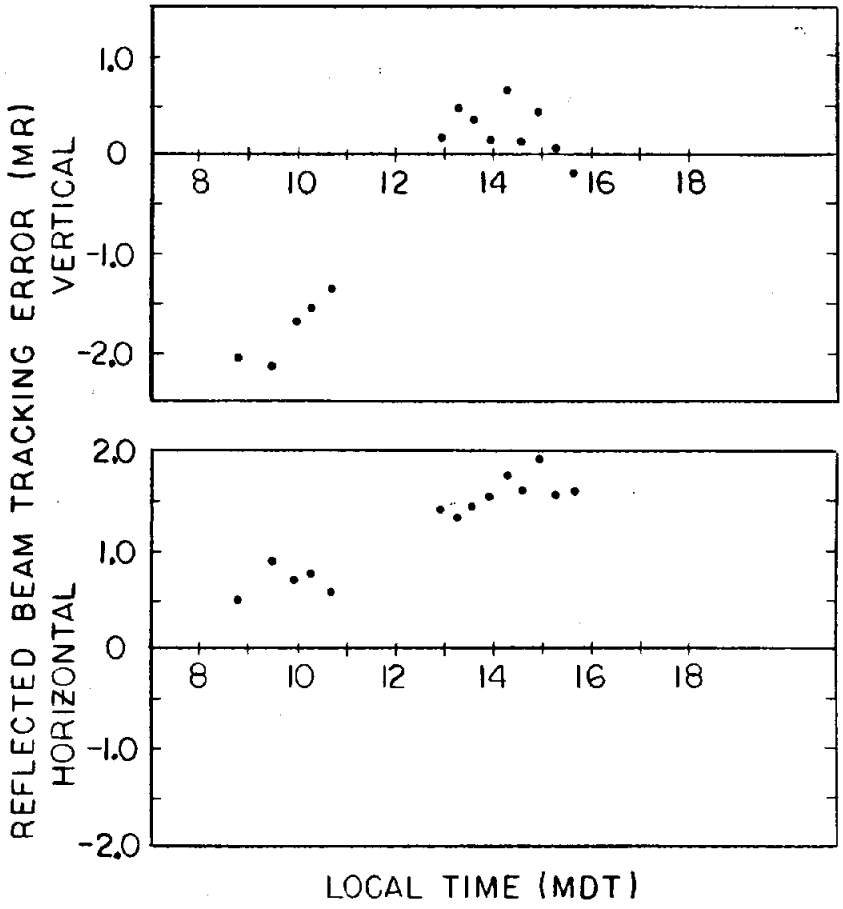

Figure A-9.12. MMC #2 Reflected Beam Angular Tracking Error (mR) prior to 40-m/s (90-mph) Retest

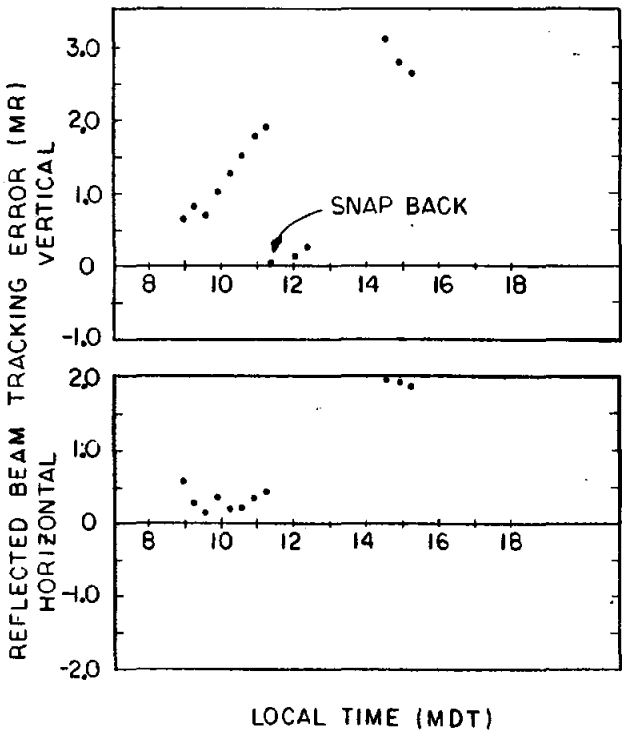

Figure A-9.13. MMC #2 Reflected Beam Angular Tracking Error (mR) following 40-m/s (90-mph) Retest

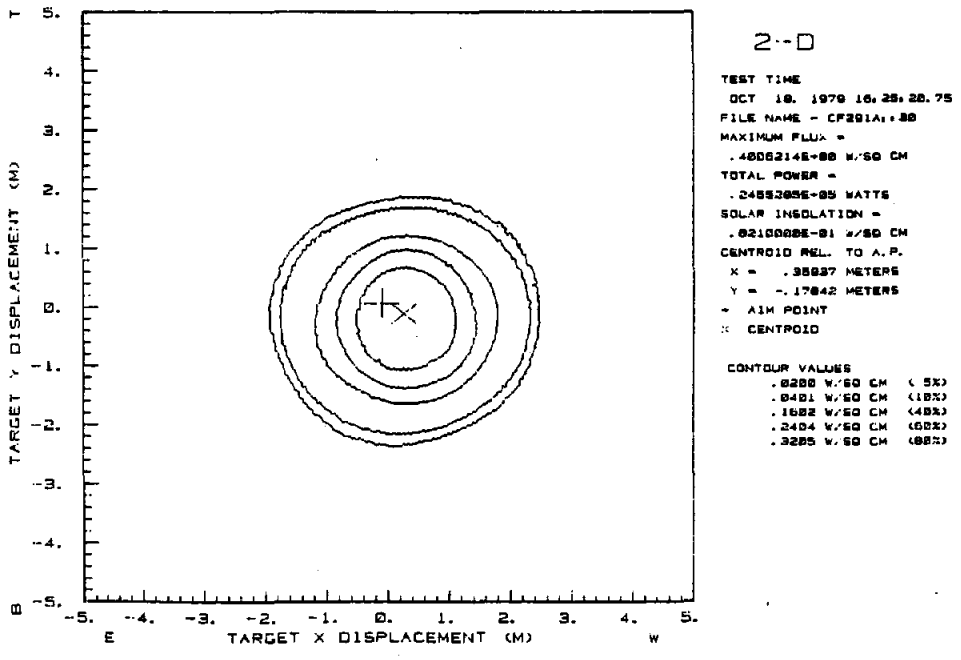

Figure A-9.14. MMC #2 Reflected Beam Angular Tracking Error (mR) prior to 40-m/s (90-mph) Retest

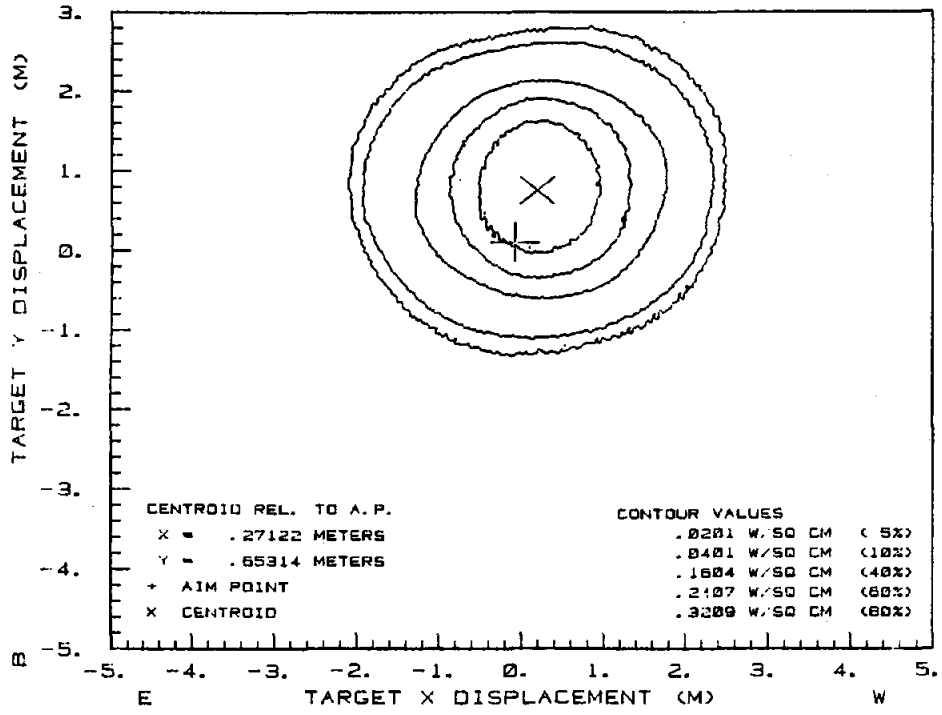

Figure A-9.15. MMC #2 Beam Quality Data following 40-m/s (90-mph) Retest

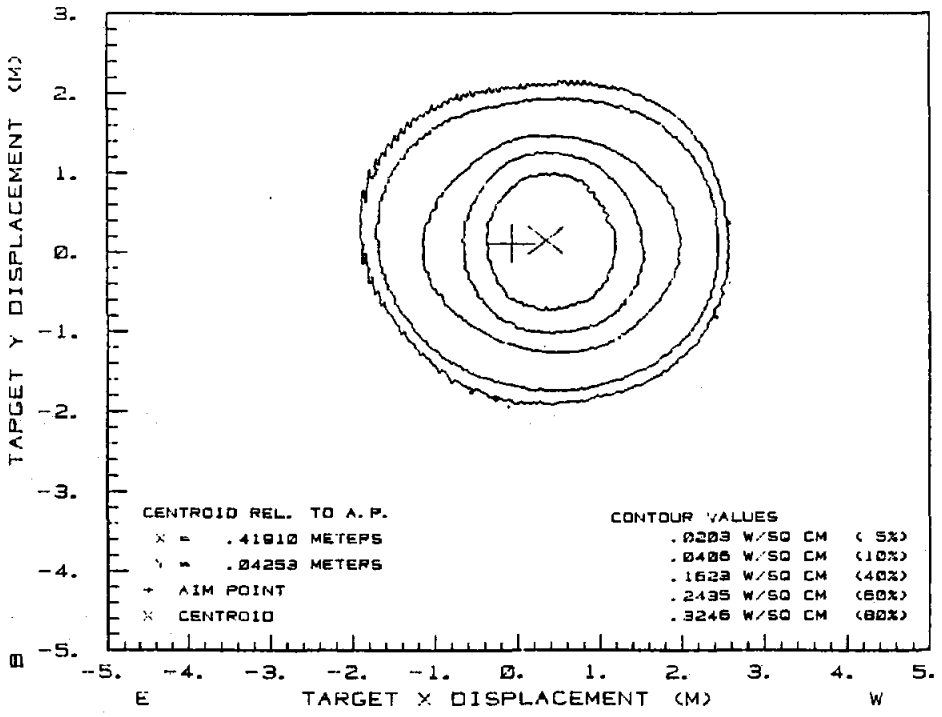

Figure A-9.16. MMC #2 Beam Quality Data following 25-Percent Overload Retest

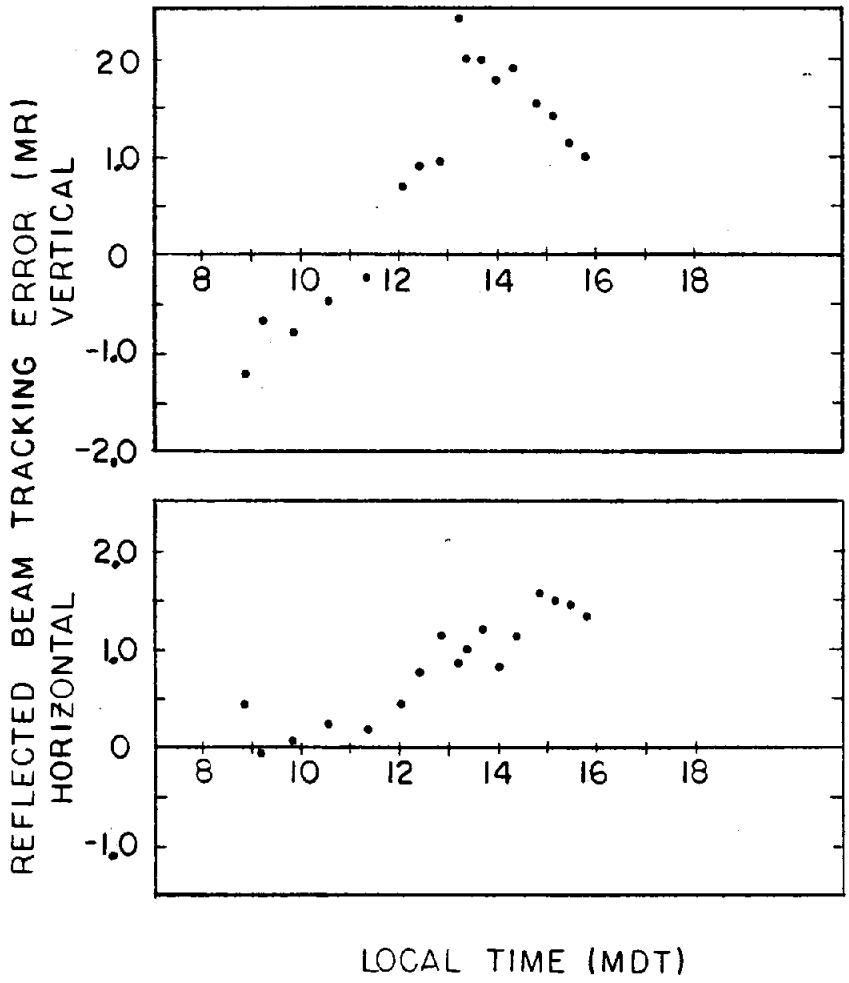

Figure A-9.17. MMC #2 Reflected Beam Angular Tracking Error (mR) following 25-Percent Overload Retest

Conclusions

From the results of this test it was concluded that the MDAC heliostat design suffered no significant beam quality or tracking accuracy degradation from the simulated 40-m/s wind loading. There was also sufficient margin of safety in the design to survive with no significant performance degradation simulated loads that were 25 percent above the 40 m/s wind load case.

The initial test of the MMC heliostat indicated an inadequate design, since both tracking accuracy and beam quality were significantly degraded by the simulated 40-m/s wind load. Welding the crossbeam to elevation tube interfaces on the heliostat eliminated the beam quality degradation problem as verified by a retest. Increasing the preload on the azimuth axis bearings, however, did not eliminate the occurrence of a residual deflection in the drive unit following the load testing. This residual deflection caused an unacceptable degradation in tracking accuracy. Additional testing was scheduled to identify the cause of the residual deflection and to arrive at an acceptable solution to the problem.

SECTION B--STRUCTURAL DRIVE ASSEMBLY TESTS

Introduction

The overall purposes of the structural drive assembly tests are: (1) to characterize the backlash and torsional stiffness of the azimuth and elevation drives of each design, (2) to determine whether the drive mechanisms will backdrive under load, and (3) to assess the adequacy of the motor torques under required loads.

These tests were performed at the static test frame located at SNLL on drive units consisting of all mechanical hardware between the top of the heliostat pedestal and the main elevation beam. A shortened (36") elevation beam was supplied by each contractor. Loads were applied to the drive units through the main beam in both azimuth and elevation by a pair of hydraulic linear actuators operating from a single computer-controlled pressure source. These equal and opposite loads resulted in a "pure moment" with no net force. Thus, the moment was the same at any point in the drive mechanism for a given load level. Elevation tilt or azimuth twist of the main beam was measured either with inclinometers or with a pair of base-mounted linear displacement gauges, depending on the load configuration.

The results of this testing were combined with the results of the NASTRAN structural analysis to determine whether the specification for maximum static deflections under a 27-mph wind load were met. Also, torsional stiffnesses for the drive mechanisms determined by this testing were used in the dynamic computer modelling of the heliostats to determine natural vibrational frequencies of the two designs.

Test B-1: Backlash and Stiffness

Objectives

The objective of this test was to measure the backlash and torsional stiffness characteristics of the azimuth and elevation drive mechanisms of both designs.

Description

Angular deflection versus applied torque was measured for the azimuth and elevation tracking drives of each test unit. For each drive axis and for the tracking positions indicated in the following paragraphs, three wind load levels were applied: (1) 27 mph--maximum wind at which beam performance requirements must be met, (2) 50 mph--maximum wind at which heliostats must operate and survive (not stowed) without subsequent impact on performance, and (3) 56 mph--which represents a 25-percent overtest to evaluate load-margin capabilities.

Using the criteria that a 20° wind angle of attack results in the maximum moment when the heliostat is operating in 50-mph or less wind loads, Table B-1.I gives the actual moment loads, calculated about the center of the reflective surface of each heliostat design, that were applied through a shortened elevation beam of each test unit (Figure B-1.1). These moment loads are computed from ASCE flat plate data (ASCE Paper 3269, Figure 5), using a moment coefficient C_m of 0.137. The torques are applied by equal and opposite forces resulting in a "pure moment" that is constant throughout the structure.

TABLE B-1.I

WIND MOMENTS AT 20° ANGLE OF ATTACK

Wind Speed (mph) at 30' above Ground	Moment (ft-lb) MMC	MDAC
27	2106	2387
50	7222	8185
56	9028	10231

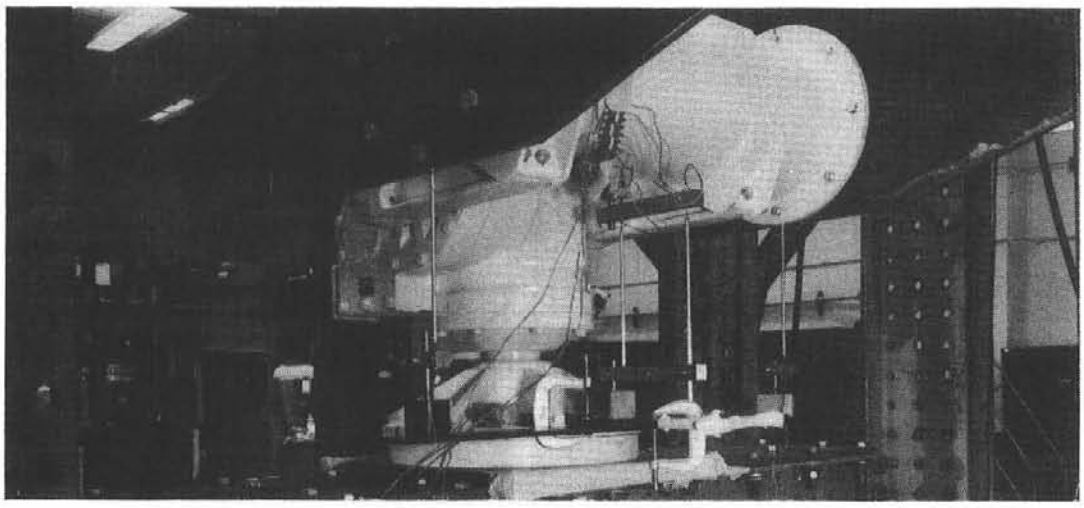

Figure B-1.1. MMC Drive Mechanism Structural Test Setup

Although the above wind moments are based on the 50-mph wind survival loads for the azimuth drives, the same moment loads were applied to the elevation drives, since the actual differences are insignificant and survival loads of the elevation drives are governed by the 90-mph wind in the stowed position (refer to Section A, Test A-9).

For each of the above moment loads applied, the drive unit was program loaded slowly to the maximum load at a uniform rate of 8000 ft-lb/min, with continuous measurement of angular deflection being automatically recorded. The load was then reduced to zero at the same uniform rate and simultaneously reversed until the same maximum load was applied in the opposite direction. Again, the load was reduced to zero and then repeated through the same reversing loads for another three cycles.

Azimuth Test Positions--Since the azimuth drive designs of both contractors' heliostats are symmetrical about the azimuth axis, their load/deflection response would be basically the same in any azimuth orientation. It was therefore only necessary to measure the three deflection vs moment loads at a single arbitrary azimuth position.

For applying the three moment loads through the elevation beam into the azimuth drives, the elevation beam was placed in the tracking position that corresponds to the mirrors being in a vertical orientation.

Elevation Test Positions--The three reversing moment loads previously described were applied to each of the three elevation beam positions that correspond to the following mirror orientations:

--mirrors face up
--mirrors at 45° elevation
--mirrors vertical

Inclinometers, one mounted on top of the main beam and one mounted on the drive mechanism base plate, were used to measure elevation tilt (Figure B-1.2). Azimuth twist was measured with two linear displacement transducers mounted from the base plate. The transducers also monitored the motion of the main beam, as shown in Figure B-1.3. Applied torque and angular deflections were recorded at 10-percent increments of the maximum torque.

Results

Torque versus angular displacement curves are shown for the MMC and MDAC drive mechanisms in Figures B-1.4 and B-1.5, respectively, for a 27-mph wind load. Results are plotted for the elevation drive in three positions and for the azimuth drive in one position. It is interesting to attempt to separate the "backlash," as exemplified by the jump in angular displacement near zero load, from the "stiffness," characterized by the flatter parts of the curves at the load extremes. The MMC azimuth drive is the clearest example of this separation.

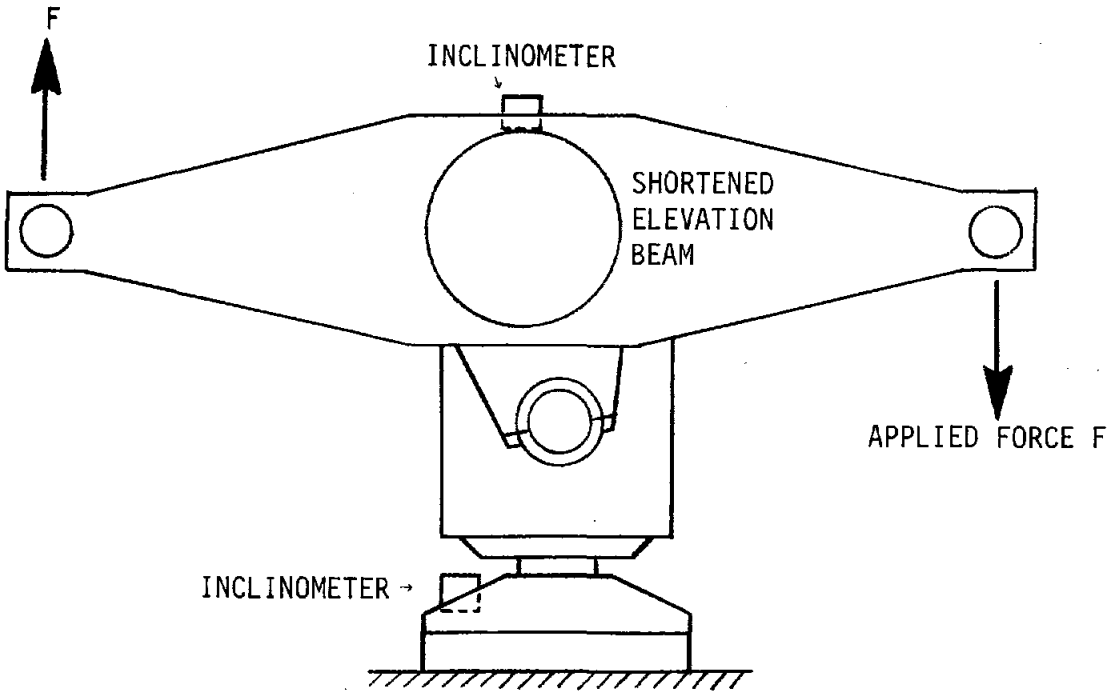

Figure B-1.2. Drive Mechanism Structural Test Setup for Elevation Test. Pure moment is applied with equal and opposite forces. Inclinometers measure tilt.

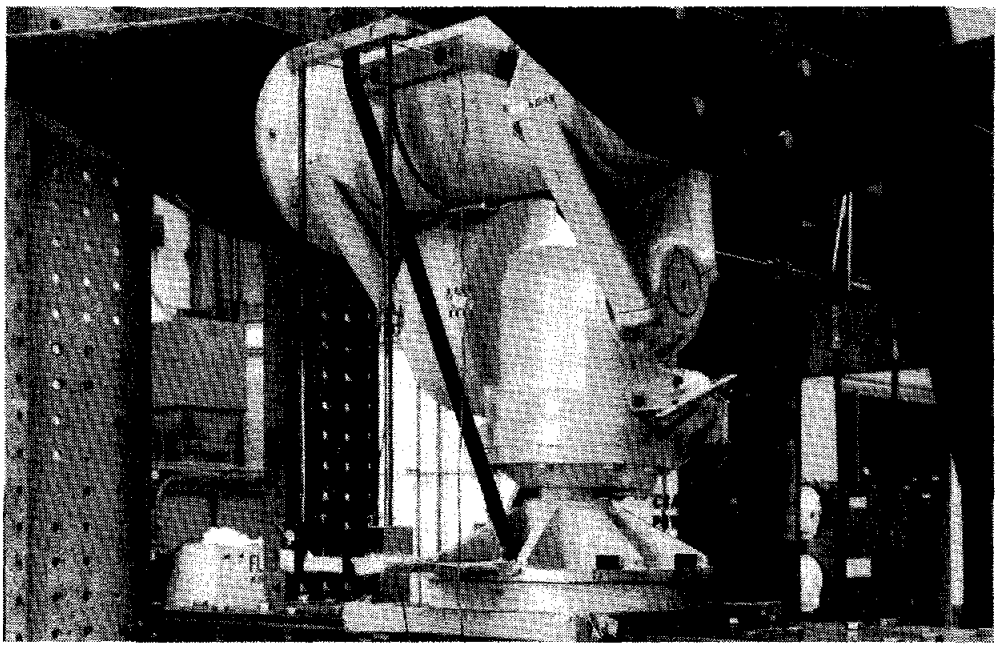

Figure B-1.3. MMC Unit in Azimuth Test. Twist of elevation beam was measured with two linear displacement gauges mounted from the base plate.

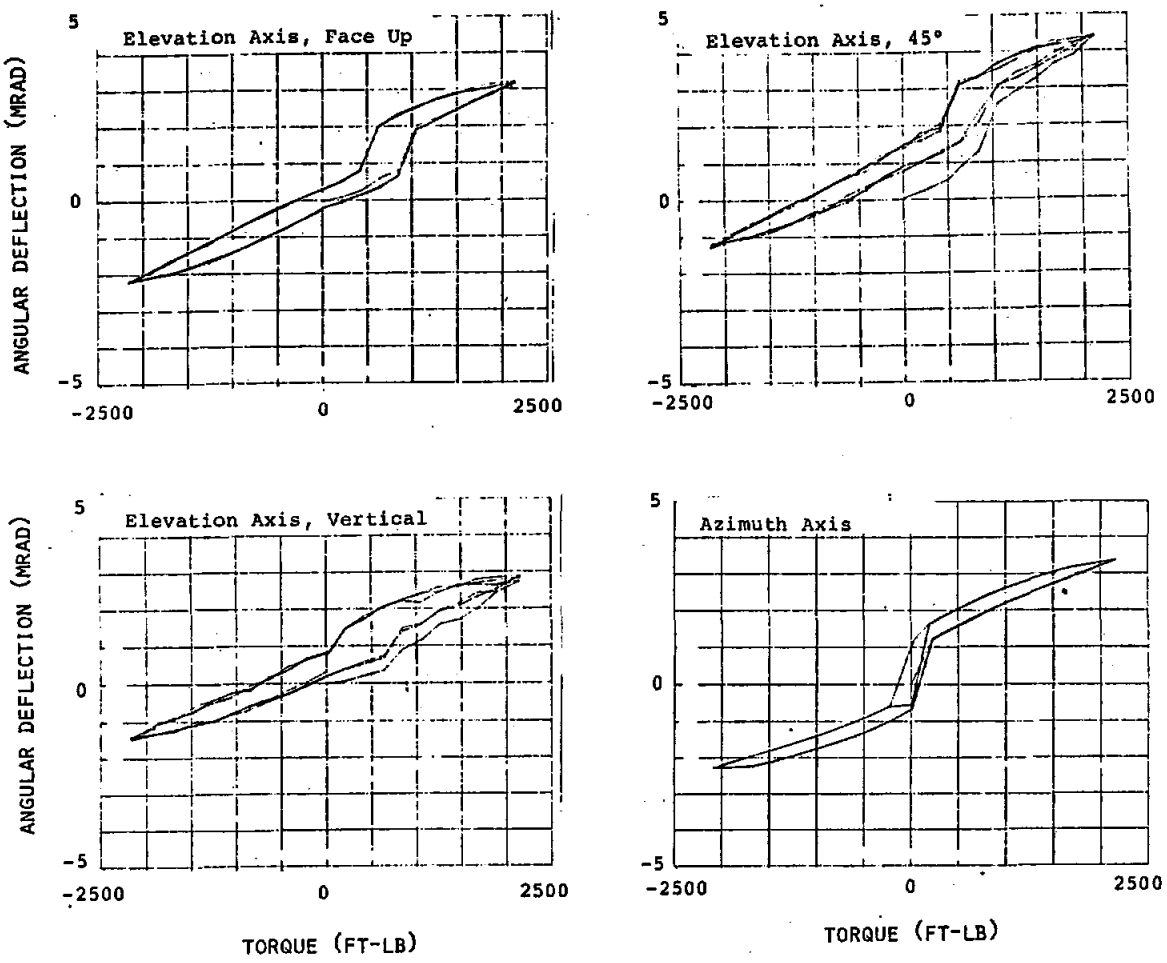

Figure B-1.4. MMC Drive Mechanism Deflections for ± 27-mph Wind Load

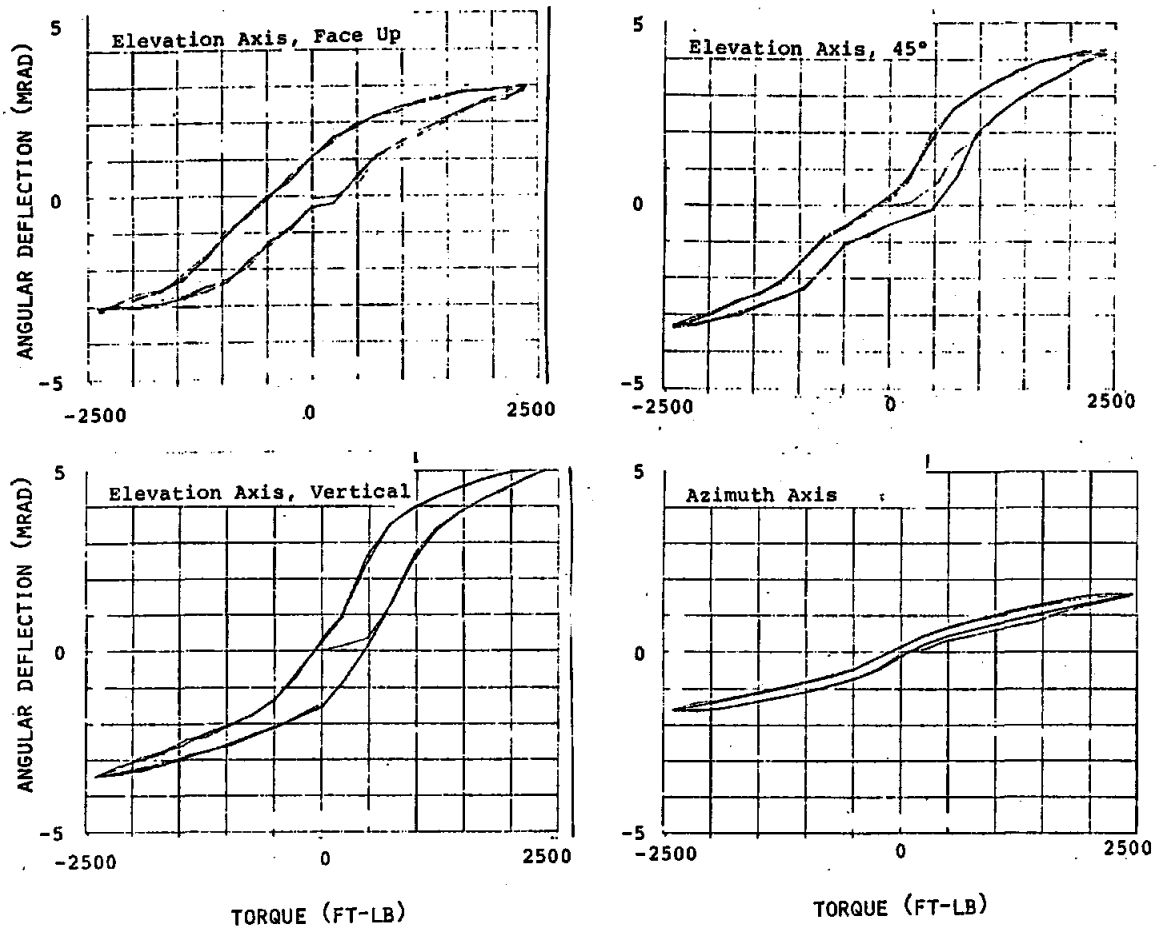

Figure B-1.5. MDAC Drive Mechanism Deflections for ± 27-mph Wind Load

The MMC elevation and azimuth drives have approximately equal total compliances and heliostat deflections in a 27-mph wind and were seen to be within specification.

The MDAC azimuth drive has very little compliance, showing almost no backlash and high stiffness. The MDAC elevation drive, however, is seen to suffer large angular deflections that worsen as the heliostat position is changed from face-up to vertical. The MDAC elevation drive unit had such large deflections that, when combined with the NASTRAN-calculated deflections of the remainder of the heliostat, the specified 3.60-mrad deflection of the reflective surface was exceeded in a 27-mph wind. MDAC stated that the excessive deflection was due to improper adjustments in the elevation jacks. A retest of the MDAC elevation drive was performed.

MDAC was allowed to make two adjustments to the elevation tracking and stowage jacks: (1) the backlash in the linear actuators was adjusted and (2) the jack barrels were tightened into the trunnion blocks and bottomed. The drive was retested with the drive in a "mirrors vertical" configuration. The

results showed a decrease in the peak-to-peak angular deflection of 1.44 mrad. It was shown that this reduction in deflection was enough to bring the MDAC heliostat within specification without any hardware changes.

The results of the 27-mph and 50-mph wind load tests are summarized in Table B-1.II. The drives were also subjected to loads 25 percent in excess of the 50-mph wind load as an overtest. The azimuth drives are required to withstand a 50-mph wind load without damage. Both designs took the 50-mph wind and a 25-percent overload with no apparent damage. The 50-mph wind load and the 25-percent overload were performed on the elevation drive for information only, as the maximum load condition for the elevation drive occurs in a 90-mph wind and was tested in Section A, Test A-9.

TABLE B-1.II

PEAK-TO-PEAK ANGULAR DEFLECTIONS (mrad) OF DRIVE MECHANISMS UNDER LOAD

Wind Load	Contractor	Azimuth Drive	Elevation Drive Face Up	Elevation Drive 45°	Elevation Drive Vertical
27 mph	MMC	5.7	5.4	5.7	4.4
	MDAC	3.1	6.1	7.2	8.3 (6.8)*
50 mph	MMC	19.5	20.5	21.1	18.0
	MDAC	9.7	12.9	17.2	17.9 (16.3)*

*After adjustment of backlash in jacks.

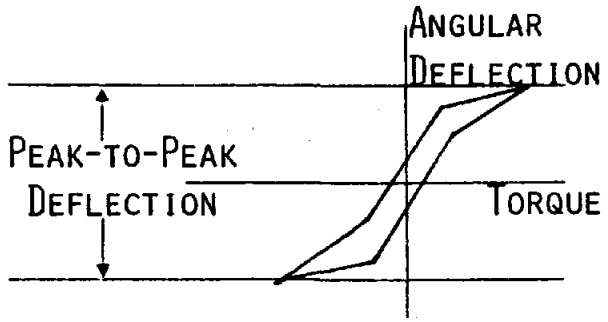

Conclusions

In Table B-1.III, the results of this test are combined with NASTRAN structural analysis results to determine a worst-case pointing error in a 27-mph wind. The drive mechanism deflection was assumed to be one-half of the peak-to-peak deflection shown in Table B-1.II. The total pointing error should not exceed 3.60 mrad. It is seen that the MMC heliostat met this

requirement by a comfortable margin in both azimuth and elevation. The MDAC heliostat was very stiff in azimuth, but initially did not meet specifications in elevation and was only marginal after MDAC made corrective adjustments.

TABLE B-1.III

RESULTS OF WIND LOAD ANALYSIS

	MMC		MDAC	
	Azimuth	Elevation	Azimuth	Elevation
Pedestal and Mirror Support Structure Deflection (mrad)[a]	± 0.36	± 0.43	± 0.75	± 0.91
Measured Drive Mech. Deflection (mrad)[b]	± 2.86	± 2.82	± 1.56	± 3.38 (± 2.66)[c]
Total Pointing Error (mrad)[d]	± 3.22	± 3.25	± 2.31	± 4.29 (± 3.57)[c]

[a]Deflections calculated with NASTRAN for a 27-mph wind at 20° angle of attack for either elevation or azimuth.

[b]Measured drive mechanism compliance = ± (peak-to-peak deflection/2).

[c]Values in parentheses were measured after backlash adjustments on MDAC elevation drive were made.

[d]Specification requires this value to be less than 3.60 mrad.

Test B-2: Mechanical Drift

Objective

The objective of this test was to determine whether the azimuth drive mechanisms will mechanically drift or "backdrive" when submitted to their maximum survival load. (Mechanical drift of the elevation drives was evaluated in Test A-9, Section A, since the maximum survival load on the elevation mechanisms occurs at the 90-mph wind in the stowed position.)

Description

Upon completion of the azimuth series of programmed moment loads vs angular deflection, the moment load was increased back up to 50-mph load equivalent (in either direction) and held there long enough to assure that no drift or "backdriving" was occurring. The load was then increased to 56 mph equivalent and again evidence of mechanical drift was sought.

Results

Both azimuth drive designs showed no evidence of backdrive in either a 50-mph wind load or a 25-percent overload.

Conclusion

The high gear ratios of these drive mechanisms preclude backdriving under load.

Test B-3: Motor "Stall" Torques

Objective

The objective of this test was to determine whether the drive motors can produce enough torque in both the azimuth and elevation axes to drive the heliostats against a 50-mph wind load.

Description

The azimuth and elevation mechanisms were driven against resisting moment loads, which represent the 50-mph wind loads and the 56-mph (25-percent overtest) margin evaluation. The basic moment loading mechanisms employed in Tests B-1 and B-2 were used to provide the resisting moment loads.

The loading mechanism in a load-control mode was set to a 50-mph wind load and the drive mechanism motor was energized. The drive mechanism was observed to drive against a constant moment for 30 seconds. When no evidence of stalling occurred during the 50-mph test level, the test was repeated at the 56-mph load level that provided assessment of load-margin capability.

Results

Both azimuth and elevation drive mechanisms of the two designs were able to drive against the 50-mph wind load and the 25-percent overload with no indications of motor stall. The measured current draws at slew speed were recorded as follows:

	MMC (110 VDC, amps)	MDAC (208 V, 30, amps/phase)
Azimuth		
No Load	0.47	1.0
50-mph Wind	1.9	1.3
Elevation		
No Load	0.64	1.0*
50-mph Wind	2.5	1.7*

*Value measured for both tracking and stowing jack motors.

Conclusion

Motor power is sufficient to drive a heliostat without stalling in a 50-mph wind for both designs with at least a 25-percent margin.

SECTION C--ENVIRONMENTAL DRIVE ASSEMBLY TESTS

General

The primary purpose of this test series was to assess the capability of each contractor's drive assembly (AZ-EL drive mechanism) and its associated HC and HFC systems to meet their operational and survival requirements under the specified conditions of temperature extremes and moisture exposure. A secondary objective was to obtain additional life-cycle data under these environments that, in conjunction with the limited life-cycle data obtained from the ambient tested CRTF units (Section A, Test A-8), would provide a basis to judge the 30-year life potential and anticipated maintenance problems of both designs.

To achieve these objectives, production representative drive mechanisms and control systems were tested, but the mirror modules and their supporting structures were only weight simulated for mass/CG offset loading, plus an assumed nominal 15-mph wind load. The general configuration of the test drive assemblies as furnished by the two contractors are shown on MMC Drawing 40M500-5132729 and MDAC Drawing ID22715. Figure C-1 shows both contractors' units installed in the environmental test chamber at Pacific Missile Test Center, Point Mugu, CA.

Besides the heliostat test hardware shown inside the chamber, each contractor was required to furnish an external (outside the chamber) controller that would substitute for the normal HAC functions. As a minimum, each contractor was to provide manual control capability to any heliostat position, plus an automatic 24-hr/day operating cycle that would result in approximately 90° of azimuth and elevation travel at combined track and slew rates of about 0.5 mrad/s. The following control system descriptions give more specifics as to how the contractors fulfilled these various requirements.

MMC Heliostat

The heliostat control system consisted of the HFC and HC installed in the pedestal, with incremental encoders installed on each output axis. The azimuth encoder is installed inside the pedestal to the underside of the gear box/pedestal adapter, and the elevation encoder is installed outside on the gear housing wall in line with (and sensing) the elevation shaft rotation. A test component, stimulator, was used to send the heliostat commands and to control the cycling. The stimulator was located outside the chamber and was

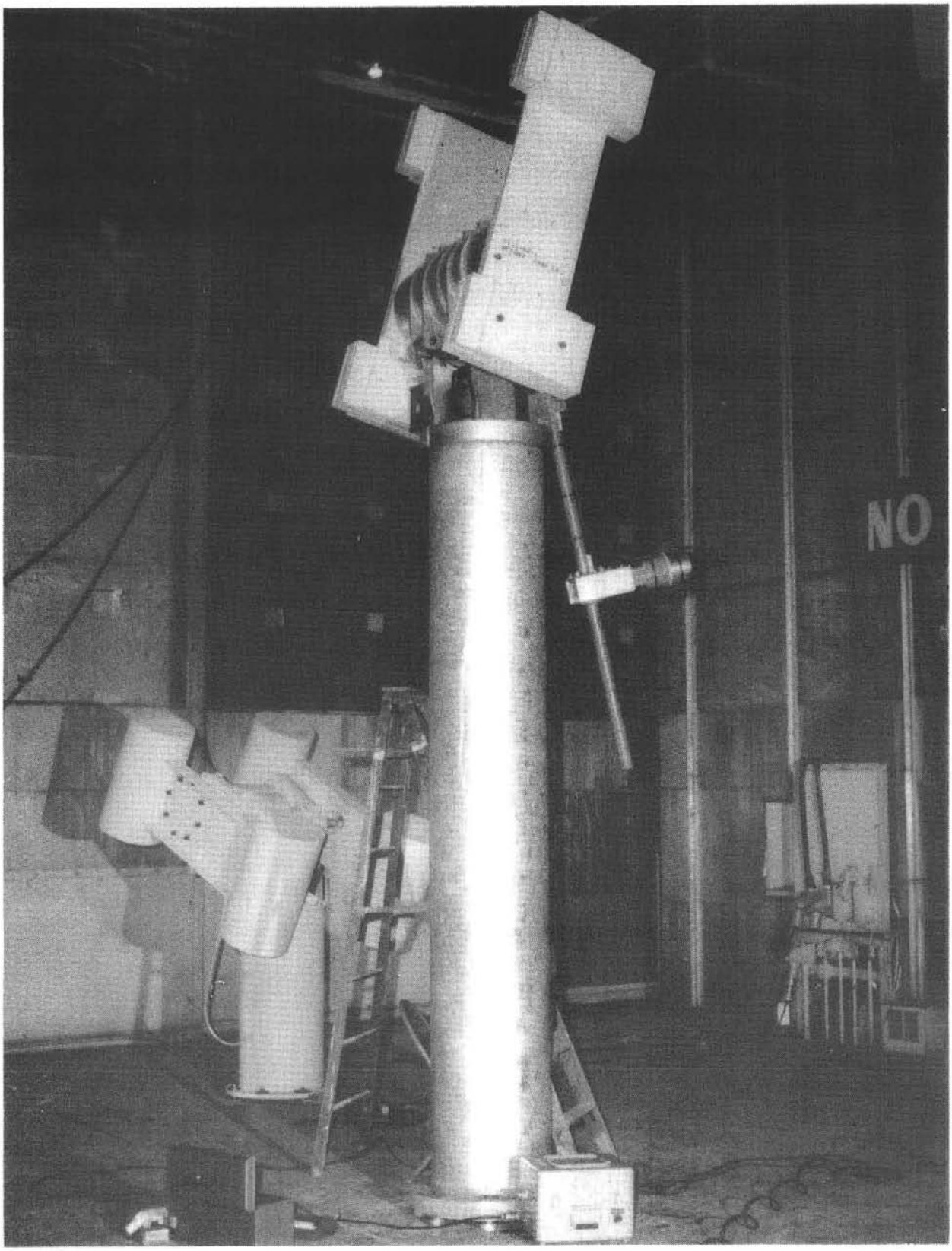

Figure C-1. MMC and MDAC Test Drive Assemblies Installed in Environmental Test Chamber

connected to the HFC by a cable. The stimulator acted as the HAC and the HFC passed commands to the HC that moved the heliostat to the desired position.

MDAC Heliostat

The heliostat control system consisted of an HFC and HC; however, during the first three tests only the HC was operated. The HFC was installed and powered but not operated. The HFC program memory was not available until the high temperature cycle, Test C-4. The Portable Control Unit (PCU) was used to send commands to the HC, and later to the HFC, to control the heliostat movement and cycling. A special program was installed in the HC for Tests C-1 through C-3 that accomplished the cycling. After the HFC program was installed, it controlled the cycling, and the HC software was changed to represent the production version. In each case the components containing the programs were Programmable Read Only Memories (PROM). The HFC had a special PROM containing the operating software and the cycling routines. The normal HFC contained only minimal software in PROM. The operating software was down-loaded from the HAC. Since the HAC was not available, and the PCU did not have the capability to down-load software to the HFC, a special PROM was used for these tests.

During the first three tests the HC could not operate the heliostat over the desired 90-degree movement in each axis. The cycle was redefined as 66 degrees in azimuth and 70 degrees in elevation.

Test Description

The overall environmental drive test plan, as shown in Figure C-2, spans eight, seven-day weeks in the temperature/humidity chamber, with approximately a week's time allowed before testing to install and check out the units. Because of schedule and economic constraints, it was established that the test would start at a fixed deadline date, regardless of a contractor's readiness, and that only minimum delays would be tolerated in the test conductance if a contractor's unit broke down. If repair or replacement could not be accomplished in a reasonable time, or within the environmental test conditions existing in the chamber, then the testing took precedence and the contractor would suffer in the evaluation.

The basic plan involved testing in two parts: the first part consisted of approximately 5-1/2 weeks of temperature extremes, with Part 2 covering moisture exposures for the remaining 2-1/2 weeks. Following this, both units were immediately disassembled and inspected for evidence of moisture penetration, plus signs of malfunction or abnormal wear. Temperature testing was further divided into three high and low performance or survival ranges required in the specification (Tests C-1 through C-3). The tests then were repeated at 25 percent overtest levels (with additional cycling) to determine if prior acceptable performance was only marginal or not (Tests C-4 through C-6). Test C-7 consisted of nearly two weeks of 94-perent humidity exposure

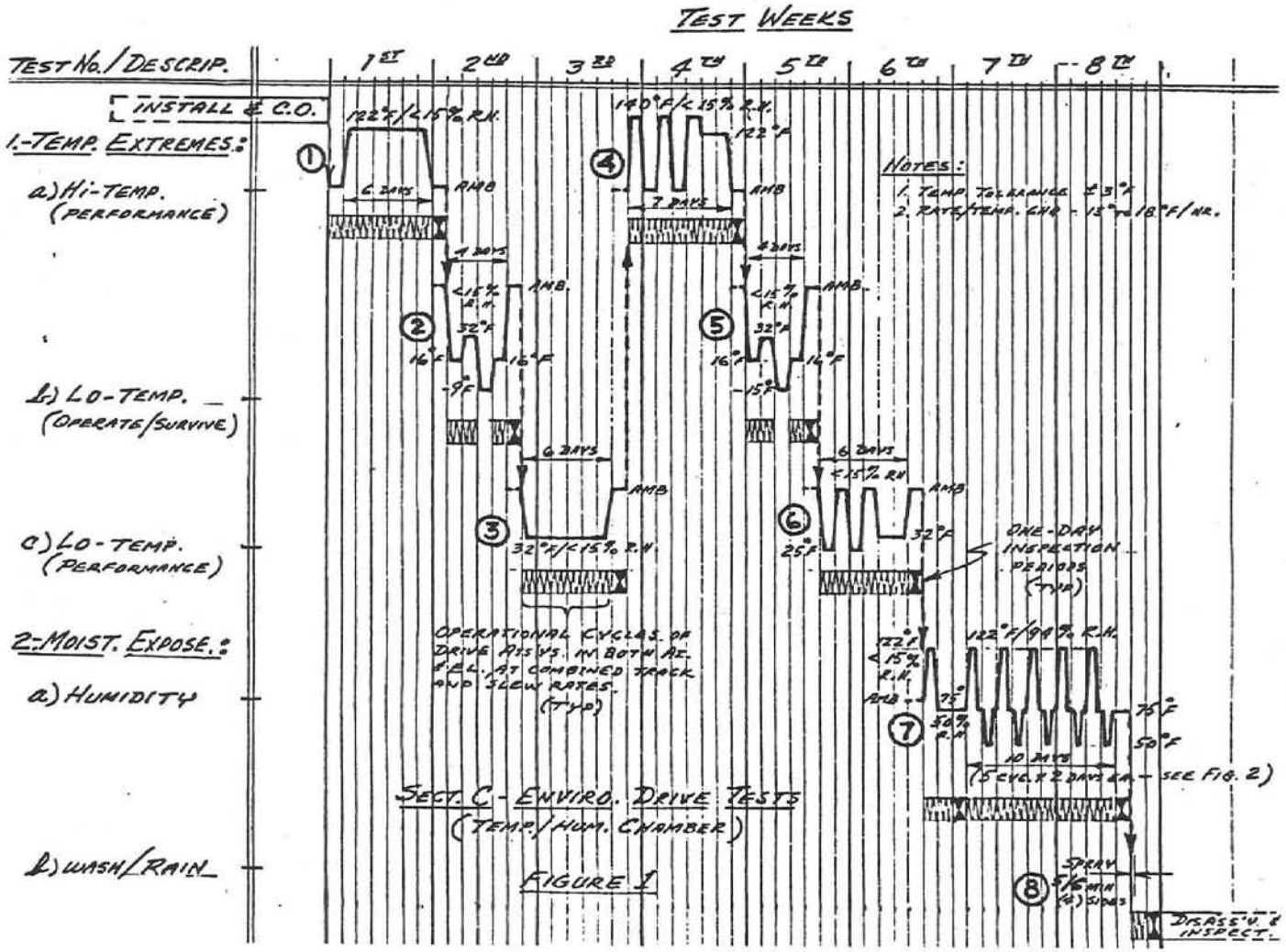

FIGURE 1

Figure C-2. Environmental Drive Test Plan

(after a short initial drying-out cycle) aided by two-day cycles of alternate high and low temperature pumping action. Test C-8 is the final environmental test in which water is sprayed directly on the overall drive assembly and controls to simulate a mirror wash or wind-driven rain. Figure C-3 shows the portable stand that was rigged with nozzles to apply the spray.

Figure C-3. Rain Fixture

The zig-zag bars beneath each test temperature cycle, shown in Figure C-2, represent the nearly continuous automatic operational cycle the drive assemblies were submitted to in the chamber. The principal exception to the continuous operational cycling were the one-day inspection periods following each test series, as indicated by the single cross-blocks at the end of the zig-zag bars. These one-day inspection periods allowed time for the test chamber to return to ambient conditions and for the test conductor to enter the chamber, operate the drive assemblies, and visually observe any evidence of malfunction or wear.

In-Process Test Results

The following outline delineates each test and gives the results occurring during the test or observed during the one-day inspection period at the end of each test.

Test C-1: High-Temperature Extreme

This test was at 122°F and about five percent relative humidity for six days or 144 total hours. Figure C-1.1 shows the test cycle.

The MMC heliostat completed 74 cycles of 90-degree movement in both azimuth and elevation during the test. The control system operated correctly. A small amount of oil was found to be seeping from the lower azimuth shaft/seal and from around the azimuth cover/housing interface.

The MDAC heliostat completed 133 azimuth cycles and 124 elevation cycles during the test. The control system consisted of only the heliostat controller with a special program to do the cycling. This limited the operation of the heliostat to 66 degrees in azimuth and 70 degrees in elevation. The control system operated correctly. There was oil on the floor from the azimuth gearbox and bottom seal on the elevation jack housing.

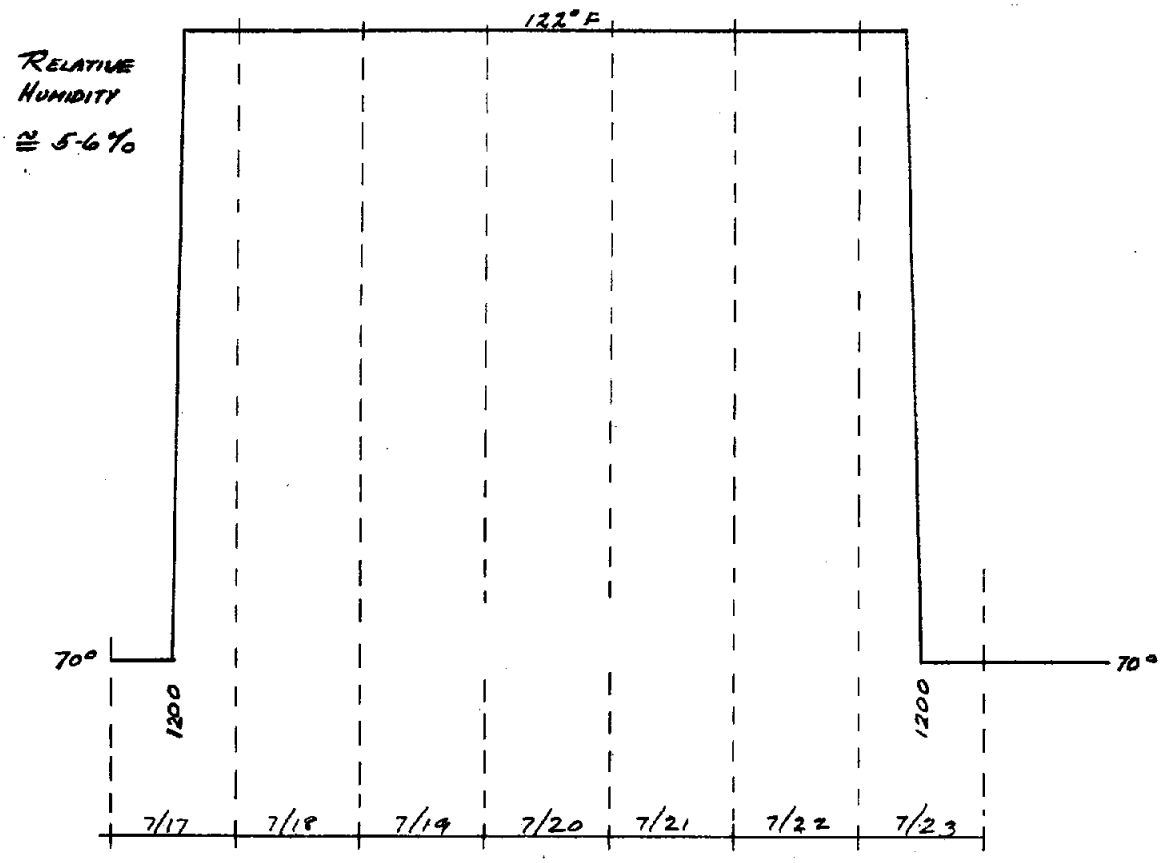

Figure C-1.1. High-Temperature Test Cycle

Test C-2: Low-Temperature Cycle

This test subjected the heliostat to the low temperature environments of 16, 32, and -9°F. Figure C-2.1 shows the test cycle. The heliostats were not operated during the -9°F portion of the test, since controller operation is not required below 16 degrees.

The MMC heliostat completed 39 cycles of 90° movement in azimuth and elevation during the test. The control system operated correctly during the test.

The MDAC heliostat completed 70 66°-azimuth, and 66 70°-elevation cycles during the test. The control system operated correctly during the test.

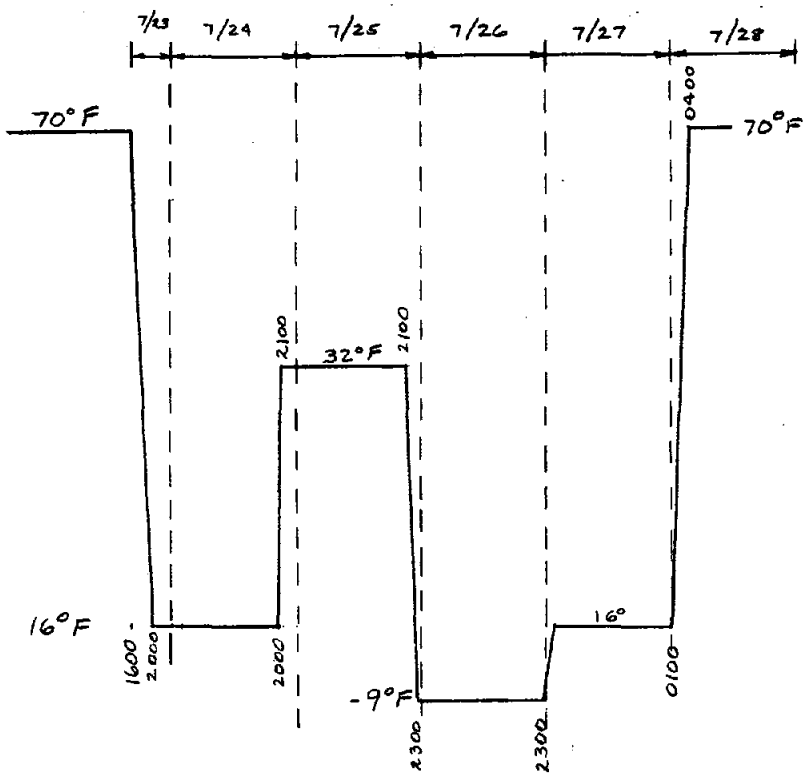

Figure C-2.1. Low-Temperature Test Cycle

Test C-3: Low-Temperature Extreme

This is a test at 32°F for six days, or 144 total hours. Figure C-3.1 shows the test cycle and any heliostat halts which occurred.

The MMC heliostat completed 63 cycles of 90° movement in azimuth and elevation. THe controller halted once during the test (MMC #1). MMC replaced an opto-isolator component in the HC. Upon postmortem the opto-isolator was found to be functional. MMC believed it was a socket problem. Testing resumed with no further problems.

The MDAC heliostat completed 114 66°-azimuth, and 106 70°-elevation cycles during the test. The controller operated correctly during the test.

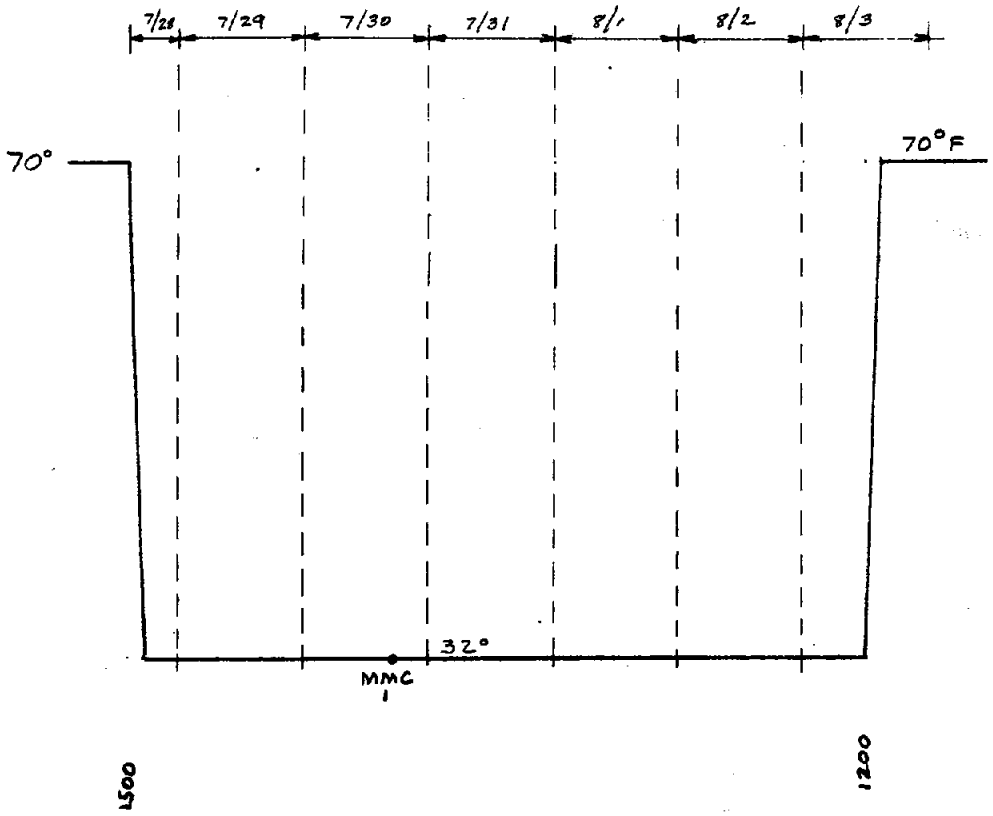

Figure C-3.1. Low-Temperature Extreme

Test C-4: High-Temperature Cycle (Overtest)

This test is a temperature cycle between 70 and 140°F for 2.5 daily cycles and one two-day hold at 122°F. Figure C-4.1 shows the test cycle and any heliostat halts which occurred.

The MMC heliostat completed 74 cycles of 90° movement in azimuth and elevation during the test. There was a malfunction of the stimulator and/or a communication error with the HFC during the test (MMC #2). The control system was restarted immediately with no further problems.

The MDAC heliostat completed 64 cycles of 90 degrees in azimuth and elevation during the test. The heliostat field controller was installed at the start of this test. This allowed the cycle to be increased to 90 degrees. As the heliostat neared 140°F the controller failed (MDAC #1). MDAC replaced the azimuth motor triacs in the HC. As the heliostat was again nearing 140°F the controller failed again (MDAC 2). MDAC replaced the HFC boards and the motor control board (A2) in the HC. The motor control board had blown circuit paths. The triacs were not damaged. The HFC had a temperature problem with one of the integrated circuits. The replacement HFC had been tested to the high temperature and worked correctly.

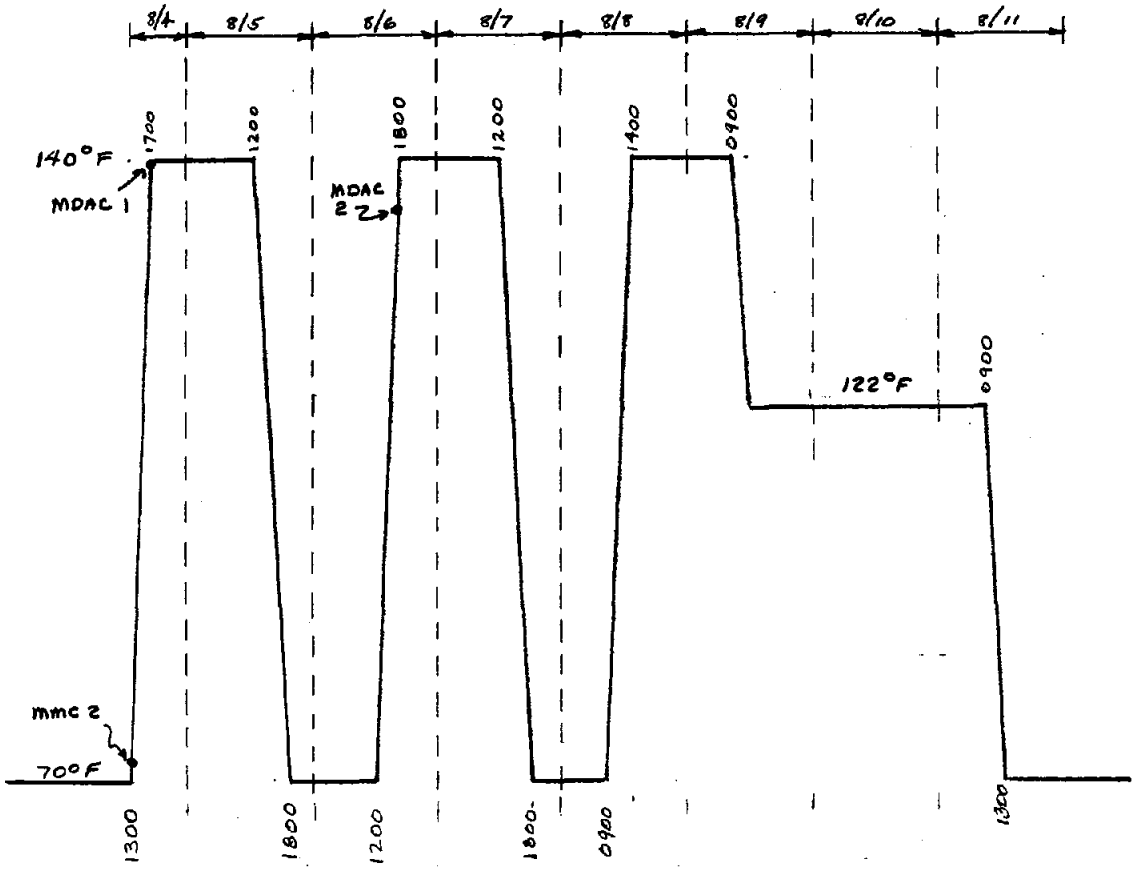

Figure C-4.1. High-Temperature Cycle (Overtest)

Test C-5: Low-Temperature Cycle

The low temperature cycle is described in Figure C-5.1. The points where the heliostats halted are noted.

The MMC heliostat completed 50 cycles of 90° movement in azimuth and elevation. The heliostat stopped once about 44 hours into the test, at 32° (MMC #3). Two attempts were required to restart the controller. This was later attributed to an HC computer software stack overflow problem. The cycling resumed with no further problems.

The MDAC heliostat completed 47 cycles of 90° movement in azimuth and elevation. While at a temperature of 25° the heliostat went to the azimuth and elevation limit and stopped (MDAC #2). MDAC changed the restart procedure to get the system cycling. A large amount of oil was observed running down the pedestal. Two pints of oil were added to the drive by MDAC (MDAC #4).

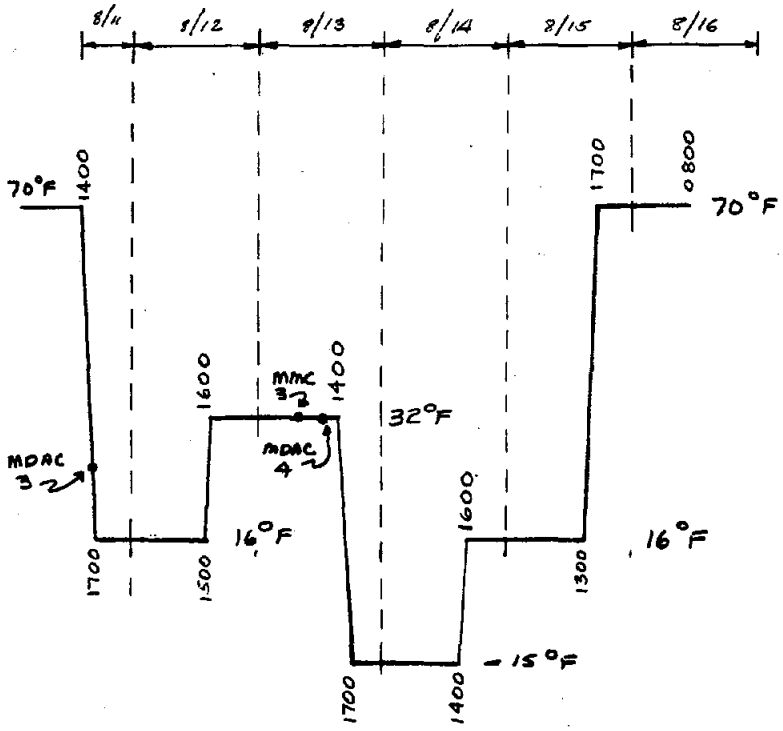

Figure C-5.1. Low-Temperature Test Cycle

Test C-6: Low-Temperature Extreme Cycle

The temperature was cycled from 70 to 25°F for three daily cycles and one cycle to 32°F. Figure C-6.1 shows the test cycle.

The MMC heliostat completed 56.5 cycles of 90° movement in azimuth and elevation. The heliostat stopped during the test (MMC #4). This was attributed to a power drop out, since the MDAC heliostat also stopped. The heliostat stopped a second time at 32 degrees and was restarted without problem (MMC #5). This was attributed to the HC stack overflow problem.

The MDAC heliostat completed 76 cycles of 90° in azimuth and elevation. The heliostat stopped during the test (MDAC #5). This was attributed to a power drop out as the MMC heliostat also stopped. The cycling resumed with no further problems.

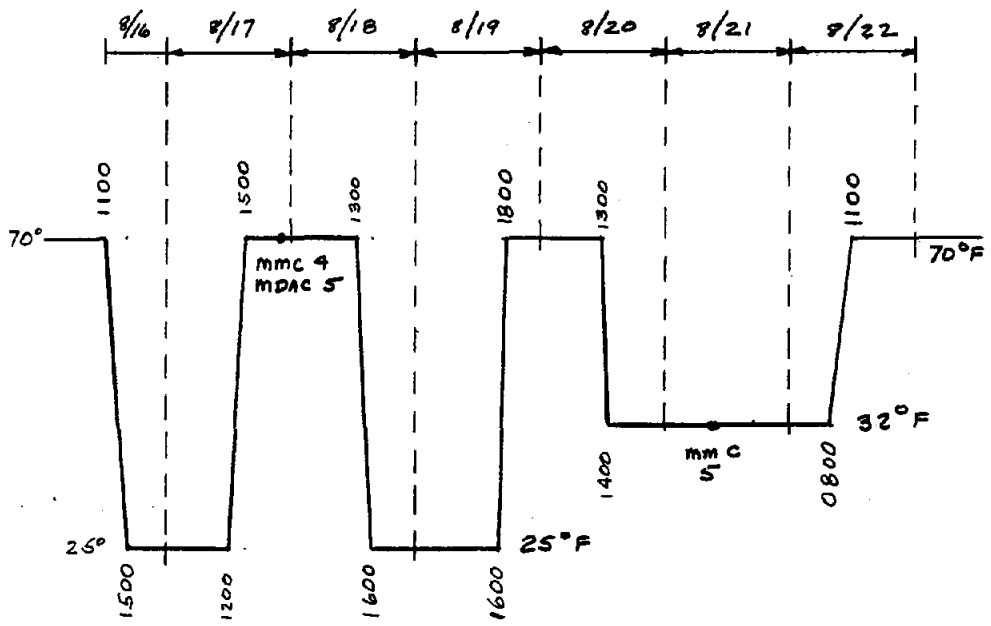

Figure C-6.1. Low-Temperature Extreme

Test C-7: Temperature Humidity Cycle

After an initial "drying out" cycle at 122°F and < 15 percent relative humidity, there was a two-day "soak" at 75°F and 50 percent relative humidity, followed by continuous exposure to 94-percent relative humidity, with cyclic thermal pumping between 50°, 75°, and 122°F. Initially, only 10 days or five thermal cycles were planned, but 14 days or seven thermal cycles were actually accomplished. Figure C-7.1 shows the test cycle and the heliostat failures that occurred.

The MMC heliostat completed 144.7 cycles of 90° movement in azimuth and elevation. There were six controller halts during the test. Three of them were during the transition from 75° to 122°F at 94-percent relative humidity (MMC #7, 9, 10). The failures all occurred at about the same time after the transition started. It was decided that the cause was due to moisture condensation on the controller circuit boards (the humidity is not controlled during the transitions). The other failures were attributed to the HC stack overflow (MMC #6, 8, 11). MMC installed a new program memory component (EPROM) with the HC stack overflow problem fixed. There were no further failures during the remaining two cycles of the test.

The MDAC heliostat completed 186 cycles of 90° in azimuth and elevation. There were four shutdowns during the test. Three were azimuth limit switch halts (MDAC #6, 7, 8). The heliostat went to the azimuth limit switch and stopped. MDAC changed the elevation cycle limit to 45 degrees so it would not go too near the limit switch. The fourth failure was a triac in the azimuth motor control board (MDAC #9). The elevation cycle was changed to 67.5 degrees for the rest of the test.

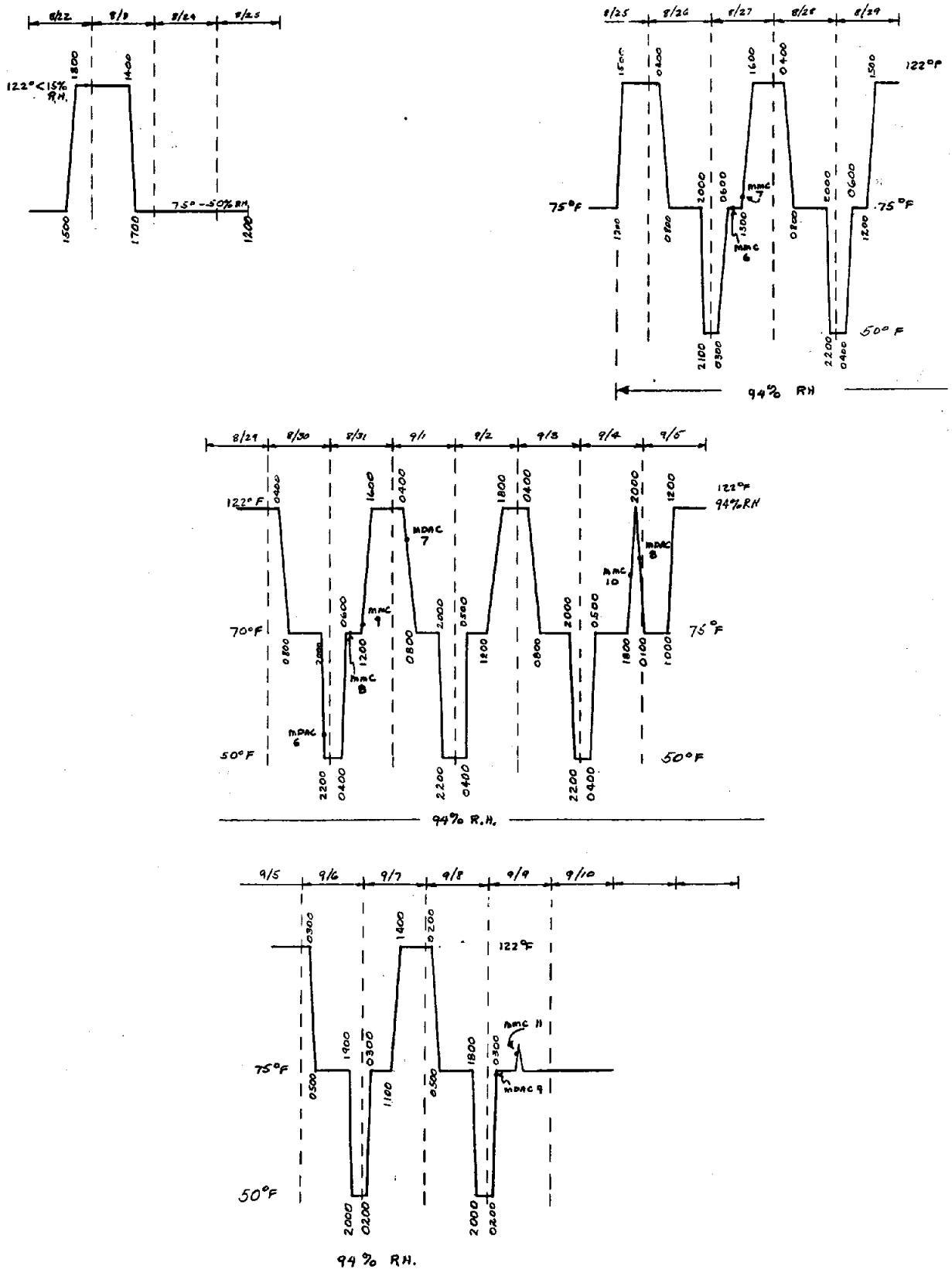

Figure C-7.1. Temperature Humidity Test Cycle

Test C-8: Wash/Rain

Both heliostats were sprayed with water for five minutes from each of four sides and then operationally cycled for one hour. Both heliostats performed satisfactorily after the test.

Posttest Inspection Results

Both heliostats were disassembled immediately after the completion of the wash/rain test. Photographs and notes were taken on the observations during the inspection. The following is a summary of the observations made, separated by control system vs mechanical drive assembly for each contractor's unit.

MMC--Drive Assembly (less control system)

No moisture had penetrated into either the AZ or EL gear box compartments (Figures C-8.1 through C-8.3). The AZ-EL gear trains and roller bearings generally looked good, with litle indication of wear occurring within the 90° cyclic loading regions on the large helical output gears (Figures C-8.4 through C-8.8).

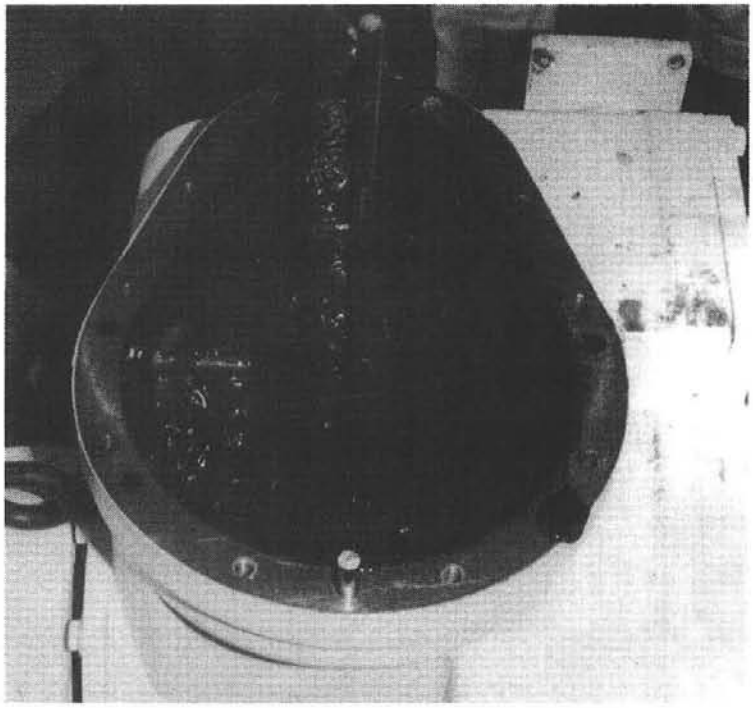

Figure C-8.1. MMC Azimuth Drive Housing after Test

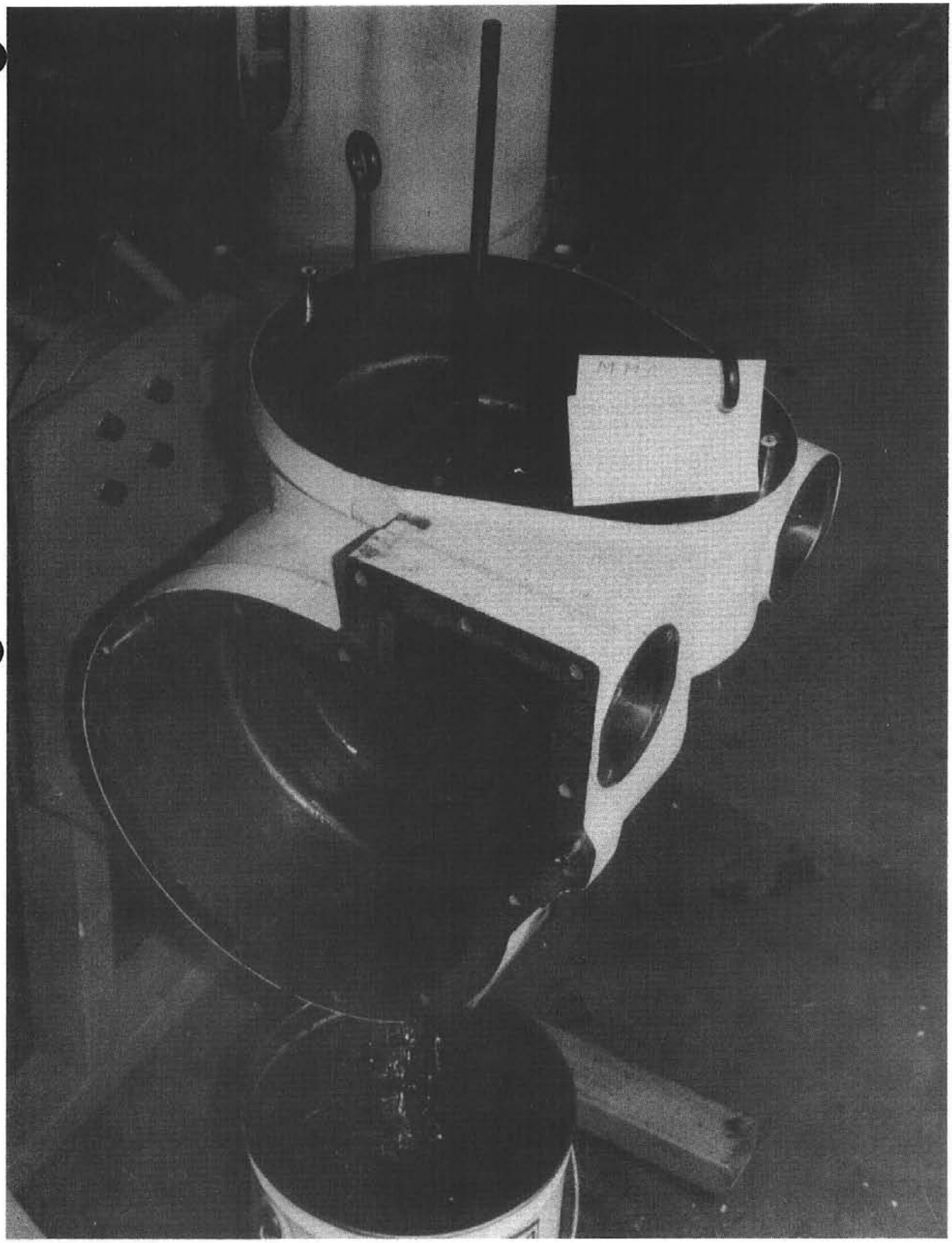

Figure C-8.2. MMC Azimuth and Elevation Housing after Test

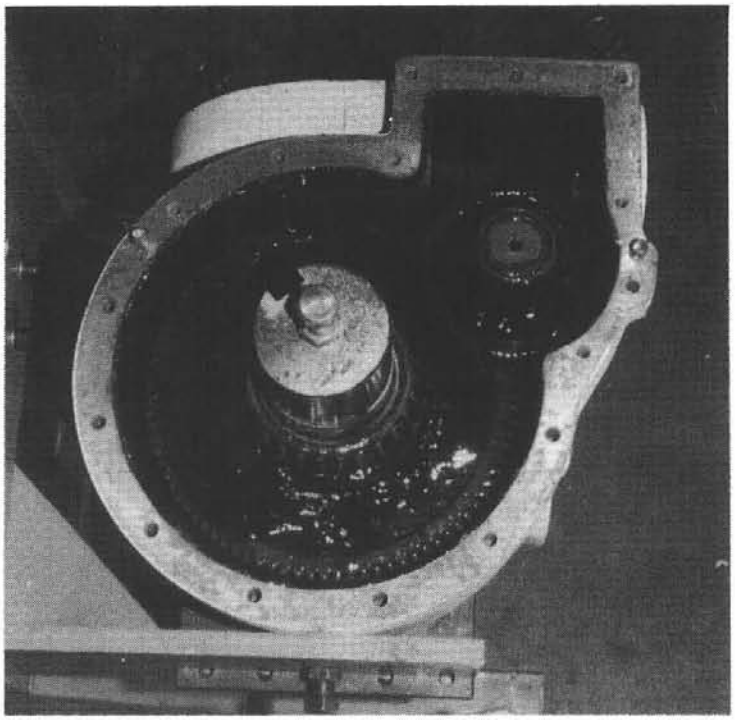

Figure C-8.3. MMC Elevation Drive Train in Housing after Test

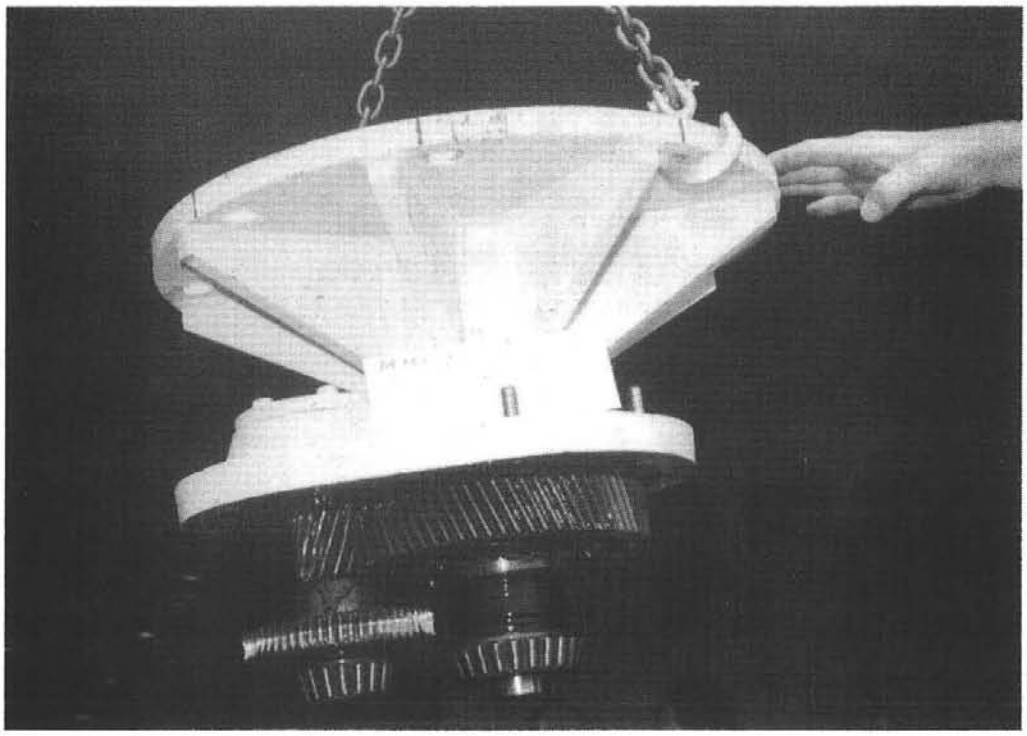

Figure C-8.4. MMC Azimuth Drive Train after Test

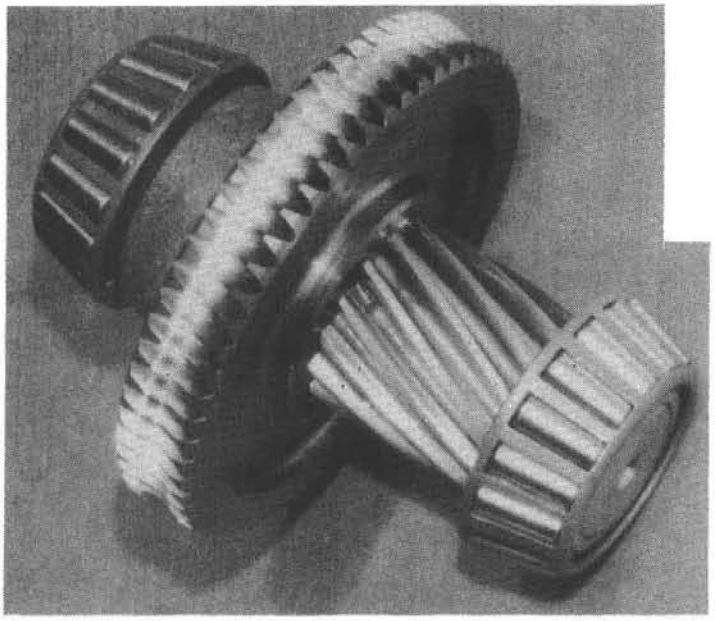

Figure C-8.5. MMC Elevation Worm Gear and Pinion

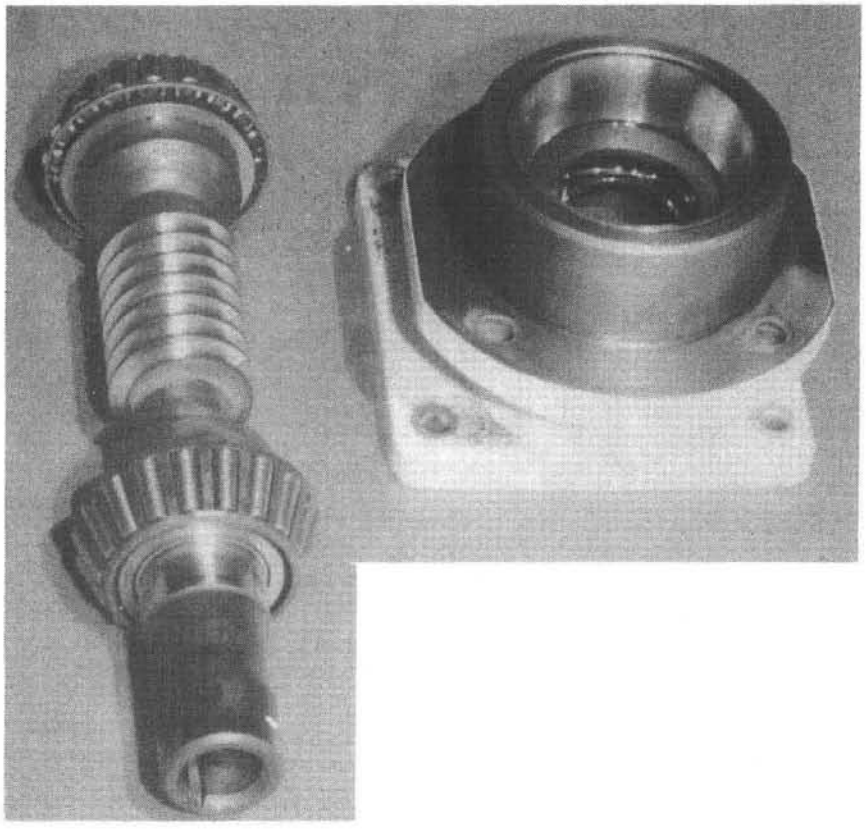

Figure C-8.6. MMC Elevation Input Worm and Shaft

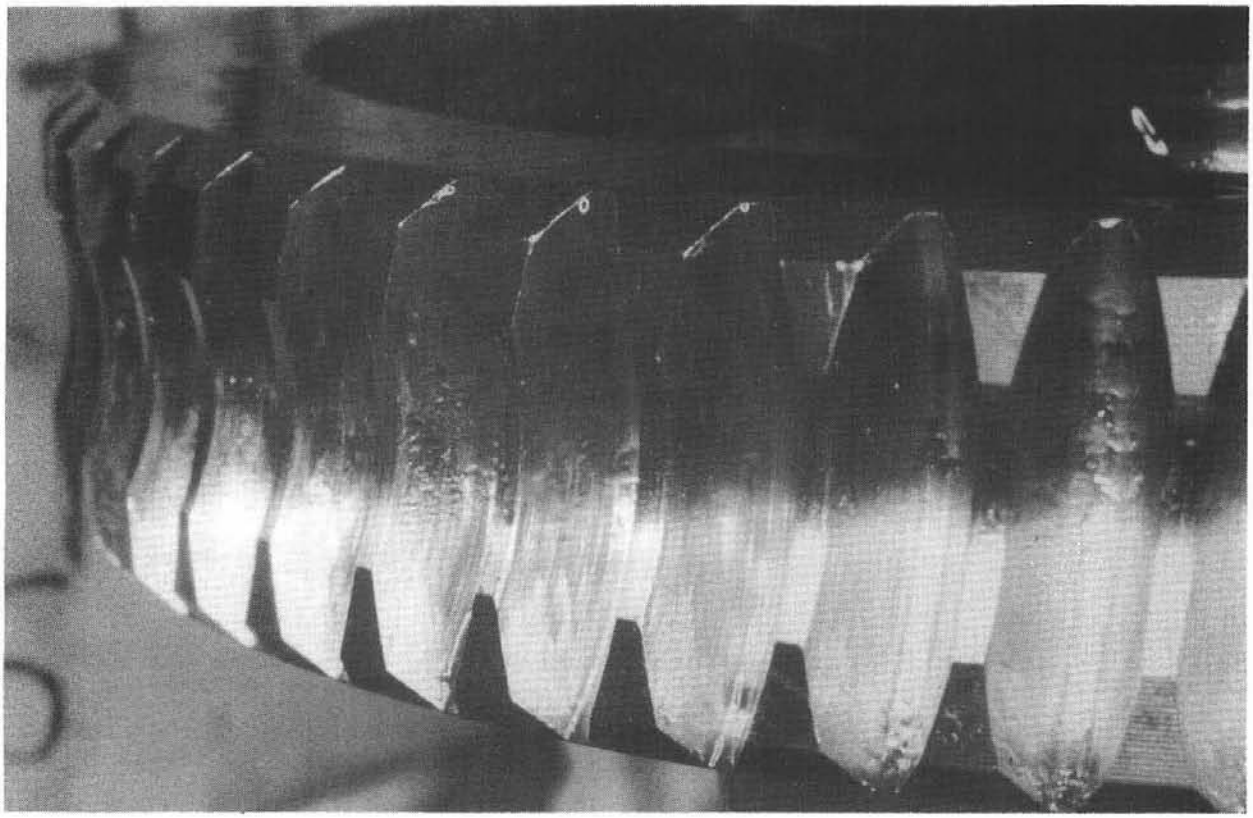

Figure C-8.7. MMC Elevation Pinion Gear after Test

Figure C-8.8. MMC Elevation Output Shaft and Gear

The localized high-bearing marks found on the elevation helical output gear (Figure C-8.9) were nearly 180° from the 90° region of our applied cyclic loading. Subsequent investigation revealed these load marks were due to a prior MMC static-load survival test.

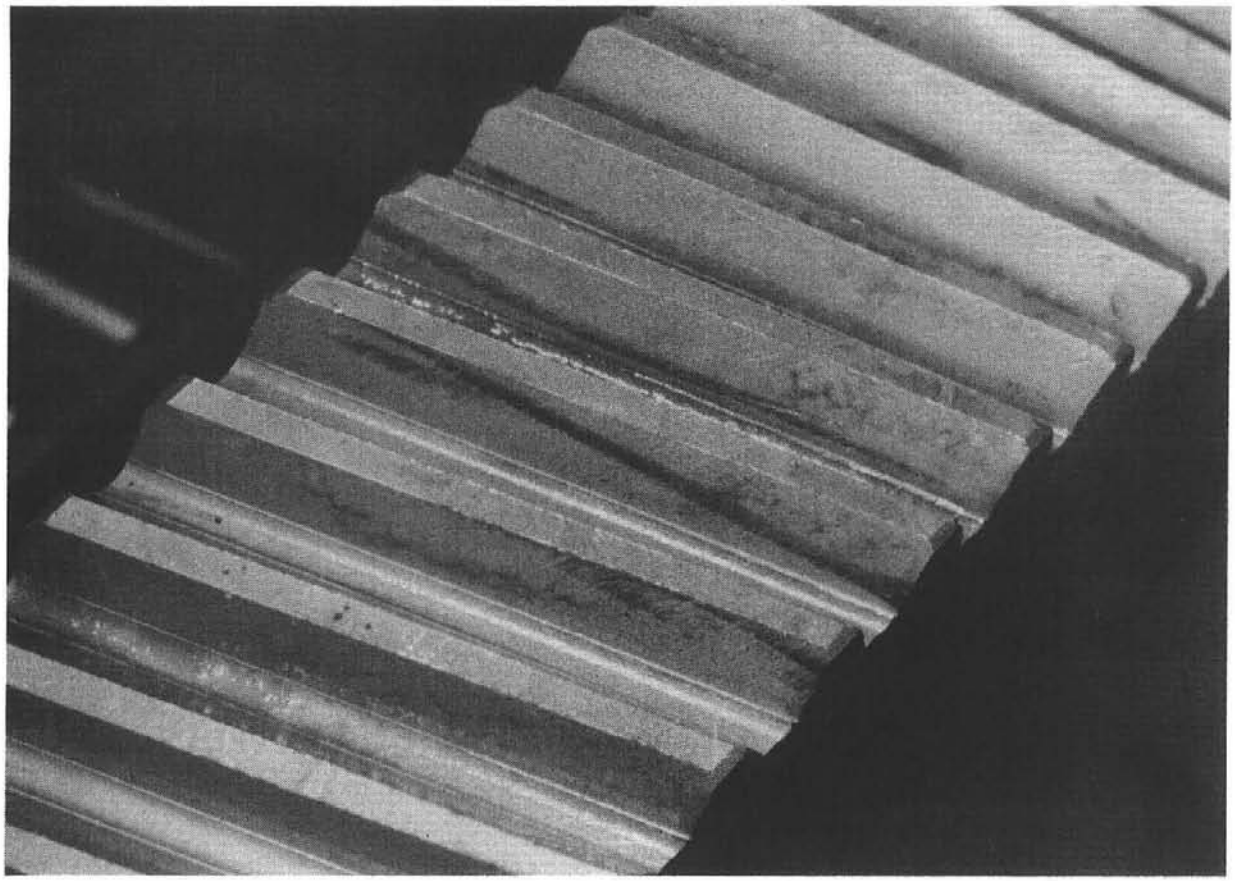

Figure C-8.9. MMC Elevation Output Gear after Test

Figure C-8.10 is a close-up of the bearing race shown in Figure C-8.6 of the overall elevation input worn-shaft and mounting flange. The numerous small depressions or surface pits seen here seem to suggest that some hard foreign material had been ground into the bearing surface, but no other evidence of foreign particles was found in the lubricant or elsewhere. Again, it was believed the damage might have occurred during some prior testing experience by MMC.

Some corrosion occurred to unprotected (unpainted) surfaces such as the exposed ends of the elevation shaft and underside of the pedestal adapter (see Figures C-8.11 and C-8.12).

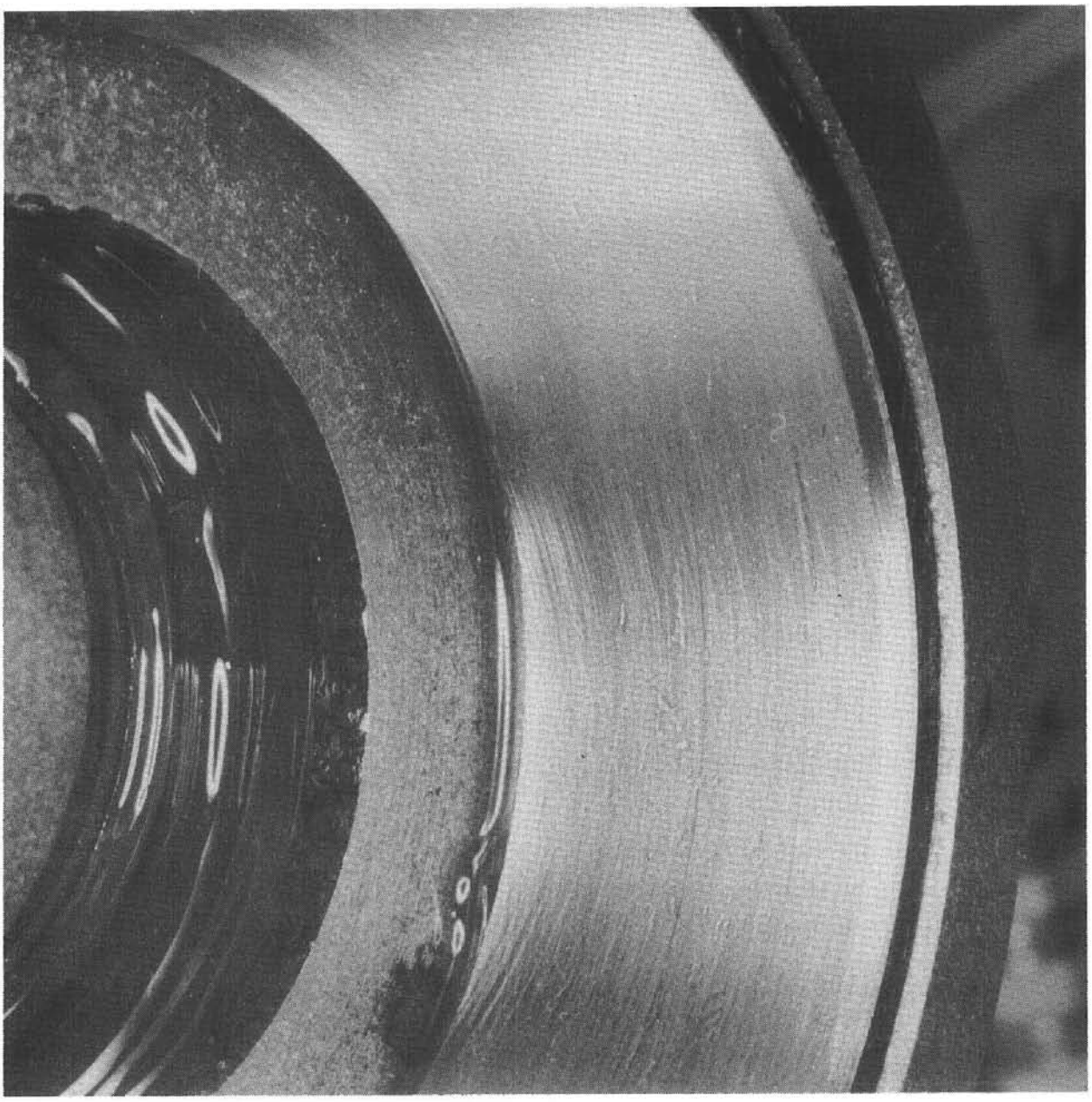

Figure C-8.10. MMC Elevation Input Flange after Test

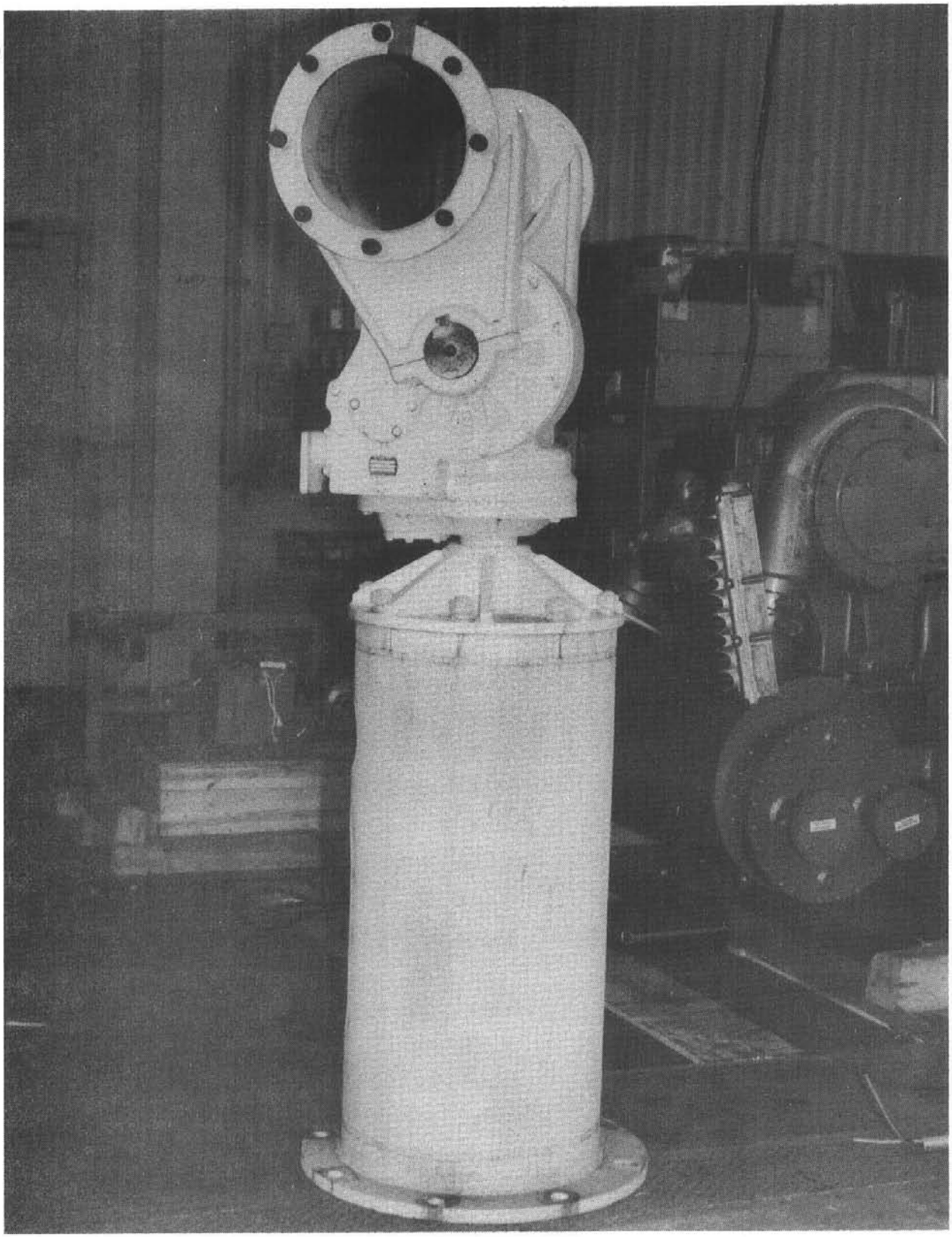

Figure C-8.11. MMC Heliostat after Test with Weights Removed

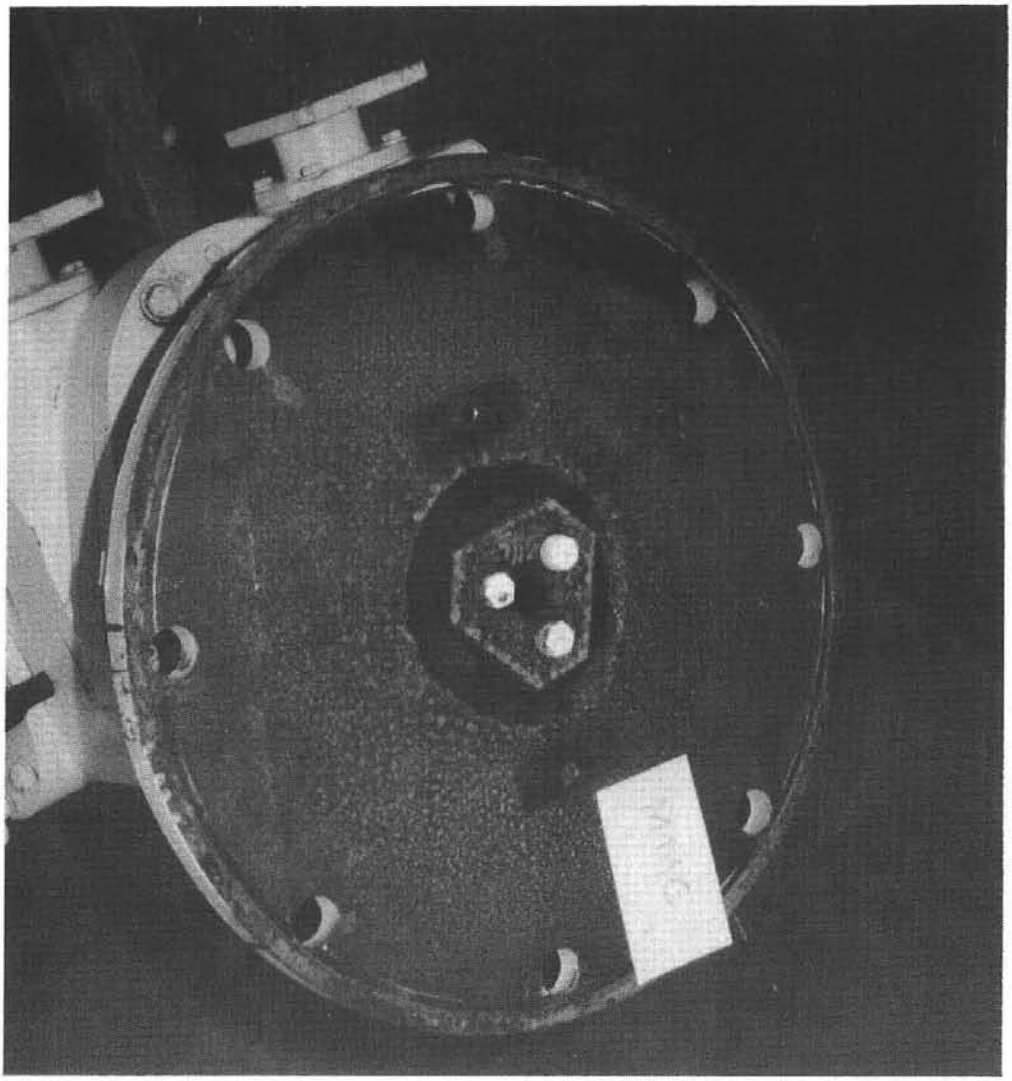

Figure C-8.12. MMC Underside of Pedestal to Drive Adaptor

MMC Control System

The controller shown in Figure C-8.13 showed no signs of corrosion or water spotting on the printed wiring boards or other internal components.

The externally mounted elevation incremental encoder shown in Figure C-8.14 had a small amount of water inside it. The azimuth encoder was installed inside the pedestal and was dry.

The motors were dry and clean. There was a slight amount of corrosion on one motor wire lug mounting nut as shown in Figure C-8.15. The motor cover was sealed with an O-ring and there was a film of oil on the O-ring, apparently to aid in assembly.

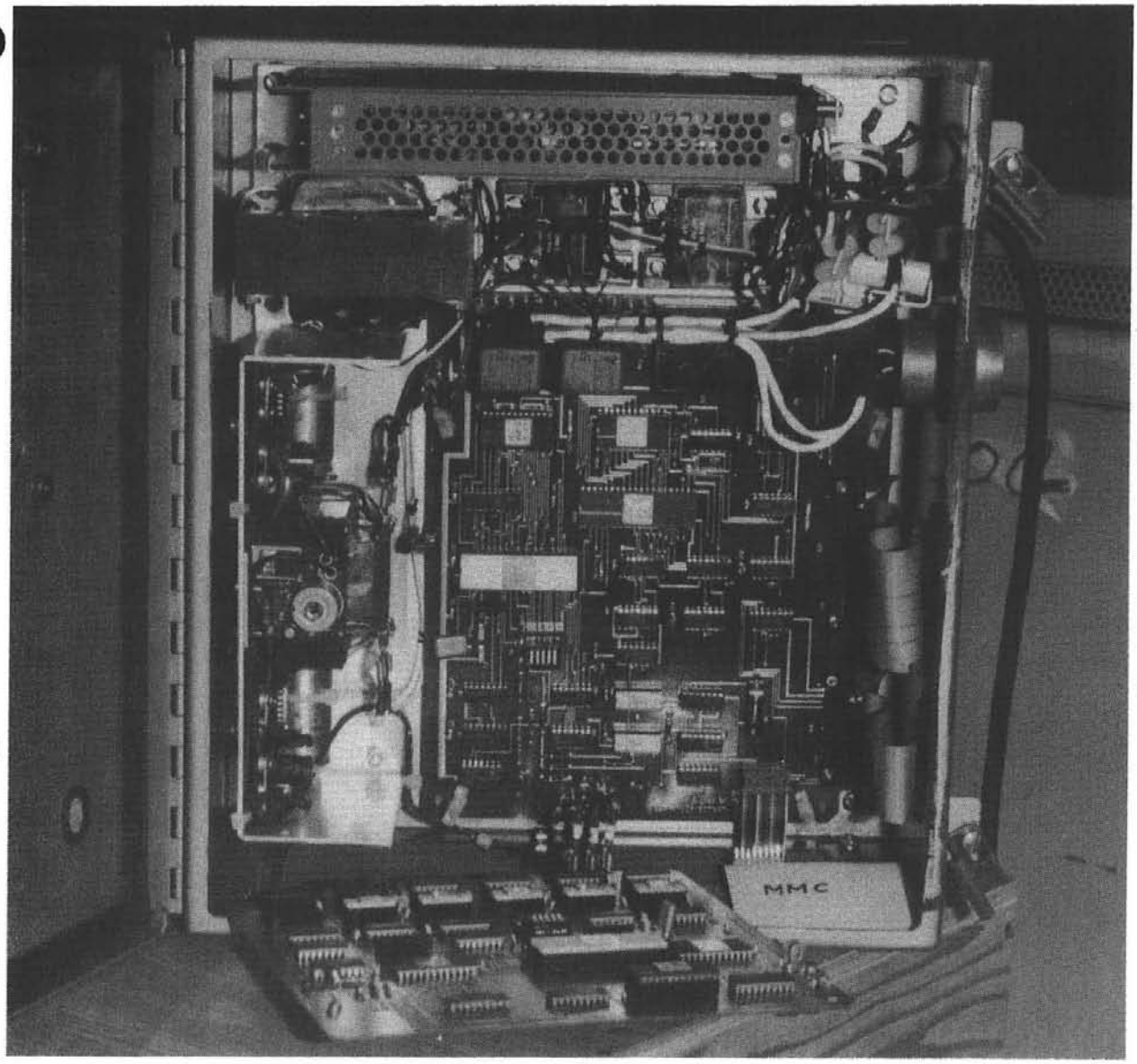

Figure C-8.13. MMC Control Box after Test

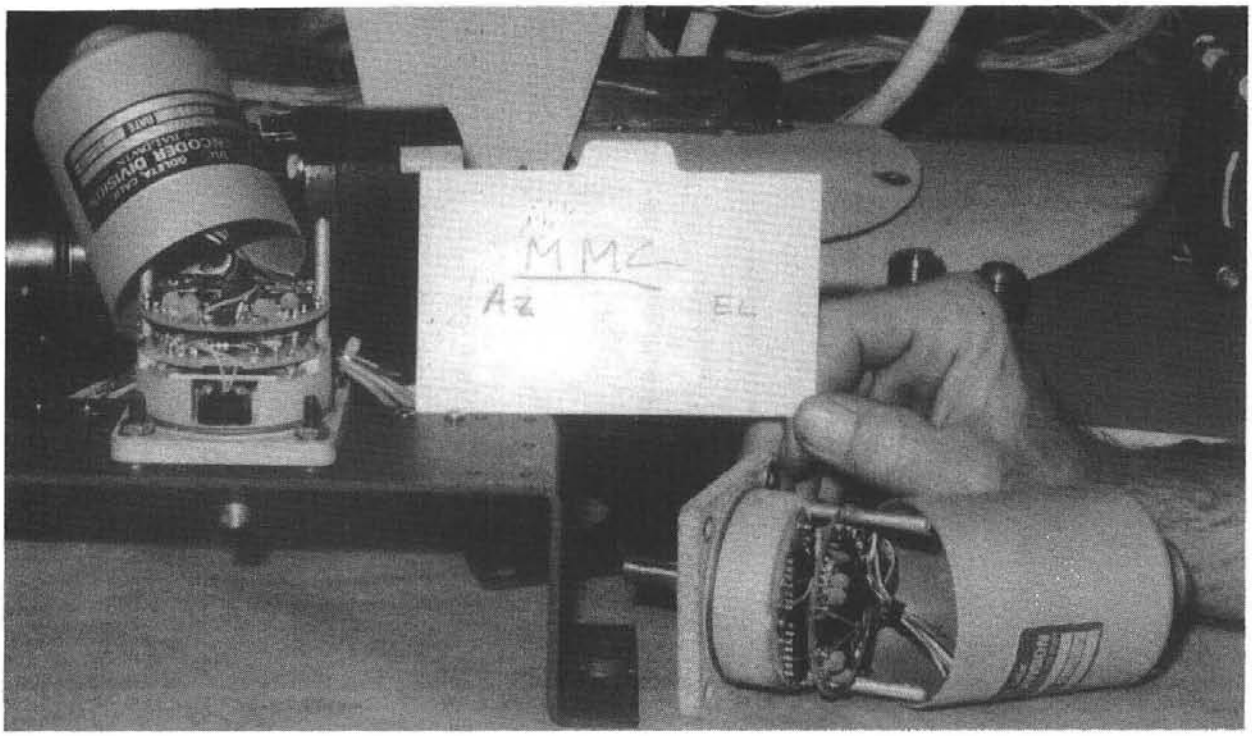

Figure C-8.14. MMC Elevation and Azimuth Encoders with Housing Removed after Test

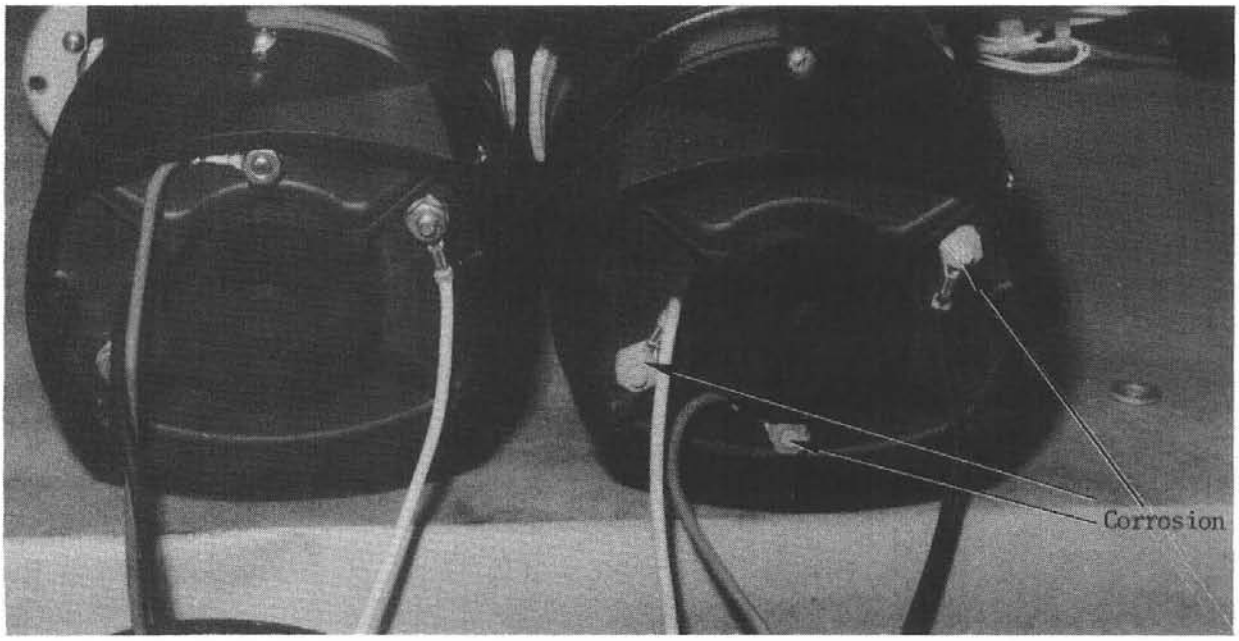

Figure C-8.15. MMC Drive Motor with Bell Covers Removed after Test

The cables and connectors showed no signs of deterioration or damage. The limit switches appeared to be undamaged but the mounting hardware was rusted (Figure C-8.16), which would make removal difficult.

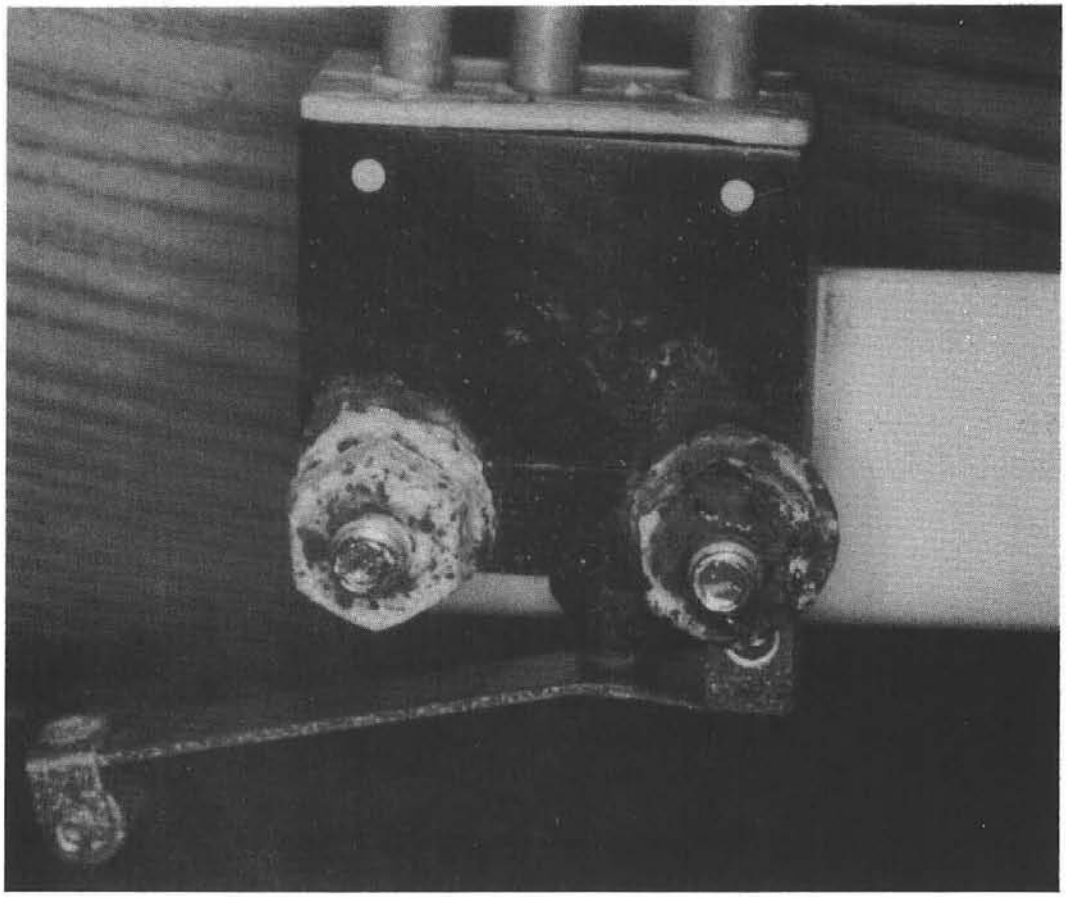

Figure C-8.16. MMC Elevation Limit Switch after Test

MDAC Drive Assembly (less control system)

Overall galvanize treatment of external surfaces showed considerable deterioration in comparison to painted surfaces (Figures C-8.17 through C-8.21).

Drag-link pivot bushings showed severe wear and galling of the plastic bearing material (Figures C-8.20 and C-8.21).

There was no apparent penetration of moisture into EL jack assembly (Figure C-8.22) or into AZ harmonic drive housing (Figures C-8.23 and C-8.24), but considerable penetration occurred into upper encoder housing, as shown in Figures C-8.18 and C-8.19. Some penetration occurred past AZ worm/gear bearing retainers and seals (Figure C-8.25).

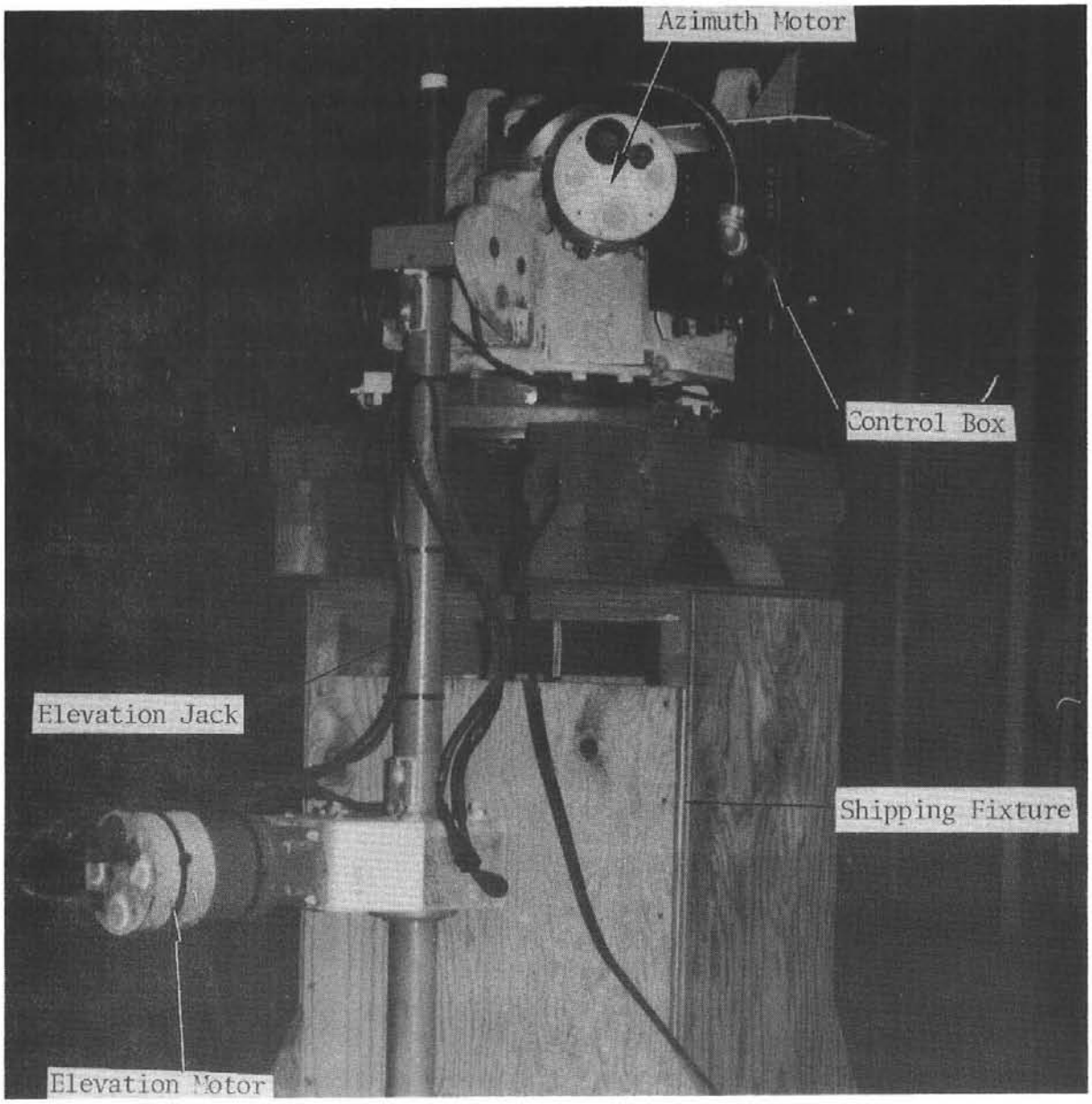

Figure C-8.17. MDAC Drive Mechanism after Completion of Environmental Drive Test

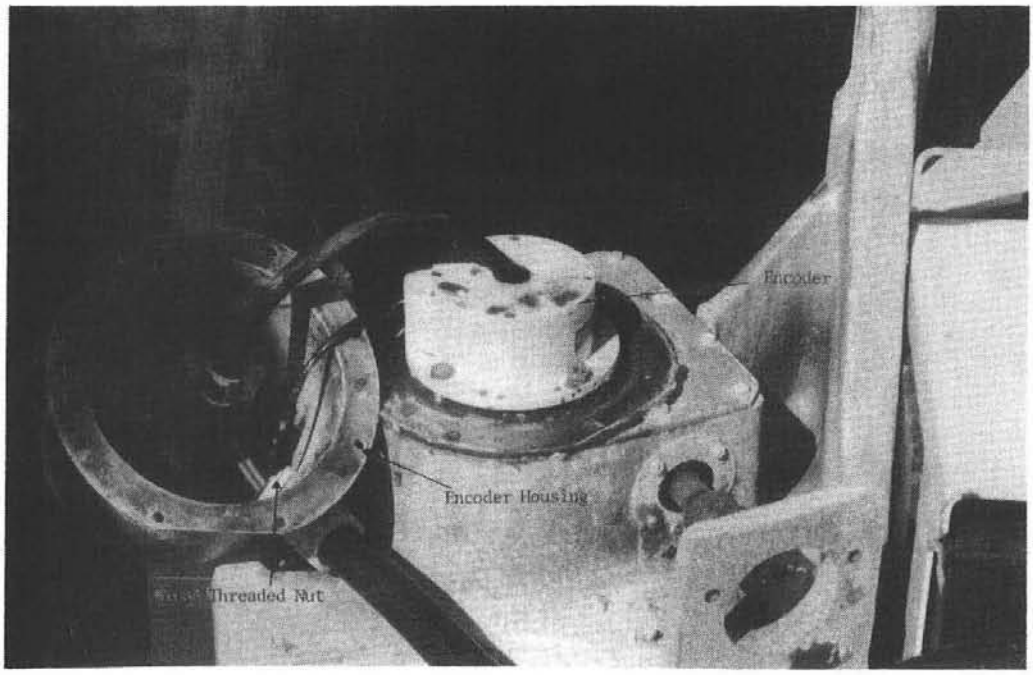

Figure C-8.18. MDAC Drive with Encoder Housing Removed

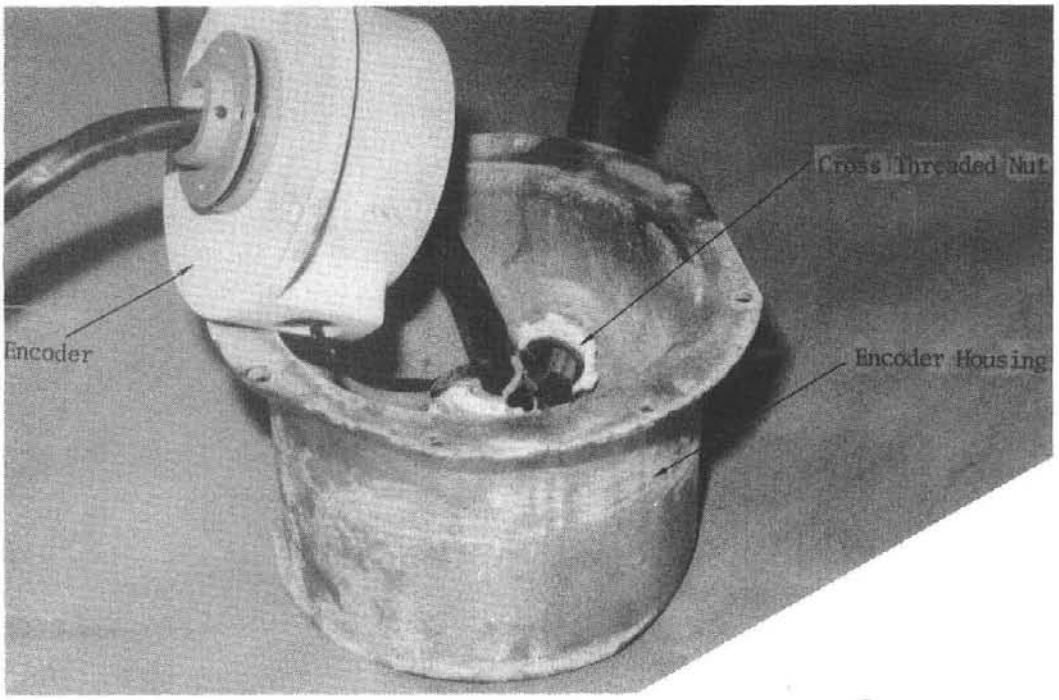

Figure C-8.19. MDAC Encoder and Housing

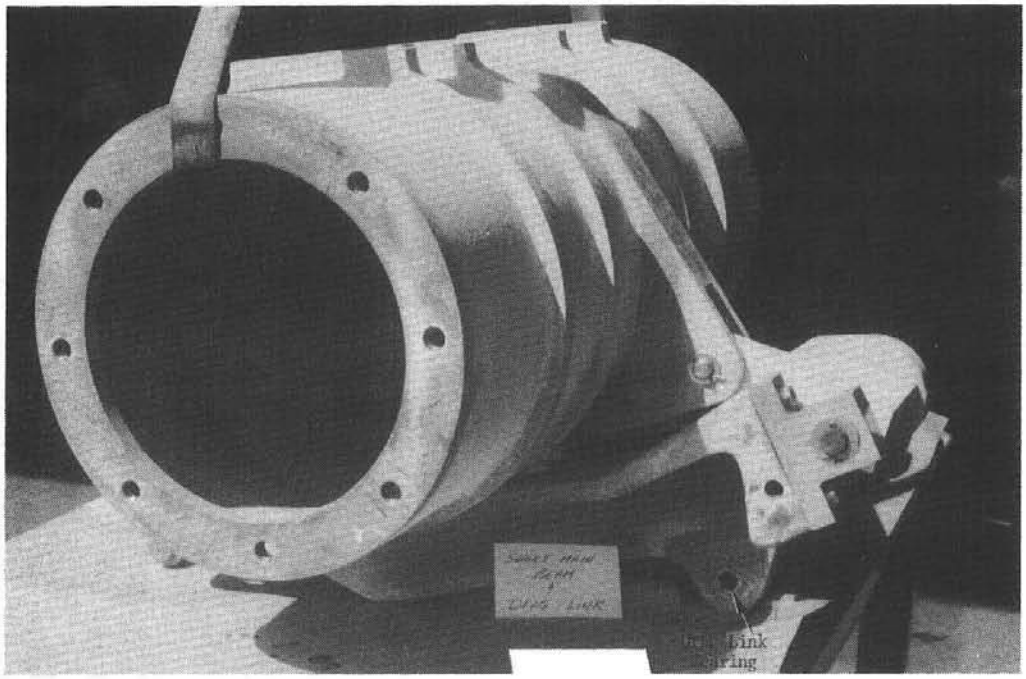

Figure C-8.20. MDAC Torque Tube Drag Link Assembly after Test

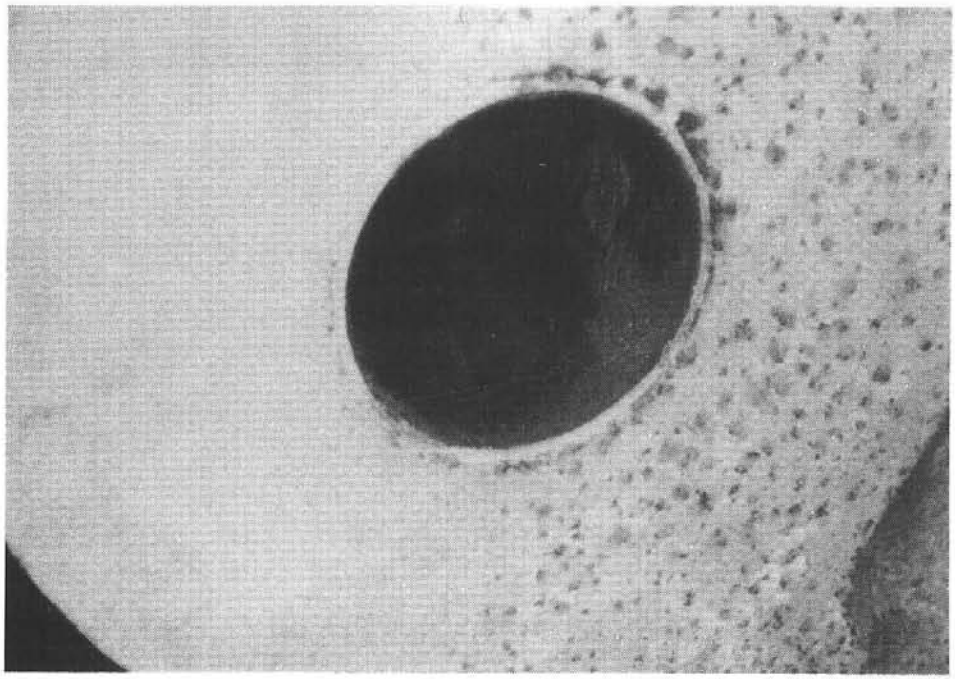

Figure C-8.21. MDAC Drag Link Bearing after Test

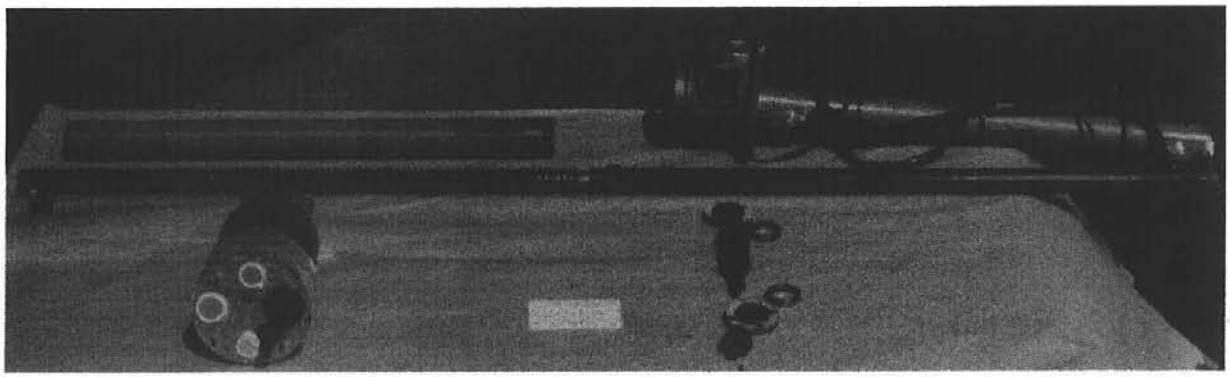

Figure C-8.22. MDAC Elevation Drive after Test

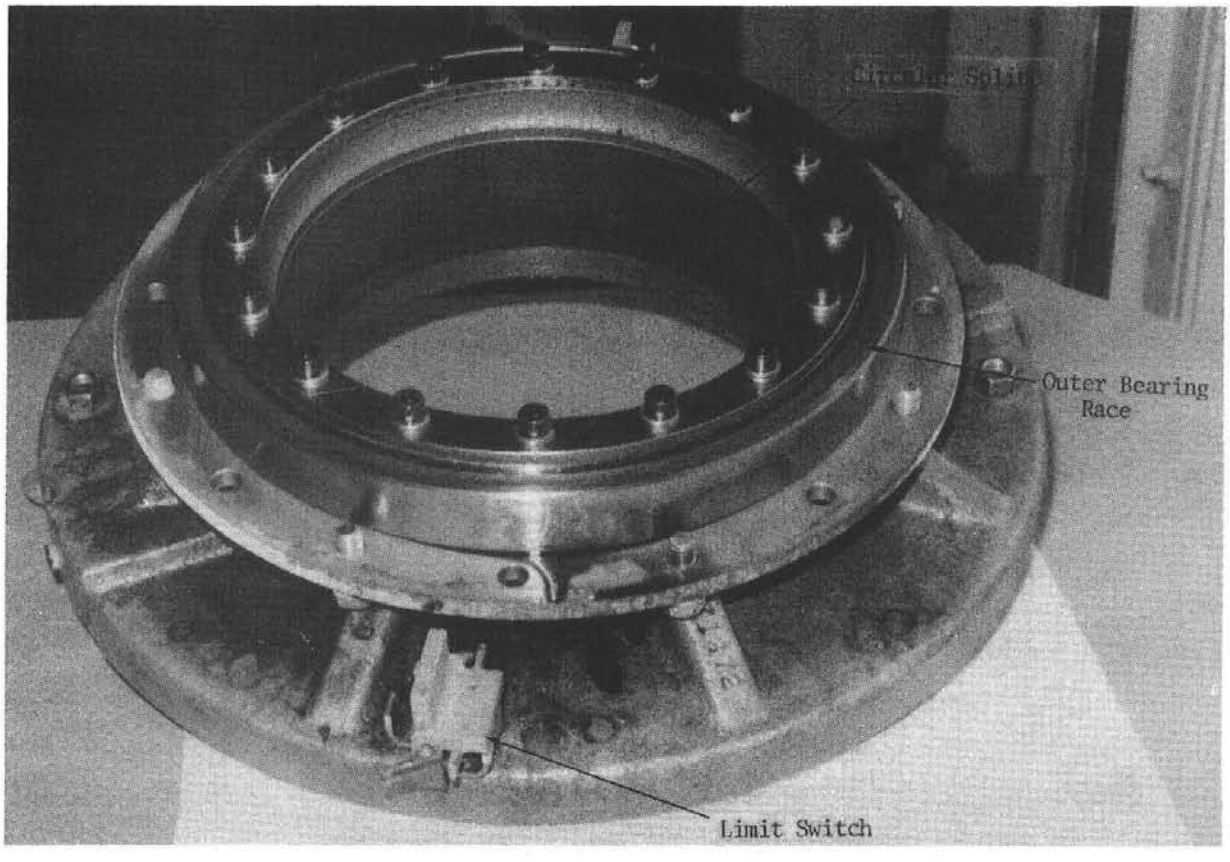

Figure C-8.23. MDAC Harmonic Drive Circular Spline Assembly after Test

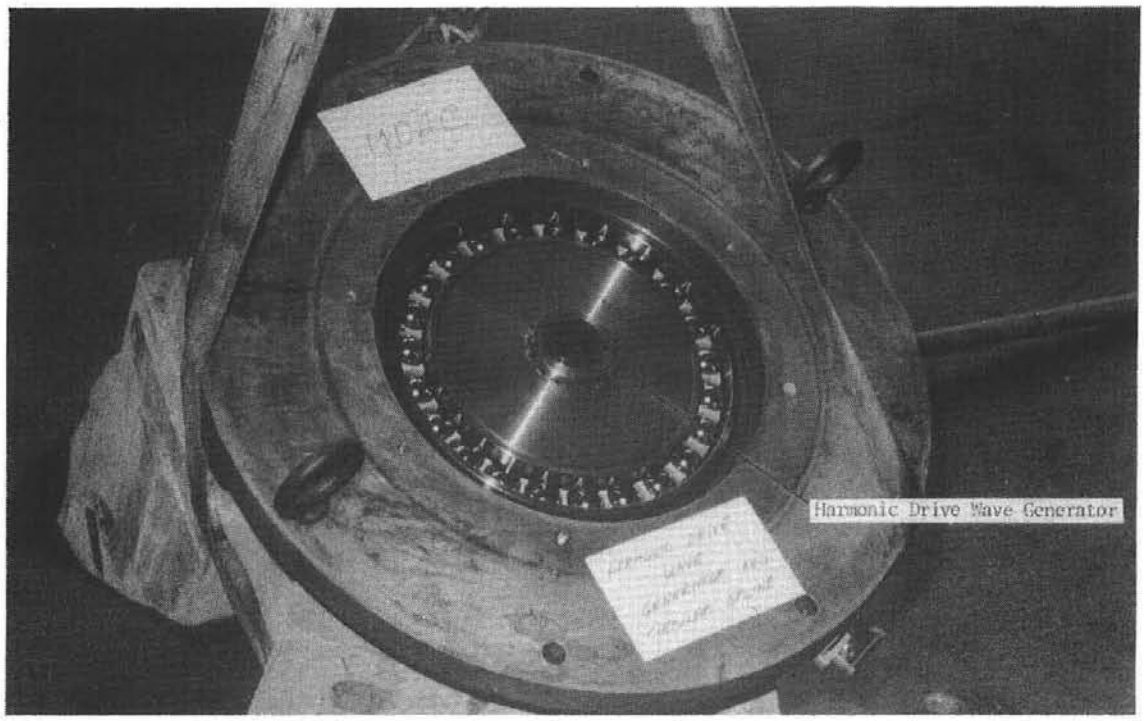

Figure C-8.24. MDAC Harmonic Drive Wave Generator and Circular Spline Assembly

Figure C-8.25. MDAC Azimuth Drive Housing

Underside of EL jack-screw shaft evidenced considerable galling between it and the trunnion block bore (Figures C-8.26 through C-8.28). Cause is due to relatively high lateral load on screw shaft resulting from mass/cg offset of entire jack/motor drive assembly. Motor drive couplings were severely rusted (Figure C-8.29).

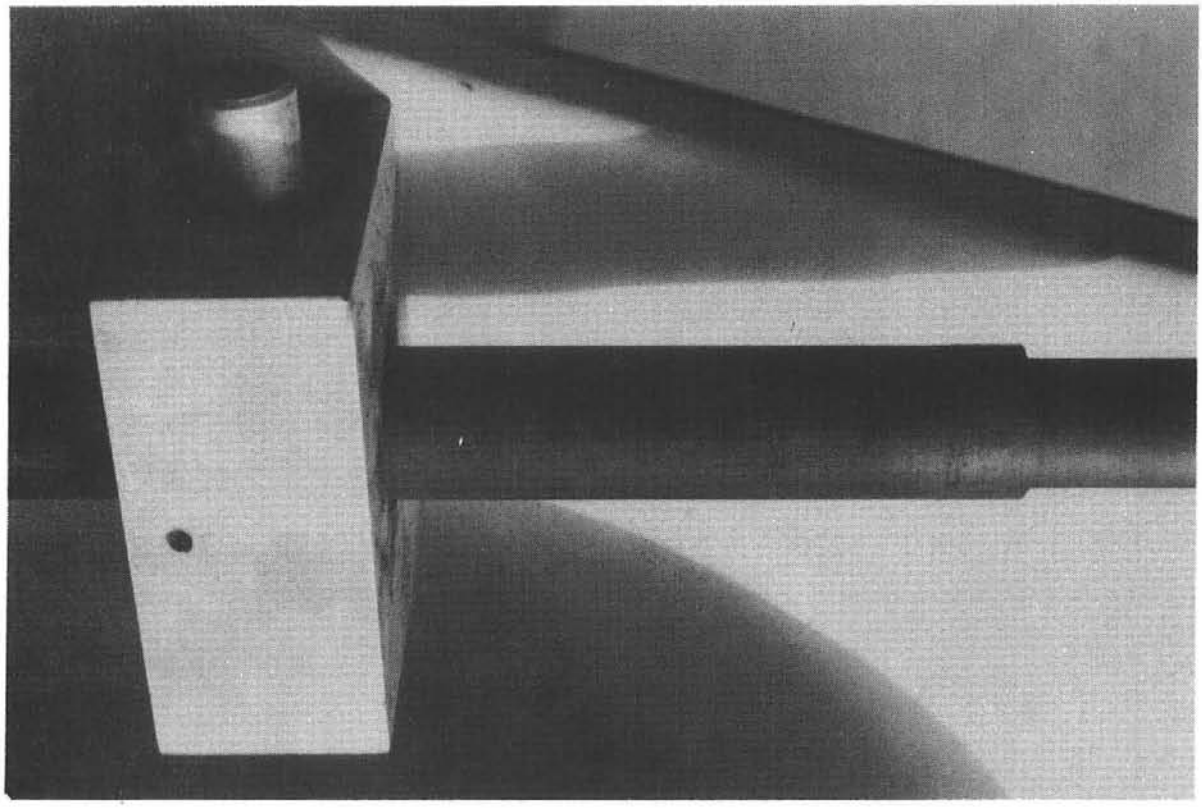

Figure C-8.26. MDAC Trunnion Block and Elevation Jack Shaft after Test

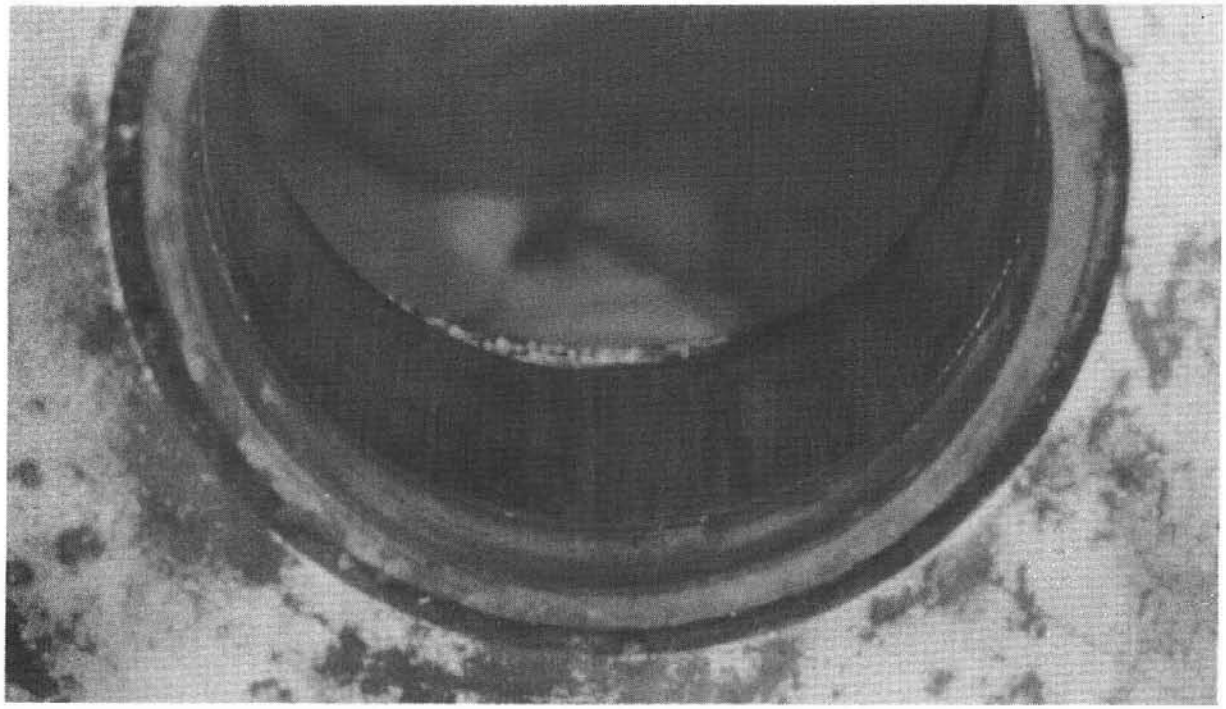

Figure C-8.27. MDAC Trunnion Block Bearing after Test

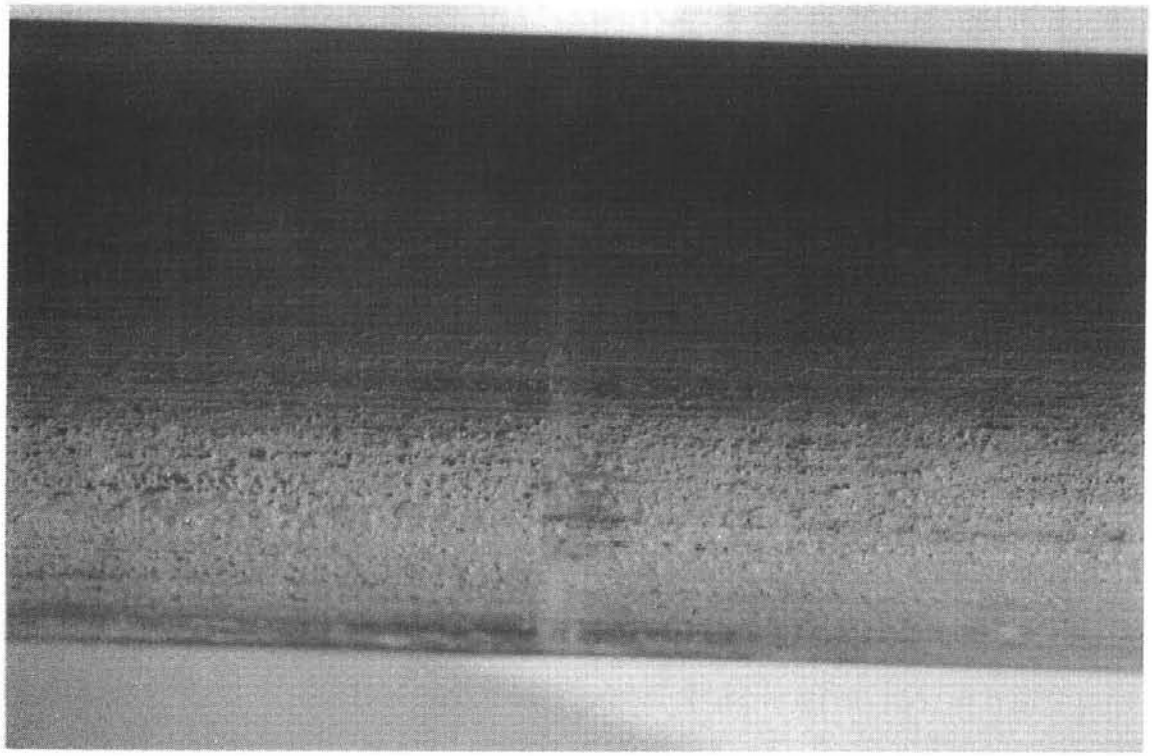

Figure C-8.28. MDAC Elevation Jack Shaft after Test

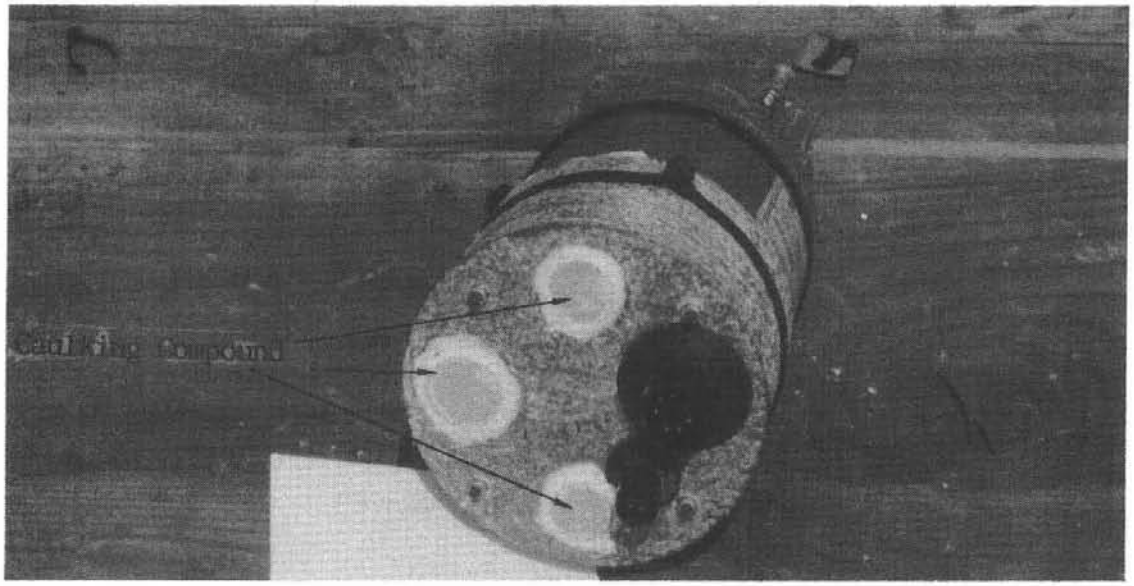

Figure C-8.29. MDAC Azimuth Drive Motor after Test

MDAC Control System

There were no signs of corrosion or water spotting on the printed wiring boards or other internal components of the controller, as shown in Figures C-8.30 and C-8.31. The motor controller board (A2) was replaced just prior to the wash/rain test so it had not seen all of the environments.

There was no cable damage and there was no connector corrosion. The incremental encoder cover on the drive motor was removed and about a teaspoon of water was found inside. The inside was wet all over and the motor shaft was corroded (Figure C-8.32).

The elevation absolute encoder was opened and no moisture or corrosion was observed. The unit is O-ring-sealed and the optical element was clean (Figure C-8.33).

There was water and corrosion under the azimuth encoder cover. The conduit coupling installed in the cover was cross-threaded which apparently allowed water to enter (Figure C-8.19).

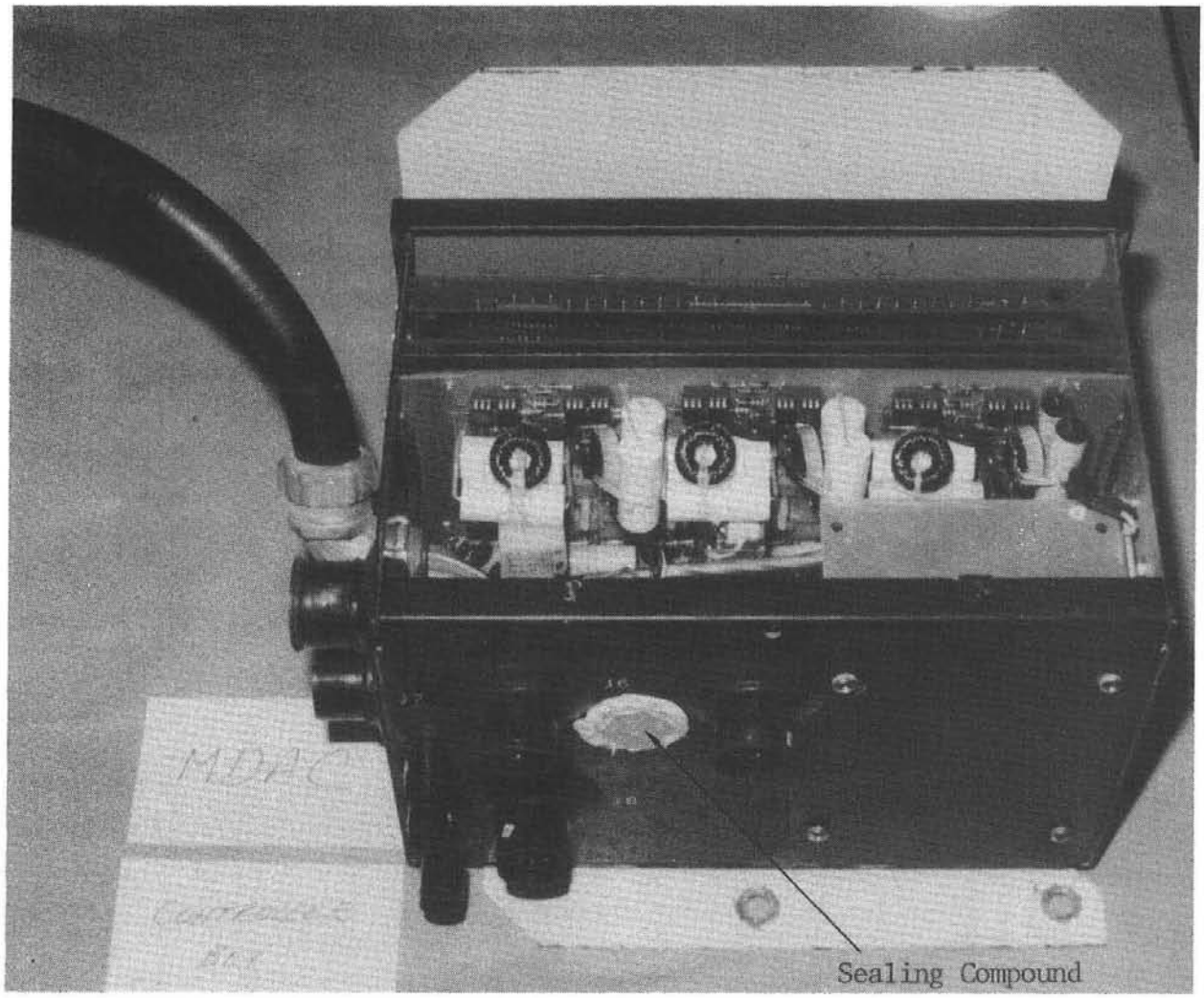

Figure C-8.30. MDAC Controller Box with Cover Removed

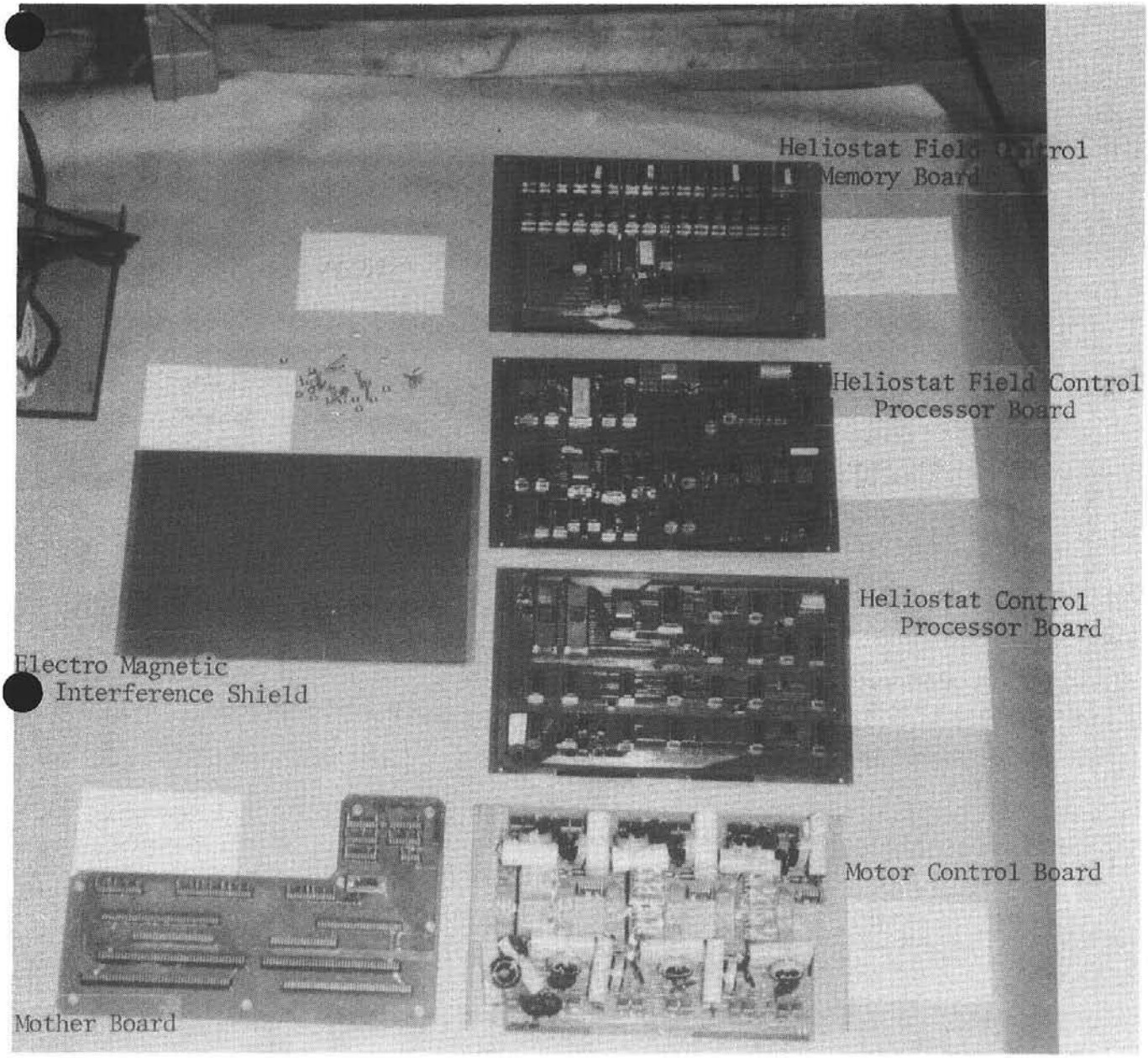

Figure C-8.31. MDAC Boards from Control Box

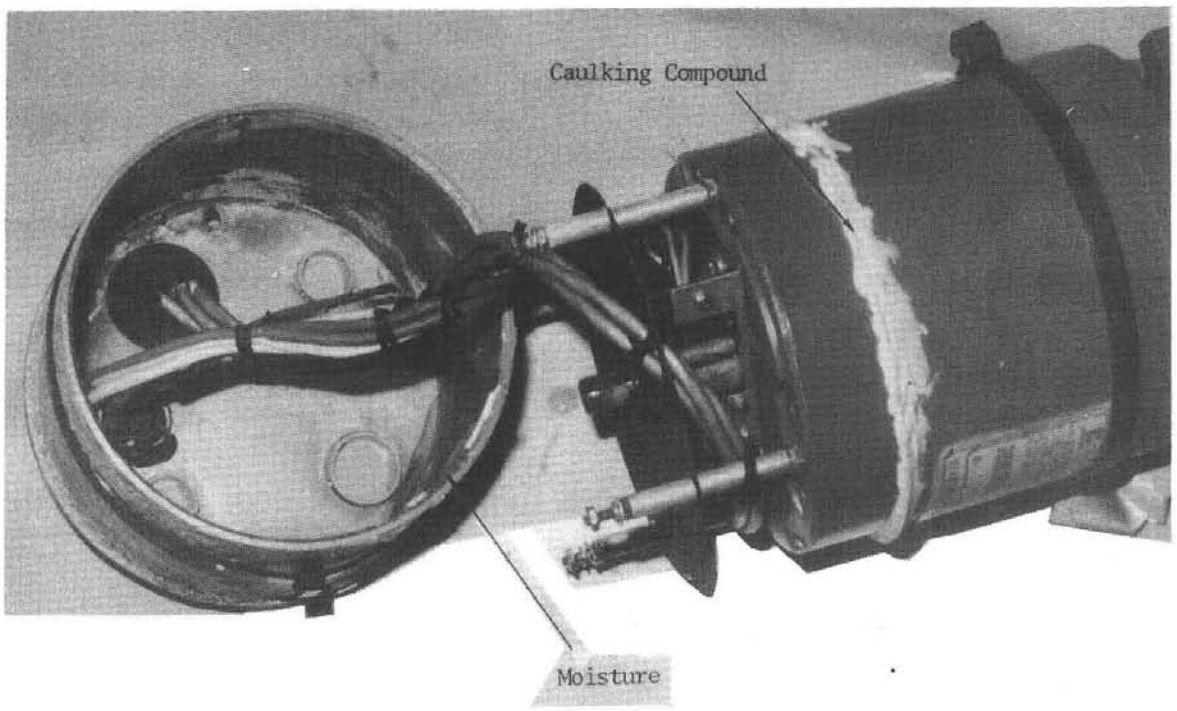

Figure C-8.32. MDAC Azimuth Drive Motor with End Bell Removed

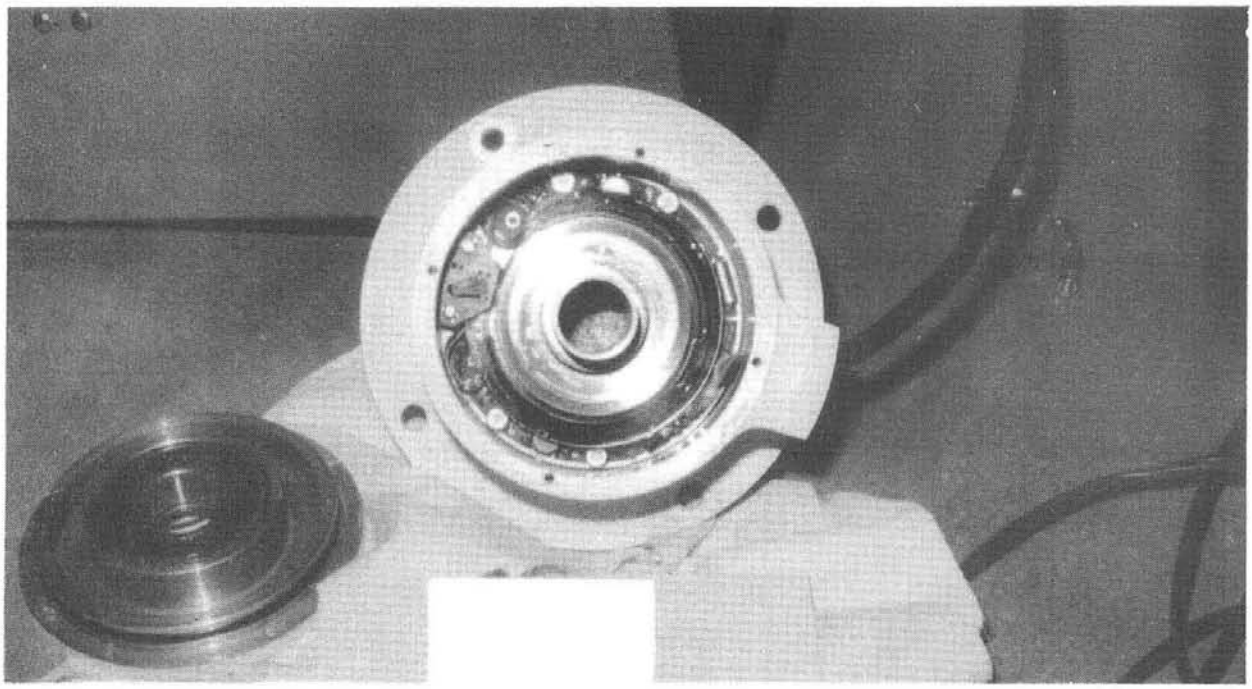

Figure C-8.33. MDAC Encoder Disassembled

SECTION D--MIRROR MODULE TESTS

Test D-1: Residual Glass Stress

Objective

The objective of this test was to measure the combined residual and fabrication-induced stresses along the edges of the glass.

Description

A reflection polariscope was used to measure stress along the edges of the mirrors (as close to the edge as possible) at six-inch intervals. Stresses in all six mirror modules from each contractor were measured.

Results

No stress was detectable in any of the measurements made in the six MDAC mirror modules. The accuracy of the measurement technique is $\pm$ 50 psi. This result is not surprising because the MDAC mirrors are fabricated with an induced curvature about one axis only (cylindrical curvature).

Significant stresses were measured in the MMC mirror modules. All of the stresses were compressive up to 400 psi, except for one mirror module where a tensile stress of 250 psi was measured at three consecutive points along one long edge. The highest stresses were found toward the middle of the edges. Because the MMC mirrors are fabricated with a two-axis (spherical) curvature, compressive stresses are to be expected along the edges of the mirrors.

Conclusions

From the results of the MDAC mirror module stress measurements, it may be concluded that the PPG low iron float glass supplied by SNL has no significant residual stress. Also, the fabrication technique of MDAC using a cylindrical curvature and a room-temperature curing adhesive apparently induces no stresses into the glass. The MMC design, using a spherical curvature and an elevated temperature curing adhesive (250°F) does induce stresses in the mirrors, but these stresses are compressive at the edges of the glass. The tensile stress measured in one of the MMC mirrors must be assumed to have been a fabrication anomaly. It can be concluded that residual or manufacturing stresses are not a design concern for either mirror module design.

Test D-2: Specular Reflectivity

Objective

The objective of this test was to determine the specular reflectivity of the mirrors for a solar-weighted wavelength spectrum.

Description

There currently exists no portable reflectometer that can measure the solar-weighted specular reflectance of mirrors. Therefore, reflectance measurements were made with laboratory equipment on small (6x6-inch) mirror samples supplied by the contractors. These measurements were made with a Beckman DK-2 hemispherical reflectometer for a solar-weighted spectrum and a bi-directional reflectometer at 500 nm for collection apertures from 1 to 15 mrad. The results were correlated with measurements made on each of the six mirror modules of the two designs with the following portable equipment: Beckman portable reflectometer (350 to 2500 nm, not a solar-weighted spectrum), SNL portable specular reflectometer (5 mrad incident beam with a peak at 550 nm), and Gier Dunkle Solar Reflectometer Model MS-251 (measures solar-averaged hemispherical reflectance).

Results

The test results are summarized in Table D-2.I. The results given are an average value plus an indication of the spread for all of the data taken.

TABLE D-2.I

REFLECTIVITY MEASUREMENTS ON 6x6-INCH SAMPLES AND FULL MIRROR MODULES

	MMC		MDAC	
Equipment	6x6" Samples	Full Modules	6x6" Samples	Full Modules
Beckman DK-2 (solar-averaged spectrum)	0.899 ± 0.010	-	0.890 ± 0.010	-
Beckman DK-2 (at 500 nm)	0.950 ± 0.001	-	0.935 ± 0.001	-
500 nm Bi-directional	0.936 ± 0.001	-	0.920 ± 0.007	-
Beckman Portable	-	0.875 ± 0.004	-	0.874 ± 0.001
Sandia Portable	0.945 ± 0.002	0.943 ± 0.004	0.938 ± 0.003	0.939 ± 0.003
Gier-Dunkle MS-251	0.856 ± 0.003	0.850 ± 0.006	0.851 ± 0.002	0.852 ± 0.004

The results show that: (1) the reflectivity of the 6x6-inch samples is the same as that of the mirror modules for each contractor, (2) the reflectivity of the MMC mirrors is higher than that of the MDAC mirrors for all comparative measurements, except for one case where measurements are essentially the same, and (3) the solar-averaged reflectivity was measured to be 0.90 and 0.89 for MMC and MDAC, respectively.

Conclusions

The reflectivity for the MMC mirrors is slightly higher than the MDAC mirrors, and the effective reflectivity of clean mirrors made with this 1/8-inch low iron float glass is on the order of 0.89-0.90.

Test D-3: Contour and Gravity Sag

Objective

The objective of this test was to measure the large-scale mirror contour at room temperature and the change in contour due to gravity sag.

Description

Mirror contour measurements were made at 15 points with the beam dial indicator instrument shown in Figure D-3.1. Each displacement gage was initially nulled with the instrument resting on a microflat table. Measurements were then made on the mirror with the mirror module resting on leveling studs that were screwed into the mirror module attachment points. The measurements were then repeated with the mirror module loaded uniformly with sandbags that were equal in total weight to the weight of the mirror module. All six mirror modules from each contractor were tested.

Results

The first set of measurements (without the sandbags), to be called W_1, is comprised of the natural contour of the mirror (W_o) and the gravity sag (W_g). The second set of measurements (W_2) made with the sandbag loading has the natural contour plus twice the gravity sag. That is:

$$W_1 = W_o + W_g$$

$$W_2 = W_o + 2W_g$$

The natural contour and the gravity sag are determined from the two measurements W_1 and W_2 by the following simple equations:

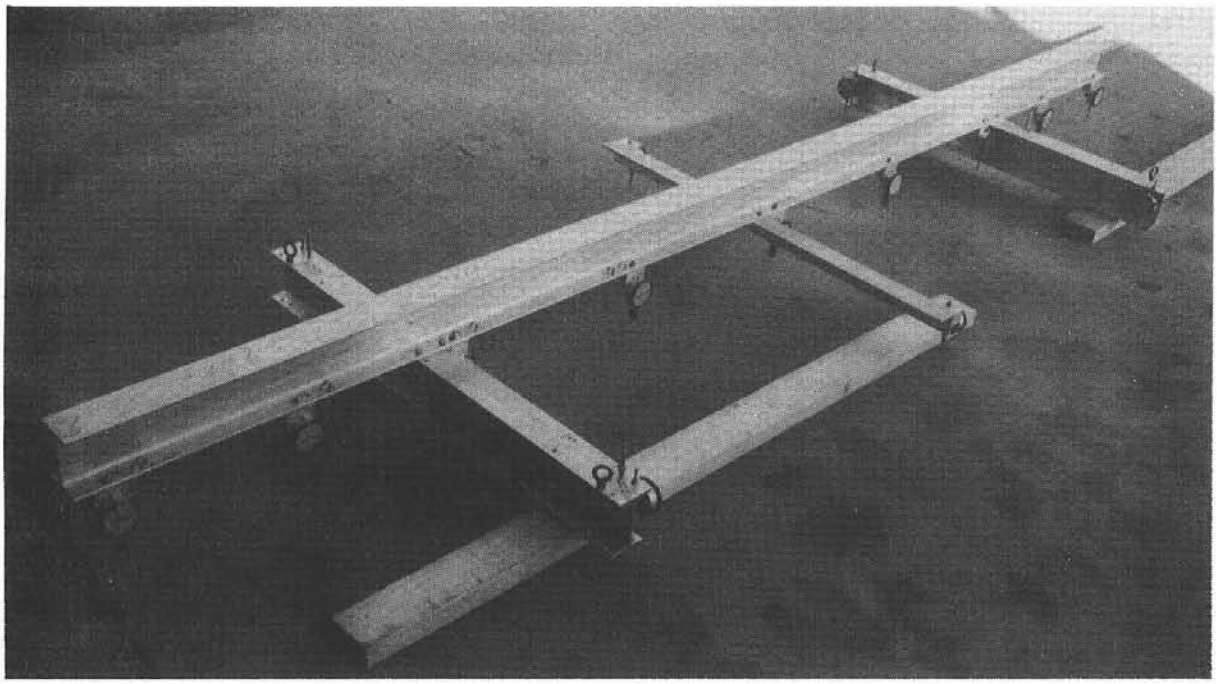

Figure D-3.1. Beam-Dial Indicator Instrument for Measuring Mirror Contours

$$W_g = W_2 - W_1$$

$$W_o = W_1 - W_g$$

The resulting contours taken along the center line (long direction) of each of the six mirrors for both designs are plotted in Figures D-3.2 and D-3.3. The average focal length for the MMC mirrors is 897 feet at 80°F, and the average focal length for the MDAC mirrors is 1486 feet at 78°F. The gravity deflections (0.002 inch maximum for MMC, 0.005 inch maximum for MDAC) change these contours by an insignificant amount. However, the gravity sag measurements do confirm that the MMC mirror modules are stiffer than MDACs. Finally, it is noted that the curvatures of the MDAC mirrors are more consistent than those of the MMC mirrors.

Conclusions

Mirror contour changes due to gravity sag are insignificant for these designs. The MMC mirror modules are stiffer than MDAC's. The MDAC mirror curvature is more consistent than MMC's.

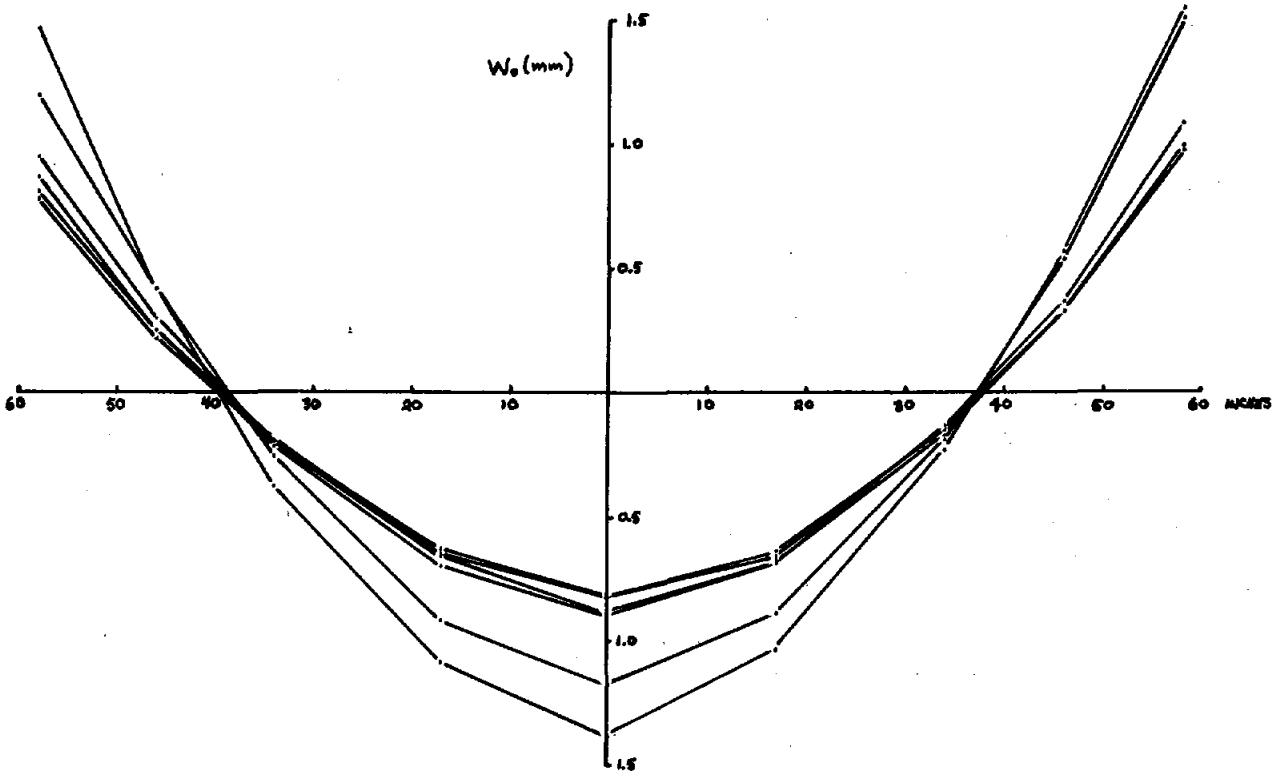

Figure D-3.2. MMC Mirror Curvatures at Room Temperature for Six Mirror Modules

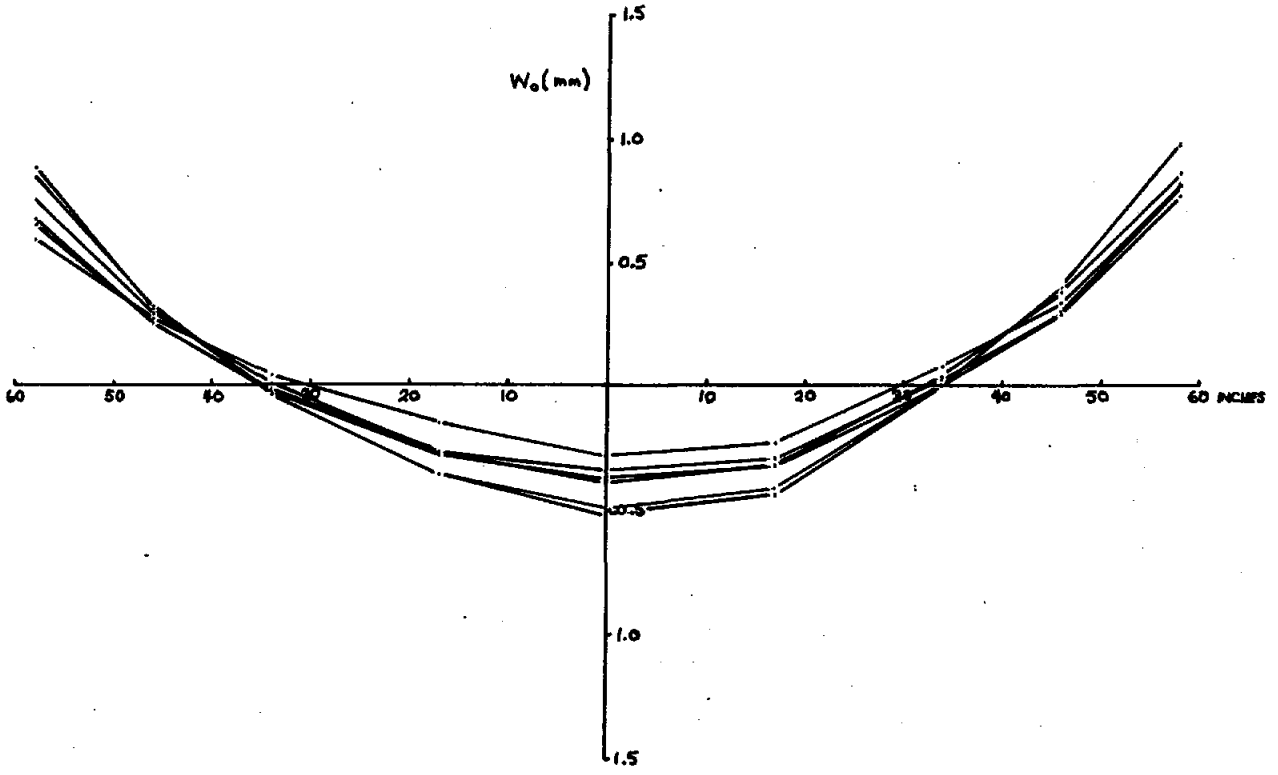

Figure D-3.3. MDAC Mirror Curvatures at Room Temperature for Six Mirror Modules

Test D-4: Mirror Waviness

Objective

The objective of this test was to measure the effective mirror waviness that impacts an overall beam quality.

Description

Mirror slope error measurements were made with a reflected laser ray-trace set up at SNLA. Six ray-trace sweeps were made on each mirror, three parallel to the long edge of the mirror and three parallel to the short edge of the mirror, as illustrated. Two mirrors of each design were measured.

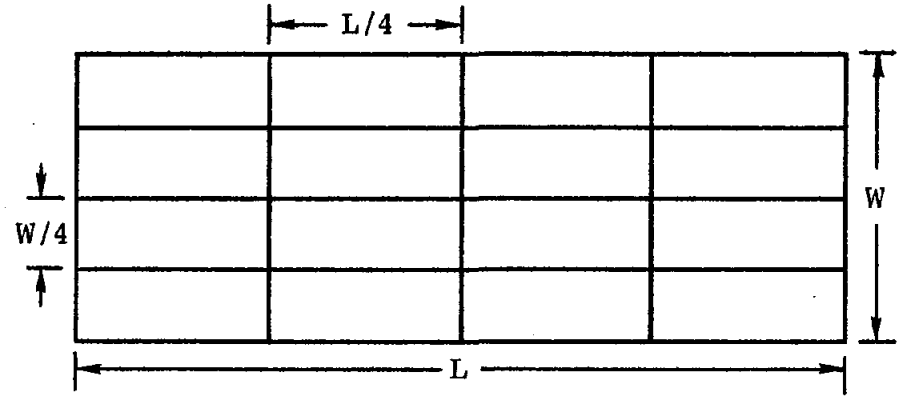

Slope errors due to rigid body rotation (tilt) and overall curvature (focusing) were subtracted from the ray-trace measurements during the final data reduction.

Results

An example of the raw data taken from a laser ray-trace scan is shown in Figure D-4.1. The scan was parallel to the long axis of a mirror. The reduced data for this example are shown in Figure D-4.2. Note that the scale is now different. The slopes due to tilt and overall curvature have been subtracted from the raw data, leaving a measure of the effective waviness of the mirror.

The root mean squre (RMS) value of the mirror slope errors measured in the mirrors is summarized in Table D-4.I. The magnitude of the waviness for all of the mirrors is seen to be on the order of 0.20-0.25 mrad, except for the short direction of the MMC mirrors where the slope error is almost double the other measurements. This additional waviness is apparent in all of the MMC mirrors and is due to a waviness built into the MMC bonding table. The effect is mostly cosmetic and should be correctable by smoothing the bonding table.

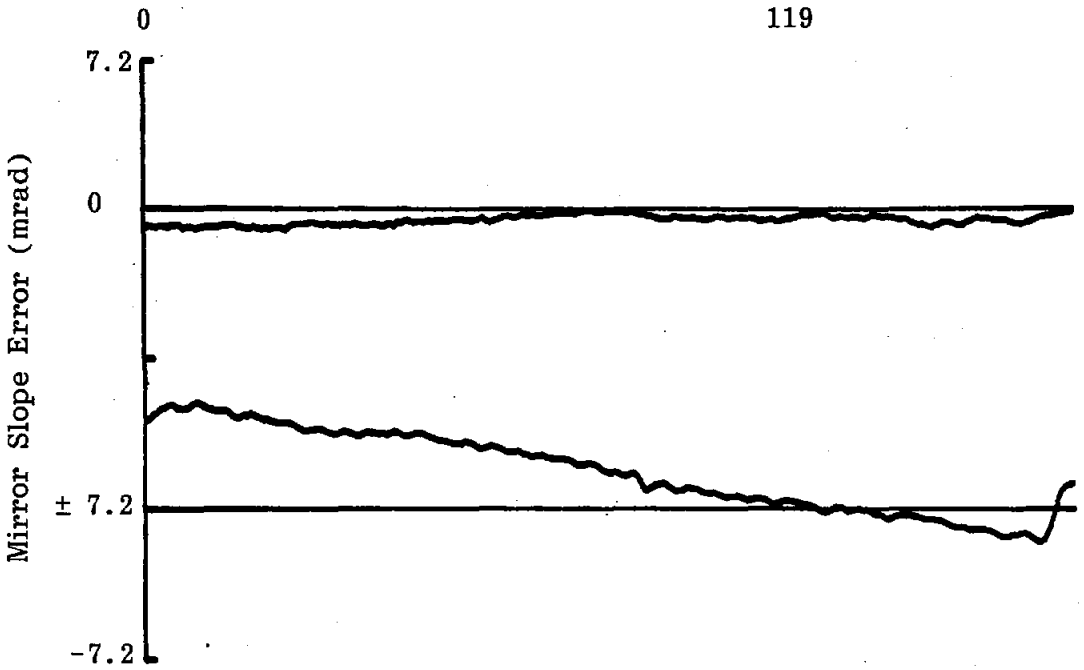

Figure D-4.1. Laser Ray-Trace Scan on Mirror, Raw Data (x axis)

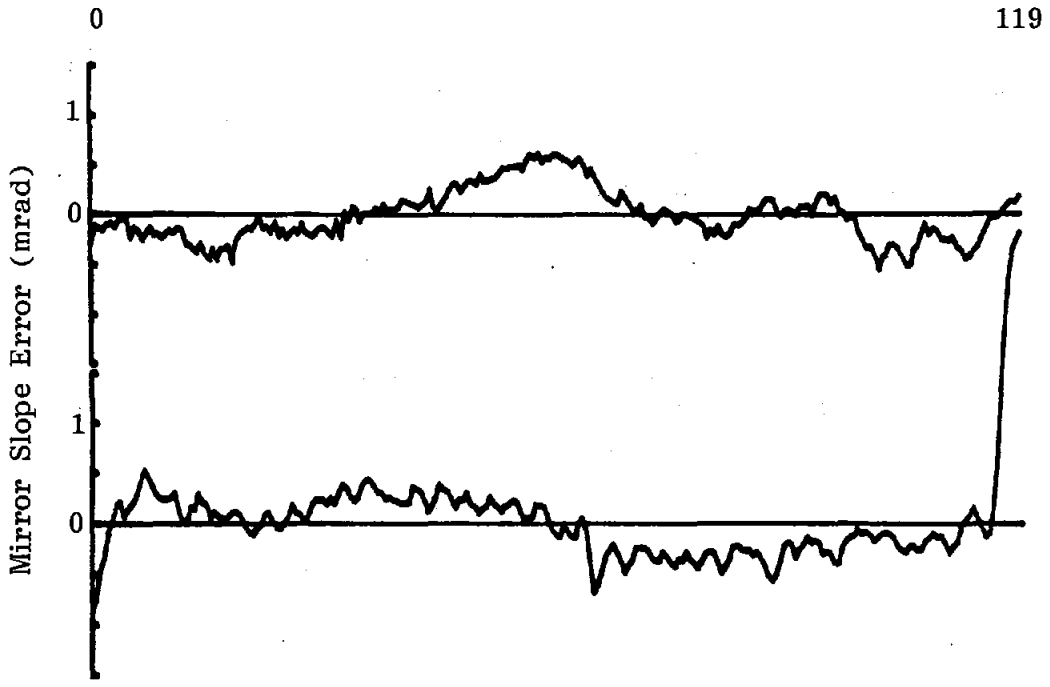

Figure D-4.1. Laser Ray-Trace Scan on Mirror, Reduced Data (x axis)

TABLE D-4.I

MIRROR SLOPE ERRORS MEASURED BY LASER RAY-TRACE

Mirror Module	RMS Slope Error* (mrad) Long Direction**	Short Direction**
MMC #7	0.22	0.36
MMC #8	0.23	0.43
MDAC #2	0.26	0.16
MDAC #6	0.25	0.24

*Overall curvature of the mirror has been subtracted.
**Each value represents the RMS of three sweeps.

Conclusions

Waviness on the order of 0.25 mrad RMS slope error has no significant effect on reflected beam spread due to the size of the solar disk. Waviness on the order of 0.40 mrad may have a small contribution to beam spread but was not detectable in the CRTF BCS measurements and should be correctable in the mirror module fabrication process.

Test D-5: Hail Test

Objective

The objective of this test was to determine whether the mirror module can meet the hail impact requirements.

Description

Two mirror modules from each contractor were subjected to 3/4-inch hail impacted on the glass at 65 ft/s, and 1-inch hail impacted on the backside at 75 ft/s. At least 20 simulated hailstones (3/4-inch ice balls) were propelled at and perpendicular to the glass. Fifteen of the shots were concentrated at the edges and the corners of the glass and five shots were aimed toward the center of the glass. Ten of the 1-inch ice balls were propelled at the backside of the mirror at various locations. Temperature of the ice balls was between 20 and 25°F during testing.

Results

No damage occurred to any of the mirror modules tested, except for slight indentations on the backs of the MDAC units. An existing crack in one of the MDAC mirrors (induced by careless handling) was subjected to hail impact at the crack tip and no crack extension was observed.

Conclusions

Both mirror module designs met the hail survival requirements.

Test D-6: Wind Load Glass Stress

Objective

The objective of this test was to determine the stress in the glass due to wind loads.

Description

Two mirror modules from each contractor had six SR-4 strain gages mounted on the glass surface in the following locations:

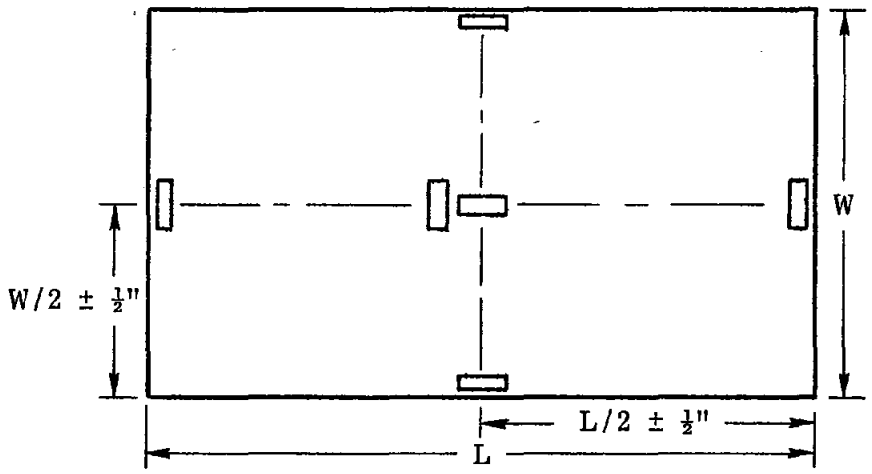

The four gages on the sides were mounted as close to the glass edge as possible. To minimize errors, gages from the same lot were used and all gage wire leads were the same length.

The mirror modules tested were placed mirror face up on a flat table, resting on the leveling screws installed in the mounting pads. The strain gages were initially nulled. The mirror module was then loaded with 2-1/2-lb sandbags in the configuration shown in Figure D-6.1. The strains were read immediately and again after one hour. The sandbags were then removed. The strain gages were again nulled and the test was repeated.

25 mph wind loads simulated with sandbag loading.

Load = PA, P = 2.38 q, $q = \frac{1}{2} \rho V^2$

Uniform load distribution assumed

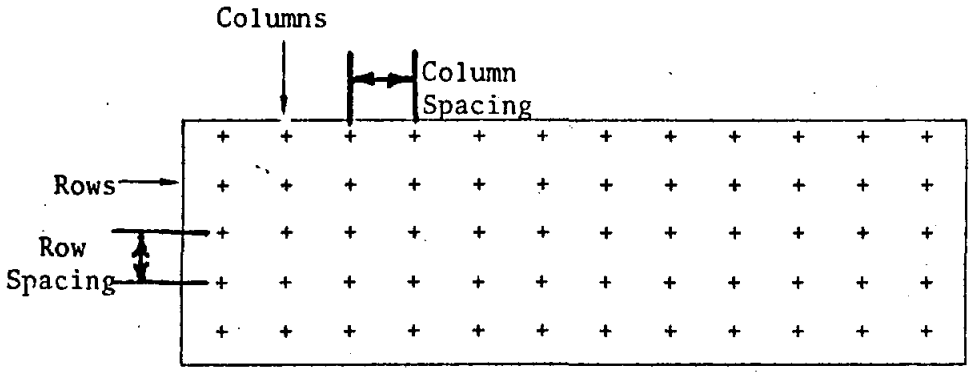

Sandbag Locations

	MMC	MDAC
Number of Rows	5	5
Row Spacing (in)	8 5/8	9 5/8
Number of Columns	11	12
Column Spacing (in)	10 7/8	10 3/8
Total Number of Sandbags (2-1/2 lbs ea.)	55	60
Total Simulated Wind Loads (lb)	137.5	150.0

Figure D-6.1. Simulated Wind Loads on Mirror Modules (sandbag loading)

Results

Sandbags were available for a simulated 25-mph wind loading. It was planned to then scale up the resulting stresses to an equivalent 50-mph wind. The measured strains were too low to be read with any accuracy with the

equipment used. However, it appeared that the stresses for a 50-mph wind load were less than 200 psi maximum for both designs. Since this stress was acceptable, the test was not modified or repeated.

Conclusions

Both designs effectively minimize glass stress due to wind loads. Higher test loads are needed to accurately determine wind-induced stress by this technique.

Test D-7: Thermal Stress/Contour

Objective

The objective of this test was to determine the change in mirror contour and stress in the glass with temperature change.

Description

Two mirror modules from each contractor, instrumented with strain gages, were temperature cycled between -9 and 122°F, per Test D-8, for two complete cycles at the beginning of this test. The mirrors were then held overnight at a constant temperature of 70°F. In the morning the contour (W_1) was measured per Test D-3 (contour and gravity sag), the strain gages were nulled, the temperature recorded,and the temperature raised to 122°F and held there for two hours. Again, the contour was measured, the strains read, and the temperature recorded. The temperature was then lowered to and held at 70°F for two hours before again measuring the contour, and recording the strains and the temperature.

The mirror modules were held at 70°F overnight and the same series of measurments were repeated for a temperature cycle between 70 and 32°F. Subsequently, the first cycle and measurements were repeated. Finally, the second cycle was repeated with two changes: the temperature was lowered to -9° rather than 32°F and the mirror contour was not measured.

Results

No meaningful data was obtained from the strain measurements. The strains were too low and the temperature compensation inadequate for measurements to be made by this technique.

Contour measurements along the centerline parallel to the long axis of the mirrors are shown for one of the MMC and one of the MDAC mirrors in Figures D-7.1 and D-7.2, respectively, at three different temperatures.

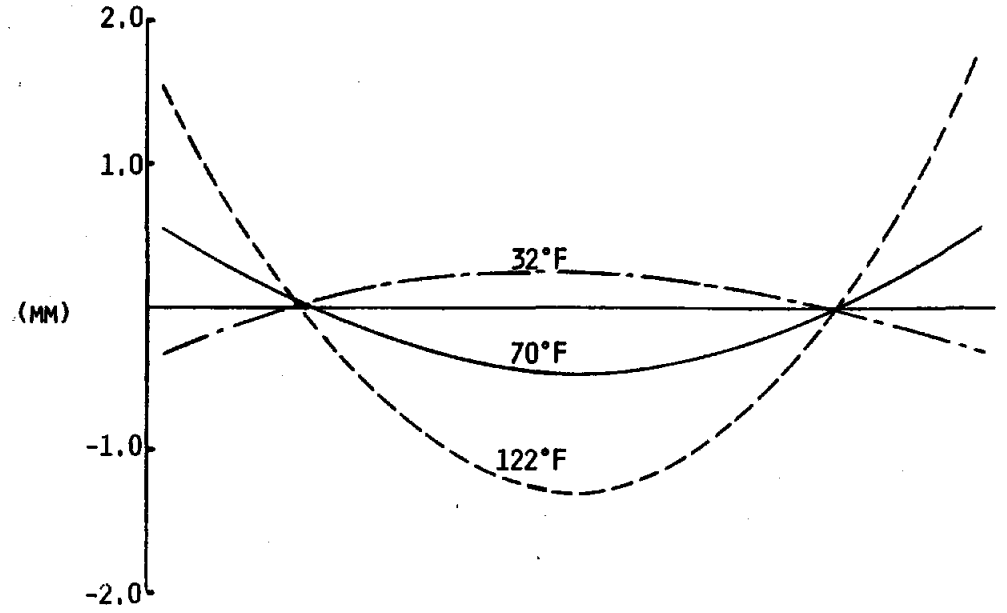

Figure D-7.1. MMC Mirror Contour at Different Temperatures

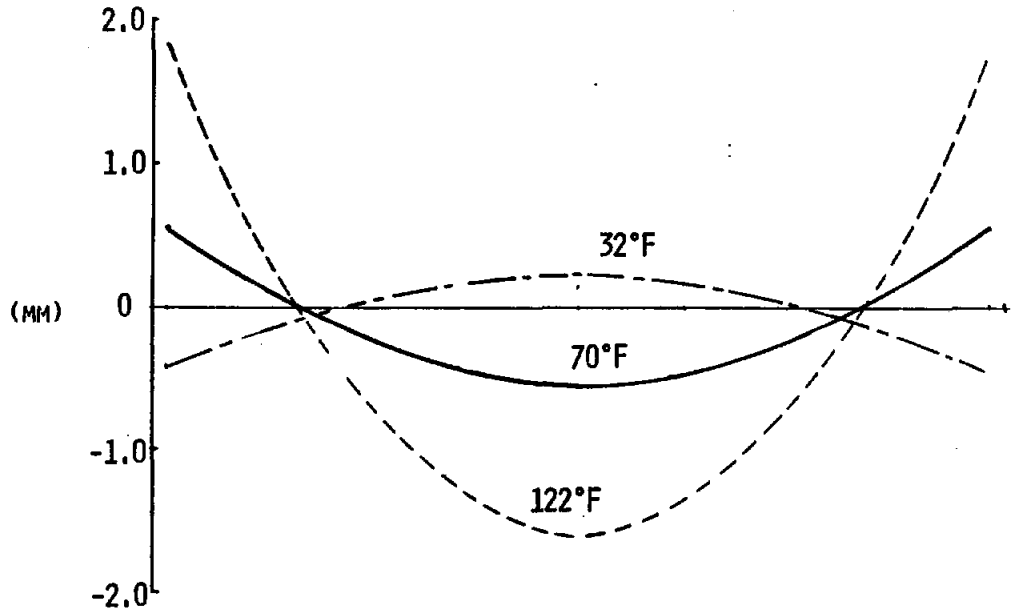

Figure D-7.2. MDAC Mirror Contour at Different Temperatures

A focal length was calculated for each mirror contour measurement by fitting a parabola by the least-squares method to the centerline data. The inverse of the focal length as a function of temperature is plotted for each mirror in Figures D-7.3 and D-7.4.

It can be seen that the MMC mirrors are always concave or focused over the temperature range (32°-122°F) at which the beam quality requirement must be met. The MDAC mirrors, however, are seen to become convex, or defocused, at temperatures between 45 and 50°F. This is due to an insufficient curvature induced during fabrication.

A second observation made is that the MDAC mirrors change contour more for a given temperature change than do MMCs. This is due primarily to the thinner core material used in the sandwich design.

Conclusions

The MDAC mirrors have insufficient curvature resulting in convex mirrors within the operating temperature range. For this reason, the MDAC heliostat does not meet the beam quality requirement at lower temperatures. The MMC mirrors have sufficient curvature to remain focused throughout the operating temperature range. The MDAC mirror modules exhibit a greater change in curvature with temperature than do the MMC mirrors.

Test D-8: Thermal Cycling

Objective

The objective of this test was to demonstrate structural and functional integrity of the mirror module; specifically, to determine if any damage or change in mirror curvature results from thermal cycling between the temperature extremes.

Description

Four mirror modules from each contractor were temperature cycled for 40 days (80 cycles) between -9°F and 122°F (with uncontrolled humidity), as shown below.

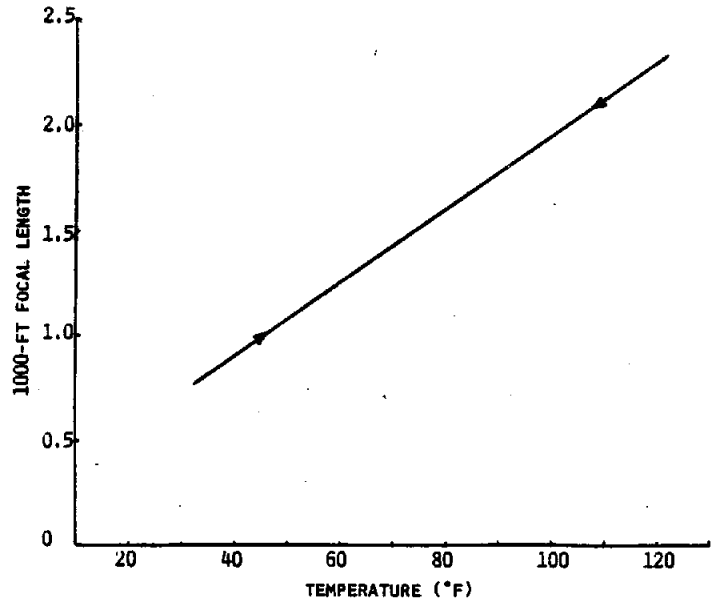

Figure D-7.3. MMC Mirror Module, Curvature vs Temperature

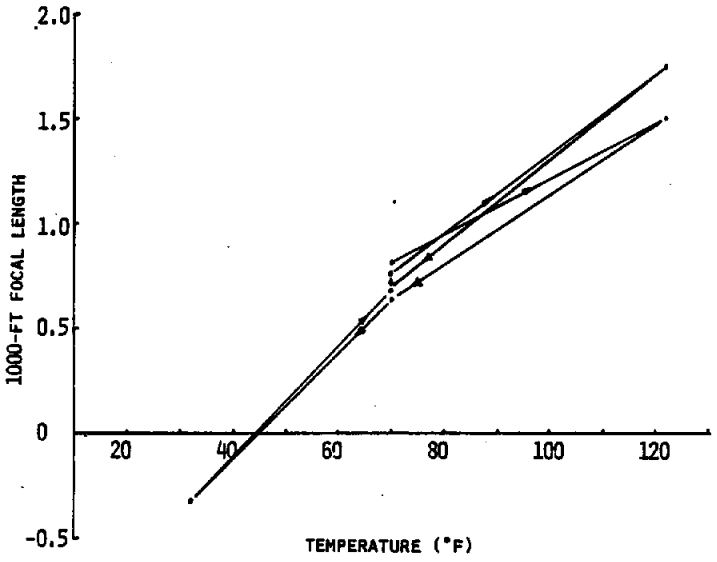

Figure D-7.4. MDAC Mirror Module, Curvature vs Temperature

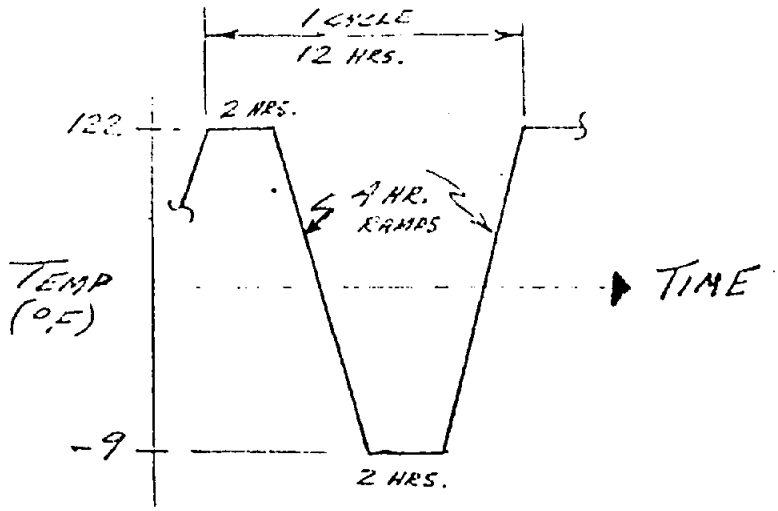

TEMPERATURE CYCLE

Before and after cycling, the mirror modules were closely inspected and the mirror contours (W_1) were measured. The mirror modules were held at a constant ambient temperature for at least six hours before the contour measurements were made, and this temperature was recorded with the contour data.

Results

No damage was observed in any of the mirror modules as a result of the temperature cycling. Contour measurements before and after cycling revealed no change in contour.

Conclusions

The two designs effectively minimize thermal stresses. The edge seals saw no thaw-freeze damage. There was no preferential creep in the adhesive layers or in the MDAC styrofoam core which would result in curvature change.

Test D-9: Temperature/Humidity Cycling

Objective

The objective of this test was to demonstrate moisture seal integrity of the two mirror module designs when subjected to a quasi-accelerated aging test consisting of alternating high and low humidity, ultraviolet radiation, and temperature cycling.

Description

Following Test D-8, four mirror modules from each contractor were temperature/humidity cycled for 30 days in accordance with the plan shown in Figure D-9.1. The significant aspects of the test plan were as follows:

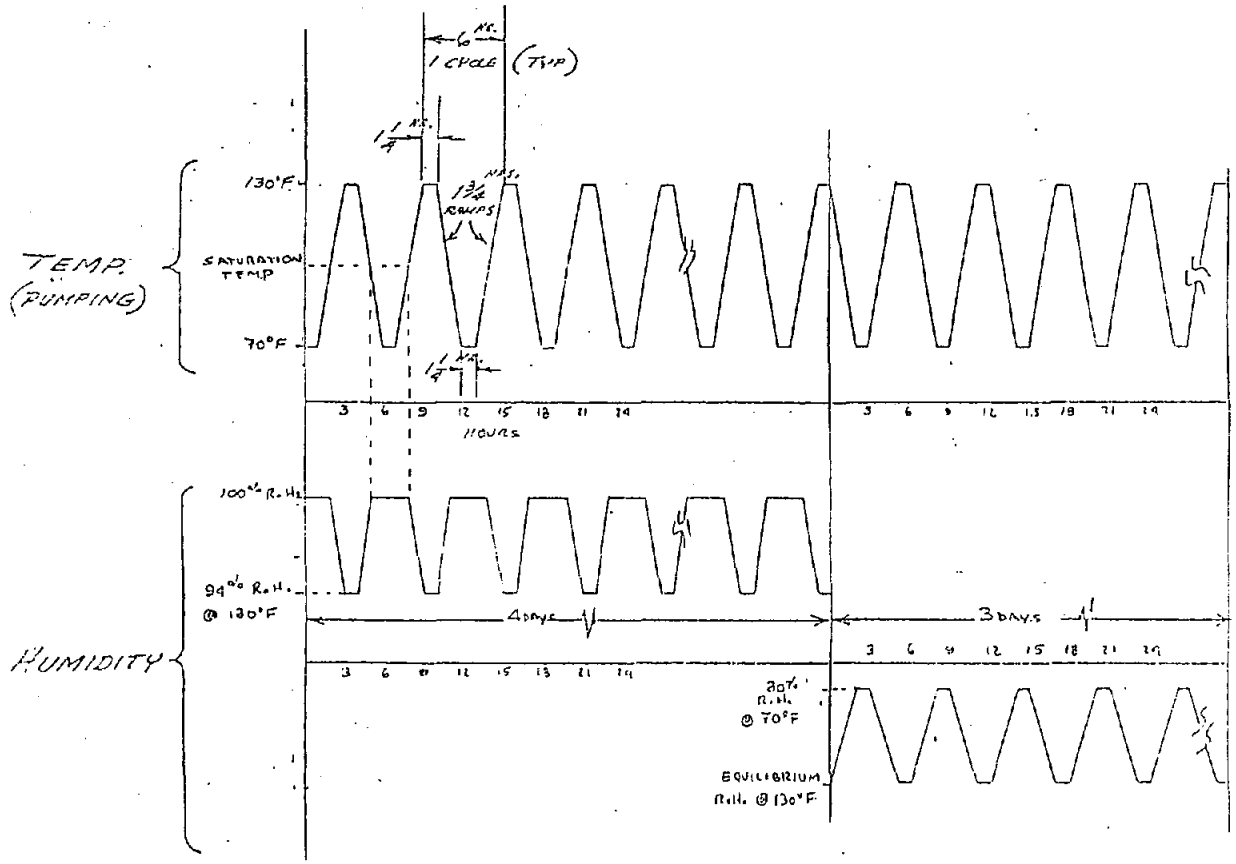

Figure D-9.1. Temperature and R.H. Cycles for Accelerated Aging Tests

Temperature Cycling--The temperature was cycled between 70 and 130°F for 30 days. The higher than normal temperature was used to provide faster aging acceleration and "thermal pumping" for the high humidity exposures. (Temperatures in excess of 130°F might have atypical effects on the sealant materials used.)

Relative Humidity--The R.H. cycle provided a very wet period (four days) and a very dry period (three days) alternating throughout the duration of the test. This cycle promotes degradation of the sealants due to photolytic oxidation (wet period) and sealant bake out (drying and cracking). During the wet cycle, R.H. was to be controlled to not less than 94 percent at 130°F, and not greater than 30 percent R.H. at 70°F for the dry cycle.

Ultraviolet Light--A source of UV light similar in spectra to solar UV at Air Mass 1 was scheduled to shine continuously on portions of the module edge seals. (UV intensities greater than this may also give atypical results.)

Wetness--Wetness was to be provided during the R.H. cycle since condensation was assumed to form on the module at the lower temperatures of the four-day wet period.

Instrumentation--Preceding this test, a specially designed humidity/pressure sensing probe (Figures D-9.2 and D-9.3) was installed in the edge cap of some of the mirror modules. The bellow-sealed striker/penetrator was not actuated until after the probe fixture was bonded, cured, and instrumented with R.H. and pressure gages. This probe was designed to preclude any contamination from the external environment within the mirror modules. After 30 days of cycling the mirror modules were visually inspected and their contours (W_1) were measured again.

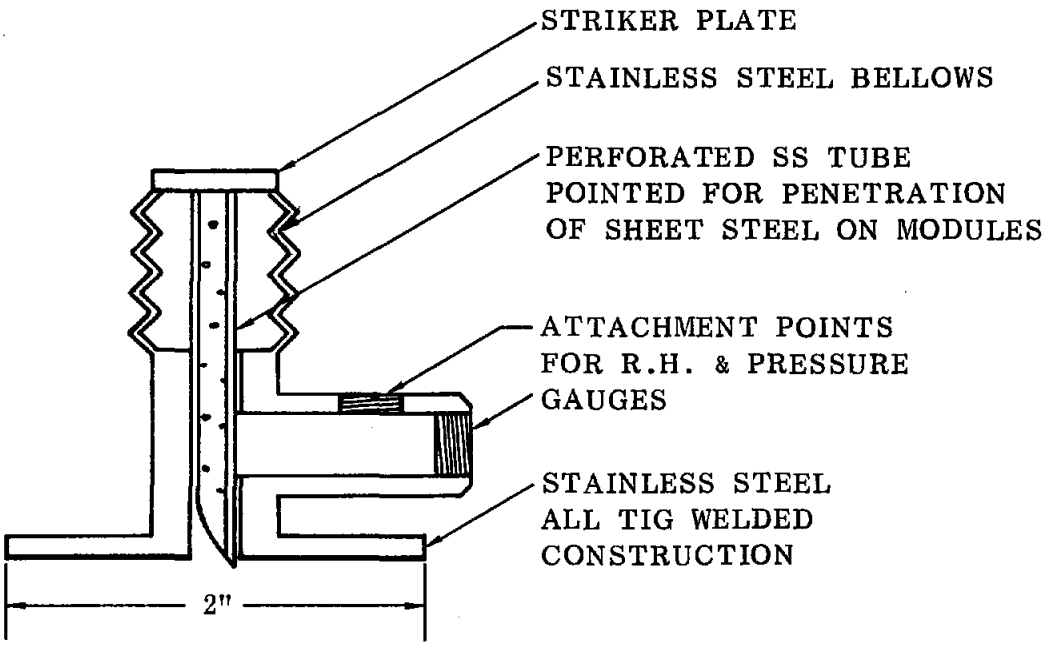

Figure D-9.2. Cross-sectional View of Fixture for Attaching R.H. and Pressure Gauges on Mirror Modules

Figure D-9.3. Pressure-Humidity Transducers Mounted to Mirror Module

In the test, the UV lamps were never successfully implemented as planned, and therefore aging of the sealants due to UV radiation was not assessed. Also, there is reason to believe that the humidity was improperly controlled, whereas the test plan called for a temperature/humidity cycle that required 100-percent R.H. (saturation) for part of the cycle. This condition was never achieved.

After the initial 30 days of cycling, another 30 days of cycling was performed. Again, the UV lamps could not be coaxed into working for more than a short time (and were finally abandoned when one exploded). However, a water spray was added to the wet part of the humidity cycle in hopes of simulating rain.

Results

No observed mirror degradation or edge seal damage resulted from this test. One MMC mirror module was cut open and was found to have no evidence of moisture inside. However, the pressure monitors on the mirror modules indicated that whereas the MDAC units changed pressure with temperature and appeared to be sealed, the pressure within the MMC units remained fairly constant, indicating that edge seal leaks were equalizing the interior with the ambient pressure. In addition, the relative humidity gauges on the MDAC modules never departed significantly from zero percent while the gauges on the MMC modules fluctuated considerably.

Conclusions

It was concluded from this test, and from the short-term, real-life weathering of the mirror modules on the CRTF heliostats, that the MDAC units are effectively sealed.

There is evidence from this test to indicate that the MMC mirrors were not sealed, and mirror deterioration (silver corrosion) on the CRTF heliostats confirmed this suspicion.

There are two possible reasons why the CRTF mirrors exhibited silver deterioration while the mirrors subjected to an accelerated aging test in the chamber did not: (1) MMC personnel examined the edge seals of the four chamber-tested mirror modules before testing and repaired visible defects in the edge sealant, and (2) if the silver deterioration is activated or accelerated by solar radiation, the chamber-tested mirror modules would not display silver corrosion as quickly as those mounted on the heliostats.

Test D-10: Cold Water Shock

Objective

The objective of this test was to determine whether glass fracture occurs when a hot mirror module is subjected to cold water shock due to washing or rainfall.

Description

Two mirror modules of each design were visually inspected for prior crack damage and then placed in an environmental chamber at 120°F for six hours. The modules were removed and sprayed with approximately ten gallons of 60°F water within five minutes of removal. The facets were then inspected for crack damage.

Results

There was no observed damage to any of the mirror modules resulting from this test. One of the MDAC mirrors had a previously induced crack (resulting from careless handling), and this crack did not propagate.

Conclusions

Both designs effectively minimize glass stress due to thermal shock. Sudden cold rain or daytime washing is not a design concern.

REFERENCES

1. E. D. Thalhammer,"Heliostat Beam Characterization System - Update," ISA/79 Conference Proceedings, Chicago, Illinois, October 1979.

2. G. S. Phipps, "Heliostat Beam Characterization System - Calibration Technique," ISA/79 Conference Proceedings, Chicago, Illinois, October 1979.

3. F. Biggs, C. N. Vittitoe, and D. L. King, "Modeling the Beam Characterization System," ISA/79 Conference Proceedings, Chicago, Illinois, October 1979.

4. F. Biggs and C. N. Vittitoe, "The Helios Model for the Optical Behavior of Reflecting Solar Concentrators," Sandia National Laboratories, Albuquerque, SAND76-0347, March 1979.

5. C. N. Vittitoe, F. Biggs, and R. E. Lighthill, "HELIOS: A Computer Program for Modeling the Solar Thermal Test Facility - A Users Guide," Sandia National Laboratories, Albuquerque, SAND76-0346, June 1977.

6. "NASTRAN User's Guide: Level 15," NASA Contract Report prepared by Universal Analytics Inc., Los Angeles, NASA-CR2504, April 1975.

7. The American Ephemeris and Nautical Almanac for the Year 1979, Nautical Almanac Office of U.S. Naval Observatory, U.S. Government Printing Office, Washington, D. C., 1977.

8. T. A. Dellin and M. J. Fish, "A User's Manual for DELSOL: A Computer Code for Calculating the Optical Performance, Field Layout, and Optimal System Design for Solar Central Receiver Plants," Sandia National Laboratories, Livermore, SAND79-8215, June 1979.

9. P. L. Leary and J. D. Hankins, "A User's Guide for MIRVAL--A Computer Code for Comparing Designs of Heliostat-Receiver Optics for Central Receiver Solar Power Plants," Sandia National Laboratories, Livermore, SAND77-8280, February 1979.

10. E. A. Igel and R. L. Hughes, "Optical Analysis of Solar Facility Heliostats," Solar Energy 22, p. 283-295, 1979.

11. A. D. Watt, "Circumsolar Radiation," Sandia National Laboratories, Albuquerque, SAND80-7009, April 1980.

12. D. F. Grether, J. E. Nelson, and M. Wahlig, "Measurement of Circumsolar Radiation," Progress Report No. 1, NSF Grant AG-536, Lawrence Berkeley Laboratory, NSF/RANN/SE/AG-536/PR/74/4, January 31, 1975.

UNLIMITED RELEASE

INITIAL DISTRIBUTION

J. E. Bear, 1535
M. L.Shannon, 1541; Attn: H. W. Nunez, Jr., and H. B. Thomas
G. E. Brandvold, 4710
D. L. King, 4713
B. W. Marshall, 4713
T. B. Cook, 8000; Attn: A. N. Blackwell, 8200
B. F. Murphey, 8300
W. E. Alzheimer, 8120; Attn: C. S. Hoyle, 8122
W. E. Jorgenson, 8123
W. D. Zinke, 8123
L. Gutierrez, 8400; Attn: R. A. Baroody, 8410
D. E. Gregson, 8440
C. M. Tapp, 8460
S. G. Cain, 8412; Attn: L. J. Rosnoski, D. J. Timmer, J. E. Vanderpoorten
C. S. Selvage, 8420
V. P. Burolla, 8424
R. C. Wayne, 8450
T. D. Brumleve, 8451
W. R. Delameter, 8451
P. J. Eicker, 8451 (10)
C. L. Mavis, 8451
W. L. Morehouse, 8451
H. Norris, 8451
W. S. Rorke, 8451
D. N. Tanner, 8451
S. White, 8451
Publications Division, 8265, for TIC (27)
Publications Division, 8265/Technical Library Processes and Systems Division, 3141
Technical Library Processes and Systems Division, 3141 (2)
M. A. Pound, 8214, for Central Technical Files (3)